



UNIVERSITY OF LEEDS

Multi-scale 3D Imaging for Characterization of Microstructural Properties of Gas Shales

Mohamed S Garum

PhD thesis

Degree of Doctor of Philosophy in the Faculty of Engineering
and Physical Sciences

The University of Leeds

School of Chemical and Process Engineering

September 2021

Abstract

In recent years, gas shale has attracted renewed attention as an unconventional energy resource, with massive, fast growing and largely untapped reserves. Shale is a fine-grained sedimentary rock containing a high content of organic matter (kerogen) from which gas can be extracted. The identification of the pore structure and quantification of the geometry, sizes, volume, connectivity and distribution of extremely fine-grain pores, kerogen and minerals are all extremely significant for characterisation of gas shale reservoirs. These features determine fluid flow and ultimate hydrocarbon recovery, however they are also highly challenging to determine accurately. X-ray micro and nano-computed tomography (μ -CT and Nano-CT) combined with 3D focused ion beam scanning electron microscopy (FIB-SEM) are used in this thesis to address this challenge and to provide more information for understanding the complex microstructures in 3D from multiple scales within shale samples.

In this thesis, a state-of-the-art multi-scale imaging with multi-dimensional potential was applied to image and quantify the microstructures properties of gas shale. Samples were first imaged with X-ray micro- and nano-tomography (μ -CT and Nano-CT), and then with Focused Ion Beam Scanning Electron Microscopy (FIB-SEM) measurements. Results of image analysis using SEM (2D), μ -CT (3D), ultrahigh resolution Nano-CT (3D) and FIBSEM (3D) under backscattered electron (BSE) images reveal a complex fine grained structure at specified phases such as pores, kerogen, and minerals within samples.

The results show a low connectivity of pores and high connectivity of kerogen which suggests that porous gas flow through samples used in this study cannot be the main transport through the pores. This implies that the gas transport through the pores is unlikely to be important, but cannot be ignored, as it is very important and constitutes the basis for understanding permeability in the rock. However, the high connectivity of kerogen provides the potential pathways for gas flow throughout the whole sample.

The combination of multiscale 3D X-ray CT techniques (micro-nano) with 3D FIB-SEM provides a powerful combination of tools for quantifying microstructural information including pore volume, size, pore aspect ratio and surface area to volume distributions, porosity, permeability in shales, and also allowing the visualisation of pores, kerogen and minerals phases over a range of scales. Other methods, such as physical measurements Gas Research Institute (GRI), mercury injection (MIP), and nitrogen adsorption (N_2) are also presented in this study.

The combination of these data sets has allowed the examination of the microstructure of the shale in unprecedented depth across a wide range of scales (from about 20 nm to 0.5 mm). Overall, the shale samples from Bowland shale formation shows a porosity of $0.10 \pm 0.01\%$, $0.52 \pm 0.05\%$, and $0.94 \pm 0.09\%$ from three FIB-SEM measurements, $0.67 \pm 0.009\%$ from the nano-CT data and $0.06 \pm 0.008\%$ from one μ -CT measurement, which compare with $0.0235 \pm 0.003\%$ from nitrogen adsorption, and $0.60 \pm 0.07\%$ from MIP. The porosity was also observed

to be $0.43 \pm 0.009\%$ and $0.7\% \pm 0.007\%$ for FIB-SEM and Nano-CT methods, respectively in different shale reservoir from a Sweden formation.

The data vary due to the different scales at which each technique interrogates the rock and whether the pores are openly accessible (especially in the case of the nitrogen adsorption). The measured kerogen fraction is $32.4 \pm 1.45\%$ from nano-CT compared with $34.8 \pm 1.74\%$, $38.2 \pm 1.91\%$, $41.4 \pm 2.07\%$, and $44.5 \pm 2.22\%$ for three FIB-SEM and one μ -CT measurement. The pore size imaged by nano-CT ranged between 100 and 5000 nm, while the corresponding ranges were between 3 and 2000 nm for MIP analysis and between 2 and 90 nm for N_2 adsorption. The distribution of pore aspect ratio and scale-invariant pore surface area to volume ratio (σ) as well as the calculated permeability shows the shale sample in this study to have a high shale gas potential.

Aspect ratios indicate that most of the pores that contribute significantly to pore volume are oblate, which is confirmed by the range of σ (3–30). Oblate pores have greater potential for interacting with other pores compared to needle-shaped prolate pores as well as optimizing surface area for gas to desorb from the kerogen into the pores. Permeability has also been calculated and values of 2.61 ± 0.42 nD were obtained from the nano-CT data, 2.65 ± 0.45 nD from MIP, 13.85 ± 3.45 nD, 4.16 ± 1.04 nD, and 150 ± 37.5 nD from three FIB-SEM measurements and 2.98 ± 0.75 nD from one μ -CT measurement, which are consistent with expectations for generic gas shales (i.e., tens of nD).

The quantitative results of 2D and 3D imaging datasets across nm- μ m-mm length scales provided a view of understanding the heterogeneous rock types, as well as great value to better understand, predict and model the pore structure, hydrocarbon transport and production from gas shale reservoirs.

Declaration

I hereby declare that this work is original research undertaken by me and that no part of this thesis has been submitted for consideration towards another degree at this or any other institution.

Mohamed Garum

September 2021

Acknowledgements

First and foremost I would like to thank my supervisors Paul Glover, Piroska Lorinczi and Ali Hassanpour for their guidance and support throughout my studies. This work could not have been accomplished without their continuous motivation, endless patience and fantastic support during the difficult times. Your leadership and mentorship has helped me grow my academic potential. I will remain forever grateful for your trust and confidence in me and for inspiring me to always keep moving forward and to never give up. You are truly the greatest supervisors a student could ask for. In addition, I would also like to acknowledge to Henry Royce Institute and Libyan Embassy, who has provided the funding for this work.

I would also like to extend my sincere appreciation to the research colleagues from Imperial College London in particular **Martin Blunt, Qingyang Lin** and **Ali Raeini** and also **Kevin Taylor, Lin Ma** from the University of Manchester. I would like also to thank the Electron Microscopy and Spectroscopy Centre (LEMAS) at University of Leeds for hours of technical assistance and hands-on experimental training given to me in the laboratory and also with special thanks to **Mr John Wyn Williams** of Leeds University School of Earth and Environment for the sample preparation.

I would also like to thank any research members from the School of Chemical and Process Engineering and School of Earth and Environment who have guided and helped me during my studies, including Quentin Fisher and Carlos Grattoni.

I would also like to extend a big thank you to all the financial supporting bodies, including Pump Prime Energy Leeds award (University of Leeds), Armourers & Brasiers Gauntlet Trust grant, Henry Royce Facilities grant (University of Manchester) and London petro physical society grant for all their financial support during my PhD study.

Most importantly, I would like to dedicate this PhD thesis to my family. Words cannot capture or convey my feelings of gratitude for their immeasurable support. It is no secret that the last 3 years have been the most difficult and gruelling slog of my life, and there have been many times when I just wanted to run away. Without their encouragement to continue, persist and never give up, I would not be here today with a PhD.

From the bottom of my heart, thank you all.

The Author

Mohamed graduated with a Bachelor degree in Petroleum Engineering at Tripoli University in Libya in 2014, with a thesis titled 'Comparative Analysis of Reserve Estimation Using Volumetric Method and Material Balance on Al-Shararh Oil Field.' Mohamed was then recommended from Tripoli University for a Master degree at Cardiff University and graduated in 2017.

Mohamed started his PhD studies in Petroleum Engineering area on 'Shale gas' in School of Chemical and Process Engineering at University of Leeds in February 2018. His research interest has been focusing on the Multi-scale and Multi-dimensional Imaging of Characterization the materials including shale rock. During these three years, he has received training in various techniques such as SEM, EDX, FIB-SEM, μ -CT, Nano-CT and nitrogen (N₂) adsorption.

He has also received training in imaging processing and analysis data using multiples approaches such as Avizo® 8, 9.40, ImageJ®, and Fiji® (segmentation and analysis of multiple phases in 2D/3D image analysis). These skills and knowledge provided him an opportunity for a good understanding of multi-scale, multi-dimensional imaging for the characterization of materials over a range of scales. He has also worked part-time in both Schools as a demonstrator and support MSc and BSc students.

Mohamed has presented his research work at several national and international conferences and also has received several awards, including the award for the Best Student Presenter at the 5th World Congress & Expo on Oil, Gas & Petroleum Engineering Conference in Milan, Italy. He was twice (2019 and 2020) granted around £15,000 from the Henry Royce Institute (University of Manchester) for equipment access to X-ray facilities at Royce@ Manchester. He was also granted several travel grants during his research including 3 times of £500 from the Armourers & Brasiers Gauntlet Trust in 2018, 2019, and 2020, £400 from Pump Prime Energy Leeds in 2019, £1000 from London Petrophysical Society (LPS) in 2020, £400 from European Association of Geoscientists and Engineers (EAGE) in 2020.

Paper publication and Author contributions

Published Papers in High-Quality Peer-Reviewed Journals

1. **Garum***, M., Glover, P.W.J., Lorinczi, P., Scott, G. and Hassanpour, A., 2021. Ultrahigh resolution 3D imaging for quantifying the pore nanostructure of shale and predicting gas transport. *Energy & Fuels* 2021, 35 (1), 702-717. DOI: [10.1021/acs.energyfuels.0c03225](https://doi.org/10.1021/acs.energyfuels.0c03225).
2. **Garum***, M., Glover, P.W.J., Lorinczi, P., Drummond-Brydson, R. and Hassanpour, A., 2020. Micro-and Nano-Scale Pore Structure in Gas Shale Using X μ -CT and FIB-SEM Techniques. *Energy & Fuels* 2020, 34(10), 12340-12353. DOI: [10.1021/acs.energyfuels.0c02025](https://doi.org/10.1021/acs.energyfuels.0c02025).
3. **Garum***, M., Glover, P.W.J., Lorinczi, P., Micklethwaite, S. and Hassanpour, A., 2021. Integration of Multi-Scale Imaging of Nano Pore Microstructure in Gas Shales. *Energy & Fuels* 2021, 35(13), 10721-10732. DOI: [10.1021/acs.energyfuels.1c00554](https://doi.org/10.1021/acs.energyfuels.1c00554)

Manuscripts in Preparation for High-Quality Peer-Reviewed Journals

4. **Garum**, M., Glover, P.W.J., Lorinczi, P. and Hassanpour, A., 2021. Determining the porosity and permeability of shales using methodological pluralism (intend to submit to Marine and Petroleum Geology, currently in last stage).
5. **Garum**, M., Glover, P.W.J., Lorinczi, P. and Hassanpour, A., 2021. Multi-scale 3D quantification of pore nanostructure from Horn River shale reservoir: Examples from Western-Canada Sedimentary Basin (currently under processing).

Conference Contributions

6. **Garum**, M., Glover, P.W.J., Lorinczi, P. and Hassanpour, A., 2020. Ultrahigh resolution 3D imaging and characterisation of nanoscale pore structure in shales and its control on gas transport. In EGU General Assembly Conference Abstracts (p. 45).
7. **Garum**, M., Glover, P.W.J., Lorinczi, P. and Hassanpour, A., 2020. Investigation of Nano-Scale Structures by Using Nano-CT and FIB-SEM Approaches to Characterizing of Gas Shale. In 82nd EAGE Annual Conference & Exhibition (Vol. 2020, No. 1, pp. 1-5). European Association of Geoscientists & Engineers.
8. **Garum**, M., Lorinczi, P.W.J., Glover, P.W.J. and Hassanpour, A., 2020. Ultra-High Resolution 3D of Shales with Nano-CT and Its Control on Gas Transport. In 82nd EAGE Annual Conference & Exhibition (Vol. 2020, No. 1, pp. 1-5). European Association of Geoscientists & Engineers.
9. **Garum**, M., Glover, P.W.J., Hassanpour, A. and Lorinczi, P., 2019. Fluid Flow and Microstructural Properties of Gas Shales. In 81st EAGE Conference and Exhibition 2019 (Vol. 2019, No. 1, pp. 1-5). European Association of Geoscientists & Engineers.
10. **Garum**, M., Glover, P.W.J., Hassanpour, A. and Lorinczi, P., 2018. Institute Applied Geoscience (IAG) Conference on "Fluid Storage and Flow Gas Shales", School of Earth and Environment, Leeds, 29-30 November 2018.
11. **Garum**, M., Glover, P.W.J., Hassanpour, A. and Lorinczi, P., 2019. NERC Unconventional Hydrocarbons in the UK Energy System conference "Comparison of μ -CT, Nano-CT and high resolution FIB approaches for characterizing of shales", UK, Nottingham, 17-18 Sep 2019
12. **Garum**, M., Glover, P.W.J., Hassanpour, A. and Lorinczi, P., 2018. Petroleum Leeds Conference on "Microstructural Properties of Gas Shales", School of Chemical and Process Engineering, Leeds, 17-18 January 2018.

List of Grants

The list of the funding that have received during this study as follows as:-

1. Armourers & Brasiers' Gauntlet Trust. Grant Number 18041, 2018-2019 (**£500**).
2. Energy Leeds Pump Prime. Grant Number EP1 / SPEME/1906, 2018-2019 (**£400**).
3. Libya embassy for Access Equipment Scheme. Grant Number LB/11/018, 2018-2019 (**£3,000**).
4. 5th World Oil, Gas & Petroleum Engineering Conference. Grant Number MG/1901, 2018-2019(**£300**).
5. Armourers & Brasiers' Gauntlet Trust. Grant Number 19011, 2019-2020 (**£500**).
6. Henry Royce Institute for Access Equipment at (X-ray facilities at Royce@Manchester). Grant Number EP/19/0044, 2019-2020(**£15,000**).
7. Libya embassy for Access Equipment Scheme. Grant Number LB/05/019, 2019-2020 (**£3,000**).
8. London petro physical society. Grant Number LPS/1359, 2019-2020(**£1,000**).
9. Henry Royce Institute for Access Equipment at (X-ray facilities at Royce@Manchester). Grant Number EP/20/008, 2019-2020 (**£3,000**).
10. EAGE PACE grant for 82nd EAGE Annual Conference and Exhibition. Grant Number EAGE/GD/MG19, 2020-2021 (**£250**).
11. Libya embassy for Access Equipment Scheme. Grant Number LB/19/020, 2020-2021 (**£3,000**).
12. Armourers & Brasiers' Gauntlet Trust. Grant Number 20810, 2020-2021 (**£350**).
13. Leeds Doctoral College Grant. Grant Number 15/109, 2020-2021(**£500**).

Table of Contents

Abstract	2
Declaration.....	4
Acknowledgements	5
The Author	6
Paper publication and Author contributions	7
Table of Contents	8
List of Figures	13
List of Tables	18
List of Abbreviations.....	19
Chapter 1	20
1 Introduction and Research Objectives.....	20
1.1 Introduction.....	20
1.2 Research Aim and Objectives	21
1.2.1. Overall Aim	21
1.2.2. Specific Objectives	21
1.3 Thesis layout.....	22
Chapter 2	24
2 Literature Review	24
2.1 Introduction.....	24
2.2 Overview of shale gas reservoirs	24
2.2.1 The shale gas system.....	26
2.2.2 Porosity.....	28
2.2.3 Pore sizes	30
2.2.4 Pore types.....	32
2.2.5 Pore connectivity	35
2.2.6 Permeability.....	36
2.2.7 Gas storage and transport through pores	38
2.3 Gas shale imaging techniques	39
2.4 Upscaling techniques	46
2.4.1 GRI technique on crushed shale	46
2.5 Summary	48
Chapter 3	49
3 Experimental techniques and methodology	49

3.1 Introduction.....	49
3.2 Shale sample collection and preparation.....	49
3.2.1 Sample collection	49
3.2.2 Shale sample preparation.....	51
3.3 Overview of experimental methods	54
3.3.1 Petrophysical and geochemical techniques	54
3.3.2 Pore characterisation, gas storage and flow analysis	55
3.3.3 2D imaging techniques.....	58
3.3.4 3D imaging methods	59
3.5 Comparison of Multi-scale imaging μ -CT, Nano-CT and FIB-SEM techniques.....	64
3.6 Imaging processing	65
3.6.1. Stack alignment.....	65
3.6.2 Filtering.....	66
3.6.3 Thresholding & Segmentation	67
3.7 Quantification based on the imaging.....	68
3.7.1 Equivalent diameter	69
3.7.2 Aspect ratios	69
3.7.3 Surface-area-to-volume ratio	71
3.7.5 Permeability prediction.....	74
3.8 Summary	74
Chapter 4	75
4 Micro- and nano-scale pore structure in gas shale using μ -CT and FIB-SEM techniques.....	75
4.1 Introduction.....	76
4.2 Materials and methods	77
4.2.1 Rock samples and preparation	77
4.3 Imaging techniques.....	77
4.3.1 X-ray μ -CT	77
4.3.2 Dual beam FIB-SEM.....	79
4.4. Results.....	81
4.4.1 3D reconstructions of gas shale volumes	81
4.4.2 Pore volume distribution.....	84
4.4.3 Pore aspect ratio distributions	88
4.4.4 Pore surface area to volume ratio	92
4.5 Permeability	96
4.6 Discussion.....	98
4.7 Conclusions.....	101

Chapter 5	102
5 Integration of Multi-Scale Imaging of Nanoscale Pore Microstructure in Gas Shales.....	102
5.1 Introduction.....	103
5.2 Material and methods.....	104
5.2.1 Sample material and preparation	104
5.2.2 X-Ray Diffraction	104
5.2.3 Nitrogen gas adsorption measurements.....	104
5.2.4 Mercury injection capillary pressure measurements.....	104
5.2.5 Multi-scale 2D/3D imaging techniques	104
5.3 Results.....	107
5.3.1 Mineral composition analysis and kerogen fraction	107
5.3.2 3D Microstructure of gas shale volumes	107
5.3.3 Pore volume distribution.....	109
5.3.4 Pore size distribution.....	110
5.3.5 Pore aspect ratio distributions	114
5.3.6 Pore surface area to volume ratio	116
5.4 Discussion and interpretation	117
5.5 Conclusions.....	118
Chapter 6	120
6 Ultrahigh resolution 3D imaging for quantifying the pore nanostructure of shale and predicting gas transport.....	120
6.1 Introduction.....	121
6.2 Material and methods.....	121
6.2.1 Rock samples and preparation	121
6.2.2 Experimental procedure.....	124
6.2.3 Supporting measurements	125
6.3 Results.....	126
6.3.1 Comparison of 3D microstructure of gas shale volumes.....	126
6.3.2 Pore volume and size distribution	129
6.3.3 Pore aspect ratio distributions	134
6.3.4 Pore surface area to volume ratio	137
6.4 Gas Transport Simulation in Kerogen	139
6.5 Kerogen and pore connectivity	143
6.6 Conclusions.....	144
Chapter 7	146
7 Measurement and calculation of gas shale permeability.....	146

7.1 Introduction.....	147
7.2 Material and methods.....	148
7.2.1 Rock samples and preparation	148
7.2.2 Overview of methods used.....	149
7.2.3 Crushed GRI simulation	152
7.3 Results.....	153
7.3.1 Mineral composition analysis	153
7.3.2 Permeability estimation theory	154
7.3.3 Hydraulic connectivity estimation theory	156
7.3.4 Permeability results	157
7.4 Discussion and interpretation	160
7.5 Conclusion	163
Chapter 8	164
8 Conclusions and Future Work	164
8.1 Conclusions.....	164
8.2 Future work suggestions	166
8.2.1 Correlative imaging	166
8.2.2 Modelling based imaging	167
9. References.....	168

List of Figures

Figure 2 1 Shows how the gas producer it from the well by hydraulic fracturing (Lehr, 2019).....	27
Figure 2 2. Map of the gas production in various countries with unit of Bcf (source: BP Statistical Review of World Energy, 2019).....	28
Figure 2 3. The porosity and pore size distribution (PSD) measurements used by to different techniques within shale ga (IUPAC, 1994, Loucks et al., 2012).....	30
Figure 2 4 A diagrammatic representation the pore structure in shales, open pores, closed pores, and pore size distribution in shales (Loucks et al., 2012).....	31
Figure 2 5 Backscattered electron (BSE) images from different shale reservoir samples showing the kerogen content and porosity. Arrows have been added for the identification of kerogen (black arrows) and pores (white arrows) (Curtis et al., 2012).	33
Figure 2 6 A schematic diagram representation of the interparticle and intraparticle pores (Loucks et al., 2012).	34
Figure 2 7 Examples of interparticle and intraparticle pores within shale from different shale reservoir samples (Loucks et al., 2012, Jiao et al., 2014).	34
Figure 2 8 Example of the pore fracture within shale (Zhang et al., 2018).	35
Figure 2 9 Shown gas distribution from macro-scale to micro-scale in the shale reservoir (Guo et al., 2015).....	39
Figure 2 10 Overview of techniques for imaging and characterisation of shale rock sample with the corresponding scales (Ma et al. 2017).....	43
Figure 2 11 μ -CT imaging of gas shale with two different types of resolutions, a) scan at higher resolutions with voxel size (0.62 μ m), showing pores, cracks and pyrite, b) an imaging at low resolutions (6.27 μ m) with largest pores corresponding to the fractures (cracks) (Ougier-Simonin et al., 2016).	44
Figure 2 12 An example of FIB-SEM showing the cross section of shale structure from different shale formations: a) Haynesville shale sample and b) Eagle Ford shale reservoir sample. White arrows indicate pores (Curtis et al., 2011).	44
Figure 2 13 3D reconstruction of FIB-SEM images showing shale structures: a) 3D image of solid, b) 3D image of kerogen, c) 3D image of pore network and d) 3D image of pyrite (Curtis et al., 2012).....	46
Figure 3 1 Illustration of the procedure of shale sample preparation. (a) Shale sample of around 4 mm using a diamond saw for cutting to slice cubes of length 2 mm. (b) A thin layer was sliced from the main sample and also using a diamond saw. (c) Glass slide and thermo-plastic wax used to hold the sample on the slide of the glass. (d) PetroThin [®] used for cutting, thin section of each side of shale. (e) The micrometer used to measure the size of shale. (f) A typical sample of size of around 500 μ m attached to a glass slide with wax for transport.	52
Figure 3 2 Sample preparation for Nano-CT and SEM using FIB: (a) shale surface area of interest (25 \times 25 μ m ²) that used in this study with a thin protective layer of platinum around (1 μ m in thickness) to offer protection and mitigation specimen charging (b-c) the area around the sample milled out; (d) the sample attached to the tip of a micromanipulator; (e) the cylinder cut free from the bulk rock; (d-h) the bottom of the cylinder welded to the tip of a grid; (i) the region of interest of around 25 μ m.	53
Figure 3 3 Classification of experimental methods used in this study.	54
Figure 3 4 Schematic of nitrogen sorption and desorption for pore size and volume distribution measurement.....	56

Figure 3 5 Five pore types based on hysteresis loops following de Boer’s identification (De Boer and Lippens, 1964).	57
Figure 3 6 The isotherms of adsorption and desorption of Nitrogen N ₂ sorption experiment used in this study.	57
Figure 3 7 Diagram of the SEM images with EDX mapping for chemical composition analysis, where (Si) the light pink region is silicon, the area shown in yellow is Iron (Fe), the green area is oxygen (O), the carbon (C) is shown in red, the pink is potassium (K) and the brown is magnesium (Mg).	59
Figure 3 8 Schematic illustration of X-ray tomography images acquisition and reconstruction. X-ray tomography images are generated based on the principle that X-ray intensity is linearly attenuated when passing through materials of different density and atomic mass. The sample rotates around a specific axis and the detector measures the degree of attenuation, creating 2D (projections) in greyscale and then the 2D projections are reconstructed to produce a 3D volume (Landis & Keane 2010).	59
Figure 3 9 The schematic diagram of X-ray nano-tomography.	61
Figure 3 10 The Zeiss Versa 410 X-ray micro-tomography (μ-CT) device used in this work to capture 3D scans of gas shale sample. (Inset) The μ-CT consists three main components: an X-ray micro-focus source, a rotation stage to mount and control the sample and an x ray detector used in this research study.	60
Figure 3 11 (a) FIB-SEM device to capture 3D images of the gas shale sample used in this work; (b) the main components of the FIB-SEM: an electron beam, focused ion beam (FIB), platinum (Pt) gas injection needle deposited on the top of the shale surface (protective layer), and a sample stage to mount and control the sample.	63
Figure 3 12 (a) Schematic diagram of the FIB-SEM procedure where the ion beam is set at a 52° angle and an electron beam is kept as normal for scanning, (b) serial of cross-sectioning of a shale sample using a dual-beam FIB-SEM system. The ion beam (FIB) is used to remove material from the shale surface creating a cross-sectional face that can be imaged by the electron beam (SEM).	63
Figure 3 13 Overview of multiscale imaging techniques (μ-CT, Nano-CT and FIB-SEM) used in this study.	65
Figure 3 14 (a) Example of a raw image of a gas shale, together with (b) the non-local means filtered version of the same image.	66
Figure 3 15 Schematic diagrams for segmentation methods: (a) Global thresholding, (b) watershed segmentation, (c) manual segmentation.	68
Figure 3 16 Diagram illustration of an irregular pore (textured) with a fitted ellipsoid with major radii a, b and c. The subsidiary diagrams show the form of an oblate ellipsoid and prolate ellipsoid.	70
Figure 3 17 Surface area to volume ratio as a function of aspect ratio for oblate and prolate spheroids, approximating to penny-shaped and needle-shaped pores, respectively.	74
Figure 4 1 μ-CT image of sample MD-2.7 km of Bowland shale showing BSE images of a cross-section at each of the three locations A, B and C which were chosen for subsequent FIB-SEM serial sectioning.	78
Figure 4 2 SEM image of the sample of Bowland shale used for μ-CT imaging showing the different locations A, B and C that were used for FIB-SEM serial sectioning.	79
Figure 4 3 Serial cross-sectioning of a shale sample using a dual-beam FIB-SEM system. The ion beam is used to remove material from the shale surface creating a cross-sectional face that can be imaged by the electron beam.	80

Figure 4 4. BSE images of FIB cross-sections taken from different locations A, B and C (see Figures 4.1 and 4.2), pores and cracks are highlighted by yellow and red circles.	81
Figure 4 5 Schematic diagram of the procedure for analysing 3D datasets from μ -CT imaging techniques.	82
Figure 4 6 X-ray micro-tomography (μ -CT) for a shale rock sample acquired at a voxel size of 0.94 μ m. (a) Raw 2D greyscale image, (b) Non-local means filtered 2D greyscale image. (c) the kerogen shown in red, and (d) pores shown in blue.....	83
Figure 4 7 FIB-SEM assessment of the raw MD-2.7 km shale rock sample. (a) Raw 2D greyscale image, (b) non-local means filtered 2D greyscale image, (c) 3D representation of kerogen shown in red, and (d) 3D representation of pores shown in blue.	84
Figure 4 8 The distribution of pore volume on the basis of numbers of pores representing a given pore volume, for (a) FIB-SEM, and (b) μ -CT for sample MD-2.7 km of a gas shale rock from the Bowland formation. Insets show the same data on a log-log scale. The distribution of pore volume on the basis of the volume of pores representing a given pore volume, for (c) FIB-SEM, and (d) μ -CT.	88
Figure 4 9 The pore-aspect ratio distribution, (a) pore-aspect ratio distributed as a function of the number of pores obtained from γ_1 (oblate) values, (b) pore-aspect ratio distributed estimated from γ_1 values as a function of the total volume of pores, (c) pore-aspect ratio distributed as a function of the number of pores as calculated from γ_2 (prolate) values, (d) pore-aspect ratio distributed estimated from γ_2 as a function of the total volume of pores, as estimated by FIB-SEM and μ -CT using the sample MD-2.7 km of gas shale from the Bowland formation.	91
Figure 4 10 Showing the scale-invariant pore surface area to volume distribution, σ , calculated from FIB-SEM and μ -CT measurements of sample MD-2.7 km; (a) distribution with respect to the percentage of the total numbers of pores, (b) distribution with respect to the percentage of the total volume of the pores.....	95
Figure 4 11 SEM image of location C with the dimensions of cracks. Uncertainties of ± 0.02 μ m apply.	97
Figure 5 1 An overview of the Bowland gas shale sample used in this study for Nano-CT showing the region (in the top left side) and also the different locations A, B, and C that were used for FIB-SEM serial sectioning.....	105
Figure 5 2 Multiscale imaging techniques (FIB-SEM, Nano-CT and μ -CT) on the same rock sample volume used in this chapter.....	106
Figure 5 3 Overview of the X-ray nano-tomography (Nano-CT) for a shale rock sample: (a) 3D image of shale sample with a thickness of around 25 μ m, (b) representative 3D image indicating all phases in the sample. By setting thresholds on the greyscale of this 3D solid, the following features can be seen: (c) solid minerals (green), (d) mixed kerogen (red) and pores (blue), (e) the kerogen network alone (red), and (f) pores alone (blue), (g) the 3D image of pores where the colours indicate clusters of connected pores.....	108
Figure 5 4 The distribution of pore volume calculated from the Nano-CT 3D imaging datasets of the gas shale sample. The inset shows the low pore volume data on an expanded scale.....	110
Figure 5 5 The pore size distribution calculated from the Nano-CT (red) and the MIP measurements (green) were made on a sample from the same core plug. Dashed lines show native resolution limits for each technique.	112

Figure 5 6 (a) The linear isotherms and pore sizes distributions from N₂ sorption experiment, (b) the BET surface area transform at the relative pressure P/P^o, (c) BJH pore size distribution, according to pore volume, and (c) according to pore areas. 113

Figure 5 7 The pore-aspect ratio distribution, (a) pore-aspect ratio distributed as a function of the number and volume of pores obtained from γ_1 (oblate) values, and (b) pore-aspect ratio distributed estimated from γ_2 (prolate) values, estimated by Nano-CT approach using the MD-2.7 km gas shale sample. 115

Figure 5 8 The scale-invariant pore surface area to volume distribution, σ , calculated from Nano-CT measurement as percentage of the total numbers and volume of pores of the gas shale sample MD-2.7 km. 117

Figure 6 1 Multiscale imaging techniques (FIB-SEM, Nano-CT and μ -CT) used in this study..... 123

Figure 6 2 Shale rock sample of area of interest in this study for Nano-CT and FIB-SEM imaging. (1) Dark grey, kerogen; (2) medium grey, silicate matrix; (3) light grey, iron pyrites, often in framboidal form, (4) Pores (black) are too small to be seen at this resolution. The covering of the sample which appears white is the layer of Pt (5) that was initially deposited at the start of the sample preparation process..... 123

Figure 6 3 (a) Image of the sample using the FIB-SEM technique (face dimensions 25×25 μm^2), (b) 3D image of the sample using Nano-CT scanning for the same shale sample..... 124

Figure 6 4 An EDX map of a cross-section of the shale sample have used in this study for elemental mapping, where the clastic matrix (high Si, Al, K, O) can be distinguished from the kerogen (high C), and the framboidal iron pyrites are clearly shown by their associated high sulphur (S) values 125

Figure 6 5 Nano-X-Ray Tomography (Nano-CT) for a shale rock sample with an acquired resolution of 64 nm. (a) Raw 3D grayscale image, (b) representative 3D image of all phases in the sample, (c) imaged pores, (d) imaged kerogen, and (d) solid minerals..... 127

Figure 6 6 FIB-SEM for a shale rock sample shown with an acquired resolution of 20 nm. (a) Raw 3D grayscale image, (b) representative 3D image of all phases in the sample, (c) imaged pores, (d) imaged kerogen, and (e) solid minerals..... 128

Figure 6 7 Normalised pore volume distribution calculated from the Nano-CT (red) and FIB-SEM (blue) 3D imaging datasets for the same measured volume of gas shale sample using 3D image analysis implemented in Avizo® Fire 9.40 software. The inset shows the low pore volume data on an expanded scale..... 130

Figure 6 8 (a) Pore number, and (b) pore volume distributions of the equivalent pore size estimated from the Nano-CT (red) and the FIB-SEM (blue) 3D imaging datasets for the same measured volume of gas shale sample. The MIP measurements (green) were made on a sample from the same core plug. Dashed lines show native resolution limits for each technique. 133

Figure 6 9 the pore-aspect ratio distribution, plotting the overall number of pores expressed as a percentage of the total number of pores in the sample for (a) the S aspect ratio, and (c) the L aspect ratio. The pore aspect ratio as a function of total volume of pores for (b) the S aspect ratio, and (d) the L aspect ratio. In each case data is derived from 3D imaging of the same volume of gas shale sample using both FIB-SEM and Nano-CT techniques..... 136

Figure 6 10 The scale-invariant pore surface area to volume σ distributions with respect to (a) percentage number of pores and (b) percentage pore volume, each calculated from 3D imaging of the same volume of gas shale sample using both FIB-SEM and Nano-CT techniques. 138

Figure 6 11 (a) FIB-SEM image revealing kerogen (darkest areas) with some of pyrite (lightest areas) in a matrix of medium greys with a few small pores (black), (b) Gas flow in the kerogen (textured brown),

the yellow dots represent gas molecules which can flow and accumulate within the kerogen, and the white areas represent pores. 139

Figure 6 12 Shows the gas flow through kerogen (red colour) in the three directions (x, y and z) for Nano-CT and FIB-SEM. 143

Figure 7 1 Different approaches and corresponding facilities used in this study, with special requirements for sample size varying between 0.5-3 mm, as indicated..... 149

Figure 7 2 Diagram of the apparatus for GRI porosity and permeability measurements. 150

Figure 7 3 A typical plot of history match for pressure (experiment and simulation using Eclipse™) of the crushed shale sample test. 151

Figure 7 4 The pressure data recorded during the experiments. (a) charging the reference volume with a fixed mass of gas at a fixed pressure, (b) sharing the gas with the sample chamber ((Valve 1 and Valve 3 are closed with Valve 2 open).. 152

Figure 7 5 Diagram illustrating the processes of gas behaviour during pressure expansion. Once the valve is opened the gas surrounds the pores (at time $t=0$), then at time $t = t_1$ the gas starts entering the pores and at $t = t_{eq}$ the gas has fully saturated the pores. 152

Figure 7 6 Shows the theoretical variation of electrical connectivity (Eq. 7.11) and hydraulic connectivity (Eq. 7.16) as a function of porosity for the shale rock samples. 159

Figure 7 7 Shows the connectivity for each rock sample (F3, E9, MD2.7 and Grpn7) as a function of porosity as well as compare with electrical and hydraulic connectivity for the shale rock samples. 159

Figure 7 8 Particles size distribution of crushed shale samples for F3, E9 and Grpn7 samples..... 161

Figure 7 9 (a) Example of 2D of the μ -CT images on Grpn7 and E9 shale samples, respectively, with diameter of 0.5 mm at resolution of 0.94 μ m, (b) non-local means filtered have been applied on the same slice of samples. Darker grey sections represent pores as marked by **white arrows**, while the white spots are pyrite (**red arrows**) and microfractures (**yellow arrows**) as can be observed from the image (b) for Grpn7 and E9 samples, respectively..... 161

List of Tables

Table 1 1 thesis structure	23
Table 2 1 Estimate shale gas production and reserves internationally.....	27
Table 2 2 Porosity measurements for different reservoir locations with different techniques available in the literature.	29
Table 2 3 Measurements shale permeability from different shale gas reservoir samples.....	37
Table 2 4 Conventional approaches to rock characterisation applied to shales	41
Table 3 1 General description and material resources of the shale samples in this research.....	50
Table 3 2 Comparison of the operational parameters of multi-scale (μ -CT Nano-CT and FIB-SEM) techniques (as implemented in this study).....	64
Table 3 3 Measurements and calculations used in this study to quantify the petrophysical characteristics of pores within shale rock sample.....	69
Table 4 1 Summary of the rocks and images studied in this work.	97
Table 5 1. Mineralogical results from XRD measurements undertaken in this study.....	107
Table 5 2. Summary of the rock sample data obtained by different techniques (Chapter 7 contains a full discussion on calculated permeability).....	108
Table 5 3 Summary of petrophysical properties of gas shale rock sample in this study from N ₂ sorption (BET) and mercury injection porosimetry (MIP) techniques.	112
Table 6 1 Comparison between the two imaging techniques of the main parameters measured in this paper.....	126
Table 6 2 The calculated permeabilities in the x, y and z directions obtained from simulation for Nano-CT and FIB-SEM and measured in the laboratory.....	142
Table 7 1. The X-ray diffraction analysis results (XRD, Mineral composition by wt %) and total organic carbon (TOC) as weight percentages for shale samples.....	153
Table 7 2 The porosities results of the investigated rock samples obtained by different measurements.....	157
Table 7 3 The permeabilities results of the rock samples investigated in this study, obtained by different methods.	158
Table 7 4 The hydraulic connectivity results for the shale rock samples investigated in this study, obtained by different approaches.....	158

List of Abbreviations

2-D Two-dimensional

3-D Three-dimensional

XRD X-ray Diffraction

TOC Total Organic Carbon

SEM Scanning Electron Microscopy

BSE Back-Scattered Electron

SE Secondary Electron

EDS Energy Dispersive X-ray Spectroscopy

TEM Transmission Electron Microscopy

FIB Focused Ion Beam

XCT X-ray Computed Tomography

μCT Micro Computed Tomography

NanoCT Nano Computed Tomography

BET Brunauer– Emmett–Teller

MICP Mercury Injection Capillary Pressure

Chapter 1

Introduction and Research Objectives

1.1 Introduction

The increasing demand of unconventional energy resources such as shale gas has become significant in natural gas and crude oil productions recently and is expected to grow in the future. According to the Energy Information Administration (EIA) reports (EIA, 2019; 2020), increases in crude oil and natural gas production globally are driven by the increasing production of shale gas. Currently, shale gas comprises around 15% in total crude oil and 47% in total natural gas production and alone proven reserves reached 9×10^{12} m³ in USA (EIA, 2019). However, in the European Union (EU), shale gas may contribute around 5-10% to the gas production by 2030-3035 (Spencer et al., 2014). Thus, the increasing of understanding the microstructure properties in shale reservoirs is very significant for the demand of enhanced recovery and gas estimate.

Shale gas reservoirs are characterized by their low porosity (2-15%), very low permeability between (1 μ D to 1 nD), and organic richness (>2% TOC) (Britt, 2012; Clarkson et al., 2012c; Macbeth et al., 2011). Such reservoirs typically have very strong heterogeneity and anisotropy, which makes them more challenging to produce over the years. A comprehensive investigation of shale reservoirs depends on the understanding of petrophysical properties of the shale, and in particular the scale dependent properties of the matrix, pore space and organic matter.

In shale materials however, the matrix has unconnected porosity due to complex pore structure and highly heterogeneous nature. This is mainly because the sizes of pores and fractures in shales vary over many orders of magnitude; from only a few nano-meters to several tens of microns (Ambrose et al., 2010; Bai et al., 2013; Curtis et al., 2010). Consequently, the microstructure properties and pore systems cannot be described at a single scale. Therefore, multi-scale imaging techniques are required to characterize the shale microstructure. Multi-scale three-dimensional (3D) imaging is very important to image, identify and quantify shale phases, pore and kerogen distribution and their connectivity.

A combination of X-ray micro-computed Tomography (μ -CT), X-ray nano-computed Tomography (Nano-CT) and 3D of Focused Ion Beam Scanning Electron Microscopy (FIB-SEM) provides the ability in this research to accurately describe the features of shales despite the challenges presented by the heterogeneity of shale.

The main purpose of the 3D imaging characterizations is to understand the type of the pores, their geometry, size, volume, surface area and the connectivity of the pores, as well as the relationships between pores and minerals.

1.2 Research Aim and Objectives

1.2.1. Overall Aim

The overarching aim of this research is to understand the relationship between the microstructure properties and fluid transport of gas shales, including quantifying the microstructure of shales at a range of scales as well as understanding how the fine microstructure of shales controls fluid flow at all scales.

1.2.2. Specific Objectives

The main objectives of this study are:

- (1) To measure microstructural properties of gas shales from the microscale to nanoscale and to systematically characterise the pore structural distribution, including porosity, permeability, pore volume, pore size, pore aspect ratios, and surface area to volume ratio of pores.
- (2) To visualise and quantify the microstructure properties of shale rocks. The μ -CT method is used on a sample for the macroscale measurements, while the same sample is subjected to FIB-SEM microscale measurements, but at multiple locations as field of view is smaller than for the μ -CT, in order to understand the relation between the microscale and macroscale properties.
- (3) To envisage and measure the microstructure of shale within the same position using the three-dimensional imaging techniques, including ultrahigh resolution X-ray nanotomography (Nano-CT) and Focused Ion Beam Scanning Electron Microscopy (FIB-SEM) to discover and understand the complex structure in particular shale reservoirs, connectivity of fluid transport pathways and the processes which mediate gas transport on shale.
- (4) To integrate measurements made at all scales with supporting experimental measurements of rock porosity, permeability mercury porosimetry and nitrogen adsorption in order to fully characterise the rock at all probes scales.
- (5) To investigate the use of microstructure parameters primarily from 3D scanning to estimate the connectivity and permeability of the shale.

In order to achieve these objectives, 3D imaging techniques, including X-ray microtomography, Nano-tomography and 3D Focused Ion Beam Scanning Electron Microscopy (FIB-SEM) at multi-scales have been applied to image the heterogeneous shale rock. The results have been combined with laboratory measurements on porosity and permeability techniques such as Gas Research Institute (GRI), mercury injection (MIP), nitrogen adsorption (N_2) and X-ray Diffraction (XRD) analysis.

The results of this study provide a better insight into the petrophysical properties of shale and offer valuable datasets and reference to industry and academics for assessing gas storage and transport actions within gas shale reservoirs.

1.3 Thesis layout

This thesis comprises eight chapters (Table 1.1). **Chapter 1** provides a general overview of the project by mentioning the rationale, introduction to the research background, aims, objectives and thesis structure.

Chapter 2 introduces a review of the literature relevant to this work. Background information is presented related to microstructure properties of gas shale reservoirs including porosity, permeability, kerogen, gas storage and transport through pores, and also a review of multi-scale imaging techniques based on 2D/3D X-ray micro and nano tomography (μ -CT, Nano-CT) as well as 3D electron microscopy (FIB-SEM).

Chapter 3 describes the experimental methods and analytical techniques used in this research including sample selection, sample preparation and rock analysis by X-ray diffraction (XRD), X-ray micro-and nano-tomography, focused ion beam scanning electron microscopy (FIB-SEM) and also laboratory measurements such as GRI, MIP and N_2 adsorption. In addition, details of imaging processing and quantification are provided.

Chapter 4 provides results of Bowland gas shale of Northern England characterised in 2D/3D using X-ray micro-tomography (μ -CT) and focused ion beam scanning electron microscopy (FIB-SEM). The microstructure features of gas shale including porosity, pore size, pore volume distribution, and pore aspect ratio, internal surface area to volume of pore, pore connectivity have been imaged and quantified.

Chapter 5 introduces imaging and analysis of gas shale samples using 3D ultrahigh resolution X-ray nano-CT at the sub-micron scale to capture the pore and kerogen network. Laboratory measurements such as MIP and N_2 adsorption were also used to fully infer and reveal structures of gas shale at different scales.

Chapter 6 provides results for gas shale from a formation in Sweden using ultra high resolution nano-CT and FIB-SEM images under Back Scattered Electron Microscopy (BSE) mode on the sub-micron sample to resolve microstructures properties at nanometre scale as well as 3D visualisation of the pore space, kerogen and minerals on the same region of shale.

Chapter 7 presents multiple methods for calculating porosity, permeability and hydraulic connectivity using data from samples from 4 formations obtained and described in the previous 3 chapters. These data are discussed and compared with independent measures of porosity and permeability.

Chapter 8 presents the main conclusions and accomplishments of this research and provides suggestions for future work including studies related to correlative imaging and modelling of gas shales.

Chapter	Content
Chapter 1	Introduction, overview and aims of the study.
Chapter 2	Literature review from previous studies on of the microstructure properties of gas shale reservoirs as well as multi-scale imaging techniques 2D/3D.
Chapter 3	Experimental methods and analytical techniques used in this research.
Chapter 4	Results of Bowland gas shale of Northern England characterised in 2D/3D using X-ray micro-tomography (μ -CT) and focused ion beam scanning electron microscopy (FIB-SEM).
Chapter 5	Results of imaging and analysis Bowland gas shale using 3D ultrahigh resolution X-ray nano-CT at the sub-micron scale and compare with laboratory measurements (MIP and N ₂ adsorption).
Chapter 6	Results of gas shale from Sweden using ultra high resolution Nano-CT and FIB-SEM images under BSE mode on the sub-micron on same region of sample.
Chapter 7	Presents multiple methods for calculating porosity, permeability and hydraulic connectivity using multiple approaches at different scales.
Chapter 8	Conclusions and future work

Table 1 1 Thesis structure.

Chapter 2

Literature Review

2.1 Introduction

The literature related to shale gas encompasses multiple aspects, including gas storage and gas flow as well as the structural analysis of shale gas reservoirs. However, due to the complex structure of shales over a wide range of scales, gas flow within pore space and the role of kerogen are not yet fully understood. This study aims to quantify the effect of shale microstructure on porosity and pore/pore-throat sizes, and hence on permeability across a very wide range of scales using multiple methodologies, including three types of high resolution three-dimensional imaging and associated 3D image analysis. As such, we hope the research will be a valuable contribution to the oil and gas industry as well as to academia.

This chapter provides a review of the literature and current knowledge on the characterisation of microstructure properties including porosity and permeability in shale and techniques used to describe shale microstructures. This chapter starts by describing an overview of gas shales ([Section 2.2](#)). Imaging techniques with different dimension and sizes are used in this thesis and described, including an overview of the main process parameters along with upscaling techniques ([Sections 2.3-2.4](#)).

2.2 Overview of shale gas reservoirs

The term of "shale" refers to fine, grained, sedimentary rocks that result from weathered clastic processes. The term shale comprises mudstones including mainly clay minerals, siltstones and kerogen which is an organic matrix element deposited within the rock and from which shale gas and shale oil can sometimes be extracted ([Law and Curtis, 2002](#); [Bustin et al., 2008](#)).

There are general and sometimes wide, different ways of definitions of shale such as in the geology, the shale is considered as mudstone that has compacted over many years and lithified. Shales are often found with layers of sandstone, limestone, and siltstones which do not contain clay minerals, while in a petroleum system, the shale acts as the source of the rock with low permeability ([Rezaee et al., 2015](#)). The gas within the shale is generated and stored in the pore systems of the shale, and is not subject to the processes of diffusion or gas movement due to the low pore connectivity and permeability within shale rock, therefore some of the gas cannot be fully expelled from the source rock, because there is no migration into a permeable reservoir ([Curtis, 2002](#); [Glorioso et al., 2012](#)).

The existence of burnable gas from the earth has been known for over 3000 years and natural gas seeps have probably been used since prehistoric times. The first recorded production of

shale gas was in 1821 from the Devonian shales in the United States ([Vanorsdale, 1987](#)), although coal gas had been used in China from about 500 BC and in the UK since the 17th century. This production in 1821 was obtained from the Dunkirk shale in Chautauqua County, and was used to light the nearby small town of Fredonia ([Curtis, 2002](#)). More recently, shale gas has been recognized as an economic resource of an unconventional reservoir type with lower porosity and permeability than conventional reservoirs ([Bustin et al., 2008](#); [Clarkson et al., 2012](#)). The production of shale gas has also dramatically increased since 2002 ([Curtis, 2002](#)), and has been rising significantly over the past few years ([EIA, 2019](#)).

Historically, the accumulations of shale gas have been mostly ignored or unnoticed due to the cost and technical challenges of gas production from such reservoirs ([Curtis, 2002](#)). However, over the past few years' shale gas production has been the focus of many researchers and has dramatically increased, particularly in North America ([Chareonsuppanimit et al., 2012](#)). In the year 2008, there were over 40,000 producing gas shale wells in the USA ([Bustin, 2008](#)). Since then, the shale gas exploration action has been growing quickly in other areas around the world ([Jarvie, 2010](#); [Littke et al., 2011](#)). The success of shale gas is due to the recent application of fracturing strategies and advanced drilling methods ([Hill and Nelson, 2000](#); [Jarvie et al., 2007](#)). Twelve years later, by 2020, there were more than 85 thousand producing wells in the seven main shale gas formation in the US: Bakken, Barnett, Eagle Ford, Fayetteville, Haynesville, Marcellus and Woodford ([Hughes, 2015](#)). The production of shale wells has continued to increase and expand rapidly in the US with the opening of more than 150,000 wells between 2010 and 2017 ([Meko and Karklis, 2017](#)).

However, in some countries such as India ([Sharma, 2012](#)), South Africa ([Cohen, 2012](#)), Australia ([Warner, 2011](#)), and UK ([Schulz et al., 2001](#); [Mair et al., 2011](#)), the shale gas production has been blocked or stopped due to the environmental risks involved. These risks have resulted in legal restrictions on hydraulic fracturing process ([Wang, 2014](#)), that have stopped a development of shale gas around the world.

There are many general, wide definitions and concepts used for shale rock including the definition provided by ([Jackson et al. \(2005\)](#)) who have defined shale as a "hardened" and laminated rock with about 67% clay size grains which consist of fine-grained particles less than 5 μm in diameter. According to studies ([Passey et al., 2010](#); [Sondergeld et al., 2010a](#)), shale rock might also contain a different amount of silt-sized particles (up to 60 μm). Also ([Jackson et al., 2005](#)), they have also been defined the organic shale as laminated, hardened, and fissile rock containing more than 2% of the total organic carbon (TOC). Shales exhibits very low porosity (< 15%) as well as extremely low permeability with the ranges of 1 μD to 1 nD ([Britt, 2012](#); [Clarkson et al., 2012a](#); [Macbeth et al., 2011](#)). These properties make it a greater challenge to characterize and measure microstructural parameters such as porosity, pore size and pore volume distributions, as well as properties that depend strongly on microstructure, such as permeability.

Hydrocarbon production from shale reservoirs is accomplished either by hydraulic fracture stimulation or horizontal drilling (Lu et al., 2014; Sondergeld et al., 2013), which will be expanded upon in a subsequent section.

2.2.1 The shale gas system

Shale gas reservoirs are considered to be unconventional natural gas reservoir because the gas is trapped in very small, relatively unconnected pores in the reservoir (Vengosh et al., 2013), the resource is laterally and vertically more extensive than conventional reservoirs, and the gas cannot be produced by conventional vertical wells (Hill et al., 2007). Thus, the style of recovery is different from the conventional reservoirs as in the conventional reservoirs the gas can be extracted by the wells' natural pressure while in unconventional reservoirs there is need for two key technologies, namely horizontal drilling and hydraulic fracturing, in order to extract the gas from the reservoirs.

According to Majun and Dow (1994), shale may act as both a source rock and a cap-rock in conventional petroleum systems, where a trap delimited high porosity, high permeability clastic reservoir rock provides the storage of gas. For gas shale resources, the shale is the source rock, 'reservoir' and cap rock, and no conventional trap is needed. The gas exists in the resource over a much larger lateral and vertical extent, but at a much lower gas concentration, measured in volume of gas per volume of rock. This widely distributed nature of gas in shales results in the use of deviated and horizontal wells, while the low permeability of the rock requires the use of hydraulic fracturing in order to raise the permeability sufficiently to produce reasonable volumes of gas (Figure 2.1).

A shale gas reservoir might need to be re-fractured many times in order to extend the productive life of a gas well and also to retain an economic rate of production (Walser and Pursell, 2007; Cramer, 2008).

Figure 2.1 shows a schematic diagram of how the gas can be produced by hydraulic fracturing and horizontal drilling

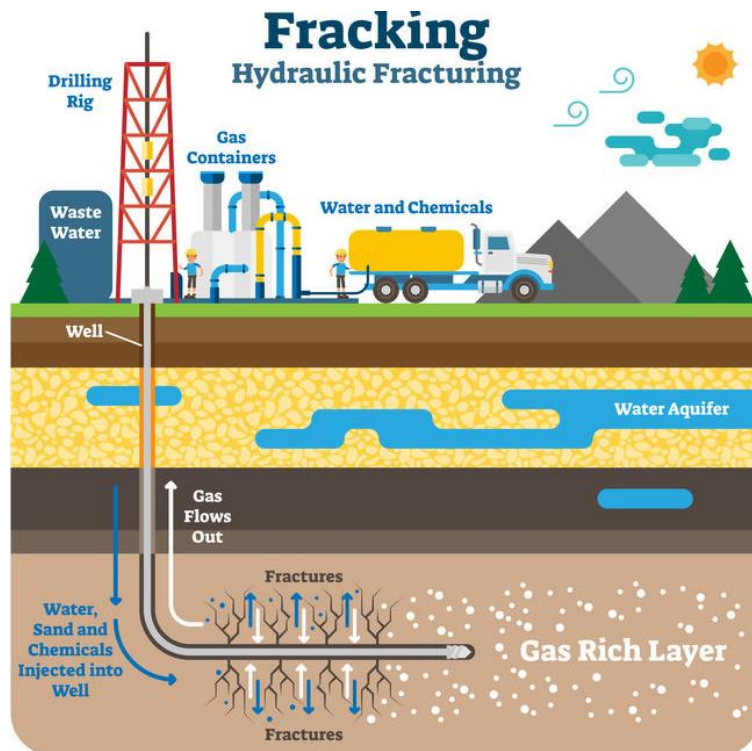


Figure 2 1 Shows how the gas producer it from the well by hydraulic fracturing (Lehr, 2019).

In recent years, hydraulic fracturing and horizontal drilling have advanced the production of hydrocarbon by stimulating the flow of gas and liquids from quasi-impermeable geological reservoirs. These technological strategies have increased the economic potential for oil and gas in many unconventional locations around the world (Rezaee et al., 2015; Kargbo et al., 2010; Table 2.1 and Figure 2.2).

The estimates of gas production along the reserves of the shale gas around the world are provided in Table 2.1. A map of the major current gas production worldwide is given in Figure 2.2.

Table 2 1 Estimate shale gas production and reserves internationally.

Region	Production (Bcf)	Kerogen Reserves (Tcf)
North America	1,662	80,000
South America	1,225	400
Asia	1,389	1,100
Africa	1,042	500
Europe	639	600
Australia	396	1,700

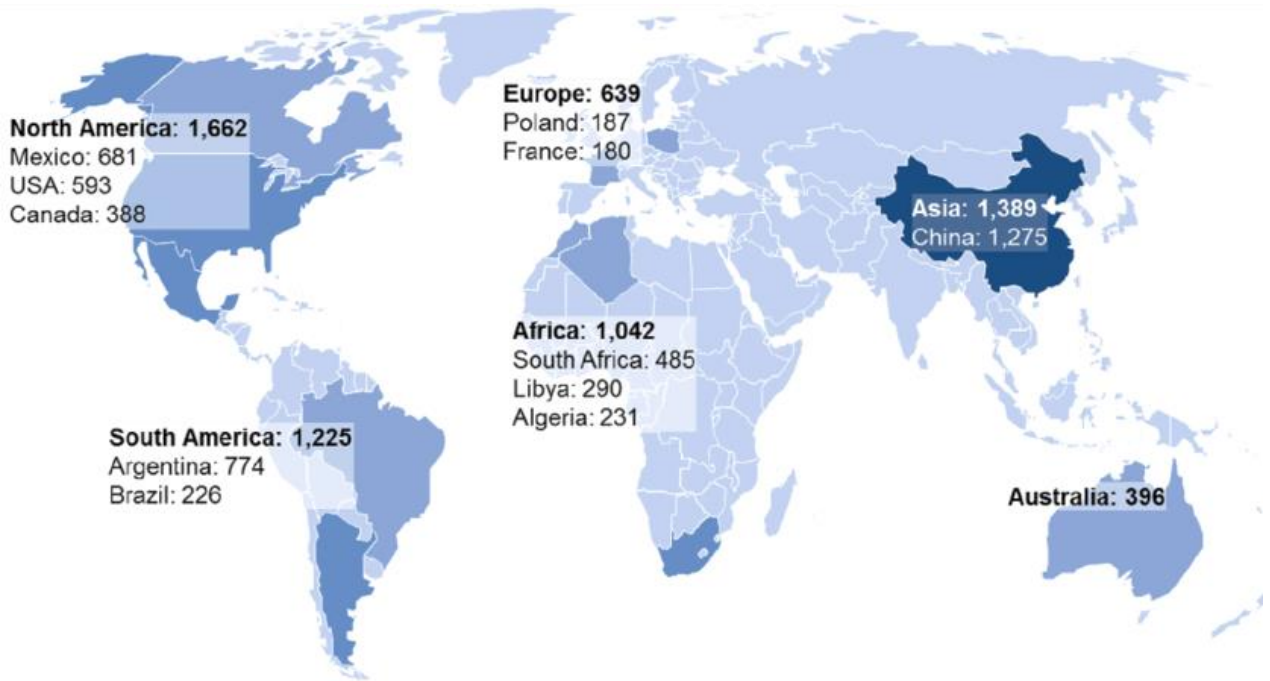


Figure 2 2. Map of the gas production in various countries with unit of Bcf (source: BP Statistical Review of World Energy, 2019).

2.2.2 Porosity

The porosity (ϕ) is the main key factor for resource assessment, oil and gas reserve estimation in particular in the shale gas reservoirs. Total porosity is defined as the proportion of pore volume (V_p) to the total rock volume. It is a fundamental property of the rock and the main important parameter for estimated the Gas-in-Place (GIP).

Porosity can be estimated by using of the measured both bulk volume (V_B) and grain volume (V_G) as has been described in the suggested practice for Core Analysis

$$V_p = (V_B - V_G) \quad (2.1)$$

$$\phi = V_p/V_B \quad (2.2)$$

Two types of porosity have been defined based on the connectivity of the pores: (i) total and (ii) effective porosity. The total porosity is accounts for overall void space in the rock, while the effective porosity represents the pores that are connected without the isolated pores. It becomes more challenging to distinguish between the total and effective porosities in the shale due unconnected pores, and extremely low permeability within shale. In addition, the preparation procedure is also extremely challenging, this preparation is very important in determine porosity within the shale, which may change the structure of the rock, such as

when the structure of the rock is changed during crushing which will have impacts on the porosity of shale.

In gas shale reservoirs the measurement of porosity is particularly challenging because the shale samples are likely organic-rich, have low porosity and ultra-low permeability with strong heterogeneity (Pan et al., 2015; Ma et al., 2016). According to previous studies and researches such as (Curtis et al., 2012; Chalmers et al., 2012; Klaver et al., 2015; Mastalerz et al., 2013; Saif et al., 2017; Ma et al., 2016) porosities in gas shales range between 0.2 to 6% (Table 2.2). These values were recorded from different gas shale reservoirs and using various techniques, such as scanning electron microscopy (SEM), focused ion beam scanning electron microscopy (FIB-SEM), X-ray computed tomography, gas adsorption, helium pycnometry, and mercury intrusion porosimetry (MIP).

Table 2 2 Porosity measurements for different reservoir locations with different techniques available in the literature.

Shale reservoir	Measurements	Porosity (%)	Reference
Barnett	SEM	2.3	(Curtis et al., 2012)
Eagle Ford	Helium and SEM	0.4-5.1	(Chalmers et al., 2012)
Horn River	Helium and SEM	2.0-5.9	
Kimmeridge	FIB-SEM	0.3	(Curtis et al., 2012)
Woodford	MIP	4.7	(Klaver et al., 2015)
Marcellus	FIB-SEM	0.2	(Curtis et al., 2012)
New Albany Shale	Gas sorption	9.8	(Mastalerz et al., 2013)
Green River	FIB-SEM	0.5	(Saif et al., 2017)
Bowland Shale	X-ray(μ -CT)	0.3-0.55	(Ma et al., 2016)

Some of these techniques either cannot detect or describe the internal pore /micro-structure (due to the limitation of their resolution), which makes it difficult to know what the technique is actually measuring. For example helium porosimetry, MIP and gas adsorption can only provide the effective pore volume (connected porosity), and the connected porosity available to each technique is different, with helium porosimetry being generally considered to have the ability to measure the largest range of pores due to the small size of the helium molecule. By contrast, the imaging techniques can measure both open and closed pores and they are usually combined with other measurements due to the limited volume/area/size of shale samples used in 3D imaging.

Accordingly, the Microscale X-ray computed tomography (μ -CT) technique performs well as a non-destructive method but can only recognize the pore throats larger than 0.7 μ m, and only

shows pores which are connected by pre throats greater than this value. Since the connectivity encountered in most shales involves pore throats which are less than $0.7 \mu\text{m}$ μ -CT cannot either recognise that connectivity or provide data which can predict the shale permeability (Bai et al., 2013; Josh et al., 2012). On the other hand the FIB/SEM method can resolve pore throats from $50 \mu\text{m}$ in size down to 10nm , which encompasses the scale at which shale pores are connected. Both techniques provide a three-dimensional visualization of internal structure of rocks (including porosity and mineral distribution) (Sisk et al., 2010; Leefink et al., 2015). The pore detection ranges of common experimental techniques with respect to length scale are shown in Figure 2.3.

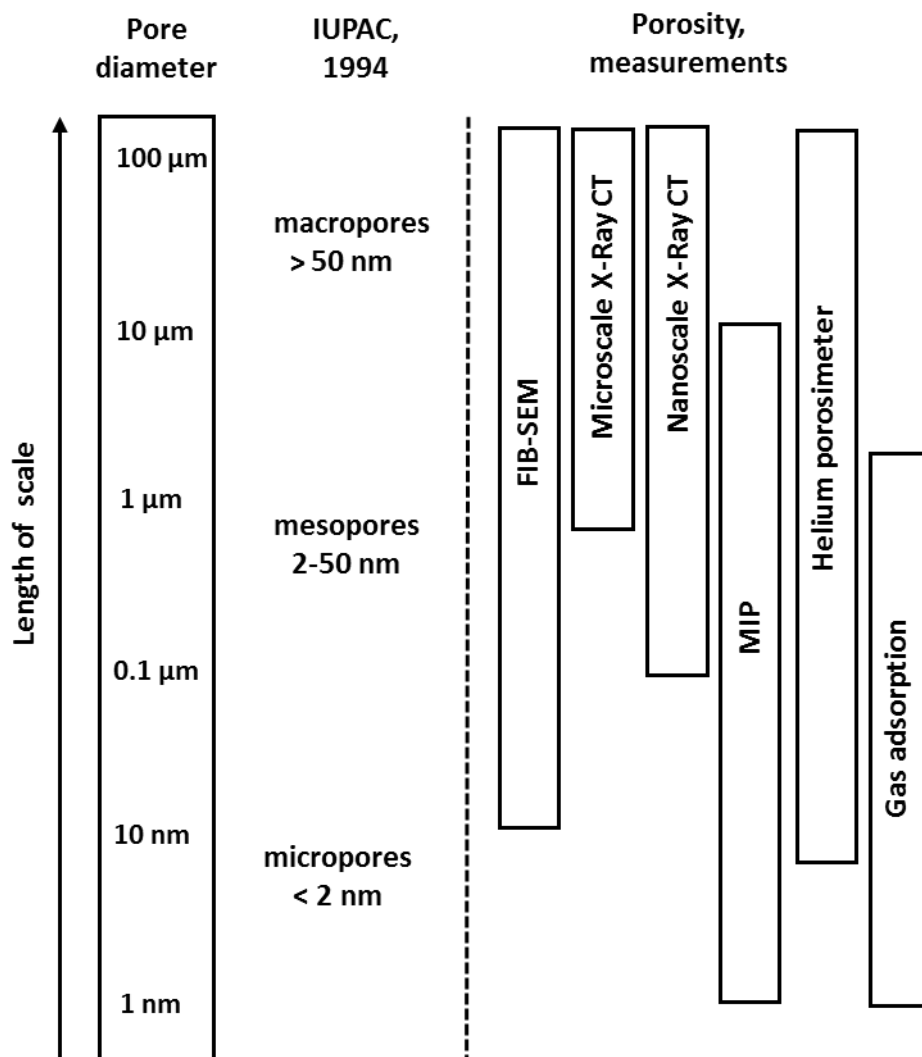


Figure 2.3. The porosity and pore size distribution (PSD) ranges characterized by different techniques within shale gas (IUPAC, 1994, Loucks et al., 2012)

2.2.3 Pore sizes

Pores are the part of rocks occupied by fluids. The pore system in shale gas reservoirs is more complex for several reasons, including the variability and heterogeneity of organic matter (OM), clay minerals and heavy minerals (Chen et al., 2014; Tuo et al., 2016; Zhang et al., 2016).

The pores in the shale gas reservoir samples have sizes ranging from a few nanometres to a few microns, covering much larger range of sizes than is encountered in carbonate and sandstone reservoirs (Shi et al., 2015; Fangwen et al., 2017). In conventional reservoir samples, the pores are divided into five types based on the sizes including: (i) macropores (>4 mm), (ii) mesoporous (4mm- 65µm), (iii) micropores (65µm-1µm), (iv) nanopores (1µm-1nm), and (v) picopores (<1 nm) (Loucks et al., 2012). In unconventional reservoir such as gas shales micro- and nanopores are commonest (Choquette and Pray, 1970, Lu al., 2017), while the presence of picopores is becoming clearer with advances in imaging techniques.

Javadpour (2009) indicated that the pore sizes in conventional reservoir rocks are usually more than 2 µm, while in unconventional reservoir such as shale rock are ranging between (1 µm to 1 nm). Nelson et al. (2009) also suggested a similar outcome namely that the pore sizes within shale in range from 0.1 to 0.005 µm and in tight-gas sandstones range from 2 to 0.03 µm. Based on the previous results and according to IUPAC classification, the pore sizes in shale reservoirs are classified into three-types which are (i) macropores (>50 nm), (ii) mesopores (2–50 nm), and (iii) micropores (<2 nm) as shown in Figure 2.4 (IUPAC, 1994, Loucks et al., 2012).

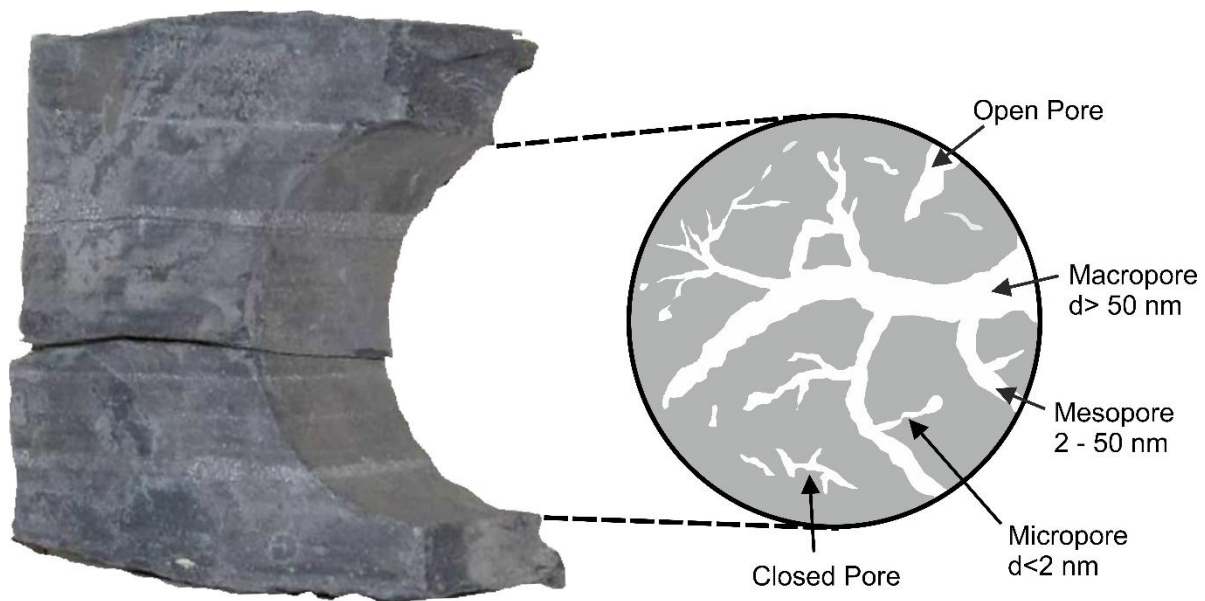


Figure 2 4 A diagrammatic representation the pore structure in shales, open pores, closed pores, and pore size distribution in shales (Loucks et al., 2012).

Numerous methods have been used to detect the pore sizes in shales including imaging techniques such as FIB-SEM (Sok et al., 2010; Ma et al., 2016), SEM (Loucks et al., 2009), penetration of fluids such as helium pycnometry (Chalmers et al., 2012), mercury intrusion porosimetry (MIP) (Klaver et al., 2012), and physical adsorption methods such as gas adsorption (Clarkson et al., 2013). Each of these methods have their own limitations in term

of pore size and resolution as can be seen in [Figure 2.3](#) and [Table 2.4](#). The details of limitations on each methods used in this thesis are reported later in section 3.5(Chapter3).

2.2.4 Pore types

The pore structure in shale rocks has different types and shapes with ranges of sizes ([Loucks et al., 2012](#)). No method or technique in isolation can fully investigate the type and range of pores in the geological materials. The type of pores that can be detected depends on the experimental method used to explore the pore structure ([Bustin et al., 2008](#)).

Pores can have different shapes (e.g., cylindrical, conical, oblate, and prolate; [Marsh, 1987](#)), and also can be considered as either open (O) or closed (C) ([Figure 2.4](#)). The open pores (O) are connected together by a network of transport giving the porosity, while the closed pores (C) are pockets of porosity that are fully isolated (i.e., gas cannot escape or enter closed pores, as shown in [Figure 2.4](#)).

The pores in shale are voids/spaces that are divided into the five main types: (i) pores within organic-matter or kerogen, (ii) pores within solid matrix including pores between grains/particles of solid minerals (interparticle pores), (iii) pores inside grains and particles (intraparticle pores), and (iv) fracture pores ([Ma et al., 2016](#); [Jiao et al., 2014](#); [Loucks et al., 2012](#); [Slatt and O'Brien, 2011](#); [Zhang et al., 2012a](#)).

(i) Pores within organic matter (kerogen)

The pores within the organic-matter (kerogen) have been studied by many researchers (e.g., [Loucks et al., 2009](#); [Curtis et al., 2010a](#); [Curtis et al., 2012](#); [Loucks et al., 2012](#); [Milliken et al., 2013](#)). They have reported that the pores within organic matter (kerogen) in shale gas systems are most likely to be irregular, ellipsoid and spherical shaped, with sizes range from about 10 to 500 nm ([Curtis et al., 2010a](#); [Loucks et al., 2009](#)).

The pores in the organic matter (kerogen) can also be hosted by different ways such as (i) mineral associated pores, with large sizes, (ii) complex pores, with large sizes and always occurring in clusters, (iii) discrete sponge-like pores, with middle sizes and irregular shapes and (iv) disconnected and isolated pores, with small sizes and a different distribution ([Ma et al., 2016](#); [Loucks et al., 2012](#); [Milliken et al., 2013](#)).

[Figure 2.5](#) shows examples of pores within organic matter (kerogen) from different shale reservoir samples by using SEM images. Arrows have been added to assist the identification of kerogen (black arrows) and pores (white arrows) ([Curtis et al., 2012](#)).

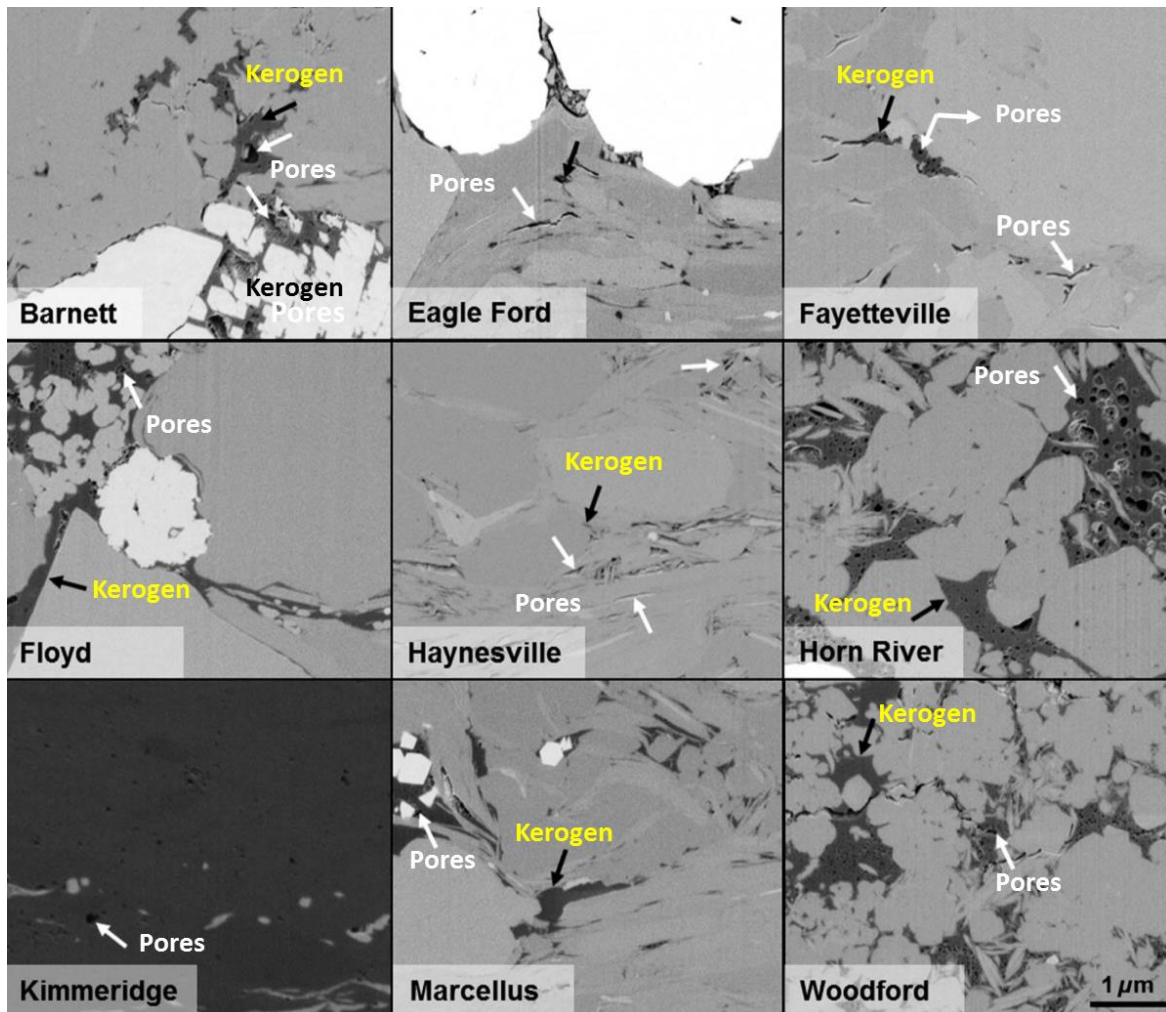
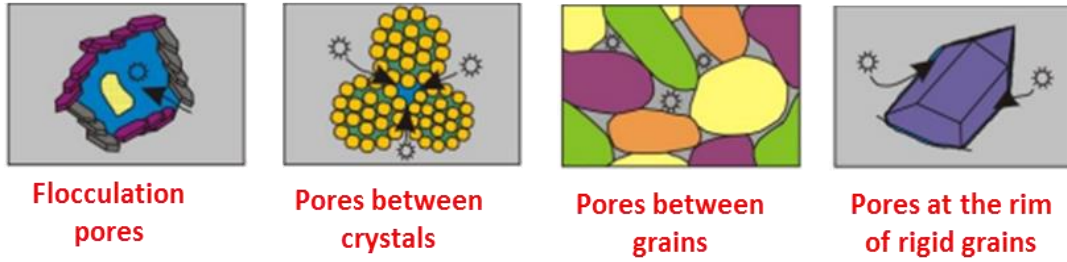


Figure 2.5. Backscattered electron (BSE) images from different shale reservoir samples showing the kerogen content and porosity. Arrows have been added for the identification of kerogen (black arrows) and pores (white arrows) (Curtis et al., 2012).

(ii) Interparticle and intraparticle pores

The interparticle pores are defined as allocated between mineral grains, crystals, clay platelets in shale (Figure 2.6); these are generally connected (Jiao et al., 2014; Loucks et al., 2012), while the intraparticle pores are pores that occur within separate particles and that are not connected, such as pyrite framboids, porous phosphate particles or within fossil bodies (Figure 2.6) (Klaver et al., 2012 and 2015). Figure 2.7 shows examples of SEM images of interparticle and intraparticle pores within shales (Loucks et al., 2012, Jiao et al., 2014).

Interparticle pores



Intraparticle pores



Figure 2 6. A schematic diagram representation of the interparticle and intraparticle pores (Loucks et al., 2012).

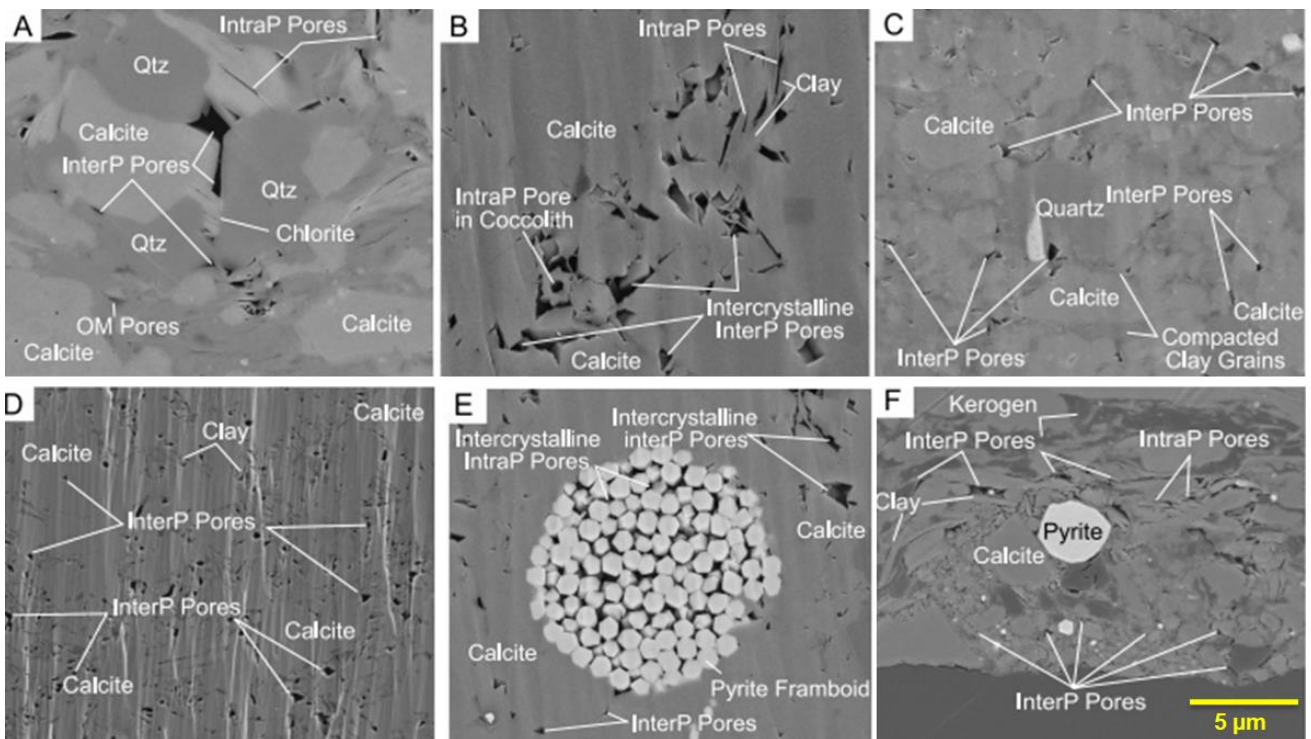


Figure 2 7. Examples of interparticle and intraparticle pores within shale from different shale reservoir samples (Loucks et al., 2012, Jiao et al., 2014).

(iii) Fracture pores

The fracture pores within shale are typical having different thickness ranging from a few nanometres to a few micrometres scale (Slatt and O'Brien, 2011, Zhang et al., 2018) and are often recognised at macro and microscale (Figure 2.8). The fracture pore is very important within shale because it controls the gas flow mechanism and composes the majority of the gas storage capacity (Zhang et al., 2017). Fractures are also widely known to affect the physical properties of rocks, such as compressibility and permeability (Walsh, 1965; Kranz, 1983). Figure 2.8 shows the pore fracture within shale that have images by SEM (Zhang et al., 2018).

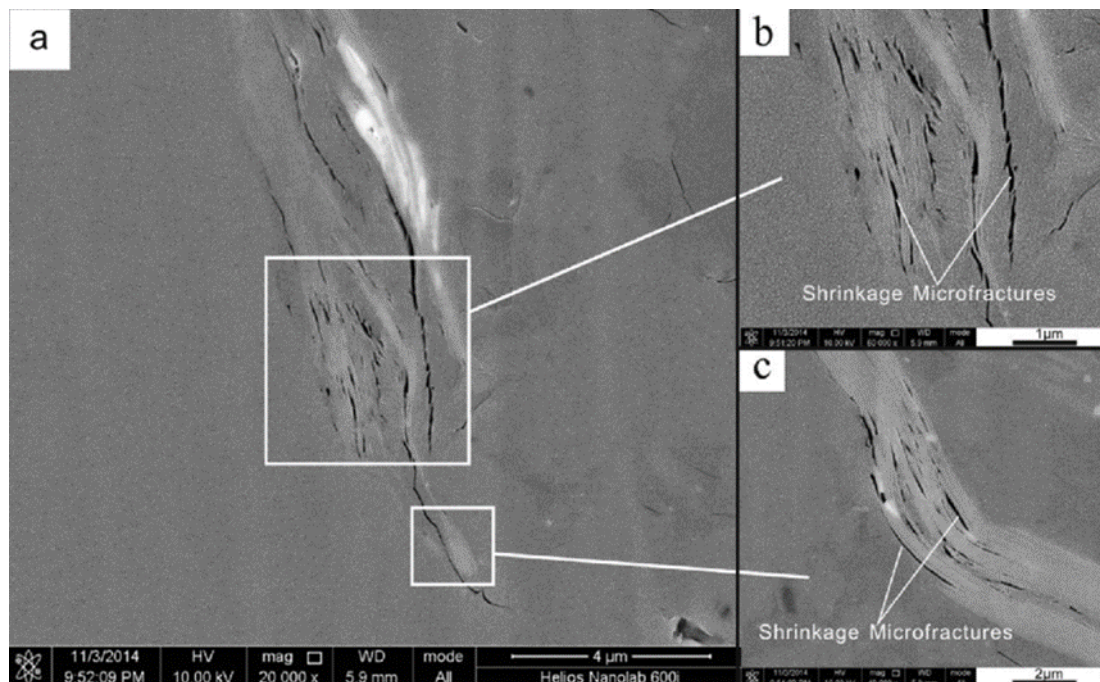


Figure 2.8. Example of the pore fracture within shale (Zhang et al., 2018).

2.2.5 Pore connectivity

Pore connectivity, within shale which defines how the pores are connected well with each other, is another important parameter in shale gas migration, production and also for describing the pore structure. Therefore, it will impact the flow /or transport through the shale rock. The majority of pores within shales are connected on the small sizes at the sub-micron to nano-scale (loucks et al., 2012; Ma et al., 2016, 2017). The small size of shales makes the imaging and quantification of pore structures such pore shape, size distribution and connectivity more challenging.

In previous studies the imaging techniques have been used for visualizing and quantifying pore connectivity within shale samples in three dimensions including non-destructive methods, such as X-ray Computed Tomography at various scales (e.g., lower resolution (μ -

CT), and higher resolution (nano-CT) (Loucks et al., 2012; Ma et al., 2016, 2017; Wang et al., 2016) and destructive instruments such as dual-beam Focused Ion Beam and Scanning Electron Microscope (FIB-SEM) (Jiao et al., 2014; Tang et al., 2016).

Lin et al. (2016) has reported that low pore connectivity of Bowland shale reservoir caused low overall porosity and permeability. They have implemented a multi-scale approach on different sizes of samples based on the field of view and spatial resolution which represent the maximum and minimum sizes of images at each scale. The results showed that at the largest scales, using the μ -CT method the pore connectivity cannot resolve at this scale due to the resolution limitation, whereas at a smaller scale the nano-CT technique still has difficulty resolving connectivity between the pores because of the voxel size limitation. However, the nano-CT is able to resolve connectivity for the kerogen. It was also found that pore connectivity can be resolved using FIB-SEM at higher resolution (nano-scale). More details on pore connectivity at different scales are reported and discussed later in the results sections (chapters 4, 5 and 6).

2.2.6 Permeability

The permeability of the rock is one of the most fundamental properties of any reservoir rock, its importance in providing a measure of the resistance of the fluid to flow and modelling hydrocarbon production. However, permeability measurement in the shale reservoirs is very complex because it often involves modelling of flow through pores.

Permeability measurement approaches can be classified into two groups: (i) steady-state (Rushig et al. 2004; Virnovsky et al. 1995), and (ii) transient (Cui et al. 2009; Brace et al. 1968). The steady-state approach provides accurate measurements for samples whose permeability is above 1 mD (Haskett et al. 1988). The permeability of almost all shales falls much below this value. Additionally, the time required to make a steady-state measurement becomes progressively longer for lower permeability rocks, to the extent that it is impracticable to perform on shales. A steady-state measurement can easily take a few days for shale rocks. Since the steady-state methods are slow to estimate permeability, other, so-called transient, methods have been developed to determine the permeability of shale rocks. These methods monitor the decay of a pressure pulse as the gas enters the rock (Brace et al. 1968; Hsieh et al. 1981; Dicker and Smits 1988; Jones 1997), and can be performed on crushed samples or shale core plugs (Cui et al. 2009). While some authors believe that these methods are also not suitable for measuring permeability within shale rocks because of several limitations such as time and sample size (Luffel and Hopkins, 1993), they represent the best experimental approaches often provide gas shale permeabilities in the order of a few tens to a few hundred nanodarcies.

The permeability of shale is very low in the range from 1 nD to 1 μ D (Table 2.3), but it's still important in the gas production and drilling procedure (Britt, 2012; Clarkson et al., 2012b; Macbeth et al., 2011; Wang and Reed, 2009).

Table 2 3 Measurements shale permeability from different shale gas reservoir samples.

Shale reservoir	Measurement	Permeability (nD)	Reference
London Clay	Constant flow	2.7 - 2120	(Dewhurst et al., 1998)
North Sea, Gulf of Mexico and Caspian Sea	Transient pulse decay technique	0.24 - 162	(Yang and Aplin, 2007)
Huron shale	Constant gas flow	0.2 - 6800	(Soeder, 1988)
Eagle Ford Shale	Gas Research Institute (GRI)	0.01 - 1	(Peng and Loucks, 2016)
Whitby shale	Pore pressure oscillation technique	3600	(McKernan et al., 2014)

Numerous different factors affect permeability, such as different pore sizes, shapes, features in shale, particle arrangement and material heterogeneity, internal structure and laminations of the sand, silt or clay components, and also the properties of shale (e.g., age, diagenesis in rock). These factors can impact and provide different outcome of shale permeability (Katsube and Williamson, 1994; Ricard et al., 2012).

However, permeability can be treated simply as a function of the characteristic grain size of the rock d , its porosity ϕ , and a parameter expressing the connectivity of the pores, here B (see section 2.2.5). The permeability is then provided by an expression approximating to $k \sim d^2 \phi^B$, where the d is the grain size of the rock and $B=3m$ for clastic rocks, where m is the cementation exponent, which is a measure of the electrical connectivity of the pore microstructure (Glover et al., 2006; Walker and Glover, 2010; Glover, 2015; Rashid et al., 2015). Pore microstructures which are progressively more badly connected have progressively higher values of m . Consequently, it is clear that the small grain sizes, low porosity and limited connectivity (high values of B) all combine to ensure that gas shales have extremely low permeabilities.

Typically, the permeability of shales ranges from 1 μ D to 1 nD (Heath et al., 2011; Heller et al., 2014, Javadpour et al., 2007), and around 85% of the published estimations of permeability represent values less than 150 nD (Javadpour et al., 2007). Although the permeability of shale is considered to be very low, it cannot be ignored. It is still very important in the drilling procedure and gas production. The permeability is a directing and controlling factor in fluid migration within shale (Best and Katsube, 1995; Ricard et al., 2012).

2.2.7 Gas storage and transport through pores

Gas in shale reservoirs is usually stored in three phases which are: (i) as free gas in micro- or nanopores between minerals, (ii) adsorbed gas at the surface of the pores or around organic matter, and (iii) gas dissolved in reservoir flow and kerogen bodies (Curtis, 2002; Ross and Bustin, 2009; Etminan et al., 2014).

The free gas phase is the bulk phase of shale gas, where the individual gas molecules are separated, are in constant random movement and continuously colliding with each other. The free gas phase will expand to completely fill up any pore volume (Ambrose et al., 2012). The amount of gas in the free phase is dependent on the temperature, pressure conditions, and also on the level of gas saturation within shale (Ecker et al., 2000).

The adsorbed gas is that gas present on the surface of pores, whether solid mineral or organic matter. The gas molecules are bound to the pore surface by weak forces of attraction (Montgomery et al., 2005). When the pores are smaller than 10 nm, gas adsorption contributes greater importance than free gas storage (Ma et al., 2015). Thus- the ability of the gas adsorbed within shale is determined by the internal specific surface area of the rock, which increases as the pores become smaller, and the amount of adsorbed gas is depends on surface chemistry and the local environmental conditions (primarily pH, temperature and pressure) (Ross and Bustin, 2007; 2009).

The dissolved gas can be found in the kerogen with low molecular weight as well as being dissolved in to a reservoir fluid (such as water and oil formation). The contribution of this dissolved gas reaches around 25% of total gas found in some shale reservoir (Ma et al., 2015) therefore cannot be ignored (Etminan et al., 2014), but is the most difficult to produce as it must diffuse out of the kerogen and progress through very small pores to the hydraulic fractures before production..

The relative amount of the gas provided by each of the three aforementioned types depends on the kerogen composition, mineral components, gas properties and reservoir conditions such as temperature and pressure (Ecker et al., 2000; Pollastro et al., 2003).

Gas transport in extremely low-permeability shale reservoirs is a complex process and difficult in the presence many of mechanisms, such as diffusion, viscous flow and slip flow (Klinkenberg et al., 1941; Guo et al., 2014), and gas adsorption-desorption. The mode of gas transport within shale depends strongly on pore sizes (Knudsen, 1934; Roy et al., 2003; Sondergeld et al., 2010; Javadpour et al., 2007).

Many researchers have studied the process of gas transport in shale gas reservoirs and some of them have used the dual mechanism approach to consider the diffuse flows in the matrix and the stress-dependent permeability in the fracture network with ignored the effects of adsorption and desorption (Ozkan et al., 2010).

Moridis et al. (2010) has considered Darcy flow as the basic mode of multi-phase flow, and has accurately described the thermophysical properties of the reservoir fluids (properties that are control surface and subsurface temperature), and non-Darcy flow, as described by a multi-phase extension of the Forchheimer equation (this equation is an empirical equation, which relates to the pressure and velocity of the flow through a porous medium) that accounts for laminar; stress-sensitive flow properties of the matrix and of the fractures, non-isothermal effects, and isotherm desorption accounting for temperature changes in the presence of various phenomena. Moridis et al. (2010) found that the production data from tight-sand reservoirs can be approximately represented without accounting for gas adsorption. However they did not consider gas diffusion in the kerogen.

Bustin et al. (2008) also studied the effect of the shale structure on gas production. However, in their study it was assumed that the matrix does not support viscous flow or diffusion mechanisms through the intrinsic pore microstructure (Bustin et al., 2008).

On the other hand, Wu et al. (2011) proposed a methodology to simulate shale gas production, but the gas adsorption-desorption were ignored in their model (Wu et al., 2011). It is very important and necessary to understand the gas model of known mechanisms and also different gas storage mechanisms that contribute to the gas transport, where the main contribution for gas flow is free gas, then dissolved gas and adsorbed gas in order to describe the gas transport behaviour in shale structure (Etmian et al., 2014). Figure 2.9 shows gas distribution within shale reservoir from macro-scale to micro-scale.

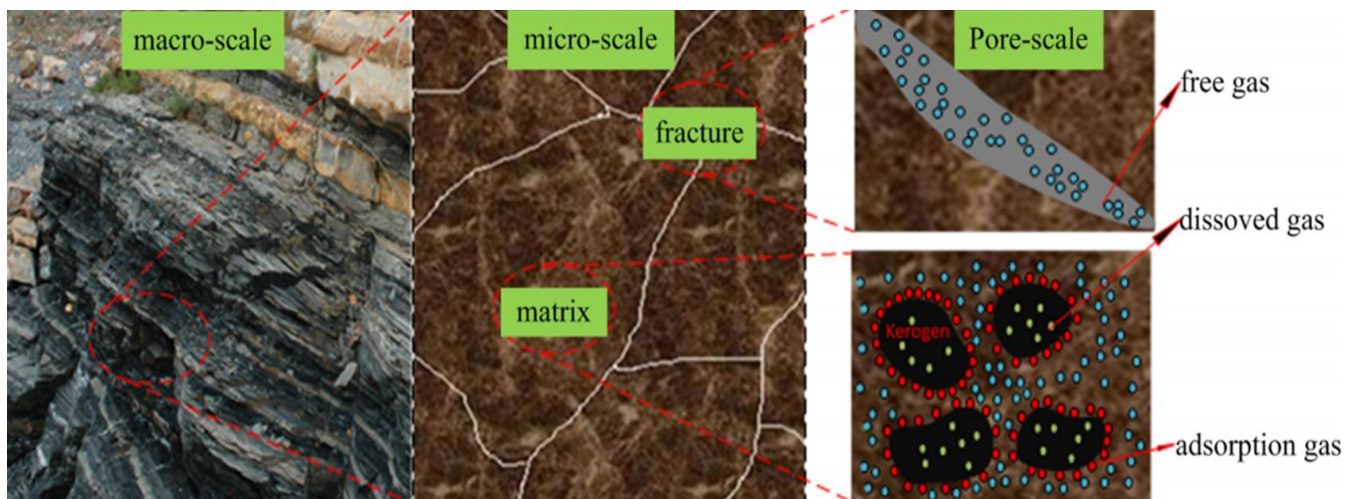


Figure 2.9. Shown gas distribution from macro-scale to micro-scale in the shale reservoir (Guo et al., 2015).

2.3 Gas shale imaging techniques

The complex nature of gas shales is well-known both in terms of its heterogeneous composition of the matrix and difference in pore sizes within the pore space (Mishra and

Akbar, 2011). Gas shale represents a classic example of heterogeneous matrix. The shale rocks are difficult to characterise petrophysically in terms of kerogen distribution and types of pores such as pore volume, size distribution, geometry and connectivity. It is not possible to resolve or characterize these properties at one length scale alone. Consequently, multi-scale imaging techniques have become important in studies of shale reservoirs properties (Lee et al., 2007; Speight, 2012b; Torsæter et al., 2012; Ma et al., 2016). In this current study, different length scales including microscale, submicron-scale, and high-resolution nanoscale have been applied in 3D imaging to describe these properties within gas shale rocks.

The quantification of microstructure properties of gas shales is very important because it provides valuable information for understanding the quality of the shale gas reservoir as well as allowing the quantification of gas storage and fluid transport through the shale. However, obtaining accurate measurement of these properties remains a major challenge due to extremely low porosity and permeability of the shales. The conventional laboratory measurements for these properties are given in Table 2.4. Three dimensional X-ray imaging and 3D image analysis can provide high quality measurements for shales for all of the parameters in this table except permeability, and permeability may be modelled from the other measured data.

The measurements must be interpreted in the light of the sample size for each type of measurement (conventional CT, μ -CT, nano-CT, FIB-SEM), as well as the relevant spatial resolution (voxel size).

Table 2 4 Conventional approaches to rock characterisation applied to shales

Property to be obtained	Conventional Method	Limitations in shales
Porosity	<ol style="list-style-type: none"> 1. Mercury Injection Porosimetry 2. Helium porosimetry 3. Saturation porosimetry 	<ol style="list-style-type: none"> 1. High pressures required may compact sample or lead to fracturing giving measurements lower or far higher than reality. 2. Only the largest of the connected pores are accounted for in the measurement. 3. Not effective or accurate due to the gross difficulties in obtaining a fully saturated sample or a dry sample that does not fall apart. 4. The sample cannot be used for further petrophysical tests due to the toxic nature of the mercury with which the sample is then saturated
Pore and pore throat size distributions	Mercury Injection Porosimetry	<ol style="list-style-type: none"> 1. High pressures required may compact sample or lead to fracturing skewing the distribution. 2. The MIP method does not measure isolated pores.
Grain size distributions	Mercury Injection Porosimetry and use of the theta transform (Glover and Walker, 2009)	High pressures required may compact sample or lead to fracturing skewing the distribution.
Pore aspect ratio distributions	2D Photomicrography using optical or electron microscopes	Only measures sample in two dimensions, where anisotropy can lead to the two measures semi-axes (2D analogue) unrepresentative of the true ellipsoidal pore structure.
Surface area to volume ratio distributions	2D Photomicrography using optical or electron microscopes	Only measures sample in two dimensions, where anisotropy can lead to the perimeter to area ratio (2D analogue) being unrepresentative of the true ellipsoidal pore structure.
Specific surface area	Nitrogen adsorption (Brunauer et al., 1938)	Difficulty in nitrogen access/draining to and from very small or isolated pores leads to underestimation of specific surface area (Brunauer et al., 1938; Van Brakel et al., 1981; Leon, 1998).
Permeability	<ol style="list-style-type: none"> 1. Steady-state permeametry 2. Pulse-decay permeametry 	<ol style="list-style-type: none"> 1. Very slow and difficult to obtain accurate measurements. 2. Can still be slow, but provides better accuracy.

Irrespective of the degree to which 3D X-ray imaging and image analysis can provide high quality measurements of a range of parameters in shales, they should, in my view, always be carried out in tandem with the relevant conventional approach, as it has been done in this thesis. The reason for this is that many of the 3D imaging techniques use very small samples, but intensively. There is always a question whether these samples are representative of the wider rock. The conventional techniques all suffer from the same problem, but their much larger sample/core sizes ensures that this problem is less pronounced.

The main current limitation of MIP is the assumption that all porous materials are considered (solid), and that the pore shape or size does not change during the application of high-pressure of liquid mercury. The extremely high-pressures applied such as a pressure up to 60,000 psi may compress or damage the sample, causing pores to close (or open), and thus producing misleading outcome on the measurements (Westermarck, 2000). This high pressure makes it impractical to measure pores smaller than 3 nm.

In the gas adsorption method the main benefit consists in the use of nitrogen, argon, carbon dioxide, helium and methane which all can obtain very small pores in the range between 2-300 nm, which catch up the most of pores in shale rock.

It should be noted that both the MIP and gas adsorption methods are macroscopic averaging techniques that can only provide data related with open porosity and do not contain direct observation of the individual pores space (Clarkson et al., 2013; Conner et al., 1986; Gregg and Sing, 1982; Mastalerz et al., 2013; Olson and Grigg, 2008; Scholten, 1967).

Previous measurements studies have used nitrogen adsorption-desorption to estimate the pore properties of Bowland shale (Ma et al., 2016), New Albany (Eastern US) (Schrodt and Ocampo, 1984) and porous materials (Sing et al., 2001). However, the most of these experimental studies have used samples of shale powder and investigative techniques have provided details about pore geometry, isolated pores and shape of the pores within shale rock.

Recently a number of imaging techniques has become a novelty and can be used for the analysis and visualize shale microstructure across multiple scales (Figure 2.10), including optical microscopy can be visualize and to measure the mineralogy of the pore features in 2D. However, with this old-style optical approach, the resolution is very limited at around 0.23 μm (diffraction of visible light limits resolution) which prevents the fine grain characteristics within gas shales from being discerned accurately (Bultreys et al., 2016). By contrast (literally) scanning electron microscopy (SEM) provides a higher resolution because electrons have a much smaller wavelength (the de Broglie wavelength of a 2 eV electron is about 0.87 nm). Hence, electrons can be used to image and resolve microstructure such as pores and kerogen from the optical regime down to the nanometre scale within shale (Lemmens et al., 2011; Loucks et al., 2009; Milliken et al., 2013; Milner et al., 2010; Pommer and Milliken, 2015; Qing

et al., 2010). To achieve a good image, the preparation of shale samples is of critical importance. For example, the mechanical polishing procedure used conventionally in the preparation of petrographic sample is not suitable for shales as this technique tends to introduce artefacts and damage the surface of the shale's fine microstructure, such as curtaining and abrasion marks. All of these can make image analysis difficult in terms of the segmentation process (Loucks et al., 2009; Rine et al., 2014; Sondergeld et al., 2010). With advanced SEM applications, even a lower amount of damage can limit the ability of study to comprehensively resolve or analyse the surface of gas shale samples. To overcome this issue and make samples flat, argon (Ar) ion beam milling can be applied to obtain high-quality SEM images of the nanostructures and microstructures in 2D with lower artefacts (Desbois et al., 2011; Loucks et al., 2012, 2009).

Despite providing high-resolution images of the nanoscale and microscale structures of shale, the SEM approach is limited to two dimensions. This is a severe limitation as all of the aspects of the shale (pore volume, matrix and kerogen) vary in three dimensions and form a complex network in three dimensions. Some researchers have used multiple-point statistics from 2D images to create 3D networks of carbonate and sandstone samples (Hajizadeh et al., 2011; Okabe and Blunt, 2004; 2005; 2007), therefore, this becomes extremely challenging in heterogeneous porous media such as gas shales. The use of Focussed Ion Beam (FIB) milling of the surface of the sample between serial SEM imaging provides the most practical approach (FIB-SEM). Here each pass of the FIB strips about 20 nm from the surface of the sample, so 250 images of a 5 mm sparte are of sample would image a cube of rock of side length 5 mm with a voxel resolution of approximately $19 \times 24 \times 20 \text{ nm}^3$.

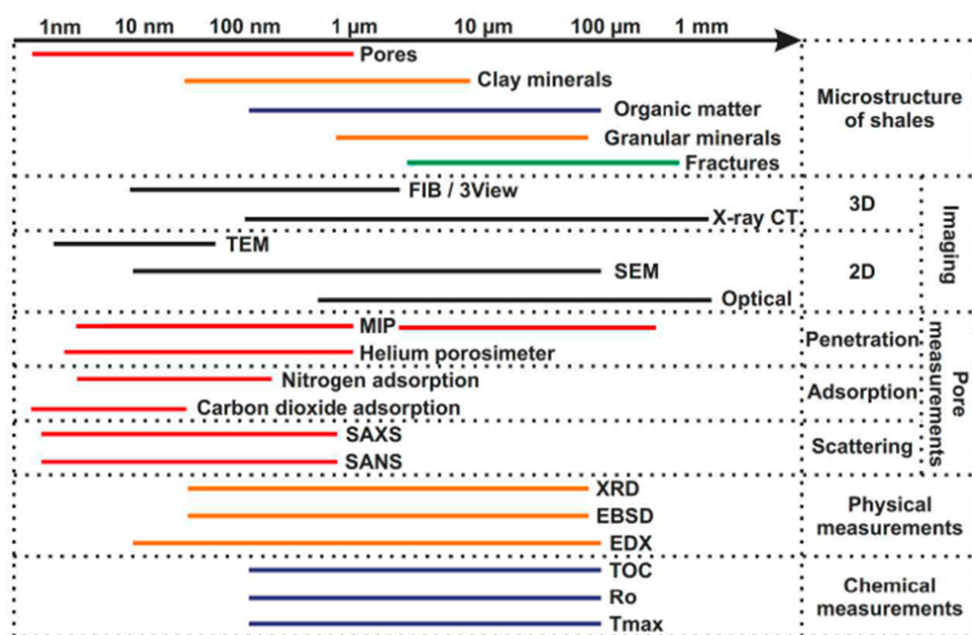


Figure 2 10. Overview of techniques for imaging and characterisation of shale rock sample with the corresponding scales (Ma et al. 2017).

In recent years, the techniques that allow direct three-dimensional visualization and quantification have become very important and helpful for characterization the internal microstructure properties within gas shale. Over the past few years, the X-ray micro-computed tomography (μ -CT) and Focused Ion Beam Scanning Electron Microscopy (FIB-SEM) have begun to be used for the analysis of different shale reservoirs. These techniques have been shown to be powerful and effective tools for representing in 3D imaging and also resolving petrophysical issues, including microstructure imaging, mineral/pores/organic matter quantification, 3D connectivity and pore size distributions (Curtis et al., 2011; Long et al., 2009; Sakellariou et al., 2003).

For gas shale, the three-dimensional imaging technique on characteristics microstructure (pore space) allows to get very important data on the 3-D distribution of pores, kerogen and minerals. Thus, the quantitative investigations would provide useful information, insights by describing the pore space geometric, and fractions volume component including pore size, shape, and connectivity. The μ -CT technique that provides numerous of advantages in the shale namely, it is non-destructive, provides physical measurements of individual 3D structures, obtains high-resolutions down up to micron level, provides a good contrast between multiphase, and also is flexible to several types of measurement processes.

Figure 2.11 shows examples of μ -CT imaging applied at different resolutions to characterise gas shale samples (showing the internal structure of the sample).

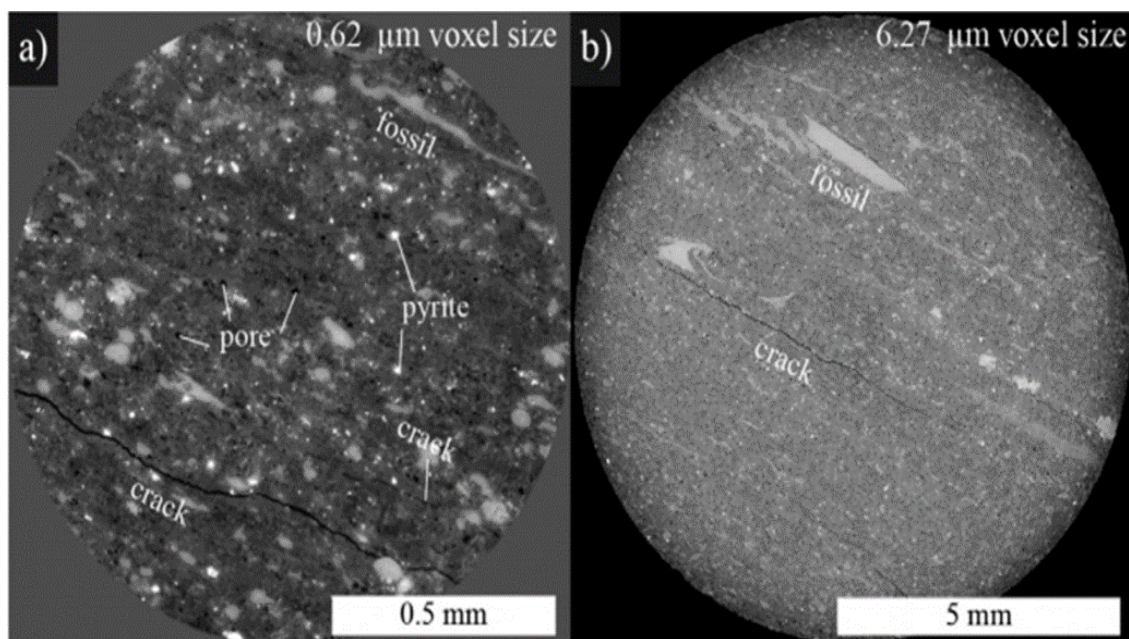


Figure 2.11 μ -CT imaging of gas shale with two different types of resolutions, a) scan at higher resolutions with voxel size (0.62 μ m), showing pores, cracks and pyrite, b) an imaging at low resolutions (6.27 μ m) with largest pores corresponding to the fractures (cracks) (Ougier-Simonin et al., 2016).

However, due to the complex microstructure in the shales, the μ -CT technique can only resolve the microstructure down up to $0.7\ \mu\text{m}$. Hence, the μ -CT technique cannot reveal the shale nanostructure as an interconnected permeable entity, even though that nanostructure exists (Bai et al., 2013; Josh et al., 2012).

The nanometer-scale resolution (Nano-CT) is able to access higher resolutions of sub-microns up to $50\ \text{nm}$. However, it still has difficulty for resolving the majority of pores within shale rocks because of the voxel size limitation (Wu et al., 2017). Consequently, it is still important for understand the basic flow properties and also resolve the pore size up to $0.05\ \mu\text{m}$ in the shale samples (Chen et al., 2013; Saraji et al., 2015).

The advances of the FIB-SEM method consists in resolving structures at nanoscale and also in providing high-quality 3D imaging of different samples at nano-scale resolution (Curtis et al., 2010; Haswell et al., 2008; Sivel et al., 2004; Krueger, 1999). Figure 2.12 presents examples of FIB-SEM cross sections of shale from different shale reservoirs, while Figure 2.13 shows an example of 3D microstructure of shale sample where kerogen is indicated in green, pores in red and pyrite in yellow.

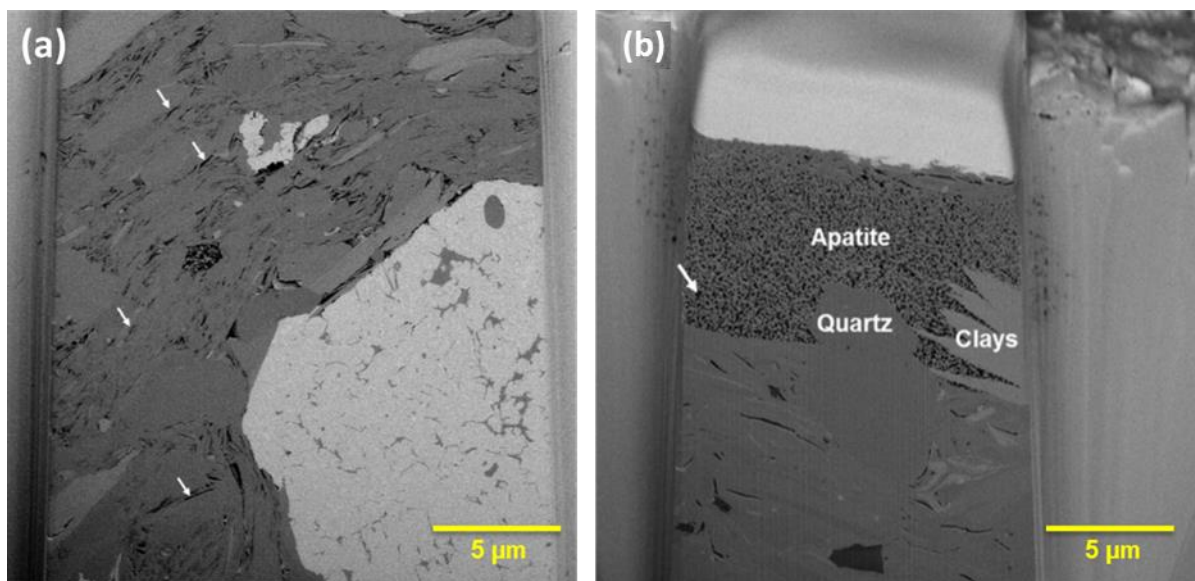


Figure 2.12. Shows the cross section of shale sample that have used by FIB-SEM from different shale formations: a) Haynesville shale sample and b) Eagle Ford shale reservoir sample. White arrows indicate pores (Curtis et al., 2011).

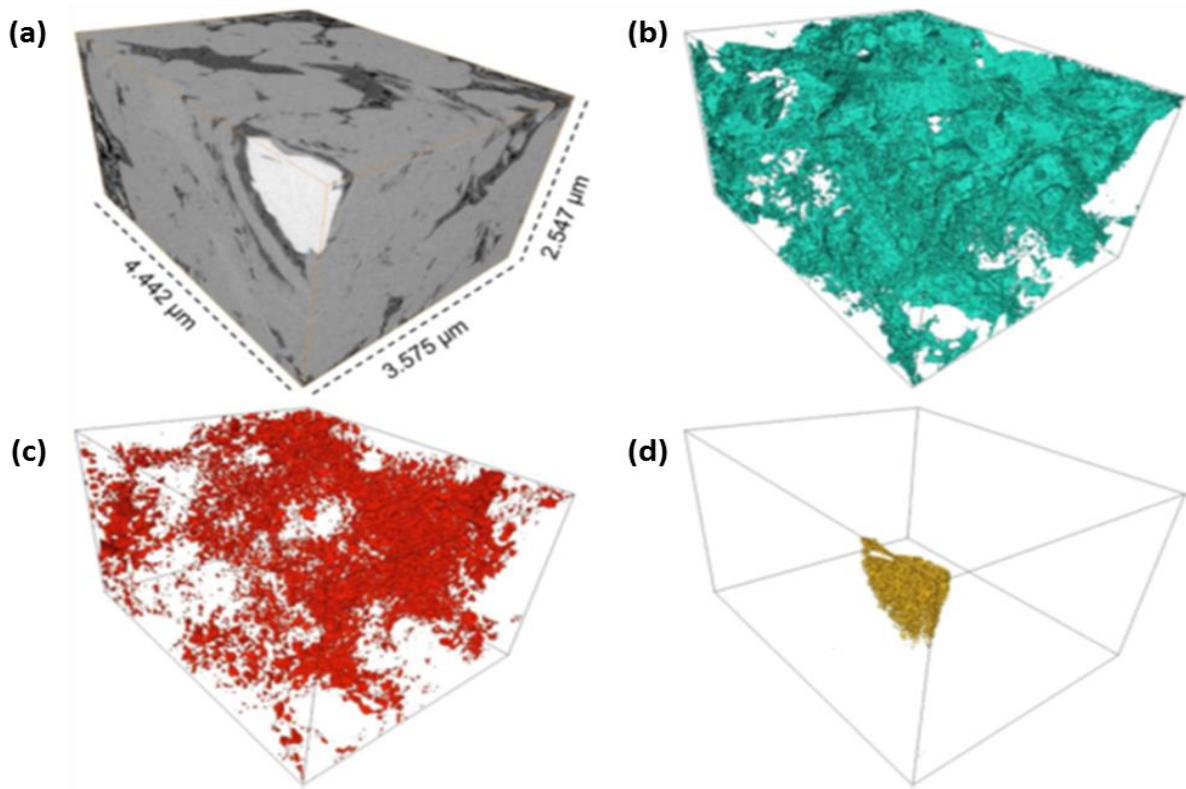


Figure 2.12. 3D reconstruction of FIB-SEM images showing shale structures: a) 3D image of solid, b) 3D of kerogen, c) 3D image of pore network and d) 3D image of pyrite (Curtis et al., 2012).

2.4 Upscaling techniques

The upscaling methods have been used in literature to provide a full information and better understanding structures of pore within shale from the nm to mm-scale (Peng et al., 2015; Zhang et al., 2012a). The typical upscaling techniques are widely used within gas shale such as Gas Research Institute (GRI) method on crushed or core plugs shale (Luffel et al., 1993).

2.4.1 GRI technique on crushed shale

The GRI measurement method was first presented by Luffel et al. (1993), and this method was developed to measure permeability and porosity of gas shale. The technique involves placing a shale sample into a chamber of known volume and allowing gas to expand isothermally into the shale sample through the chamber from a reference chamber (Cui et al., 2009; Zamirian et al., 2014). The permeability and porosity is then estimated from the pressure and time data as gas flows into the shale (Luffel et al., 1993).

Luffel et al. (1993) have reported the permeability of twenty-three samples of Devonian shale by using the GRI method. They argued that this technique avoids the misinterpretations due to the presence of micro-fractures generated by the coring and/or naturally present, because crushed particles of shale are likely to contain micro-fractures which would give misleading

results as the shale is very likely to contain cracks along micro-fractures and these are eliminated during the crushing (Fisher et al., 2017).

Since the publication of the GRI method (Luffel et al., 1993) a number of researchers have given suggestions and ideas for improving the GRI method among of them. As such Profice et al. (2012) noticed that the permeability measured with this method will depend on the particle size of same rocks.

Tinni et al. (2012) made the assumption that the crushed particles do not contain micro-fractures. However by injection of mercury and then imaging the crushed samples with μ -CT the images. Those images showed that the existence very small fractures ranging from about 10 to 20 μm in the shale. Based on these test results Tinni et al. (2012) concluded that the assumption made in GRI measurement of permeability is not valid because the crushed particles contain micro-fractures but argued that it is possible to close the micro-fractures at high pressure in crushed shale particles to get more representative permeability values. These researchers also concluded that measurement of the permeability of shale core plugs rather than crushed samples as the core plugs is more suitable technique when the crushed particle contain micro-fractures.

Luffel et al. (1993) have also described the lack of overburden stress as the main disadvantage of the crushed technique and some of studies have shown that shale permeability may decrease by several orders of magnitude as confining pressure is increased from ambient to in-situ values (Zhengwen et al., 2003). In other words, conducting measurements at ambient conditions can result in an overestimation of shale permeability by several orders of magnitude. Thus it is essential, experimentally, to simulate the overload stress in conditions that better represent those in the subsurface (Casse, 1974; Brighenti, 1989; Chenevert and Sharma, 1993; Sakhaee-Pour and Bryant, 2012).

2.5 Summary

This chapter presented an overview of the literature on shale reservoirs and of the scientific background relevant to the work undertaken in this thesis to provide an understanding of the microstructures of shale gas and to explain how to determine relationships between microstructures and flow of shale gas. The microstructure properties and fluid flow within shale is not sufficiently understood to identify a relationship between the pore structure, porosity and permeability to understand how the microstructure of the shale affects and controls fluid flow at all scales, which raised some gaps in understanding how microstructures in shale affect the different fluid properties controlling gas and fluid flows. A higher level of knowledge is needed, and this can be obtained by increased relevant research, more investigation, more analysis and more correlations between the results. The results of these microstructure properties have been given later in this thesis.

Shale reservoirs are typically extremely heterogeneous and with low porosity ranging between 2-15%, and permeability varying between 1 nD -1 μ D. Gas is stored in shale reservoirs in three phases; free gas, adsorbed gas, and dissolved gas, and the gas transport is based on Darcy flow with slippage effects. Three-dimensional μ -CT, nano-CT and FIB-SEM imaging are shown to be powerful tools for large to small scale imaging of shales, respectively, and also offer the geometrical and quantification of recognised phases such as pores, kerogen and fractures to corresponding length scales. Furthermore, the review of literature relevant to shale imaging techniques with the comparison of upscaling methods has highlighted the current studies in characterising the microstructure of gas shale including quantifying and visualizing pore. This is of interest for the multi-scale study to be undertaken in this thesis.

However, currently, the existing multi-scale imaging studies in shale reservoirs can hardly deliver information to cover all the needed aspects from microscale to nanoscale pores for single samples, and also to study the relationship between pores and kerogen based on 3D quantification.

For the goal of the multi-scale imaging of shales in this thesis, a combination of 3D of μ -CT and Nano-CT with 3D of FIB-SEM is used through a wide range of scales for investigation of the microstructure in shales and detection of the relationship between the scales. A comparison with the upscaling method is also undertaken at the end.

Chapter 3

Experimental techniques and methodology

3.1 Introduction

This chapter focuses on sample selection, preparation techniques and the multi-scale/multi-dimension (2D/3D) techniques used in this study to characterise and quantify the pore-microstructure of gas shales. It includes the experimental and imaging techniques used at each length scale, with the corresponding imaging process and support measurements (upscaling method). Initially, in Section 3.2, the sample selection and preparation for the experimental measurements are described. Section 3.3 presents the petrophysical and geochemical techniques used for analysis, with a discussion of the pore characterization (gas storage and transport) by using 2D/3D imaging techniques. The details of imaging processing with quantification based on the imaging used in this thesis are described in sections 3.3-3.5.

3.2 Shale sample collection and preparation

3.2.1 Sample collection

Shale samples were selected from different shale reservoirs with varied depths and locations as follow:

(i) The Bowland formation in Lancashire, UK ([Andrews, 2013](#)). The Bowland formation underlies the great majority of northern England and has been estimated to have a P50 total in-place gas resource estimate of 264 Tcf in its upper Bowland-Hodder unit ([Andrews, 2013](#)). The samples were analysed in this thesis collected from well number 1 in UBHU, (12 samples in total, at different depths and locations, see [Table 3.1](#)),

(ii) The Alum shale reservoir in Östergötland county, located in the southern part of Sweden. The samples from Östergötland, Sweden were cored from the shallow north and east dipping Alum shale reservoir in Östergötland. This formation is one of the shale gas exploitation attempts in Europe, with the GIP estimates of probable reserves ranging from 0.92 bcf up to 45.2 bcf ([Nielsen and Schovsbo, 2007](#)). A total of 4 Alum shale samples were analysed in this thesis, and taken from well E at depth between 110 -120 m, (for sample locations, and code, see [Table 3.1](#)).

(iii) The Fort Simpson and Horn River formations were brought from Western Canadian Sedimentary Basin (WCSB). The WCSB contains one of the largest reserves of petroleum and natural gas around the world, which producing more than 20×10^9 cubic feet of gas per day and has also been estimated to have 143 trillion cubic feet of natural gas ([Rivard et al., 2014](#)). There were 20 samples in total, and taken from depths between 2535-2705.5 m, see [Table 3.1](#).

The 20 samples provided sufficient material to test carry out imaging measurements as well as supporting measurements on core plugs and crushed materials.

The Bowland shale formation samples were provided by Cuadrilla Resources. The Östergötland were provided by Gripen Oil & Gas Company. The Canadian shale samples were provided by the British Geological Survey (BGS). These varied samples were used in this study to achieve the aims of research described in section 1.2 (Chapter 1).

The summary of all samples (locations, well names, depths, formations and the number of the samples along with their codes) are provided in [Table 3.1](#).

Table 3 1 General description and material resources of the shale samples in this research.

Sample name	Well	Location	Depth	Formation	Crushed GRI	Full core	Sample code
Clay-rich	C1	Lancashire, UK	2497.2	UBHU	Yes	Yes	CR -2.5
	C1	Lancashire, UK	2597.9	UBHU	Yes	Yes	CR -2.6
	C1	Lancashire, UK	2710.2	UBHU	No	Yes	CR -2.7
Quartz-rich	Q1	Lancashire, UK	2494.6	UBHU	Yes	Yes	QR 2.5
	Q1	Lancashire, UK	2596.5	UBHU	No	Yes	QR 2.6
	Q1	Lancashire, UK	2716.1	UBHU	Yes	Yes	QR 2.7
Intermediate-rich	IR1	Lancashire, UK	2492.6	UBHU	Yes	Yes	MD 2.5
	IR1	Lancashire, UK	2593.5	UBHU	Yes	Yes	MD 2.6
	IR1	Lancashire, UK	2706.7	UBHU	Yes	Yes	MD 2.7
Kerogen-rich	KR1	Lancashire, UK	2494.8	UBHU	No	Yes	KR -2.5
	KR1	Lancashire, UK	2597.1	UBHU	No	Yes	KR -2.6
	KR1	Lancashire, UK	2597.1	UBHU	No	Yes	KR -2.7
Gripen-7	E	Östergötland, Sweden	110	Alum Shale	Yes	Yes	A
E-9	E	Östergötland, Sweden	110.8	Alum Shale	Yes	Yes	B
E1	E	Östergötland, Sweden	111.2	Alum Shale	Yes	Yes	C
F-3	E	Östergötland, Sweden	120.3	Alum Shale	Yes	Yes	D
A1	A100B/94	WCSB	2535	Fort Simpson Formation	No	Yes	AF1
A2	A100B/94	WCSB	2535.2	FSMP	No	Yes	AF2
A3	A100B/94	WCSB	2537.4	FSMP	No	Yes	AF3
A4	A100B/94	WCSB	2538.42	FSMP	No	Yes	AF4
A5	A100B/94	WCSB	2540.1	FSMP	No	Yes	AF5
A6	A100B/94	WCSB	2542.2	FSMP	No	Yes	AF6
A7	A100B/94	WCSB	2543.2	FSMP	No	Yes	AF7
A8	A100B/94	WCSB	2543.75	FSMP	No	Yes	AF8
A9	A100B/94	WCSB	2558	FSMP	No	Yes	AF9
A10	A100B/94	WCSB	2559.1	FSMP	No	Yes	AF10
A11	A100B/94	WCSB	2570.5	FSMP	No	Yes	AF11
A12	A100B/94	WCSB	2571.9	FSMP	No	Yes	AF12
A13	A100B/94	WCSB	2575.3	FSMP	No	Yes	AF13
A14	A100B/94	WCSB	2575.9	FSMP	No	Yes	AF14
A15	A100B/94	WCSB	2589.5	MuskwaMember	No	Yes	AM15
A16	A100B/94	WCSB	2665.25	Otter Park	No	Yes	AO16
A17	A100B/94	WCSB	2670.25	OPRK	No	Yes	AO17

A18	A100B/94	WCSB	2691	OPRK	No	Yes	AO18
A19	A100B/94	WCSB	2699.1	HRF	No	Yes	AO19
A20	A100B/94	WCSB	2705.5	HRF	No	Yes	AO20

Notes. WCSB = Western-Canada Sedimentary Basin; HRF = Horn River Formation, UBHU = Upper-Bowland Hodder Unit

This research focused on 7 samples (CR-2.5, QR-2.5, MD2.5, KD2.5, MD2.7, Grpn7 , F3 and E9), which were imaged in three dimensions by various high resolution techniques including (i) Focussed Ion Beam Scanning Electron Microscopy (FIB-SEM), Micron Scale X-Ray Computed Tomography (μ -CT) and Nanometer Scale X-Ray Computed Tomography (nano-CT). The first two of these techniques were carried out at University of Leeds, while the nCT measurements were done at The University of Manchester. All analysis for characterizing the microstructural properties of the samples was carried out at University of Leeds. This included the derivation of the porosity, kerogen, pore volume, pore size and grain size distributions, the distributions of pore aspect ratio, surface area to pore volume ratio, mineral compositions analyses and permeability. The results of these measurements are all novel and are considered to compose the dataset upon which the research reported in this thesis is based.

3.2.2 Shale sample preparation

A variety of sample preparation techniques were used in this study in order to meet the different requirements of successful experimental measurements and imaging.

Initially, a piece of core plug was used to obtain a small approximately cuboid sample of shale of around 0.5 mm³ using a diamond saw and polisher (Figure 3.1f) for the μ -CT experiments. This preparation method was developed from standard thin-section preparation techniques and using its associated equipment. The same approach was used for the mercury injection test samples, but resulting in a sample of larger scale (around 1 cm³).

The cuboid samples were subjected to ion beam ablation using a FIB system in order to produce samples small enough for Nano-CT and FIB-SEM imaging measurements (side length approximately 25 μ m, Figure 3.2 I).

The preparation of samples for high resolution imaging is described in detail in the steps set out below.

- (i) Initial preparation using a diamond saw

The samples are required to be balanced and suitably small in order to produce high-quality images using μ -CT and FIB-SEM, with sample size of about 500 μ m. These were prepared in the School of Earth and Environment laboratory, University of Leeds by firstly fine cutting a small sample of shale, followed by successive polishing of the sample's surfaces, as shown in Figure 3.1. In the first step, a thin layer was sliced from the parent sample using a diamond saw. That slice was sub-divided to produce cubes of side-length of approximately 2 mm Figure 3.1(a, b). In the second step (Figure 3.1c), each cube was mounted on a glass slide (26 mm \times 48 mm) using thermo-plastic wax with a melting-point of between 80-85°C. During the third step each side of each sample was machined by turn to produce a cube of side length 0.5 mm. The machining was accomplished using a Buehler PetroThin[®] cutter/grinder (Figure 3.1d & e).

After machining one side of the developing cube, the glass slide was again placed on the hot-plate to melt the wax, allowing the sample to be turned in order to polish another face. After preparation, the sample was left attached to the slide to ensure it was protected, as shown in Figure 3.1f. The sample was only removed from the slide and cleaned just before it was required for measurement. The cleaning was carried out using acetone to dissolve the wax under an optical microscope.

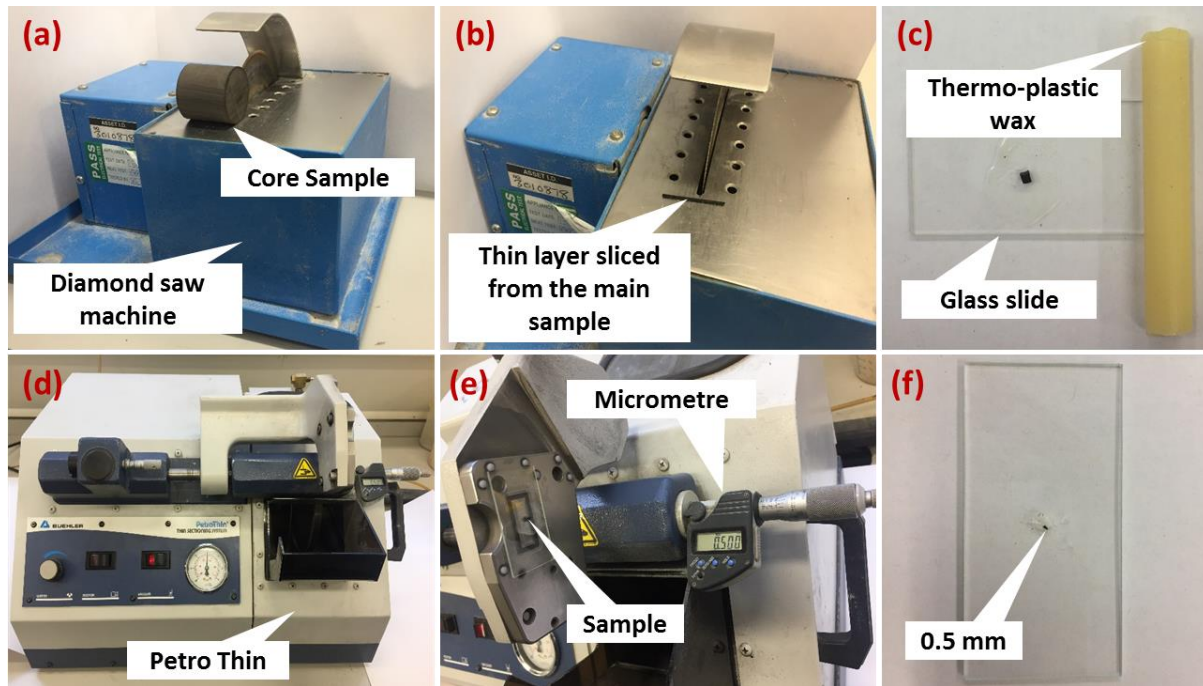


Figure 3 1. Illustration of the procedure of shale sample preparation. (a) Shale sample of around 4 mm using a diamond saw for cutting to slice cubes of length 2 mm. (b) A thin layer was sliced from the main sample and also using a diamond saw. (c) Glass slide and thermo-plastic wax used to hold the sample on the slide of the glass. (d) PetroThin[®] used for cutting, thin section of each side of shale. (e) The micrometer used to measure the size of shale. (f) A typical sample of size of around 500 μm attached to a glass slide with wax for transport.

(ii) Preparation using focussed ion beam ablation

The samples are required to be suitably thin in order to produce high-quality images using Nano-CT and FIB-SEM experiments. The mechanical crushing or laser milling of the samples does not produce small enough samples with the required geometry needed. Furthermore, crushing can cause damage to the pore network within samples (Shu et al., 2020). By contrast, the focussed ion beam ablation provides fine control, allowing very small samples to be prepared with minimal damage to the pore space, and is consequently ideal for the preparation of smooth surfaces on very small samples of shale samples for high-resolution 3D imaging (Akbarabad et al., 2017).

In this study, a thin section of shale rock sample of around 25 μm thickness was prepared for Nano-CT and FIB-SEM measurements. The stepwise preparation process developed herein is shown in Figure 3.2. The shale rock sample was prepared using an ion beam polishing system from an original core sample of around 3 mm in length and diameter. The core sample was

initially subdivided to produce cubes of side length approximately 1 mm using a diamond saw as described above. One of these 1 mm-sized cubes was loaded into the dual-beam FIB-SEM apparatus, and a selected region of interest ($25 \times 25 \mu\text{m}^2$) was identified using ion beam. The region of interest was then coated with a thin protective layer of platinum to offer protection and mitigate specimen charging (typically $1 \mu\text{m}$ in thickness; [Figure 3.2 a](#)). Subsequently, the rock volume around the platinum layer was removed by FIB milling with a 30 kV Gallium ion beam energy and a 2.5 nA beam current ([Figure 3.2 b, c](#)). In the next step, the top of the sample was carefully attached to the tip of a micromanipulator using platinum welding ([Figure 3.2 d](#)). The resulting isolated cubic shape was cut free from the bulk rock using FIB milling ([Figure 3.2 e](#)). The height of the resulting cube was typically 1–2 times greater than the diameter of the micromanipulator. In the final step, the bottom of the cube was attached to a needle by platinum welding and the micromanipulator was cut free by FIB milling ([Figure 3.2 f, g](#)). The outcome of this process was a cube of a side length of about $25 \mu\text{m}$ placed on the tip of a needle ([Figure 3.2 h, i](#)), which was mounted on a sample holder for Nano-CT measurements.

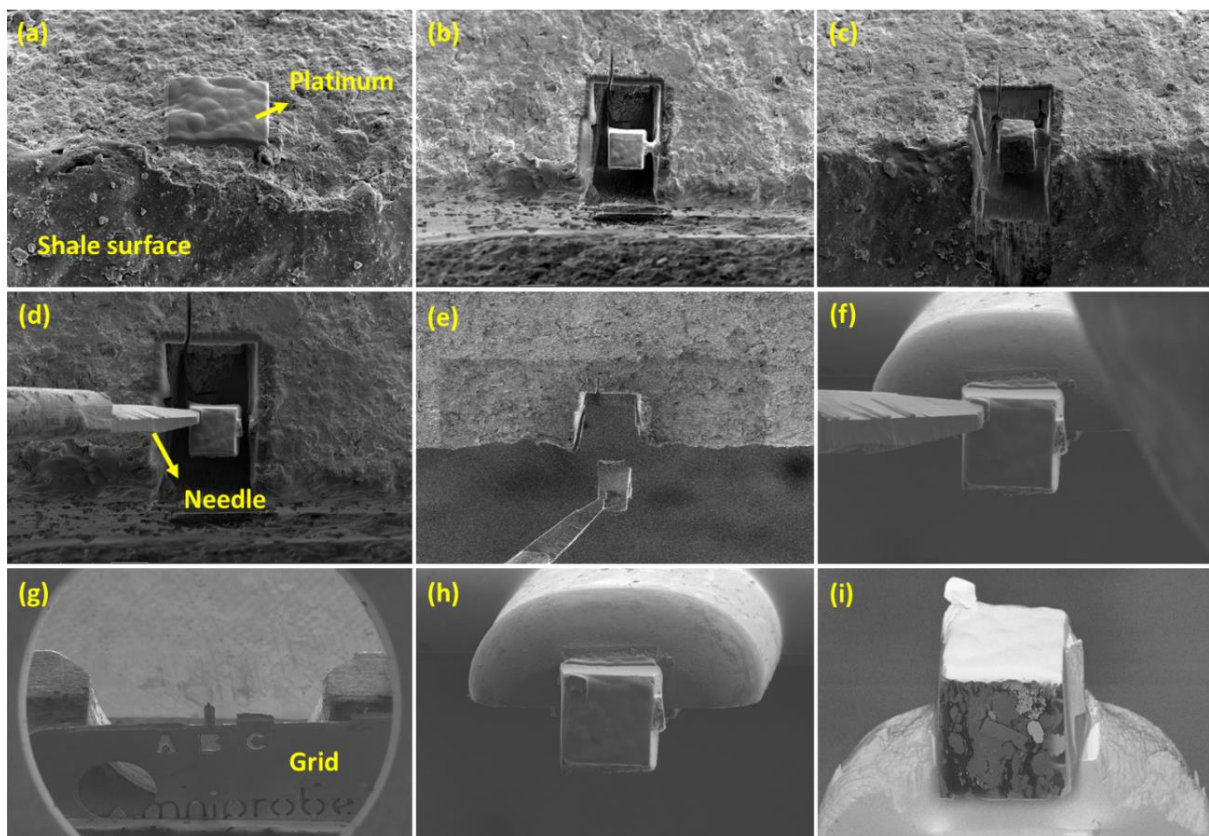


Figure 3 2. Sample preparation for Nano-CT and SEM using FIB: (a) shale surface area of interest ($25 \times 25 \mu\text{m}^2$) that used in this study with a thin protective layer of platinum around ($1 \mu\text{m}$ in thickness) to offer protection and mitigation specimen charging (b-c) the area around the sample milled out; (d) the sample attached to the tip of a micromanipulator; (e) the cylinder cut free from the bulk rock; (d-h) the bottom of the cylinder welded to the tip of a grid; (i) the region of interest of around $25 \mu\text{m}$.

3.3 Overview of experimental methods

A flowchart of the experimental techniques used in the study are shown Figure 3.3.

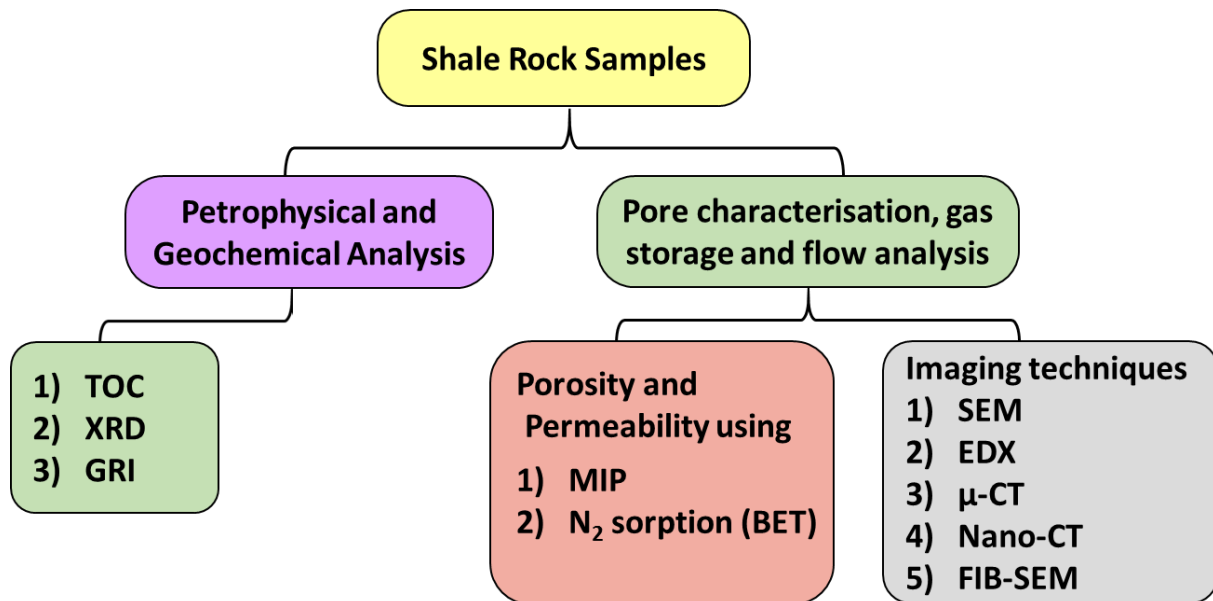


Figure 3 3 Classification of experimental methods used in this study.

3.3.1 Petrophysical and geochemical techniques

3.3.1.1 X-ray diffraction (XRD)

In this study X-ray diffraction measurements were performed in a Bruker D8 XRD with about 5 g of powdered shale sample. The measurement was carried out to confirm the sample mineralogy. Individual mineral phases within the sample were identified by using DIFFRAC.EVA[®] software and its database for mineral or phase identification. DIFFRACplus TOPAS[®] software was used to carry out quantitative XRD of the individual components to within a possible volume error of $\pm 1\%$. The measurements were carried out in the School of Earth and Environment at University of Leeds.

3.3.1.2 Total Organic Carbon (TOC)

Total organic carbon (TOC) was measured on around 5 g of powdered shale sample using a LECO SC-144DR carbon analyser. This instrument provides data on both the total carbon and total inorganic carbon present by analysing samples before and after acid treatment. Here, diluted hydrochloric acid (10 vol %) was used to dissolve the carbonate (Rather et al., 1918), the sample kept in acid for a minimum of 2.5 hours. Inorganic carbon was then subtracted from the total carbon to obtain the amount of total organic carbon. The final result is presented as a weight percentage.

3.3.2 Pore characterisation, gas storage and flow analysis

3.3.2.1 Mercury intrusion porosimetry (MIP)

The Mercury injection (MIP) analysis was carried out using a Micromeritics Autopore IV 9520 system to produce information on porosity, pore throat and pore size distributions of the shale rock sample. The measurements were carried out in the multiphase flow laboratory in the School of Earth and Environment, University of Leeds.

Initially, sub-samples of shale rock of around 1 cm³ were oven dried at 105°C for 48 hours to remove fluids (predominantly water) from the pore spaces. After drying the sample is placed into a MIP penetrometer. The penetrometer (plus sample) was placed inside the low-pressure section of the porosimeter. The evacuation of the sample is required to remove entrapped air from the pores, as this air can produce a resistant back pressure that blocks the intrusion of mercury. After outgassing the sample, the evacuated sample can be immersed in mercury by filling the glass penetrometer. The sample will not spontaneously imbibe mercury because mercury is not the wetting phase. Pressure is required to push the mercury into the sample. The pressure was increased from 1.9 to 60,000 psig in 60 steps a range logarithmic, where a time interval of 10 seconds was allowed for pressure equilibrium to be reached at each step. After reaching equilibrium at each pressure increase the volume of mercury intruded is recorded. This volume is used to estimate the pore size distribution and porosity within shale rock sample. At low pressures only the largest pores with the largest pore throats are filled with mercury. As the pressure increases correspondingly smaller pores are filled with mercury. At any given pressure mercury can access pores of a size larger than pores exhibiting a capillary pressure to mercury equal to the applied mercury pressure. The starting pressure (1.9 psig) corresponds to the largest pore-throat diameters of the sample (90.7 μm), while the highest pressure (60,000 psig) corresponds to the smallest pore throat diameter that can be measured using this technique (3 nm). Hence, the MIP technique is capable, in principle, of recognising pore throats down 3 nm, which is a slightly better resolution than provided by nanoCT and FIB-SEM, and considerably better than μCT.

The systematic errors when using the MIP on shales are discussed later in this thesis (see sections 5.3.4 and 6.2.3 in Chapter 5, and 6, respectively.)

3.3.2.2 Nitrogen sorption experiments and Brunauer-Emmett–Teller (BET) methods.

A Micromeritics Tristar 3000 nitrogen (N₂) sorption surface area analyser was used to provide information on porosity, pore size distribution and surface area of shale samples. Samples were crushed into powder (< 250 μm) then heated at 77 K under vacuum overnight (18 hours) in the School of Chemical and Process Engineering, University of Leeds.

The pore volume and pore sizes were analysed using the Barrett-Joyner-Halenda (BJH) method ([Barrett et al., 1951](#)), while pore surface areas were obtained using Brunauer-Emmett-Teller (BET) theory ([Barrett et al., 1951](#)).

The principle of nitrogen adsorption measurements is based on the gas pressure forcing the gas molecules to **absorb or soak up** to the surface of pores (Sing, 2001). When gas is in contact with pores, a specific number of gas molecules will be attracted or transported to the surface of the pores (Thommes and Cychosz, 2014). This process is known as physical adsorption. The amount of the adsorption dependent of the size of the pores, or other words, when the gas pressure starts to increase, the gas molecules fill up all small pores, which is defined as the adsorption process, and the inverse phenomenon occurs with pressure decreasing in the desorption process (Figure 3.4). The BET equation and the BJH theory are used to calculate the pore size, pore volume and surface area during the process.

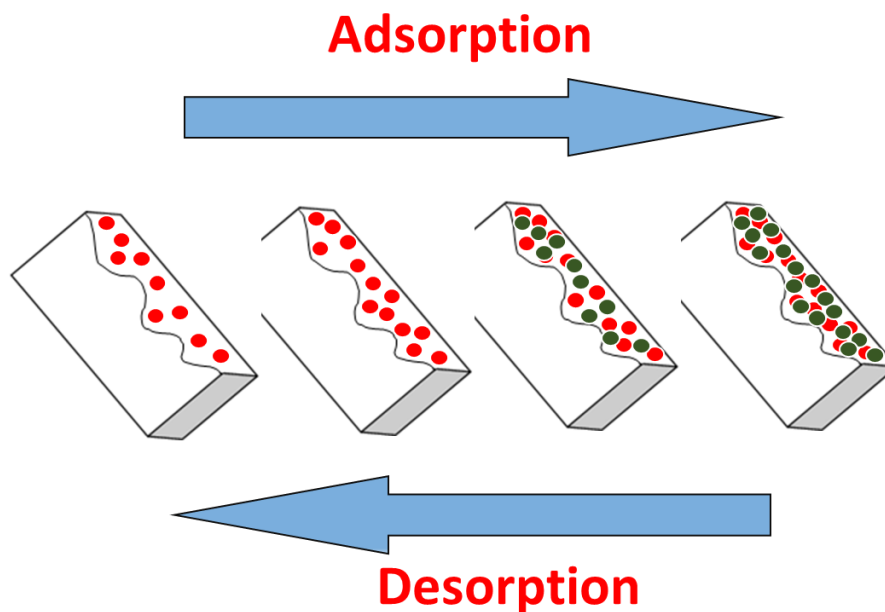


Figure 3 4 Schematic of nitrogen sorption and desorption for pore size and volume distribution measurement (Ma et al., 2016)

The isotherms of adsorption and desorption of N_2 nitrogen were used to classify pore types “shape” based on hysteresis loops following de Boer’s classification (De Boer and Lippens, 1964). Figure 3.5 shows the five types of pores by de Boer’s classification: Type A hysteresis is recognized to penny-shaped (oblate) or to have a very small aspect ratio; Type B is associated with slit-shaped pores; Type C hysteresis is produced by wedge-shaped pores with open ends; Type D loops result from wedge-shaped pores with narrow necks at one or both open ends; Type E hysteresis loop has been attributed to "ink-bottle" pores.

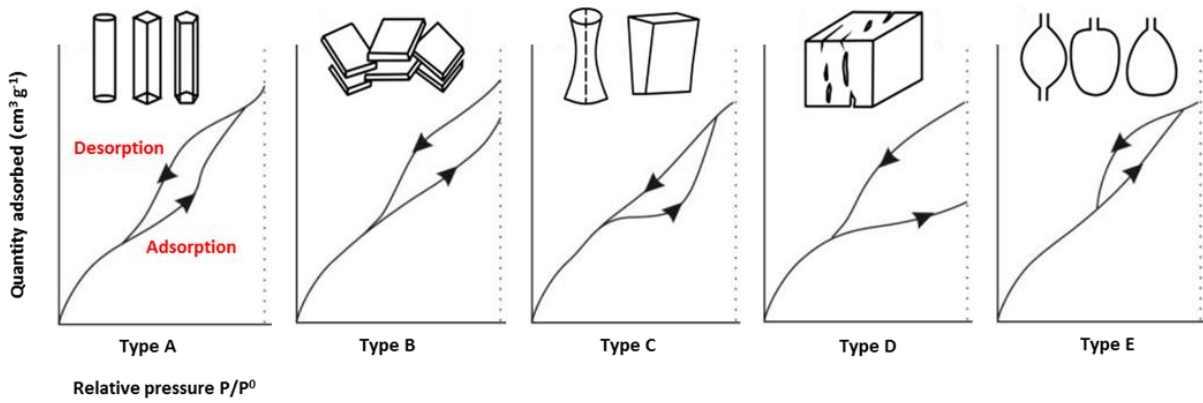


Figure 3.5 Five pore types based on hysteresis loops following de Boer’s identification (De Boer and Lippens, 1964).

Based on hysteresis loops and the identification above, the pore shape within shale rock samples in this study are interpreted to be penny-shaped (oblate, Figure 3.6, i.e., attributed to Type A) or to have a very small aspect ratio (i.e., small thickness relative to length).

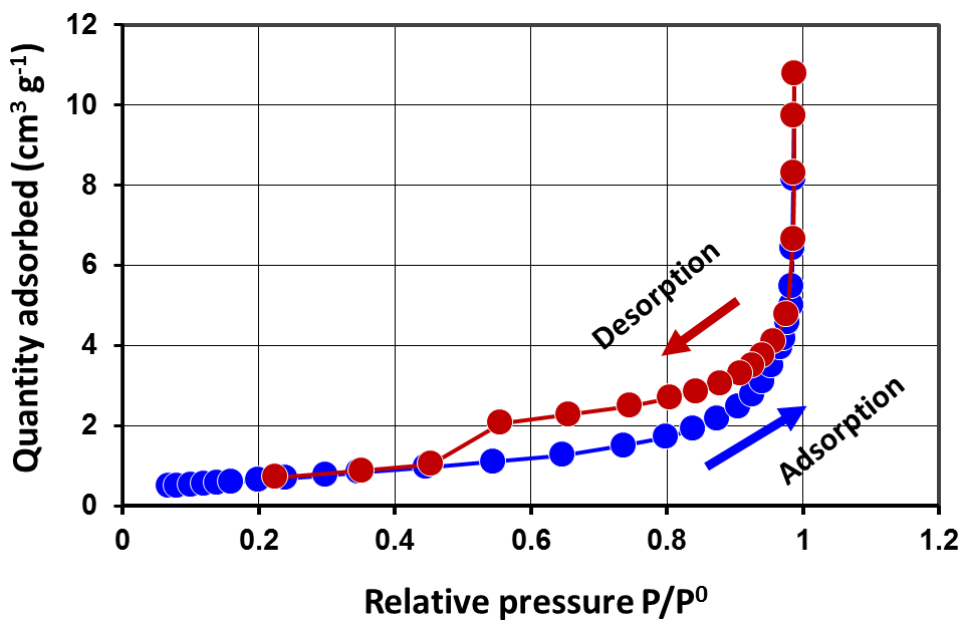


Figure 3.6. The isotherms of adsorption and desorption of Nitrogen N_2 sorption experiment used in this study.

3.3.3 2D imaging techniques

3.3.3.1 Scanning Electron Microscopy (SEM) and Energy Dispersive X-ray (EDX) analysis

Scanning Electron Microscopy (SEM) allows for the analysis the surface of the microstructure of shale samples with high resolution (below the limit of resolution of optical microscope).

Initially, SEM images of broken or mechanically polished shale samples provided only limited observations about the shale matrix (Driskill et al., 2013). However, recent applications such as ion beam polishing have greatly improved the ability of the SEM technique to produce high quality images with high magnification.

In this study, a different sizes of samples that have measured, were cut from shale sections and polished using ion beam miller. All samples were coated with carbon to prevent them from charging during ion beam milling. The samples were then analysed using a FEI Quanta 650 FEG-ESEM environmental SEM with an Oxford Instruments X-max 80 SDD (liquid nitrogen free) EDX. The data were analysed using INCA[®] 350 software.

Secondary electron (SE) microscopy was used to give information on the structure of the surface of shale samples whereas back scattered electron (BSE) microscopy (Figure 3.7) was used to assess the distribution of minerals and pore space. The electron voltage was set at 30 kV, with a spot size of 5 and an aperture of 4.

The Energy Dispersive X-ray (EDX) analysis was also used to provide the elemental compositional on the shale sample. Element mapping was performed on selected areas of shale samples by EDX mapping, and the results helped to analyse the 2D distribution of the elements inside the sample, as shown in Figure 3.7.

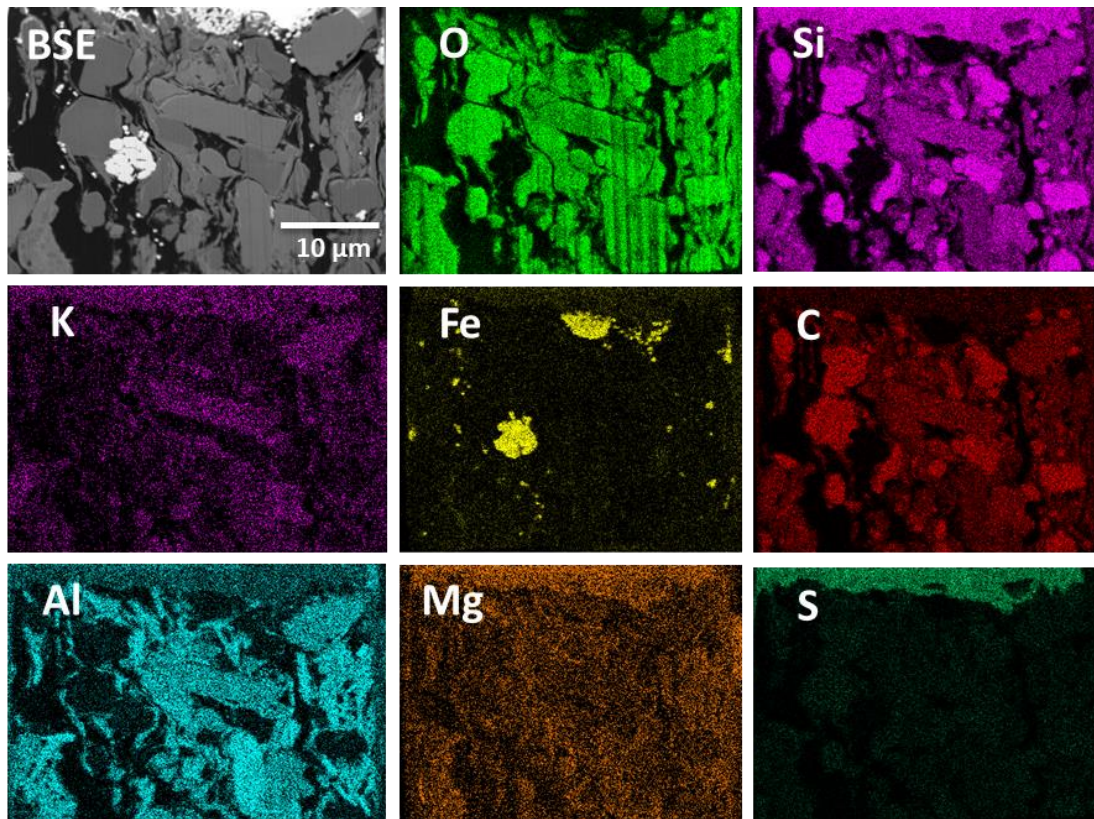


Figure 3 7 Diagram of the SEM images with EDX mapping for chemical composition analysis, where (Si) the light pink region is silicon, the area shown in yellow is Iron (Fe), the green area is oxygen (O), the carbon (C) is shown in red, the pink is potassium (K) and the brown is magnesium (Mg).

3.3.4 3D imaging methods

3.3.4.1 X-ray computed tomography

X-ray micro-computed tomography (μ -CT) is non-destructive method for the characterisation materials that provides 3D imaging of the internal structure of an object (Ketcham and Carlson, 2001; Michael, 2001).

The principle of μ -CT relies on the attenuation of X-rays by the sample due to absorption and scattering, which depends on density of the materials. The extent of attenuation along a given path across the sample is described as the proportion of the X-rays that interact with the material, and is exhibited by different grey scale values on a 2D image. Many of these 2D images, each representing the pathways of X-rays at different angles through the specimen can be analysed to produce a 3D volume (Landis and Keane, 2010). The resulting 3D images reconstruction processes are typically displayed as a series of 2D slices, but can be visualised as a semi-transparent 3D object. Either way, the resulting dataset comprises a large number of voxels, each of which has an x,y,z , position and a δx , δy , δz side lengths as well as a grey scale value (usually integer values from 0 to 255, i.e., 8 bit) representing the CT number of the material covered by that particular voxel. The CT number is a function of material density and atomic mass.

This process is illustrated in [Figure 3.8](#). Two forms of X-ray tomography technique have been used in this study, X-ray (μ -CT) and (Nano-CT), each of which has a different resolution (i.e., values of δx , δy , δz , and require different instruments and sample sizes.

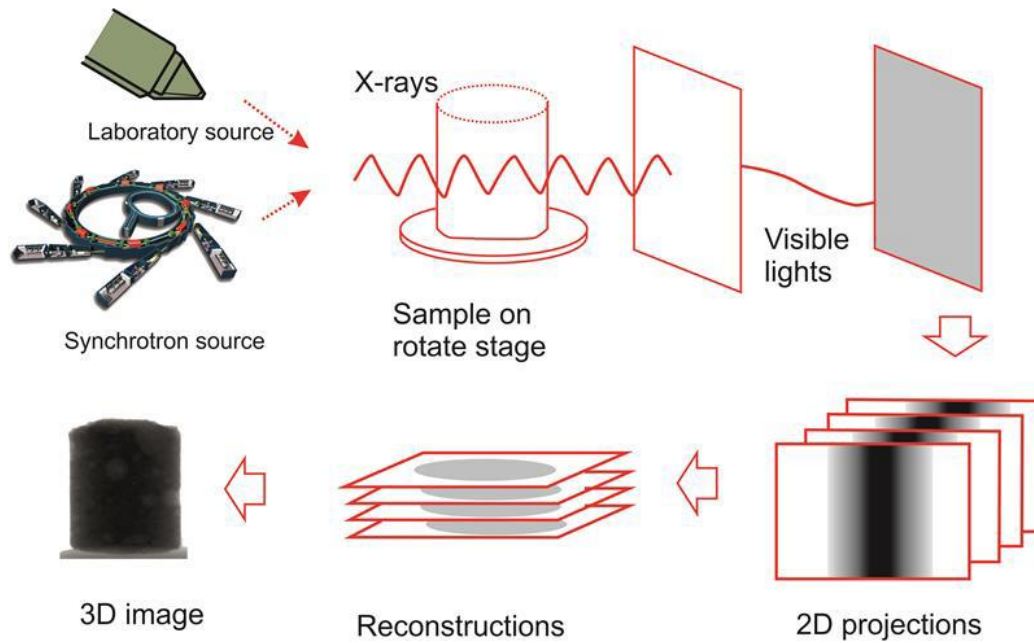


Figure 3.8. Illustration the procedure of X-ray tomography images as well as creating 2D projections and then reconstructed to the 3D volume (adapted from Ma et al., 2016).

The higher resolutions of X-ray micro-tomography and X-ray nano-tomography are implemented in lens-based systems ([Withers, 2007](#)), which use Fresnel zone plates (FZP, [Figure 3.9](#)) or glass capillary condensers to condense the 'light' which is then collected by plate of the objectives to get a highly magnified image ([Figure 3.9](#)). The X-ray (μ -CT) can provide sub-micron resolutions, whereas the nano-CT can provide even better resolutions, up to 50 nm.

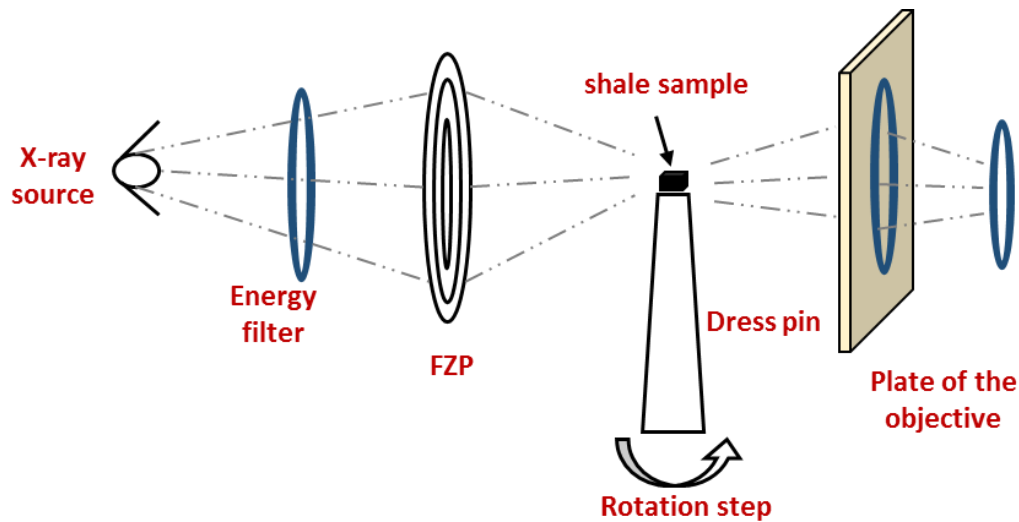


Figure 3.9. The schematic diagram of X-ray nano-tomography.

In this study, the Zeiss X-Radia 410 μ -CT instrument equipment was used to image gas shale at a micron scale, as shown in [Figure 3.10](#). The X-ray source was operated at a voltage of 80 kV with a power of 7.0 Watts. The field of view (FOV) and pixel size depend on the sample size and distances between the sample and X-ray source. The apparatus provides a pixel resolution of approximately 0.94 μ m.

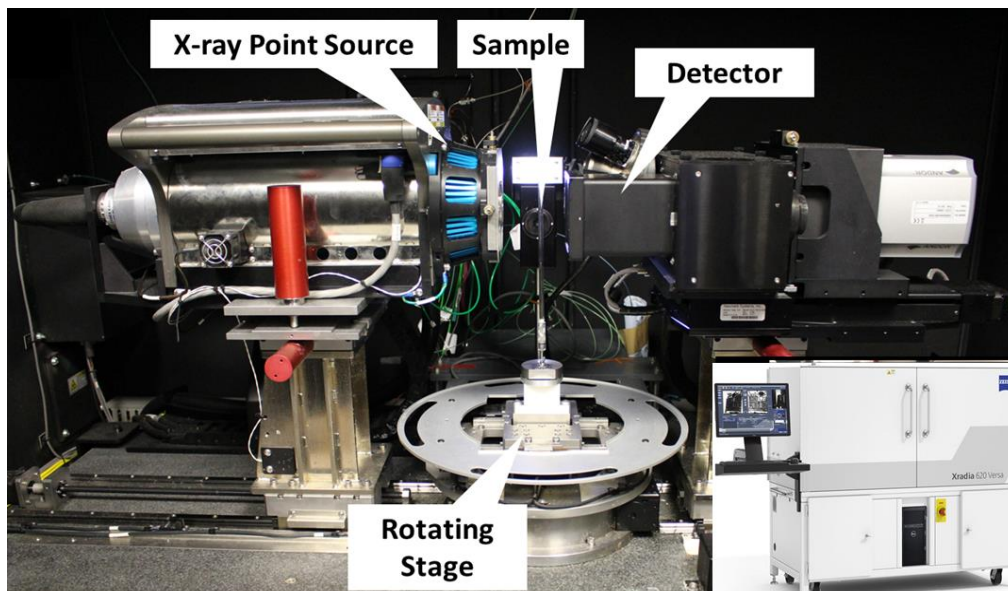


Figure 3.10. The Zeiss Versa 410 X-ray micro-tomography (μ -CT) device used in this work to capture 3D scans of gas shale sample. (Inset) The μ -CT consists three main components: an X-ray focus source, an x ray detector and a rotation stage to control and mount the sample used in this research study.

For the Nano-CT measurements, a higher resolution ZEISS Xradia 810 Ultra instrument was used (X-ray Imaging Facility, University of Manchester). The X-ray source on this instrument provides invariable X-ray beam of 35 keV energy with a power of 7.0 Watts. The instrument provides higher resolutions than the μ -CT apparatus with an imaging pixel of about 64 nm.

3.3.4.2 Focused Ion Beam scanning electron microscopy (FIB-SEM)

A dual beam of scanning electron microscope (FIB-SEM) use to remove or mill away the materials from the sample which allows sample to be cross-sectioned for slice-and-view. This procedure is based on using a FIB to milling or cuts at a chosen site in the sample. The cuts are then followed by viewing or imaging surface of the sample with SEM. During the milling, the FIB is set at a 52° angle while SEM beam is kept as normal to the sample surface, see [Figure 3.12](#). The milling and imaging process steps are repeated and results in the generation of a series of 2D images of the sample and then these 2D images can be reconstructed into a 3D grey-scale volume. This technique is particularly useful in revealing the 3D distribution of mineral types, pores, kerogen (organic matter) and porosity for gas shale samples.

In this study, the FEI Helios G4 CX DualBeam system was used to produce 3D images of gas shale volumes ([Figure 3.11a](#)). The first step necessary in order to get a good quality image in 3D is the sample coat over with carbon. This reduces charging of the area of interest by the constant incoming stream of electrons during SEM operations and ions during ion beam milling and cutting. In addition, a thin layer of a conducting material (platinum, Pt,) was also placed on the top of the area of interest. The platinum was delivered to close to the area of interest in the form of a gas by a needle gas injection system ([Figure 3.11b](#)). The platinum coating serves to protect the sample from damage and to reduce so-called curtaining artefacts during imaging ([Ishitani et al., 2004](#)). These curtaining artefacts exhibit themselves as striping in the images.

A focused beam of gallium ions (Ga^{3+}) operating at an energy of 30 keV and a beam current of 3 nA was applied for the cutting into the rock and preparing each new milled surface prior to imaging. Each surface was imaged using the SEM with a 5 kV accelerating voltage and a 0.8 nA beam current under backscattered electron (BSE) mode. The whole process resulted in a 2D stack of around 1300 slices, with each slice having a section thickness of 20 nm. The 2D image were collected using a slicing and view module. The 2D images were then reconstructed into a 3D volume.

The EDX was also used for mineral/organic identification on the shale surface; the way in which this has been operated is explained in earlier section 3.3.3.1.

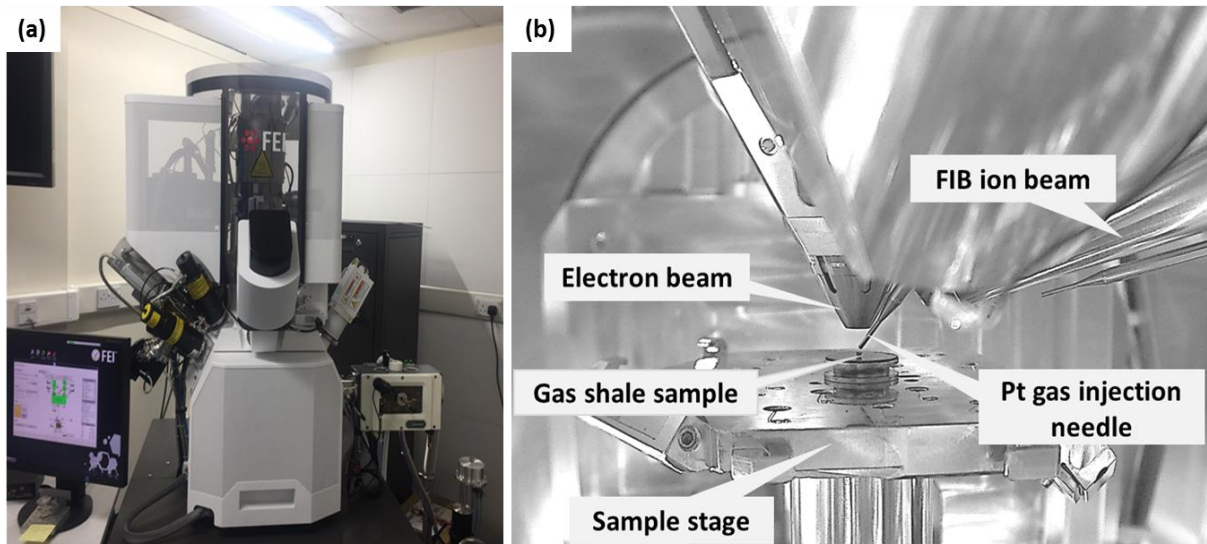


Figure 3 11. (a) FIB-SEM device to capture 3D images of the gas shale sample used in this work; (b) the main components of the FIB-SEM: an electron beam, focused ion beam (FIB), platinum (Pt) gas injection needle deposited on the top of the shale surface (protective layer), and a sample stage to mount and control the sample.

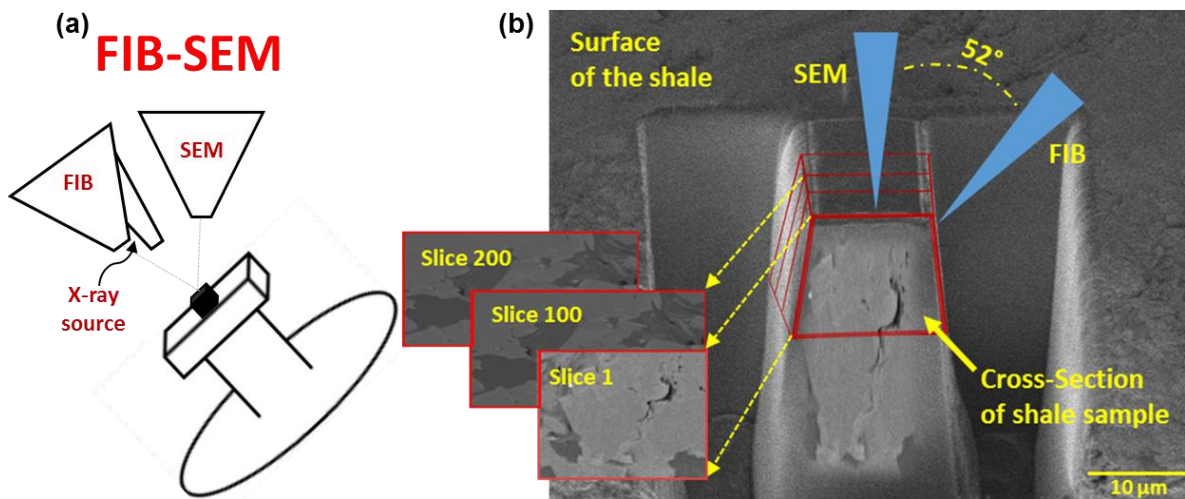


Figure 3 12. (a) a diagram of the FIB-SEM procedure where the ion beam is set at a 52° angle and an electron beam is kept as normal for scanning, (b) serial of cross-sectioning of a shale sample using a dual-beam FIB-SEM system. The ion beam (FIB) is used to remove material from the shale surface creating a cross-sectional face that can be imaged by the electron beam (SEM).

3.5 Comparison of Multi-scale imaging μ -CT, Nano-CT and FIB-SEM techniques

The novelty of imaging techniques (μ -CT, Nano-CT and FIB-SEM) have been shown to be powerful tools in this study for resolving petrophysical issues of gas shale, including the visualisation of fine microstructure (Curtis et al., 2011; Long et al., 2009), the quantification of the size distribution and morphology of the shale phases (mineral matrix, pores and Kerogen) and the 3D connectivity of the shale components that ultimately controls the ability of the pore network to transport gas (Ma et al., 2019). However, these techniques have their own limitations in terms of resolution and sample size (Figure 3.13). For example, the μ -CT and Nano-CT techniques can only determine the pore throats larger than 0.7 μm and 0.05 μm , respectively (Ma et al., 2019). These techniques show many pores to be either isolated or only connected locally (Ma et al., 2016; Saif et al., 2017). This cannot describe that the shale is permeable (Bai et al., 2013a; Josh et al., 2012), while the FIB/SEM can resolve the pore from 50 μm and 10 nm and provided good connectivity

Although μ -CT, nano-CT and FIB-SEM can yield a stack of 2D images composed of pixels with different of grayscale intensity with more or less similar scale (nano-scale). They are quite different in terms of procedure and system capabilities. Table 3.2 provides a summary of the main differences and significant parameters for each technique that have used in this study. The main key differences between these methods is that FIB-SEM is a destructive technique, in which slices of the material are physically milled away by the FIB to reveal successive cross sections which are imaged with the SEM (see Figure 3.12), while μ -CT and nano-CT are a non-destructive technique with maximum resolutions of 1 μm and 64nm, respectively.

Table 3 2 Comparison of the operational parameters of multi-scale (μ -CT Nano-CT and FIB-SEM) techniques (as implemented in this study).

<i>Aspect</i>	<i>μ-CT</i>	<i>Nano-CT</i>	<i>FIB-SEM</i>
Imaging time (hours)	~ 8-14	~ 40	5-8
Resolution (nm)	1000	64	50
No. of imaging or slices	980	1601	750
Field of View	~ 0.94 μm (x , y and z) at 1 μm resolution	~ 64 nm (x , y and z) at 64 nm spatial resolution	36, 45(x and y) at 30 K magnification, but limited in slicing direction (z)
General	Non-destructive	Non-destructive	Destructive
Imaging conditions	Atmospheric	Atmospheric	Vacuum
Considerations	Low contrast	Low contrast	Excessive brightness

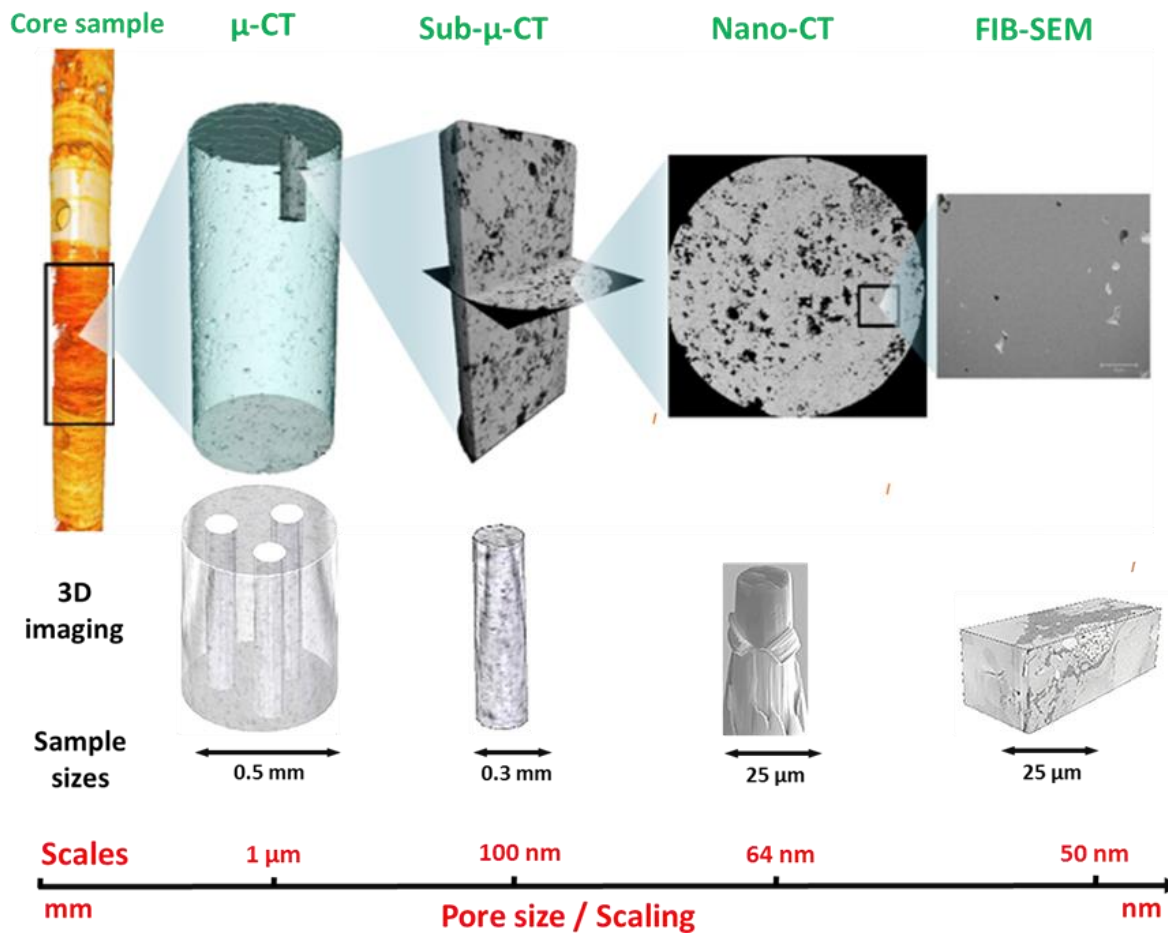


Figure 3.13. Overview of multiscale imaging techniques (μ -CT, Nano-CT and FIB-SEM) used in this study.

3.6 Imaging processing

Image filtering, processing and analysis was carried out on the 8-bit grey-scale level 3D datasets acquired by the μ -CT, nano-CT and FIB-SE occur in a number of specific steps. For example, reconstruction to build 3D data from a set of 2D slices, filtering to decrease the noise, thresholding to classify different voxels by grey-scale level, segmentation to separate different phases such as pores, Kerogen (organic matter), clays and other minerals, and finally microstructural analysis (Stauber and Müller, 2008); (Korfiatis et al., 2007; Landis and Keane, 2010). This section describes the image processing steps. The purpose of image processing is to obtain a clean fully segmented dataset that image analysis can subsequently be used to calculate the physical characteristics of the various components it images.

3.6.1. Stack alignment

Stack alignment is the primary stage in the image processing of the FIB-SEM data. Misalignment of FIB-SEM images may occur due to ion beam drift, where the charging of the surface during milling disturbs the focus of the imaging beam when imaging the new 2D slice (Schaffer et al., 2007). Realignment can be carried out in Avizo software by aligning the 2D

slices to match up the similar features for every slice, including the horizontal drift caused by the electron beam or rotated drift caused by the ion beam.

3.6.2 Filtering

The raw data images obtained from imaging systems (μ -CT, Nano-CT and FIB-SEM) that can have noise due to low energy through the surface. The image can be filtered to reduce the noise or advance the contrast. There are several filtering methods that can be used to reduce the noise which include median filtering, non-local means filtering and edge-preserving smoothing filtering.

The non-local means (NLM) filter was used in most of this study (Figure 3.14) specifically in the tomography data (μ -CT, Nano-CT) and FIB-SEM images to denoise or reduce the noise level from the imaging. The NLM filter works with a similar weighted average of all pixels in the images (similar neighbouring pixels give larger weights); in other words it evaluates how similar they are to the target pixel (Buades et al., 2005). This method was used to eliminate the noise from the imaging without blurring the contrast between the phases (pores, Kerogen and minerals) and also without losing their shapes. The NLM parameters used in this study were local neighbourhood of 5 pixels and a similarity value of 0.6 for both tomography and FIB-SEM data in 2D (same parameters with 3D) for slice stack to reduce image noise (Korfiatis et al., 2005).

This filter also has a number of advantages: (i) removes the noise from the imaging without blurring the contrast between the phases (pores, Kerogen and minerals). (ii) Eliminates the small contrast variations within all phases without negatively impacting component morphology and losing their shapes. (iii) Allows to use on 2D / 3D images and also helps to reduce the effect of imaging artefacts without decreasing resolution and voxels for all phases (Buades et al., 2005).

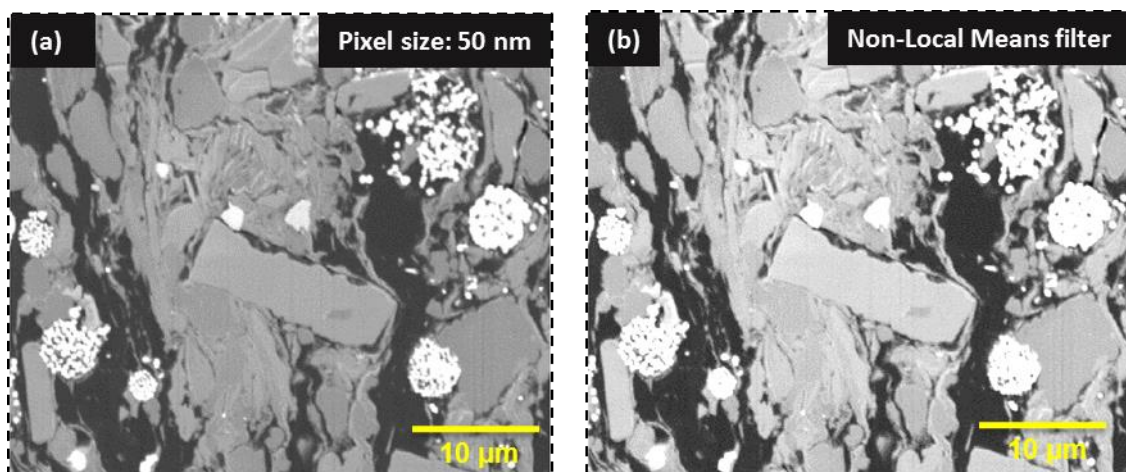


Figure 3 14. (a) Example of a raw image of a gas shale, together with (b) the non-local means filtered version of the same image.

3.6.3 Thresholding & Segmentation

Before calculating the microstructure properties of gas shale rock, the phases in the imaging have to be suitably known or identified. The segmentation in the images is that the process of separating the original image into different parts or segments according to grey scale values and is the initial step of quantification in nano-CT, μ -CT and FIB-SEM image analysis. It should be noted that the terms thresholding and segmentation are often used interchangeably, but there is a subtle difference between the two. Thresholding is the process of classifying the pixels or voxels according to whether they conform to certain rules (e.g., having a grey scale value >100), while segmentation is the separation of sets of pixels and voxels according to the same rules. One has to threshold before one can segment!

Many thresholding/segmentation techniques are available in the software package Avizo®, and the most common are global thresholding, watershed segmentation and manual segmentation.

Global thresholding is simply method of segmentation where values of the greyscale within a range are segmented as a particular phase, which could be chosen by a threshold T (line) that separates object from background (Figure 3.15a). This method can only be applied for two phases therefore it is not adequate for shales as they have multiple phases such as pores, organic matter/ Kerogen, and other minerals. To identify multiple phases, segmentation by using watershed method is better than global thresholding (Sheppard et al., 2004). The histogram of greyscale values in the watershed method can be divided into several regions according to the 'peaks' and 'valleys' (Figure 3.15b) (Sun and Luo, 2009).

In this study, the data sets from the μ -CT, nano-CT and FIB-SEM images were processed using watershed threshold method. The watershed threshold method has been applied in this study because shale imaging has multiple phases, therefore this method has identified and separated several phases (pores, Kerogen, and other minerals). The watershed technique was not distinct enough to segment phases directly in this study. Therefore, the manual segmentation has also been applied to extract the individual pores from the kerogen in each single pixel based on the colour map (Boruah et al., 2015; Lasonov et al., 2009; Gundermann et al., 2014).

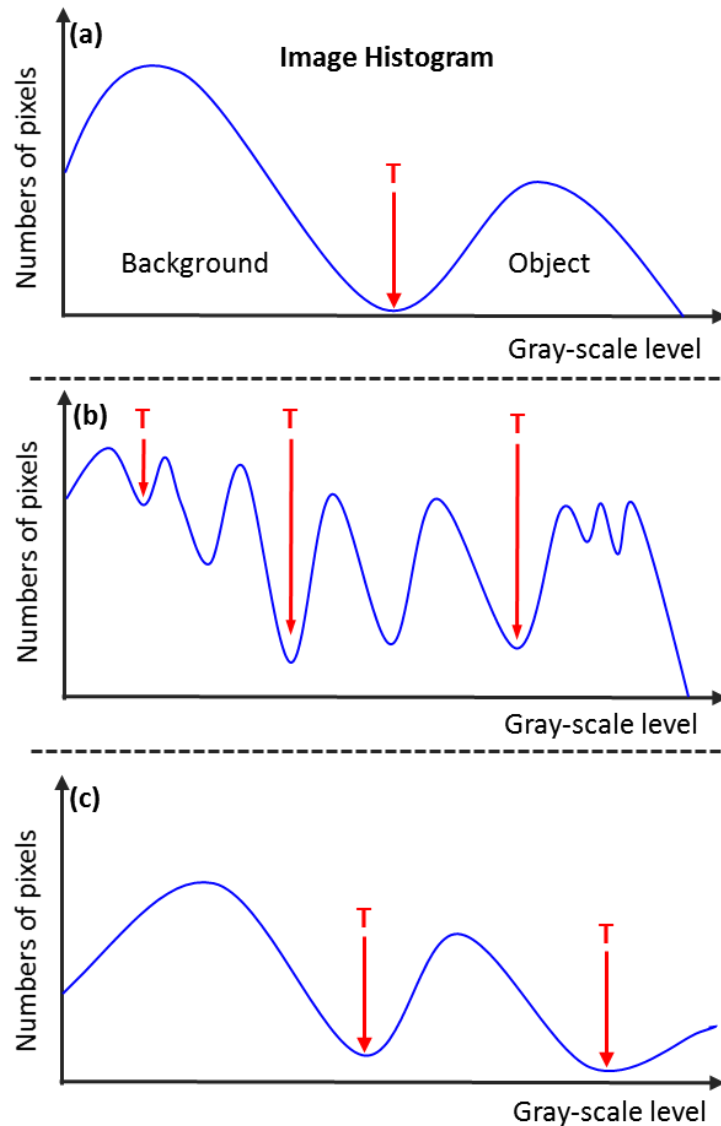


Figure 3 15. Schematic diagrams for segmentation methods: (a) Global thresholding, (b) watershed segmentation, (c) manual segmentation.

3.7 Quantification based on the imaging

The aim of the image processing was to get a fully segmented dataset for use in image analysis in order to calculate and analyse the petrophysical properties of shale based on the image and segmented phases, such as the volume, sizes, shapes, and connectivity of pores (Vlassenbroeck et al., 2007). After segmentation, each object is considered individually for different purposes of quantification (Long et al., 2009). Consequently, having isolated ‘pore’ by segmentation, the image analysis uses solely that subset of the whole 3D image that is recognised as ‘pores’.

There are many properties that may be calculated (Table 3.3); given the time constraints the analysis has been confined to the following physical properties:

Table 3 3 shows the calculations and measurements and used in this study to measure the petrophysical characteristics of pores within shale rock sample.

Measurement	Definition
Length	Average length of the pores in 3D (<i>a</i> axis, Figure 3.16), μm
Width	Minimum length of the pores in 3D (<i>c</i> axis, Figure 3.16), μm
Thickness	Maximum length of the pores in 3D (<i>b</i> axis, Figure 3.16), μm
Volume	Volume of individual pores, μm^3
Surface area	Surface of individual pores, μm^2
Equivalent diameter	Equivalent diameter of individual pores was calculated as the equivalent diameter to represent the pore size, $\left(\frac{6V}{\pi}\right)^{1/3}$, μm
Aspect ratios	The ratio of the maximum length and minimum length of pores, <i>b/c</i>
Surface-area-to-volume ratio(ξ)	Surface area per unit volume of an object or collection of objects, Surface area / volume, μm^{-1}
Scale invariant surface area to volume ratio(σ)	The conventional surface area to volume ratio multiplied by the intermediate axis of the pore, $\sigma = x_i \xi$

3.7.1 Equivalent diameter

Equivalent diameter is defined as the diameter of a sphere with equivalent volume, which can be re-arranged to have a spherical diameter representing the pore/particle size, that's the first thing have done in this work using the equation (Jennings and Parslow, 1988):

$$D_{Eq} = \left(\frac{6V}{\pi}\right)^{1/3} \quad (3.1)$$

Results given later in this work indicate that the assumption of spherical pores for the great majority of pores in shales is not representing at all the pore size , and it can better done by using ellipsoid, but have given it here as a reference point. Since most pores in shales are oblate, it is misleading to use a single pore diameter

The equivalent diameter is a particularly unhelpful parameter is gas shales because it assumes the pore, mineral or kerogen is spherical. In shales, this is demonstrably not the case. It is included only as a simplistic measurement, upon which the research has improved.

3.7.2 Aspect ratios

The aspect ratios of an element are defined as the ratios of orthonormal dimensions of the element. In this study, the pores are assumed as ellipsoids in shape with semi-axes *a*, *b* and *c* as shown in (Figure 3.16), where *b* is the maximum length of the ellipsoid, *a* is the maximum width and *c* is the maximum height. The dip and azimuthal directions of the ellipsoid are arbitrary, and consequently the ellipsoid may be positioned in any direction with respect to an externally imposed coordinate system.

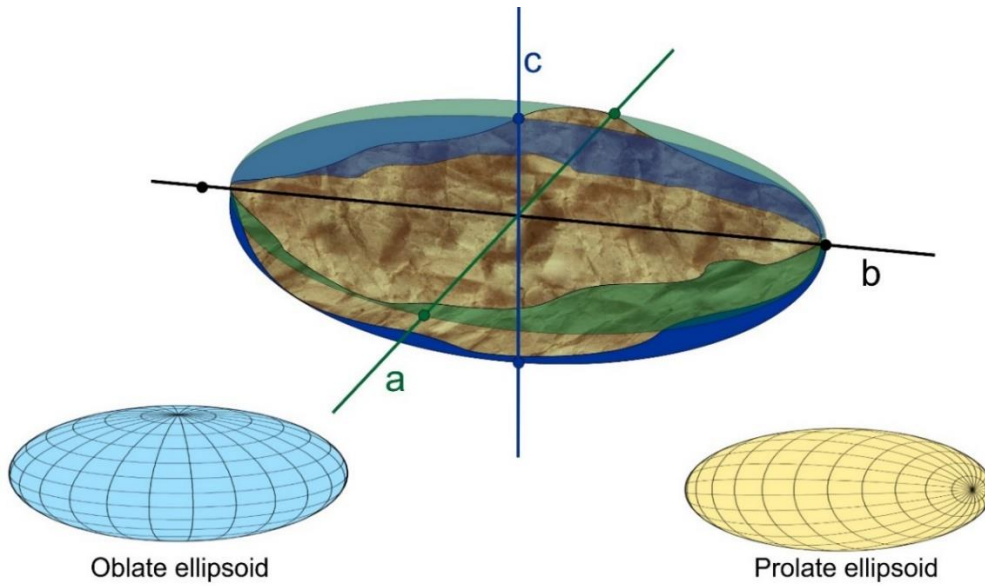


Figure 3 16. Diagram illustration of an irregular pore (textured) with a fitted ellipsoid with major radii a , b and c . The subsidiary diagrams show the form of an oblate ellipsoid and prolate ellipsoid.

The aspect ratios of pores, mineral grains and blobs of kerogen can, in principle, be calculated. However, this research has shown that only the measurement for pores is attainable and makes physical sense. Calculating the aspect ratios of individual minerals (e.g., pyrites and K-feldspar) is possible, but does not conform to the main research goals of this research, while the blobby geometry of kerogen cannot be usefully approximated by an ellipsoidal model.

Pore aspect ratio distributions have been calculated and plotted. In this work two pore aspect ratios are considered. The first is given by

$$\gamma_1 = c/b \quad (3.2)$$

Where b is the maximum dimension of the pore, and c is its width, being defined as the minimum dimension of the pore.

The second aspect ratio is given by

$$\gamma_2 = a/c \quad (3.3)$$

Where a is the radial extent of the pore mutually perpendicular to both b and c .

The pore aspect ratios are measures of the shape of the pore. If the pore is penny-shaped (oblate), $a \approx b \gg c$, with $\gamma_1 \ll 1$ and $\gamma_2 \gg 1$. If the pore is pin-shaped (prolate), $a \approx c \ll b$, with $\gamma_1 \ll 1$ and $\gamma_2 \approx 1$. The value of both pore aspect ratios is important because pores which are long and thin ($\gamma_1 \ll 1$) or have a significant sideways extent ($\gamma_2 \neq 1$) have a greater potential for connecting up with other pores, contributing to raising the chances that the pore structure forms an interconnected network which will support gas flow (Saleh and Castagna, 2004). Most grain boundary pores, parting surfaces in shales and fractures, are better modelled by oblate spheroids with $\gamma_1 \ll 1$.

It should be noted that in the calculation of the pore aspect ratios, the local Cartesian directions are rotated to ensure that they are aligned with the largest and smallest dimensions of the pore. Consequently, the pore aspect ratios are scalar quantities describing the mean geometry of pore structures and contain no information about any alignments or anisotropy of pore structure within the rock.

The results for both pore aspect ratios described above have given later in this study.

3.7.3 Surface-area-to-volume ratio

The concept of surface area to volume ratio is best understood by assuming all the pores in the rock can be described by an ellipsoid of either oblate or prolate types and its important parameter for describing the shape of the pore within shale reservoir (Glover et al., 2009). This ratio is very significant particularly in shale because large surface areas help the gas move more easily from the rock matrix and from kerogen into the pores, which is a pre-requisite to hydraulic fracturing because gas must be able to transfer into the existing small pore spaces before stimulation can improve the connectivity of the small pore spaces for gas to be produced. A high surface area ensures that the diffusion process is more efficient, not only ensuring a good initial charge of gas in the micro-pores of the shale, but also allowing those pores to be recharged quickly once initial production has removed the initially accumulated gas

The ratio of the surface area to volume can be obtained analytically if it is assumed that all pores can be represented approximately by an ellipsoid shape (Glover et al., 2009), as described earlier. In this study, the oblate spheroids have semi-axis sizes according to $a \approx b > c$, i.e., spheres squashed in the c -direction, and approximating to penny-shaped cracks or pores. By comparison, prolate spheroids have semi-axis sizes conforming to $b > c \approx a$, i.e., spheres stretched in the b -direction, and approximating to needles. The volume for two types of spheroid can be determined using

$$V = \frac{4}{3} \pi abc. \quad (3.4)$$

The surface areas of the two types of spheroid differ slightly. They are

$$S_{oblate} = 2\pi a^2 \left(1 + \frac{1-e^2}{e} \tanh^{-1} e\right), \text{ where } e^2 = 1 - \frac{c^2}{a^2}, \text{ if } a < c \quad (3.5)$$

$$S_{prolate} = 2\pi a^2 \left(1 + \frac{c}{ae} \sin^{-1} e\right), \text{ where } e^2 = 1 - \frac{a^2}{c^2}, \text{ if } a > c \quad (3.6)$$

In each case the term in brackets tends to 2 as c tends to a , the surface areas of the two types of spheroid are the same and are given by the surface area of a sphere of radius a :

$$S_{oblate} = S_{prolate} = 4\pi a^2 \quad (3.7)$$

The surface area to volume ratio for each type is then:

$$\xi_{oblate} = \frac{3a}{2bc} \left(1 + \frac{1-e^2}{e} \tanh^{-1} e\right), \text{ if } a < c, \text{ and} \quad (3.8)$$

$$\xi_{prolate} = \frac{3a}{2bc} \left(1 + \frac{c}{ae} \sin^{-1} e\right), \text{ if } a > c \quad (3.9)$$

With the value for a sphere ($a=c$) being $\xi_{sphere} = \frac{3}{a}$.

Figure 3.17 shows the surface areas to volume ratio depends on the pore aspect ratio for both oblate and prolate pore. It is clear that the surface area to pore volume ratio of the oblate pores is increases strongly as the aspect ratio increases with much greater than prolate pores. Later in this study, the gas shale samples shown that most of the pores are oblate

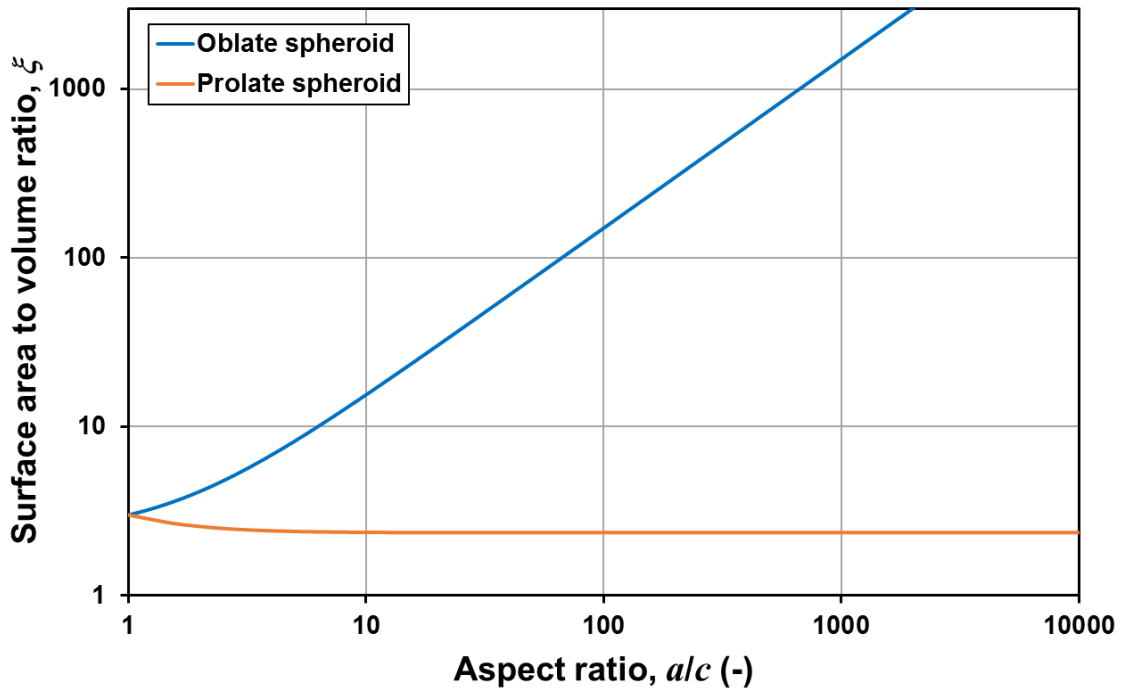


Figure 3.17. The relationship of the surface area to volume ratio with pore aspect ratio for oblate and prolate spheroids, approximating to penny-shaped and needle-shaped pores, respectively.

The surface area per unit volume of an object was measured as surface-area-to-volume ratio (ξ) (Hurlimann et al., 1994). This measurement has a minimum when the object is a sphere, and becomes larger as the sphere becomes more oblate or prolate. Later it is shown that for gas shales most pores are oblate. By having a larger pore surface to volume ratio, these gas shale pores have an increased surface area per volume. The increased surface area improves the possibility that gas in the rock matrix may diffuse into the pores and hence be producible.

However, the absolute value of the surface-area-to-volume ratio has dimensions of per length and hence varies with scale. This simple effect makes it impossible to use if objects are of different scales. The ξ of a sphere with 1 nm radius is 3×10^9 while that of a sphere with 1 μm radius is 3×10^6 , which is also the ξ of an extremely oblate pore with one semi-axis approximately one million times greater than another.

A Scale Invariant Surface-area-to-volume Ratio (SISAVR) has been developed to overcome this problem, and have used it to create valid SISAVR distributions that include data for pores at all scales. The SISAVR have called and give it by symbol σ in this work is

$$\sigma = x_i \xi, \quad (3.10)$$

Which is the conventional surface area to volume ratio multiplied by the intermediate semi-axis of the ellipsoidal pore (x_i). The value of σ varies from 3, which represents a sphere to infinity as the ellipsoidal pore becomes more oblate or prolate. The results sections are presented later in this thesis (Chapter 4, 5 and 6).

3.7.4 Image-based Permeability Simulation

The permeability of the samples has been calculated from the measured characteristics of each sample (connectivity within the kerogen and pore network in the image sets). The data in this work have been tested using (Gilbert Scott, 2020) approaches. The combined data with Scott, G modelling has enabled to describe the gas transport in the shale (Gilbert Scott, 2020).

The approaches have used the Finite-Difference Geometrical Pore Approximation (FDGPA) method, which considers (i) the gas to behave as a fluid within the kerogen and pore systems, (ii) the gas to have a single phase incompressibility (i.e., to have a constant density), (iii) the gas to be a Newtonian fluid (i.e., to have a constant dynamic viscosity), and (iv) for the flow to be small enough to be laminar.

The results for the calculated shale permeability along the x -, y - and z -axis respectively are presented in Chapter 6.

3.7.5 Permeability prediction

Permeability is one of the most important parameters for characterizing shale gas reservoirs because it governs the ease of access to the hydrocarbon within the shale reservoir. However, in shale material this parameter is extremely difficult to obtain directly due to the highly heterogeneous pore microstructure and the extremely small size of the pores within shale.

Permeability has been predicted using five different methods including μ -CT, Nano-CT, FIB-SEM, RGPZ and N_2 Permeability, each of these approaches and the results for the calculated shale permeability are described along the discussion in Chapter 7.

3.8 Summary

In this chapter, the analytical methods and experimental techniques have used as part of the multi-scale imaging and characterization of the microstructure of gas shale in this research were discussed. Results from multiple scale (micro-and nano-scale pore structure) methods (2D SEM analysis and 3D μ -CT and FIBSEM) are reported in Chapter 4. Chapter 5 presents studies by complement work in Chapter 4 using nano-CT with along (N_2) nitrogen adsorption and (MIP) mercury intrusion porosimetry. Chapter 6 discusses results from using nano-CT with Ultra-high Resolution FIB-SEM on the same position of shale rock sample. Chapter 7 described the results of the measurements and calculations of shale gas permeability.

Chapter 4

**Micro- and nano-scale pore structure in gas shale
using μ -CT and FIB-SEM techniques**

4.1 Introduction

The internal pore microstructure of shale rocks has received significant attention from researchers for decades since it can provide valuable information in understanding the quality of the shale reservoirs such as pore volume and pore size, pore aspect ratios, surface areas, porosity and permeability (e.g., Peng et al., 2012). However, these properties remain a major challenging topic due to the extremely complex, heterogeneous and anisotropic microstructure of shales (Lazar et al., 2015), which arises from the extremely small size of the pores and low porosity between 2% and 15 % (Chalmers et al., 2012; Klaver et al., 2015), as well as their very low permeability, typically below 10^{-18} m² (McKernan et al., 2011).

The microstructure properties in the shale are very important as they control gas storage and fluid transport through the shale. Thus, having a better understanding of how the shale microstructures and porosity control the permeability is critical, and would be hugely beneficial. Such knowledge would increase our ability to identify sources of shale gas and produce it more efficiently (Ougier-Simonin et al., 2016). For example, the wettability of the shale is largely controlled by the distribution of pores, in both organic and inorganic materials (Ambrose et al., 2010), so information about the distribution of pores in shales is extremely important.

This chapter provides an improved insight into the microstructural properties of shale such as pore volume and pore size, pore aspect ratios, surface area to volume ratios, porosity, permeability, pore network structure and connectivity, all of which are crucial to understanding hydrocarbon flow behaviour within gas shale reservoirs.

This chapter also describes a methodology for a single shale rock sample of side length around 500 µm by combining two advanced imaging methods. The µ-CT method has been used on a sample for measuring micro-scale pores. Nano-scale pores have been investigated with the FIB-SEM technique has been used to make higher resolution measurements at specific multiple locations on the same sample that was used for the µ-CT measurements, each of which has a smaller field of view. Consequently, in this approach, a link can be made between two different measurement scales, and the internal pore microstructure of Bowland gas shale reservoir can be characterised over the entire scale range.

The dual method, multi-scale approach has a number of advantages:

- (i) the damage which occurs when the main sample is prepared is common to all measurements, simplifying the problem of understanding which aspects of the measurements are native to the specimen and which are caused by preparation for all measurements, irrespective of scale, resolution and field of view;
- (ii) The high resolution FIB-SEM measurements can be made at specific locations chosen with the aid of the 3D µ-CT data to be either representative of the whole sample, or to investigate specific aspects of features occurring in the whole specimen;

(iii) Sufficient FIB-SEM measurements can be made to ensure that their mean behaviour represents that measured by the μ -CT measurements, but at much higher resolution.

The results in this chapter provide a valuable information to understand the relationships between the microscale and macroscale properties of the shale sample with the impact of heterogeneity, pore and kerogen distributions and their connectivity.

4.2 Materials and methods

4.2.1 Rock samples and preparation

The gas shale samples used in this chapter were obtained from the Bowland formation, collected from a depth of 2.7 km in a gas shale resource in Lancashire, UK. Further details on the sample collection with code and locations are provided section 3.2.1

In this study two different high-resolution imaging techniques were used, each of which probes a different scale, in the attempt to cover a wider range of scales than would be possible to cover with a single technique alone, and to examine the extent to which each technique observes microstructural features at different scales with the primary aim of understanding the petrophysical properties of the Bowland shale, including porosity and the microstructural distribution of pore volume.

The two techniques which have been used in this study are 3D X-ray Micro-Computed Tomography scanning (μ -CT), and focused ion beam scanning electron microscopy (FIB-SEM), which uses a focused ion beam to successively strip material from the surface between scans.

Imaging has been possible with both techniques on a single quasi-cubic sample with a characteristic side length of about 500 μm , as implemented in this work. High resolution imaging such as that carried out in this work requires very small samples, whose preparation is time-consuming and requires significant care. The higher the resolution required, the smaller the samples must be. The preparation of such a sample were discussed in Chapter 3 (Section 3.2.2).

4.3 Imaging techniques

4.3.1 X-ray μ -CT

A Zeiss Versa XRM-410 X-ray Microscope was used to image the internal structure of gas shale samples. The samples were mounted on a rotary stage, exposed by a microfocus X-ray source and imaged in transmission onto a detector. The X-rays transmitted through the sample hit the scintillator crystals to give off visible light, which is then focused by the optical objective lens and converted into a digital image by the visible light charge-coupled device (CCD). A series of images (projections) are taken at incrementally spaced angles around 360° as the sample is rotated. The μ -CT instrument settings at 0.94 μm voxel sizes. Again, more details on the settings and principles of X-ray micro-tomography are provided section 3.3.4.1. Figure 4.1 shows a μ -CT image of a part of a sample, superimposed on which are three selected locations (A, B and C) from which correlative FIB-SEM images and data were subsequently taken. In this figure, the three panels are the BSE-SEM images of the

surface at these locations. [Figure 4.2](#) shows the corresponding SEM image for the whole volume of the sample measured by μ -CT, again with three different locations A, B and C marked.

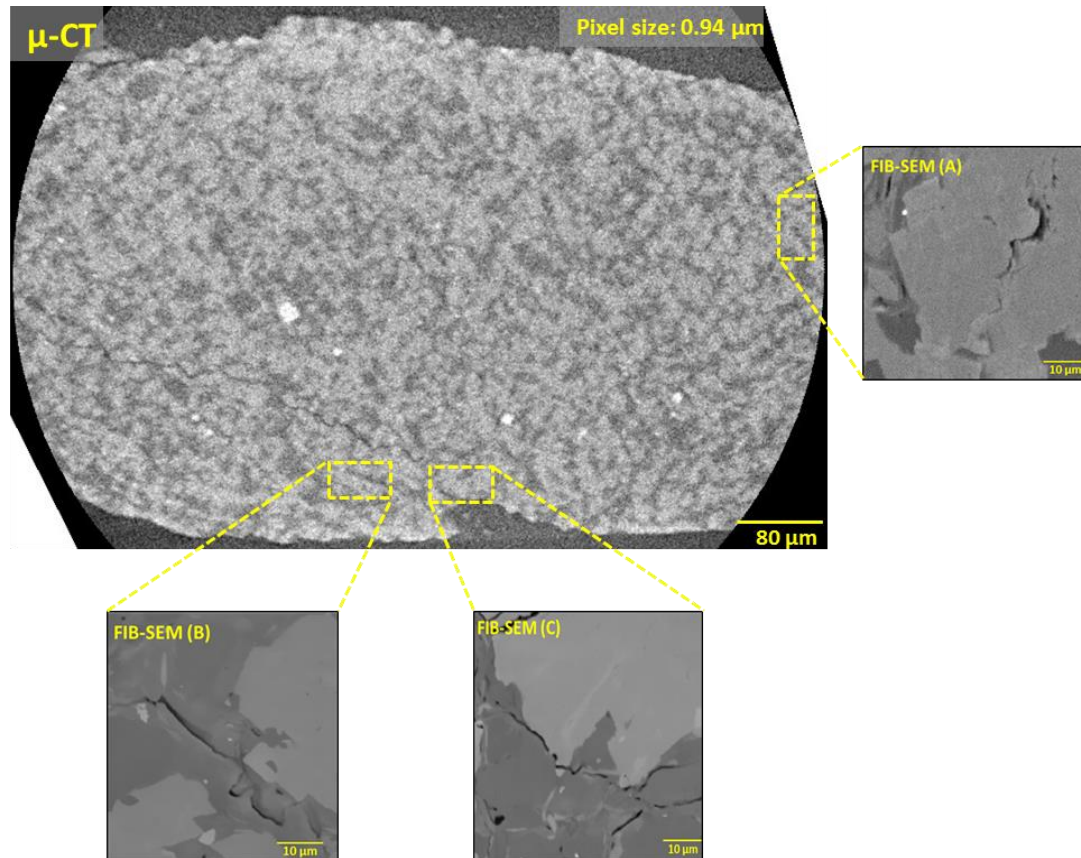


Figure 4 1. μ -CT image of sample MD-2.7 km of Bowland shale showing BSE images of a cross-section at each of the three locations A, B and C which were chosen for subsequent FIB-SEM serial sectioning.

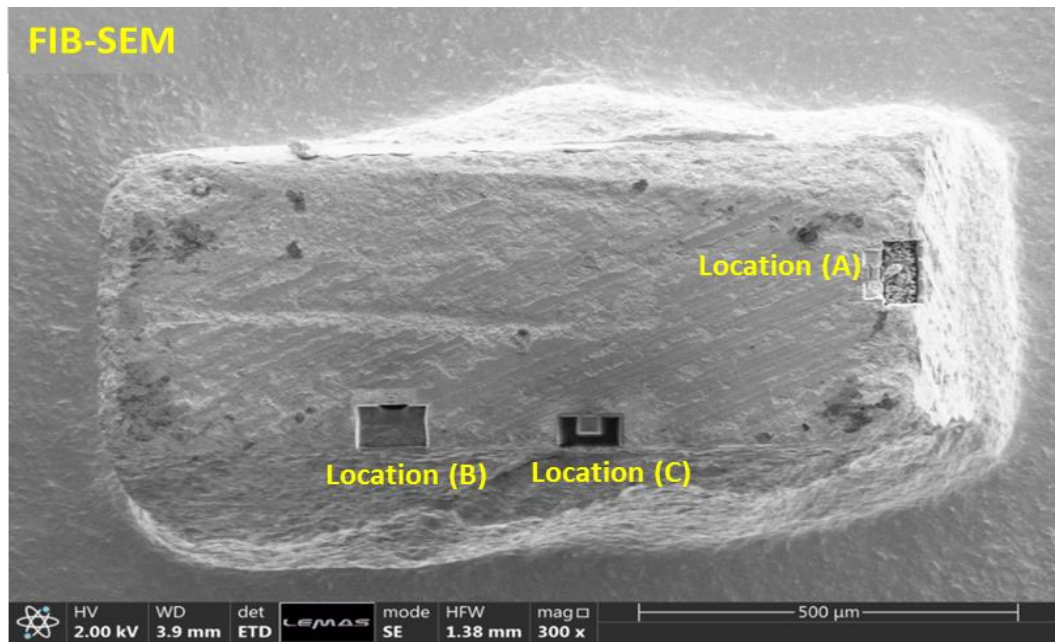


Figure 4 2. SEM image of the sample of Bowland shale used for μ -CT imaging showing the different locations A, B and C that were used for FIB-SEM serial sectioning.

4.3.2 Dual beam FIB-SEM

The dual-ion beam (FIB-SEM) system has also been applied in this study (FEI Helios G4 CX Dual Beam), which allows for the sample to be cross-sectioned and imaged *in-situ* using 30 keV electrons from an integrated SEM with a pixel resolution of $18 \times 24 \times 20 \text{ nm}^3$. The FIB milling removes the material from the surface of the sample (see [Figure 4.3](#)), giving the SEM access to a new surface to image. Reiteration of imaging and milling, a process known as “slice and view”, allows a 3D volume of the rock sample to be imaged. The voxel size for this work is approximately $19 \times 24 \times 20 \text{ nm}^3$, with a typical imaged volume of $20 \times 20 \times 1 \text{ }\mu\text{m}^3$.

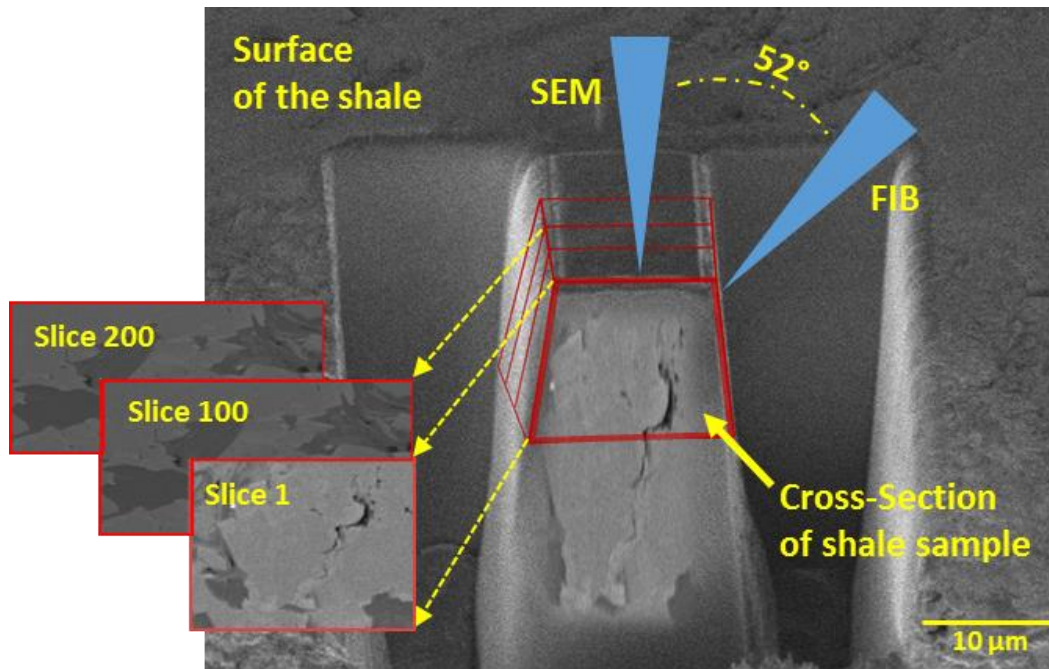


Figure 4.3. Serial cross-sectioning of a shale sample using a dual-beam FIB-SEM system. The ion beam is used to remove material from the shale surface creating a cross-sectional face that can be imaged by the electron beam.

Three separate locations (A, B and C) within the μ -CT sample were chosen for FIB-SEM analysis, as shown in Figures 4.1 and 4.2. Figure 4.4 shows BSE images of three separate regions A, B and C within samples taken from the same shale site prepared in cross-section. These images show significant differences in their microstructure and the size of their pores. Since the backscattered electron yield is sensitive to the average atomic number, it provides means of differentiating the constituents of the microstructure dependent on whether they are composed of light or heavy elements. In Figure 4.4A, cracks (black) appear to be connected, while smaller dark areas (yellow circles) are isolated pores, which appear unconnected at the scale of the imaging, but may be connected at a finer scale.

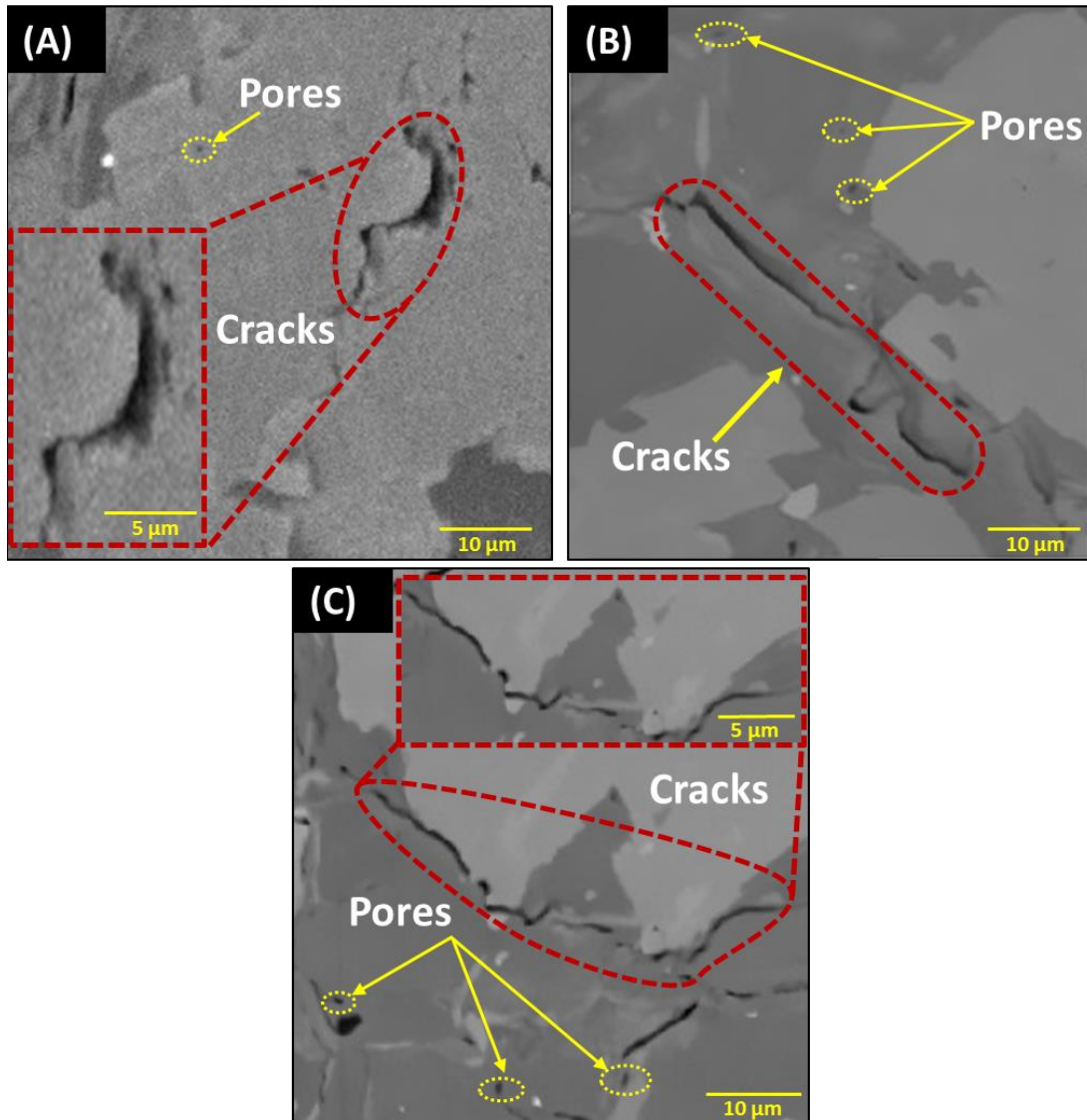


Figure 4.4. BSE images of FIB cross-sections taken from different locations A, B and C (see Figures 4.1 and 4.2), pores and cracks are highlighted by yellow and red circles.

4.4. Results

The microstructural properties obtained using μ -CT and FIB-SEM techniques can be described by a range of parameters, including porosity, permeability, pore volume, and pore size, pore aspect ratios, the surface area to volume ratio of pore and their distribution with scale; these results are presented in the following subsections.

4.4.1 3D reconstructions of gas shale volumes

The quantitative data presented in this section were calculated from 3D reconstructions of both μ -CT and FIB-SEM image data using 3D image analysis software. An example of a

reconstruction from μ -CT images is shown in [Figure 4.5](#). The data set comprised of 1000 2D images, each comprising of square pixels with a side length of $0.94 \mu\text{m}$.

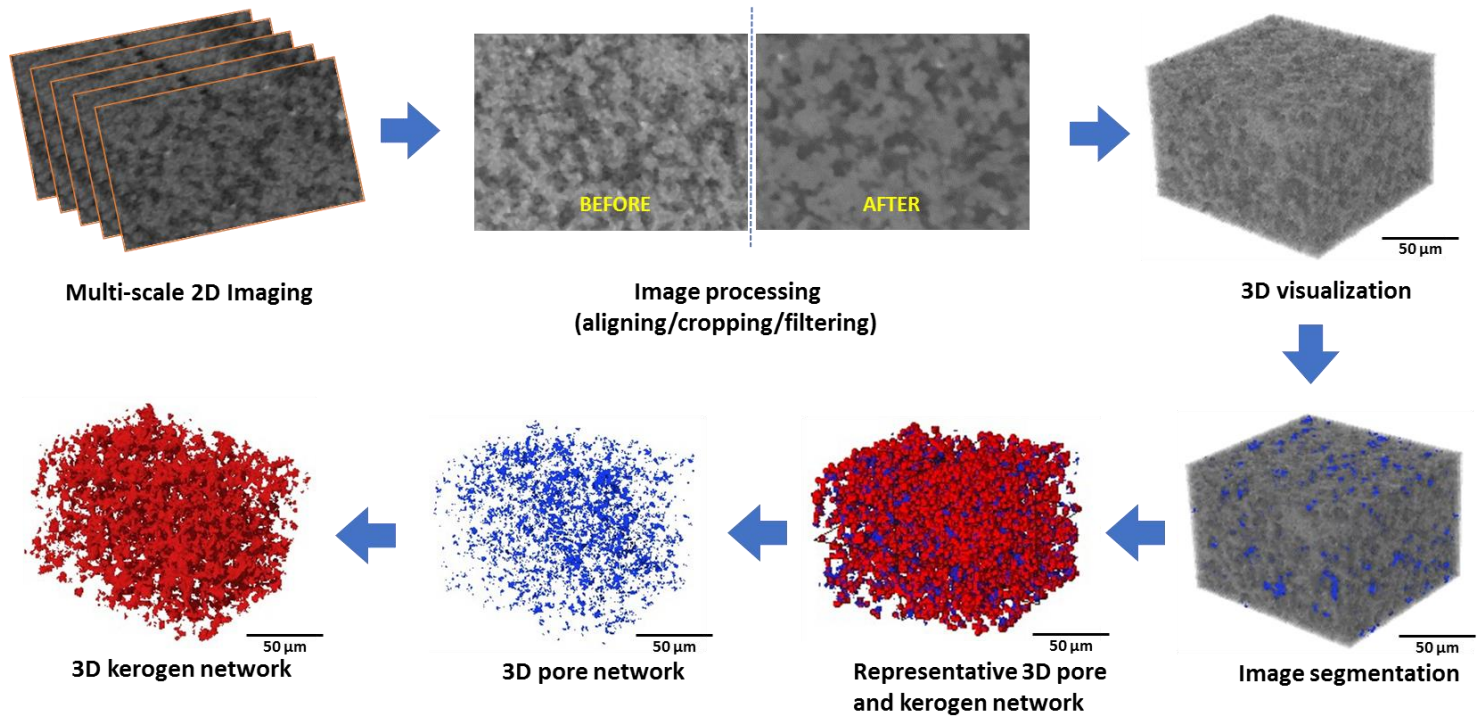


Figure 4.5. Schematic diagram of the procedure for analysing 3D datasets from μ -CT imaging techniques.

[Figure 4.6a](#) shows a raw 2D greyscale image of the sample. Using the greyscale of this raw data, threshold values can be set to define microstructural features of interest, particularly the kerogen and pores. Surfaces can then be generated around these regions within the thresholds. [Figure 4.6b](#) shows the ‘non-local means’ filtered 2D greyscale image, this filter helps to remove the noise from the SEM and μ -CT images without damaging the images and keeping the same resolution of the pores. The filter has been applied with parameters of a local neighbourhood of 5 pixels and a similarity value of 0.5. The workflow and imaging processing in this study as shown in earlier [Figure \(4.5\)](#) such as aligned, cropped, filtered and segmentation have followed a number of researchers ([Korfiatis et al., 2007](#); [Li et al., 2016](#); [Stauber et al., 2008](#); [Buades et al., 2005](#); [Boruah et al., 2015](#); [Saif et al., 2015](#); [Gundermann et al., 2014](#); [Iassonov et al., 2009](#)). [Figure 4.6c-d](#) displays the 3D images of the kerogen and pores, respectively. A qualitative inspection of the connectivity of the pores and kerogen can then be performed, which is based on the thresholding/segmentation procedure described in Chapter 3. For the estimated kerogen network observed in this sample, [Figure 4.6c](#) shows the kerogen in red and appears to be connected across the volume. The pore connectivity apparent from [Figure 4.6d](#) is less than that of the kerogen, with some interconnected pore

spaces and some isolated pore spaces within the volume. These results suggest that the sample has a very small pore volume of only 6%, which may indicate that the pore system in the Bowland Shale has extremely low connectivity; this has also been reported by [Ma et al. \(2016\)](#). Thus the isolated pore space is unlikely to be important for gas transport at the different scales. However, the high fraction observed for the kerogen (44.5%) becomes particularly important and provides potential pathways for gas transport throughout the samples ([Heller et al., 2014](#); [Javadpour et al., 2009](#)), but over a longer timescale. As a result of unconnected pores, the connectivity of kerogen suggests similar levels of connectivity to the published results of the Bowland shale reservoirs from [Ma et al. \(2016\)](#).

[Figure 4.7a](#) shows a 2D greyscale image of FIB-SEM shale of Location A, while [Figure 4.7b](#) shows the non-local means filtered 2-D greyscale image. [Figure 4.7c](#) is a 3D representation of the kerogen present in the sample. This image shows the connectivity of the kerogen network across the $19 \times 24 \times 20 \text{ nm}^3$ sample volume. [Figure 4.7d](#) shows the pore spaces ranging in length from several nanometers to a few micrometers, that they vary in shape from spherical to elongated, and that they are connected, at least from a qualitative point of view. The volume contributions of kerogen and pores for the reconstructed raw gas shale volume from the FIB-SEM measurement were 34.8% and 10.0% respectively.

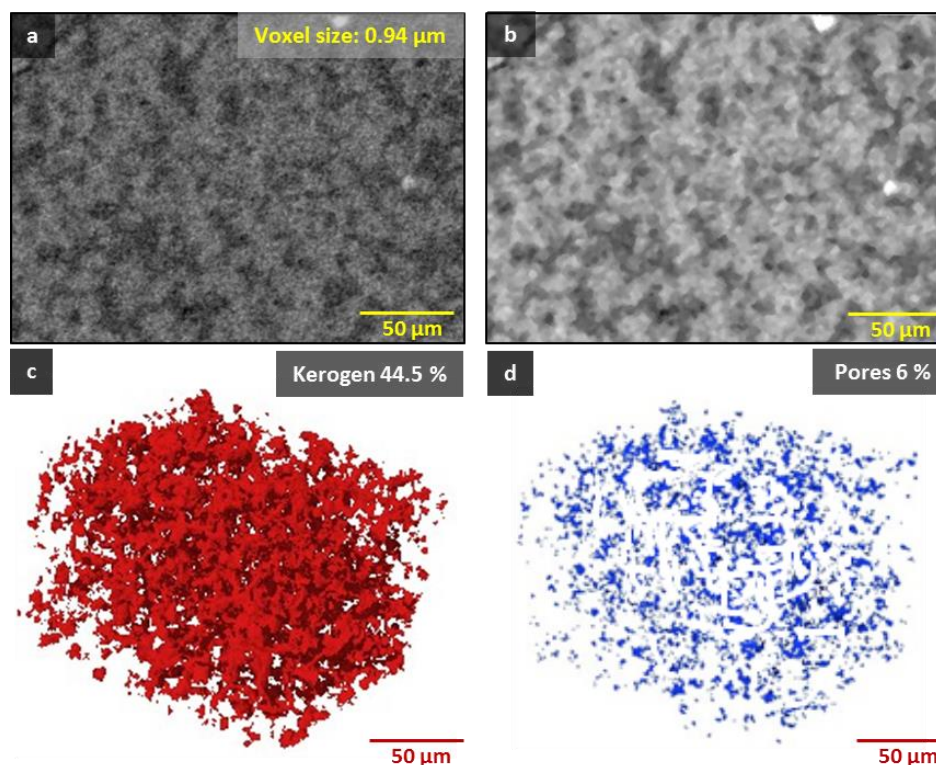


Figure 4.6. X-ray micro-tomography (μ -CT) for a shale rock sample acquired at a voxel size of 0.94 μm . (a) Raw 2D greyscale image, (b) Non-local means filtered 2D greyscale image. (c) the kerogen shown in red, and (d) pores shown in blue.

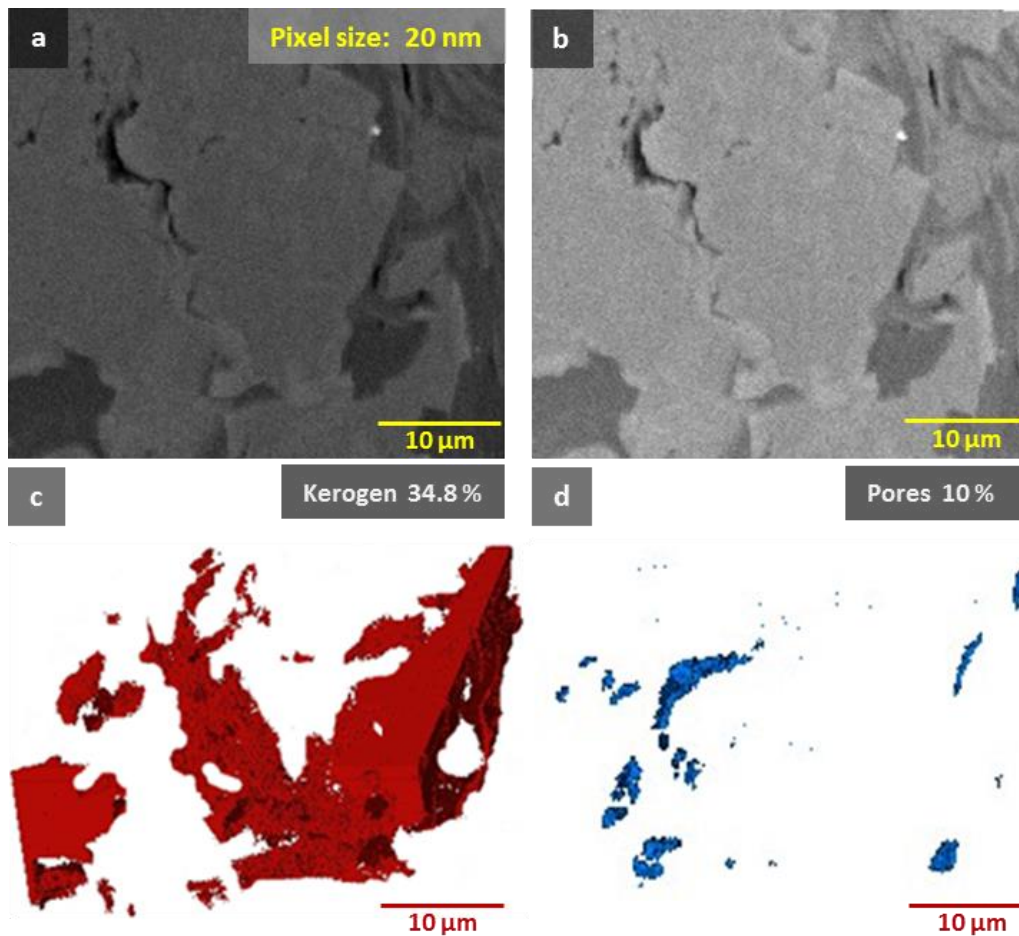


Figure 4.7. FIB-SEM assessment of the raw MD-2.7 km shale rock sample. (a) Raw 2D greyscale image, (b) non-local means filtered 2D greyscale image, (c) 3D representation of kerogen shown in red, and (d) 3D representation of pores shown in blue.

4.4.2 Pore volume distribution

The 3D reconstructed volumes were used to estimate the relative frequency distribution of the volume of individual pores by both pore number and pore volume. [Figure 4.8](#) shows histograms of pore-volume distribution as measured by FIB-SEM for the three different locations A, B, and C indicated in [Figure 4.2](#), together with the pore-volume distribution as measured by μ -CT on the wider sample ([Figure 4.1](#)). The FIB-SEM and μ -CT data interrogate completely separate scales, with no overlap. Hence, the FIB-SEM data is shown in parts (a) and (c) of [Figure 4.8](#), while the μ -CT data is shown in parts (b) and (d). The distribution of pore volume can be displayed in terms of the percentage number of pores with a given pore volume, which is shown in parts (a) and (b) of the figure, or in terms of the percentage volume of pores represented by a given pore volume, which is shown in parts (c) and (d) of the figure.

The differences in the curves is solely due to their difference in the scales of operation. In each case measurements increase as pore volume decreases until the resolution of the method is reached, with the minimum volume corresponding to the volume of the cuboidal voxel represented by that limiting resolution. Consequently, the relatively low resolution of the μ -CT technique ($0.94\ \mu\text{m}$) cannot discriminate individual pores where the size of any of their dimensions is less than $0.94\ \mu\text{m}$, if they are present. By contrast, the FIB-SEM scan can recognise pores with a minimum extent of $0.02\ \mu\text{m}$ for FIB-SEM-A and $0.05\ \mu\text{m}$ for the other two FIB-SEM samples. If the pores were equant, the minimum pore volumes would be about $1\ \mu\text{m}^3$ and $0.00001\ \mu\text{m}^3$ for the μ -CT and FIB-SEM data, respectively. The fact that the data finishes at higher values than these ultimate limits is an indication that some very fine pores are unmeasurable because one of their dimensions is lower than the resolution even when other dimensions are above it.

In principle the FIB-SEM method can recognise pores as large as $20\times 20\times 1\ \mu\text{m}^3$, but the power law distribution shows that the chances of the volume being measured by the FIB-SEM method containing one of these larger pores is very small, and if it did so the volume would be unrepresentative of the wider sample. Hence [Figure 4.8a](#) shows negligible pore volumes larger than $0.02\ \mu\text{m}^3$ even though the μ -CT measurements ([Figure 4.8b](#)) confirm they exist.

The apparent lack of data between $0.01\ \mu\text{m}^3$ and $0.9\ \mu\text{m}^3$ shown in [Figure 4.8](#) does not indicate that no pores exist with these volumes, but that such pores are not recognised by either of the two techniques that have been used. A third technique would be needed to fully investigate the sample. Nano-scale CT (Xn-CT) measurements (with a voxel size of *cca.* $0.05\times 0.05\times 0.05\ \mu\text{m}^3$) allow a fuller understanding of the pore microstructure and such measurements are presented in Chapter 5.

Parts (c) and (d) of [Figure 4.8](#) show the same data but plotting the fraction of the total pore volume represented by pores of a given volume. Comparing this data with the data for pore number shows clearly that while pores with small volumes dominate in number, they do not dominate in volume. Indeed, for both FIB-SEM and μ -CT data, the larger less numerous pores contribute equally significantly to the overall pore volume.

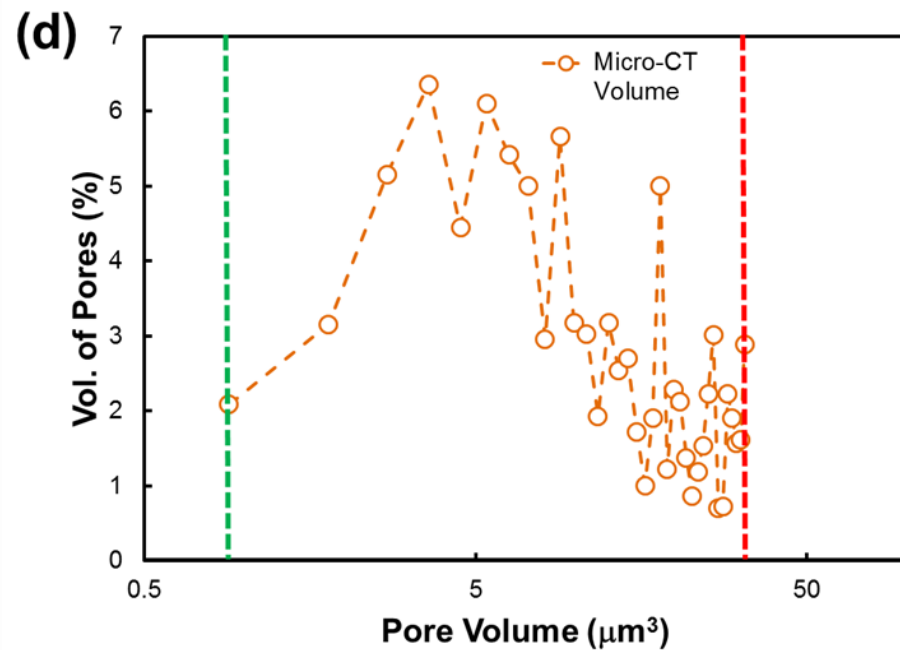
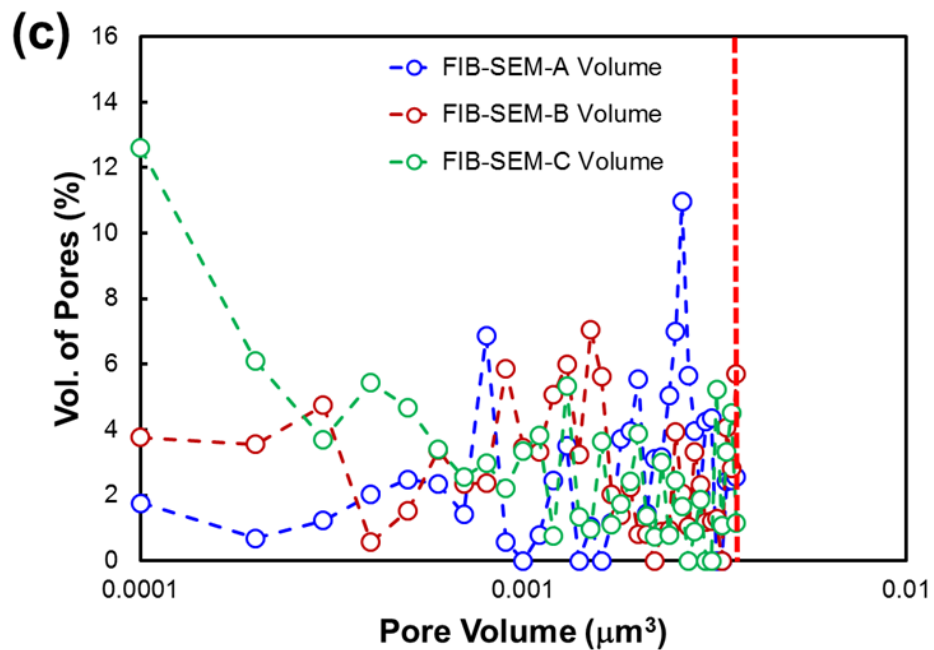
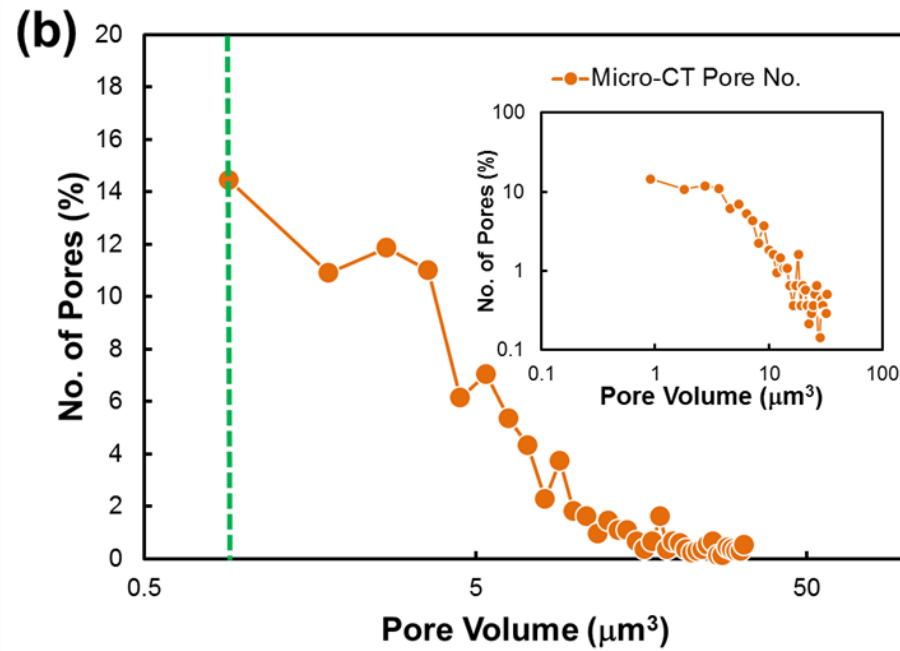
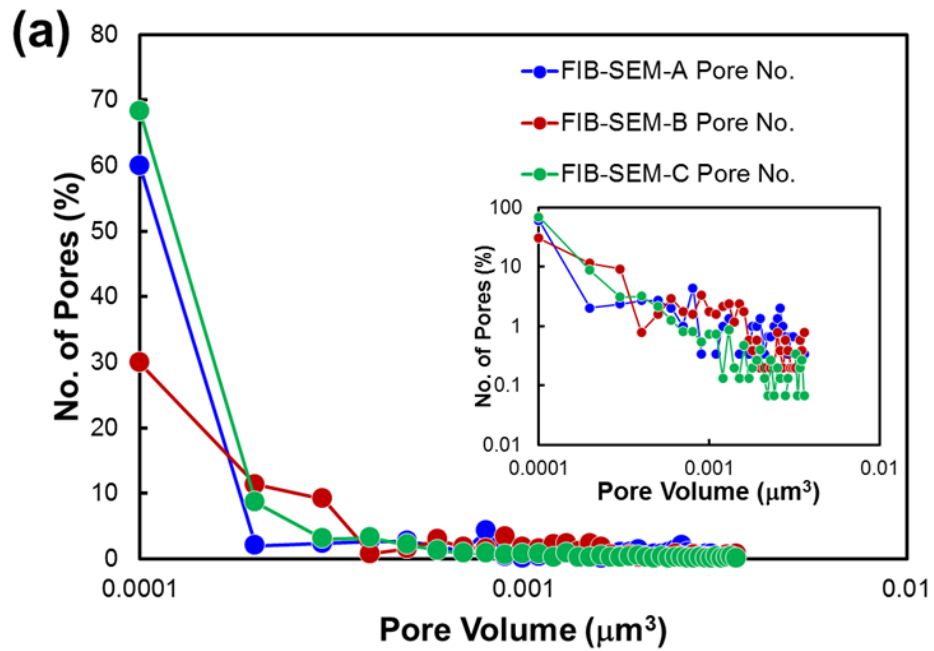


Figure 4.8. The distribution of pore volume on the basis of numbers of pores representing a given pore volume, for (a) FIB-SEM, and (b) μ -CT for sample MD-2.7 km of a gas shale rock from the Bowland formation. Insets show the same data on a log-log scale. The distribution of pore volume on the basis of the volume of pores representing a given pore volume, for (c) FIB-SEM, and (d) μ -CT. Dashed lines show native resolution limits for each technique.

Each of the two techniques provides data over a specific range of scales and represents that data as a relative frequency. That is to say, each set of measurements assumes in the calculation of the relative frequency that there is no pore volume existing at scales lower than its resolution or higher than its field of view. This is clearly not true. The result is that the data in Figure 4.8 for the three locations measured by FIB-SEM can be compared directly, the data for the two techniques (any of the FIB-SEM curves and the μ -CT curve) cannot be compared as both are subject to an unknown scaling. This problem could be obviated by an overlap in measurement ranges, but there is insufficient overlap to do so in this case. The implementation of a third technique whose imaged data spanned both of the techniques would supply a solution, and help scale each of the curves such that they represented the same relative frequency. Such a technique exists in nano-CT imaging, it is recommended that this approach is also used, and this is reported in the next chapters.

4.4.3 Pore aspect ratio distributions

The three-dimensional shape of any pore can be approximated by the use of pore aspect ratios. The most common approach is to assume that any pore can be represented by an ellipsoid, as defined earlier in chapter 3 and that shown in Figure 3.16. Pore aspect ratios are the ratios of the radii in any two of the x , y , and z directions, which are labelled a , b and c in the figure. While a total of six pore aspect ratios can be defined, three are simply inverse of the other three, and of the basic three, only two are required to fully define the shape of the ellipsoid. Consequently, two pore aspect ratios have been chosen for use in this study.

The first is given by $\gamma_1 = c/b$ (Figure 4.9a and b), where b is the maximum dimension of the pore, and c is its width, being defined as the minimum dimension of the pore. The second aspect ratio is given by $\gamma_2 = a/c$ (Figure 4.9c and d), where a is the radial extent of the pore mutually perpendicular to both b and c . Further details on the definitions of the pore aspect ratios are provided section 3.6.2.

Figure 4.9 shows a plot of the distribution of the number and volume of pores as a function of the pore aspect ratio, as estimated by both FIB-SEM and μ -CT techniques. Parts (a) and (b) show the γ_1 aspect ratio distribution in terms of number and volume, respectively. In both of these graphs a value approaching unity indicates a more equant pore. The pore number distribution (Figure 4.9a) shows that there are negligible equant pores, but significant numbers of pores occur in the range $0.8 > \gamma_1 > 0.1$, which is equivalent to saying

that the pores in the shale have a long axis between 1.25 and 10 times longer than their smallest axis (width or aperture). It is interesting to note that the range of pore shapes indicated by all four measurements are similar for the FIB-SEM-A and μ -CT data despite these two techniques measuring different populations of pores at very different scales. There seems to be a propensity of pores with a value of about $\gamma_1=0.2$ (length equal to five times the aperture) in the FIB-SEM-A and μ -CT data, and a preference for about $\gamma_1=0.47$ for the other two FIB-SEM measurements.

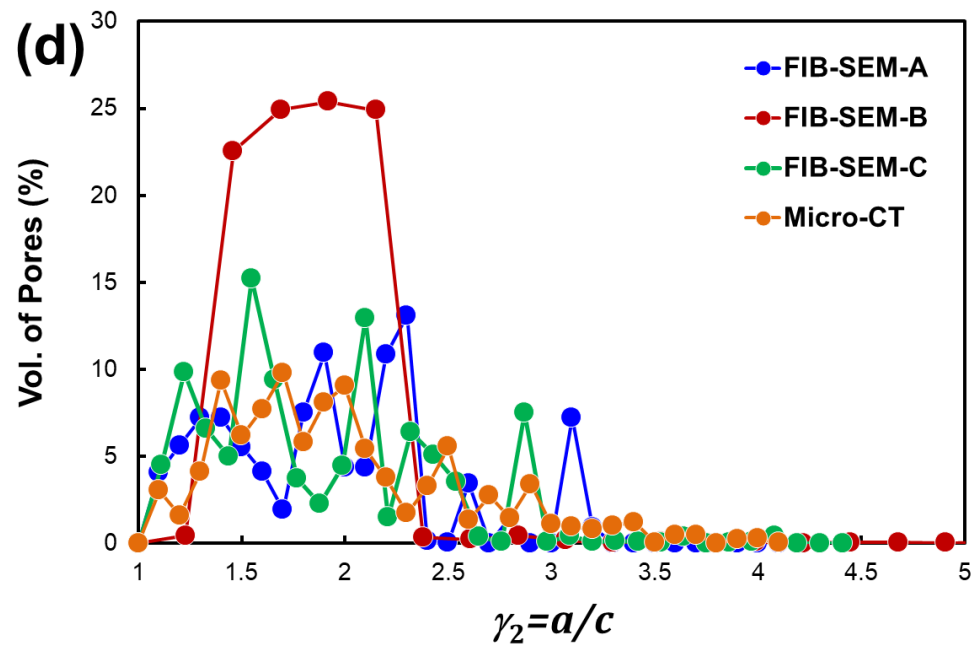
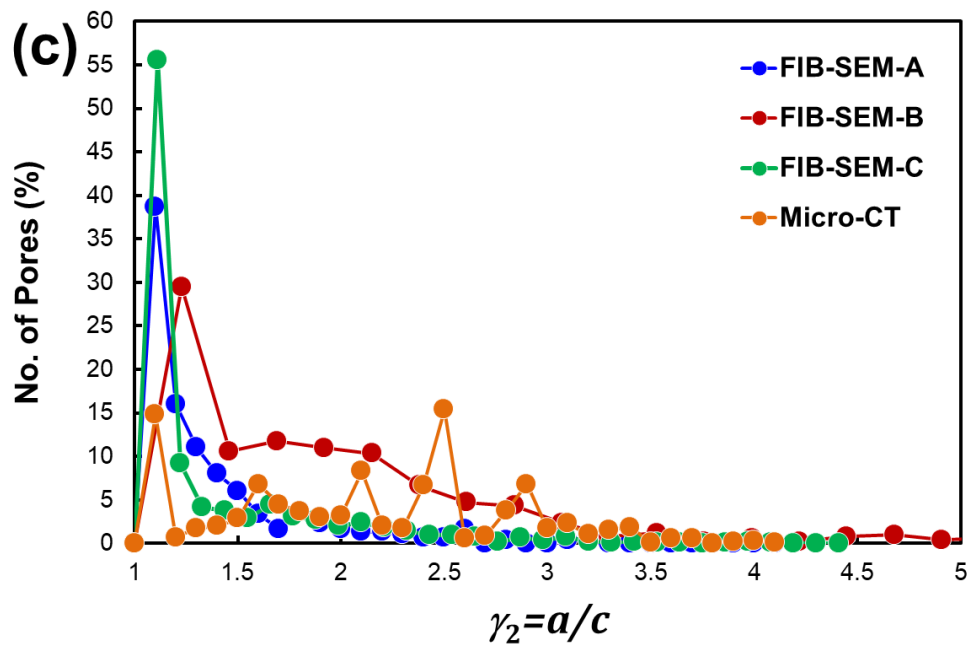
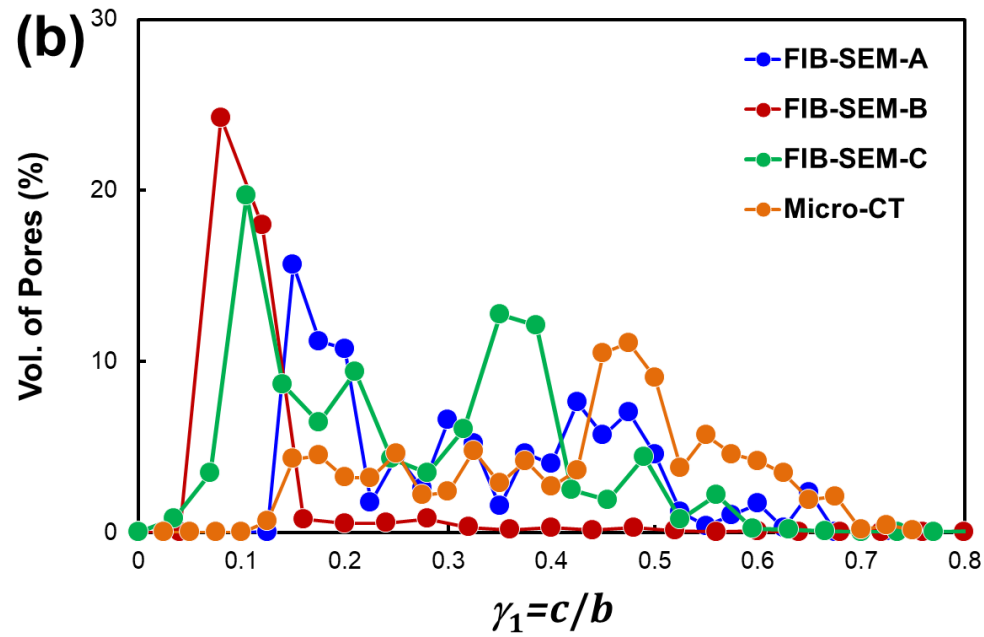
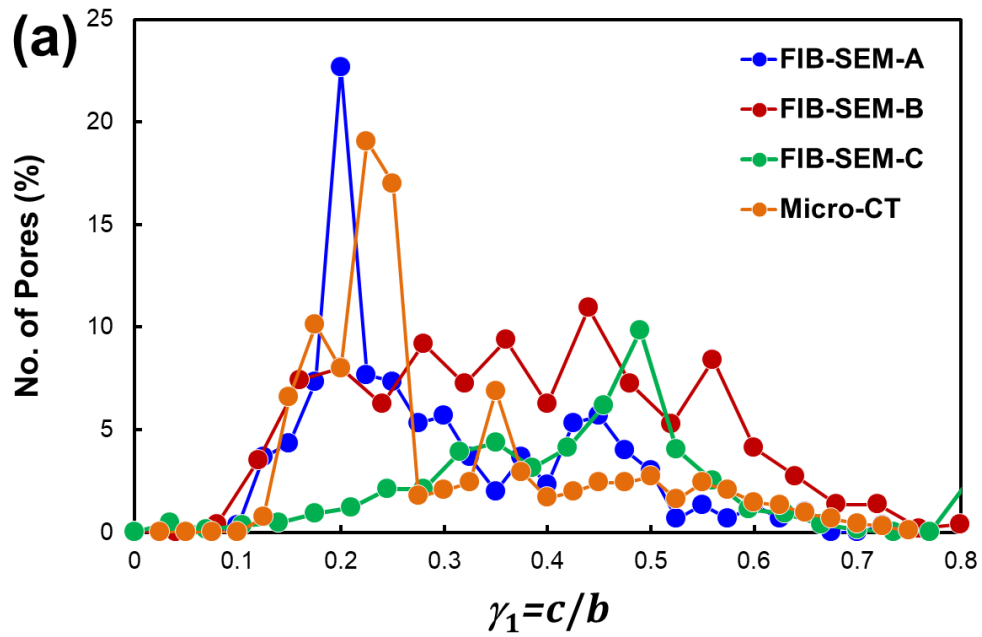


Figure 4.9. The pore-aspect ratio distribution, (a) pore-aspect ratio distributed as a function of the number of pores obtained from γ_1 (oblate) values, (b) pore-aspect ratio distributed estimated from γ_1 values as a function of the total volume of pores, (c) pore-aspect ratio distributed as a function of the number of pores as calculated from γ_2 (prolate) values, (d) pore-aspect ratio distributed estimated from γ_2 as a function of the total volume of pores, as estimated by FIB-SEM and μ -CT using the sample MD-2.7 km of gas shale from the Bowland formation.

The number distribution, however, does not necessarily represent the relative importance of pores at each scale in a balanced way. It cannot, for example, be used to infer which pores provide better gas storage capacity because it treats pores of all sizes equally when those which are larger clearly will contribute more to gas storage. Thus, it has also plotted the volume of pores against their pore aspect ratios. [Figure 4.9b](#) shows a plot of the percentage of the overall pore volume represented by pores with different γ_1 values. When viewed this way, significant volumes of pores occur in the range $0.7 > \gamma_1 > 0.05$, which is equivalent to saying that the pores in the shale have a long axis between about 1.5 and 20 times longer than their smallest axis (width or aperture). All of the FIB-SEM data is in agreement that the majority of the pore volume is in the form of pores with $\gamma_1 > 0.25$ (4 times longer than wide), while the larger scale μ -CT data has a maximum at about $\gamma_1 = 0.475 \pm 0.035$, while FIB-SEM-C has a subsidiary peak at about $\gamma_1 = 0.37 \pm 0.04$.

Consequently, the data presented in this study indicates strongly that the pores in this shale are at least twice as long as wide and up to 20 times in many cases, with the longer, thinner pores occurring at the smaller scales, measured by FIB-SEM, and the more equant pores occurring at the larger scales and measured by μ -CT.

Parts (c) and (d) of [Figure 4.9](#) show the distribution of γ_2 values with respect to percentage pore number and percentage pore volume, respectively. In these plots a value of γ_2 approaching unity indicates that the breadth of the pore approaches that of its width. Since it is known the length is larger than these two measures, a value of unity indicates a prolate pore. The pore number distribution shown in [Figure 4.9c](#) suggests that the greatest number of pores in the samples, whether measured by FIB-SEM at all of the locations or by μ -CT is close to unity, and that consequently the pores in the shale are overwhelmingly prolate, at least from the point of view of pore number.

[Figure 4.9d](#) shows the same data in terms of percentage pore volume. This figure shows that most of the pore volume is present in pores which have $1.5 < \gamma_2 < 3$, indicating that pores which represent significant volume are slightly flattened (penny shaped) but never more than three times as broad as they are wide, while those truly prolate pores that represent the peaks in [Figure 4.9c](#) account for less than 5% of the pore volume overall.

Once again, it is worth noting the similarity in the γ_2 behaviour between the FIB-SEM data and the μ -CT data even though the data is for four different populations of pores at two very different scales.

Different shales will exhibit different aspect ratios, implying differences in pore connectivity and consequently in their gas permeabilities. Shales which have lower values of γ_1 and higher values of γ_2 should offer the greatest permeability. Therefore, the results suggest that there is no clear difference in the pore aspect ratio distributions measured by FIB-SEM and by μ -CT, the large number of pores with $\gamma_1 \ll 1$ and $\gamma_2 \gg 1$ existing at nanoscale and imaged using FIB-SEM may represent a pervasive nanoscale pore network that cannot be recognised by μ -CT imaging.

Shales are highly heterogeneous materials in which the macroscopic nature is controlled by fractures or cracking. Therefore, fractures in shales are of wide interest and critical important factors, especially in environmental applications.

Fractures or cracks are one of the main causes of reservoir compartmentalization, and understanding their impact on fluid flow is very important for predicting reservoir performance and planning development strategies. They are also connected to microstructural properties which are related to the orientation of the pores (Fisher et al., 2018; Fauchille et al., 2014). In this study the morphology of subsurface cracks can be seen clearly in Figure 4.4, and show significant differences in their microstructure such as shapes and sizes and also appear to be connected. Therefore these are likely to contribute to controlling the permeability in combination with other rock properties such as porosity and grain sizes.

4.4.4 Pore surface area to volume ratio

The pore surface area to volume ratio (ξ) is another potential useful indicator of pore shape. A spherical pore represents the most efficient use of surface area to contain a given volume, while higher values of surface area to volume ratio indicate the presence of a larger surface area per unit volume of pore space, which occurs as the pore shape changes from that of a perfect sphere, particularly if the pore becomes oblate.

The shape of the pores can be significant in shale gas reservoirs in a number of ways. For example, pores that are more spherical are much less likely to collapse under externally applied pressure than crack-like or linear pores, which tend to close easily when subjected to only a small normal stress (Curtis et al., 2011). Consequently, sub-horizontal crack-like pores observed in samples at surface pressures are very unlikely to remain open at reservoir depths. However, long, thin pores are more likely to interact with other pores and cracks, making them much more effective at increasing pore connectivity and leading to higher permeability (Glover et al., 2009). Perhaps most importantly, large surface areas

facilitate the diffusion of gas initially trapped in the matrix of the rock and in the kerogen into the pore spaces within the shale (Glover et al., 2009). This is an essential stage before hydraulic fracturing can open up access to these small pore spaces. A high surface area thus ensures that the diffusion procedure is more efficient, not only ensuring a good initial charge of gas in the micro-pores of the shale, but also allowing those pores to be recharged quickly once initial production has removed the initially accumulated gas.

High values of surface area to volume ratio might indicate a flatter pore shape. Unluckily, the surface area to volume ratio has dimensions of per-length which means that smaller pores also generate high surface area to volume ratios than larger pores of the same shape. In order to be able to construct surface area to pore volume distributions as a function of scale (e.g. of pore size), it is necessary to have a measurement of pore surface area to volume ratio that is independent of scale. Consequently, a new parameter has to be defined which incorporates the effect of surface area to volume, but normalises it in such a way that the parameter is unitless, and hence will be invariant to pore size.

The concept of surface area to volume ratio is best understood by assuming all the pores in the rock can be described by an ellipsoid of either oblate or prolate types, as described earlier in chapter (Figure 3.16).

In this study, the long axis of an ellipsoid is defined as b , the smallest axis as c , and the intermediate axis as a . Oblate spheroids have semi-axis sizes according to $b \approx a > c$, i.e., spheres squashed in the c -direction, and approximate to penny-shaped cracks or pores. By contrast, prolate spheroids have semi-axis sizes conforming to $b > a \approx c$, i.e., spheres stretched in the a -direction, and approximate to needles. The volume of both types of spheroid can be calculated using the formula:

$$V = \frac{4}{3} \pi abc. \quad (4.1)$$

The surface areas of the two types of spheroid differ and can be expressed fully by using elliptic integrals which are outside the scope of this study (Abramowitz et al., 1988)

However, the value of the surface area to volume ratio for a sphere is $\xi_{sphere} = \frac{3}{a}$, and that value becomes larger if the sphere decreases in size. The surface area to volume ratio also becomes larger as the ellipsoid becomes more oblate.

In order to remove the functional dependence of surface area to volume ratio on the size of the pores, the conventional surface area to volume ratio ξ have multiplied by the intermediate semi-axis of the ellipsoid a to give a new measure σ , which is independent of scale, being unitless. The definition of the new scale invariant surface area to volume ratio is:

$$\sigma = a\xi. \quad (4.2)$$

The value of σ varies from 3, which represents a sphere, to infinity as the ellipsoidal pore becomes more oblate or prolate. Values $\xi < 3$ are undefined.

Figure 4.10 shows the distributions of the percentage number and percentage volume of pores as a function of the scale-invariant surface area to volume ratio, σ , as measured by both μ -CT and FIB-SEM techniques. Considering the pore number distribution (Figure 4.10a), the values obtained from all three FIB-SEM measurements and the μ -CT measurement are in agreement. No values are less than 3, but there are peaks in all of the distributions close to 3. This agrees well with the pore volume (Section 4.4.2) and aspect ratio data (Section 4.4.3), and is expected to describe the preponderance of very small pores that are accounted for by a single voxel in each of the measuring techniques.

It should be noted that the value of σ for a cubic voxel is 6, but decreases as it becomes a cuboid shortened in one direction. This is consistent with the values of the peaks in Figure 4.10a. However, this figure also shows measurable numbers of pores with values of σ extending to about $\sigma=18$, indicating the presence of pores which have a significantly enhanced surface area for their volume.

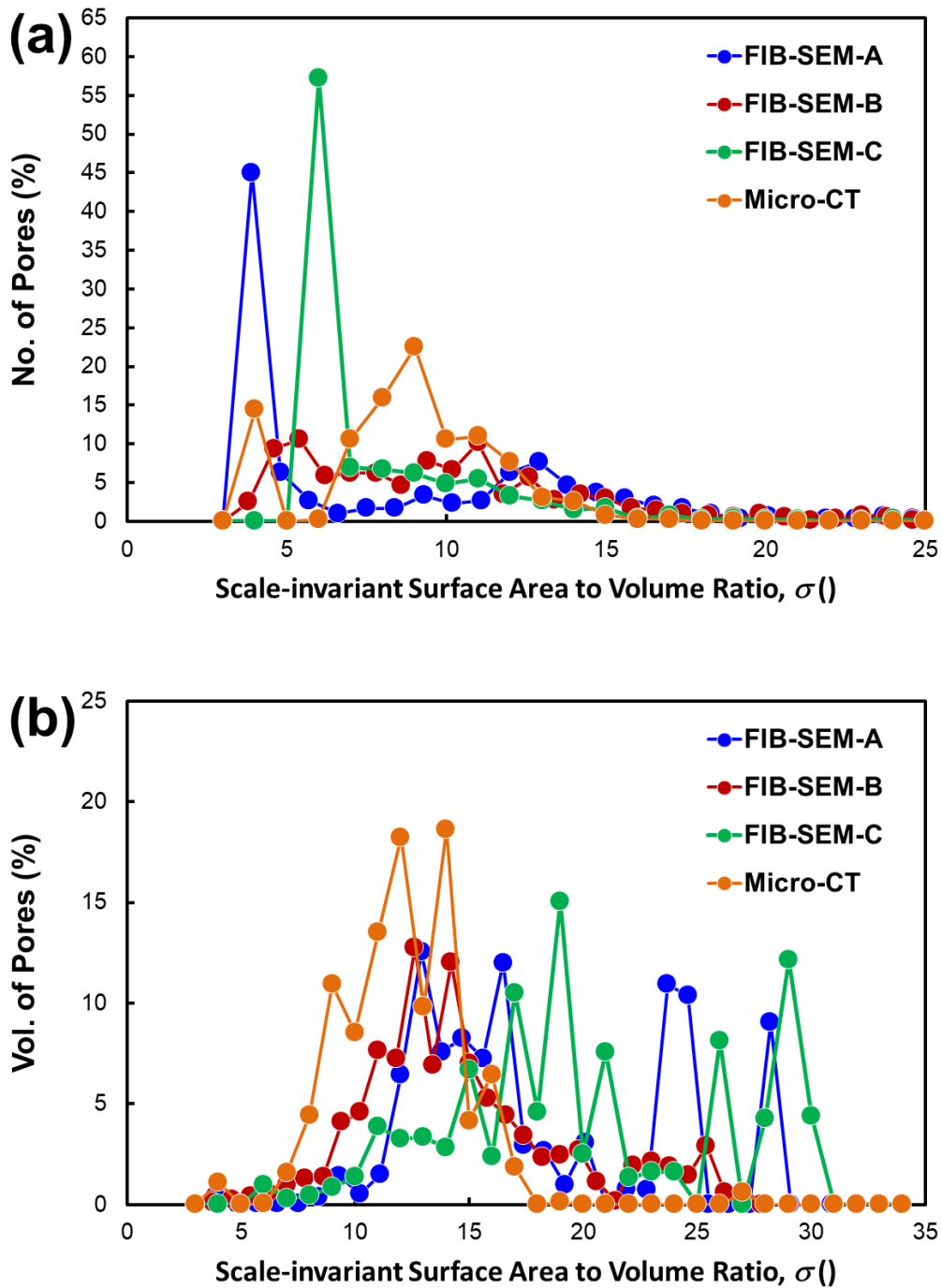


Figure 4.10. Showing the scale-invariant pore surface area to volume distribution, σ , calculated from FIB-SEM and μ -CT measurements of sample MD-2.7 km; (a) distribution with respect to the percentage of the total numbers of pores, (b) distribution with respect to the percentage of the total volume of the pores.

When the percentage volume contribution of each value of the scale-invariant surface area to volume ratio is considered (Figure 4.10b), it is clear that all three of the FIB-SEM measurements and the μ -CT measurement are in agreement that the pores which contribute significantly to the overall pore volume have scale-invariant surface area to volume ratios which are large, falling in the range $10 < \sigma < 30$.

Consequently, it can be indicated that there are pores of significant pore volume in the shale sample which have a large surface area for gas desorption.

4.5 Permeability

The permeability of a rock can be estimated by using the conventional pore surface area to volume ratio, ξ . The mean effective pore radius can be calculated following the approach used by Johnson et al. (1986), where they defined an effective pore diameter $\xi=2V_p/S_p$, where V_p is the pore volume and S_p is pore surface area of pores (Johnson et al., 1986). Thus, the parameter A is defined by $A=2/\xi$. The A -value is a measure of the aperture for fluid flow which controls the permeability in the sample according to the relationship $k = A^2/8F$, where $F = \phi^{-m}$ is the formation factor of the rock (Glover et al., 2010). In this equation the value of A describes the size of opening pores between the grains which allow the passage of fluid, while the formation volume factor contains information about how inter-connected those pathways are (Glover et al., 2009; 2015). The formation volume factor was not measured directly in this work, but was estimated using the measured porosity for the sample and an assumed value of the cementation exponent $m=3$. This value was chosen since the cementation exponent m for shales is known to vary between about 2.34 and 4.17 (Revil and Cathles, 1999).

Using the method described previously, the calculated permeabilities for the MD-2.7 sample were found to be 13.85 ± 3.45 nD, 4.16 ± 1.04 nD, 150 ± 37.5 nD and 2.98 ± 0.745 nD for FIB-SEM locations A, B, C and from μ -CT, respectively (Table 4.2). These values are broadly in agreement with recent upscaled permeability determinations for the Barnett shale (Peng et al., 2015). It is worth observing that Location C does have a larger permeability and porosity than locations A and B as well as at a larger scale from μ -CT measurements, this is because Location C contains a large crack as can be seen in Figure 4.4c, which would give higher porosity and permeability values.

The dimensions of the interconnected pores have an important role in the estimation of permeability, and hence an appropriate theoretical method for the effective pore radius or pore throat size is required. In order to validate the previous permeability calculations, Avizo® software has been used on SEM images of samples to measure the equivalent circular diameter of a crack.

Figure 4.11 shows an SEM image for Location C with a large crack. The crack has a length of about 10.4 ± 0.02 μm , and is approximately 0.2 ± 0.02 μm wide. The equivalent diameter of the crack has been calculated with following equation (Jennings et al., 1988):

$$d_e = 1.3(ab)^{0.625} / (a + b)^{0.25}, \quad (4.3)$$

Where; d_e is equivalent diameter (μm), a is the length of crack (μm) and b is the width of the crack (μm). For the crack shown in Figure 4.12 the equivalent diameter from Equation 4.3 was

found to be about $1.12 \pm 0.06 \mu\text{m}$. This value can also be used to represent the characteristic pore size in the Johnson et al. equation given above (Johnson et al., 1986), with $m=3$, the permeability is predicted to be $131.54 \pm 13.15 \text{ nD}$, which is remarkably consistent with the value obtained from the value of ξ calculated earlier for this location ($150 \pm 37.5 \text{ nD}$).

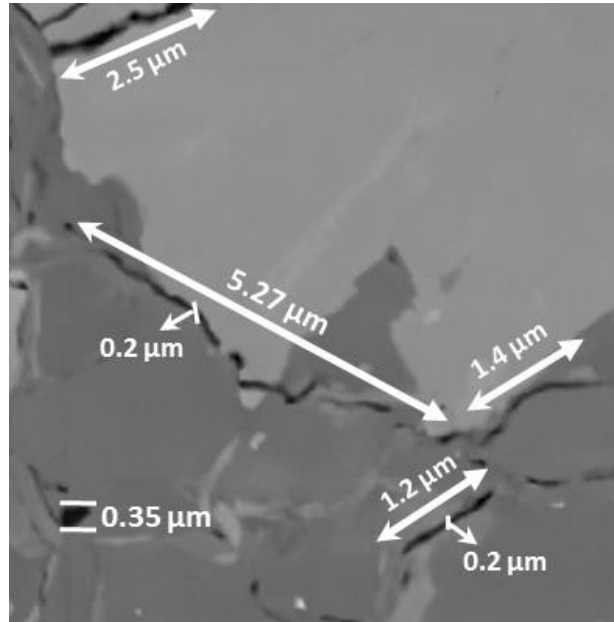


Figure 4 11. SEM image of location C with the dimensions of cracks. Uncertainties of $\pm 0.02 \mu\text{m}$ apply.

The summary of the results obtained in this study presented in Table 4.1 shows the most significant data including porosity, image size and voxel size for the sample MD-2.7 km obtained using both FIB-SEM and μ -CT techniques.

Table 4 1 Summary of the rocks and images studied in this work.

Sample	Figures	Method (Location)	Physical sizes	Voxel sizes	Measured Porosity (%)	Measured Kerogen (%)	Calculated Permeability (nD)
MD-2.7 km	4.1 & 4.2	FIB-SEM (A)	$23 \times 17 \times 30 \mu\text{m}^3$	$14 \times 24 \times 20 \text{ nm}^3$	0.10 ± 0.01	34.8 ± 1.74	13.85 ± 3.45
MD-2.7 km	4.1 & 4.2	FIB-SEM (B)	$34 \times 25 \times 40 \mu\text{m}^3$	$27 \times 34 \times 50 \text{ nm}^3$	0.52 ± 0.05	38.2 ± 1.91	4.16 ± 1.04
MD-2.7 km	4.1 & 4.2	FIB-SEM (C)	$28 \times 22 \times 40 \mu\text{m}^3$	$21 \times 26 \times 50 \text{ nm}^3$	0.94 ± 0.09	41.4 ± 2.07	150 ± 37.5
MD-2.7 km	4.1	μ -CT	$0.5 \times 0.5 \times 0.5 \text{ mm}^3$	$0.93 \times 0.93 \times 0.93 \mu\text{m}^3$	0.06 ± 0.008	44.5 ± 2.22	2.98 ± 0.745

The porosities of intermediate-rich samples for locations A, B and C (i.e., pore volume/ total volume of rock) were found to be 0.10%, 0.52%, 0.94%, respectively. Location C had a significantly higher porosity than the other two; possibly due to the cracks which can be seen in Figure 4.4.

While it is pleasing that the combination of FIB-SEM, μ -CT imaging and 3D image analysis has produced a reasonable value of porosity on the basis of this sample, it is recognized that the approach needs to be validated using independent porosity measurements such as nano-CT on samples; Chapter 5 reports and analyses such measurements.

4.6 Discussion

In this chapter, a single shale sample was imaged in 3D and quantitatively image analysed at multiple scales with multiple techniques in order to obtain a more accurate characterisation of the Bowland shale reservoirs. Although a few studies on Bowland Shale reservoirs have previously considered multiple scales of observations (Ma et al., 2016), none of these has been as comprehensive, imaging a single sample volume using μ -CT measurements, then making higher resolution FIB-SEM within the original sample volume but at specific multiple locations, each with a smaller field of view.

The results of the imaging in our study show that FIB-SEM analysis indicates that most pores in the scale range measured by that technique have a volume in the range $10^{-5} \mu\text{m}^3$ to $0.0036 \mu\text{m}^3$, while from μ -CT analysis measured pore volumes are from $0.9 \mu\text{m}^3$ to $31.5 \mu\text{m}^3$ (Figure 4.8). These data represent the measurement of two different populations of pores existing at different scales and measured with the different techniques. The lack of overlap in the scale ranges of the FIB-SEM and μ -CT data means that no reasonable combination of the data into a single dataset with a wider scale range can be carried out, and hence these data have been plotted separately. Additional data is required from another source if the FIB-SEM and μ -CT datasets are to be integrated. The nano-CT 3D imaging method may fill this gap, and this has been reported in Chapter 5.

It has been recognised that the data presented in this chapter are also skewed by the preponderance of small pores at the limits of the resolution of each technique, which are exhibited as a large number of single voxel pores. Plotting the distributions to show the percentage contributions to the pore volume shows that the smaller number of pores with larger pore volumes account for more of the overall pore volume of the rock.

Clearly, the two different techniques are measuring different populations of pores which occur at different scales; one at the micrometre scale and the other at the nanometre scale. Consequently, it can be inferred that the use of μ -CT data to characterise a shale will fail to take account of that population of pores which is smaller than the resolution of the μ -CT technique. Such a failure might be extremely significant if the nanoscale pores prove to control the connectivity of the pore network, which is likely to be the case since pores imaged by μ -CT seem very isolated (Figure 4.6), which has also been observed in the work of Ma et al. (2016). Nevertheless, the experimentally determined permeability of shales, though small, is measureable, falling in the range 10-250 nD, showing that some pore connectivity at some scale must exist. Equally, sole use of FIB-SEM measurements will fail

to detect pores in the microscale range, missing potential significant contributions to the overall porosity, and hence the available storage capacity of the shale rock.

The smallest pore visible obtained for the sample from FIB-SEM has a volume of $6.532 \times 10^{-6} \mu\text{m}^3$ in Location A, which corresponds to a pore diameter of 25.5 nm if a spherical pore is assumed, or 18.7 nm if a cubic voxel is assumed. The smallest pore imaged by this technique is, therefore, not necessarily the smallest pore in the rock because the voxel size for this technique is $19 \times 24 \times 20 \text{ nm}^3$, as discussed in Chapter 3. The largest volume in this location was about $0.027 \mu\text{m}^3$, equating to a pore diameter of about 411 nm, which may be similarly constrained by the size of the imaged volume ($20 \times 20 \times 1 \mu\text{m}^3$).

The data given in [Figure 4.9](#) has shown that pores which contribute significantly to the pore volume of the rock have aspect ratios indicating that they are broader than their smallest dimension by up to five times, but critically that they may be up to 10 or 20 times their aperture in length, for both the larger population of pores imaged by μ -CT and the smaller scale pores imaged by FIB-SEM. These high aspect ratio pores are more likely to interlink and give these shales a larger permeability, which is consistent with the permeability values as shown in [Table 4.1](#).

Data presented in [Figure 4.10](#) shows that pores which contribute significantly to the pore volume of the rock also have significantly raised values of scale-invariant surface area to volume ratio. Pores with large surface area to volume ratios allow for a much more efficient desorption of gas from the matrix and kerogen into the pores and hence contribute to efficient gas production.

Consequently, it can be stated that the shale studied in this work combines three important interlinked characteristics, in that the pores which compose the significant proportion of the pore volume, have shapes that enhance their interconnectivity and hence permeability, while also enhancing gas desorption from the matrix and kerogen into the pore space.

The shape of pores is also significant in defining the geomechanical properties of the rock. Shales have an inclination to plastic behaviours and any tendency towards weakness is likely to result in the closure of fractures and pores. While it is generally accepted that high aspect ratio, high surface area to volume penny-shaped pores and cracks are much more prone to closure than those with low aspect ratios and low surface areas to volume ([Glover et al., 2010, 2015](#); [Curtis et al., 2010](#)), many other factors, such as the *in situ* stress, rock strength, pore pressure, also affect the geomechanics of a pore and of the fracture network. It is not therefore possible to definitively associate high aspect ratio, high surface area to volume pore spaces with the volume and duration of gas production. Consequently, on balance, high aspect ratios and large surface areas are beneficial for shale in terms of gas production.

It has been indicated in the literature that not only pore volume and size, but also pore and fracture surfaces are fractal (Nolte et al., 1989; Bahr, 1997; Ogilvie et al., 2006). If so, such fractal cracks or pores can in principle have a surface area to volume ratio that is infinite. Therefore, it should be considered that some samples might have much higher surface areas due to the roughness of their surfaces, which do not substantially increase the pore volume but provide much larger pore surface areas. Approaches that take into consideration the fractal distribution of properties such as porosity and grain size are now being implemented in new reservoir modelling approaches and used to create fractal permeability models for shale gas flow (e.g., Al-Zainaldin et al., 2018; Glover et al., 2018; Geng et al., 2016; Li et al., 2016).

The main limitation of FIB-SEM and μ -CT imaging for all measured parameters is that they have sharply defined scale ranges which do not overlap. Consequently, pores which appear at either a lower or higher resolution than the resolution or field of view will not be taken into consideration. It is possible to plot the data on a combined scale, as this has been done in Figure 4.8, but there is no method for scaling the FIB-SEM and μ -CT distributions such that they represent the same relative frequency. Such an integration would have been possible if the ranges for each of the measurements overlapped, but unfortunately they do not. This is a particular problem for generating a pore volume distribution across a wide range of scales, or in the estimation of permeability, where the relative heights of peaks in the relative frequency measurement would allow the dominant pore volume or volumes to be ascertained. One solution would be to find a 3D imaging method that operates over a range of scales overlapping with both the FIB-SEM and μ -CT imaging techniques. Such a methodology exists in nano-scale CT imaging. The imaging has been carried out and the results are reported in following chapter.

4.7 Conclusions

In this chapter, Bowland shale rock samples have been imaged using the two advanced imaging technologies (FIB-SEM and μ -CT) in order to investigate the microstructure of gas shale at a wide range of scales (from 20 nm to 0.5 mm). The results show a complex microstructure that varies significantly between different regions in the sample and as a function of scale.

Samples were primarily composed of different amounts of pores and kerogen. The porosity varied from 0.06% to 0.94% and the kerogen fraction varied from 34.8% to 44.5%. Overall, the pore volume observed by SEM for the three locations spanned over a range of $10^{-5} \mu\text{m}^3$ to about $31.5 \mu\text{m}^3$, while the corresponding range for μ -CT analysis was between $1 \mu\text{m}^3$ to $1 \times 10^3 \mu\text{m}^3$. Computer-generated 3D renderings of shale volumes were reconstructed from serial sectioning and imaging-enabled qualitative analysis of kerogen and pore connectivity across the volumes. Quantitative analysis of these renderings allowed for estimates of percentage kerogen and porosity by volume for the shale samples. Estimated distributions of pore aspect ratio and surface area to volume ratio showed that an important feature of a shale gas rock is its connectedness which regulates permeability. Consequently, the results in this study have suggested that pores in the scale range accessed by the μ -CT technique are apparently isolated, but the smaller pores imaged using FIB-SEM form a connected pore network which engages with the larger pores measured by μ -CT. Hence, the larger pores control the porosity and storage capacity of the rock, while the smaller pores control the ability of fluid to flow through the rock.

The shape of the pores can be significant in shale gas reservoirs because pore shape regulates the rate of gas desorption and ultimately controls the recharging of gas in pores and fractures. The scale-invariant pore surface area to volume ratio (σ) for pores which contribute significantly to the overall pore volume has been found to range from 10 to 30. The pore shape also controls the mechanical properties of the rock and the likelihood that pores will interlink to form a pervasive pore network for fluid flow.

Chapter 5

Integration of Multi-Scale Imaging of Nanoscale Pore Microstructure in Gas Shales

5.1 Introduction

Previous work in Chapter 4 provided valuable insight into the microstructural properties of gas shale by combining two advanced imaging methods namely the μ -CT method for micro-scale investigations and FIB-SEM measurements for representing the whole shale rock sample. In this chapter, scale range of the earlier work is extended by using high-resolution X-ray Nano-computed tomography (Nano-CT), to first map the petrophysical properties of shale samples including porosity, pore volume and pore size distributions, pore aspect ratio, surface area to volume ratio and pore connectivity.

This chapter considers supporting measurements in the form of low pressure (N_2) nitrogen adsorption and high pressure (MIP) mercury intrusion porosimetry on the same core plugs that were used for Nano-CT imaging. This allows the supporting measurements to be interpreted in the light of the imaged microstructures at different scales within the shale.

X-ray nano-computed tomography (Nano-CT) has been used to provide direct visualization and quantitative assessment of geological samples ([Andrew et al., 2013](#); [Berg et al., 2013](#); [Cnudde and Boone, 2013](#); [Dann et al., 2010](#)), including gas shale rocks ([Ma et al., 2016](#)). The main advantage of Nano-CT is that it allows non-destructive access to the internal structure of objects down to a smaller scale than is available with μ -CT. Similar to μ -CT, the Nano-CT technique provides qualitative and quantitative data about the structure and morphology of 3D samples and features (pores, kerogen, minerals, etc.).

Although valuable, the previous work in Chapter 4 is limited to some extent due to the scaling issue (limitation of FIB-SEM and μ -CT imaging), which results in an incomplete understanding of the microstructure of shales at the nanometer scale, due to time constraints for data that need to be captured such as fast scanning times, preparation small sample sizes and controlled conditions are required. All of these challenges can be currently met experimentally by using laboratory-based Nano-CT systems.

This chapter begins by outlining the material have used in Section 5.2 along with multi-scale 2D/3D imaging described in. Section 5.3 presents the results, including mineralogy of the samples and the full characterization of its microstructural properties. Section 5.3. discusses the supporting measurements and their interpretation in the light of the imaging measurements. Calculations of permeability and connectivity have also been carried out, but as these parameters are derived from the results indirectly, they are presented separately in Chapter 7. The discussion of the results from this chapter is presented in Section 5.4. Finally, the findings are summarised in the conclusions section.

5.2 Material and methods

5.2.1 Sample material and preparation

The gas shale sample used in this chapter (MD-2.7 Km, see Table 3.1) was selected from a 2700 m depth from the Bowland shale formation which is present across a large part of the central and northern UK (the same sample as used in Chapter 4).

A very small cuboid sample (side length about 25 μm) was prepared from the reservoir rocks by using FIB-SEM system as a manipulation and preparation tool. The preparation of such a sample were discussed in chapter 3 (section 3.2.2).

5.2.2 X-Ray Diffraction

An X-ray diffraction (Bruker D8 XRD) measurement was performed to determine the mineralogical phases within the shale samples (Table 5.1). Again, the preparation and measurements setting of the samples were presented in chapter 3 (section 3.3.1)

5.2.3 Nitrogen gas adsorption measurements

The nitrogen (N_2) gas adsorption measurements were also made on the same sample using a Micromeritics Tristar 3000 instrument in the School of Chemical and Process Engineering at the University of Leeds. This procedure provided information on porosity and pore size, internal surface area, pore volume, as well as pore and surface area to pore volume distributions. Further details on the measurement and samples preparation are provided chapter 3 (section 3.3.2.2).

5.2.4 Mercury injection capillary pressure measurements

The Mercury injection (MIP) measurements were also carried out using a Micromeritics Autopore IV 9520 system in the School of Earth and Environment, University of Leeds (Rosenbrand et al., 2015). The measurement was carried out on a chip sample of around 2 mm size with a weight of around 10 g. Again, further details on the preparation and drying of samples are provided chapter 3 (section 3.3.2).

5.2.5 Multi-scale 2D/3D imaging techniques

Three methods were used to visualise and quantify the 3D microstructure of a sample of Bowland gas shale. The methods are (i) Focused Ion Beam Scanning Electron Microscopy (FIB-SEM), (ii) nano-scale X-ray computed tomography (nano-CT), and (iii) micron-scale X-ray computed tomography (μ -CT). Taken together, the three measurement methods allow length scales from 10^{-3} m to 10^{-9} m to be imaged and quantified.

Micrometer and nanometer scale data have been presented earlier in the thesis (Chapter 4). This chapter bridges the gap between those different scale measurements by using high-resolution Nano-CT measurements on the same sample (Figure 5.1). The Nano-CT measurements have a voxel size of approximately $64 \times 64 \times 64 \text{ nm}^3$ which may be compared

with $940 \times 940 \times 940 \text{ nm}^3$ for μ -CT and $18 \times 24 \times 20 \text{ nm}^3$ for FIB-SEM (see Table 3.2 in Chapter 3). The relative scale ranges of each method is shown in Figure 5.2.

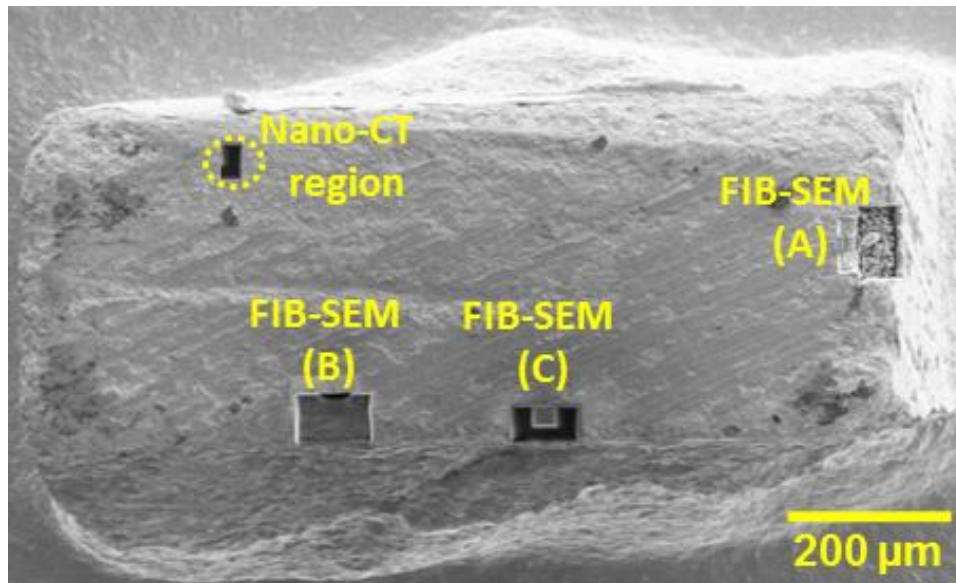


Figure 5.1. An overview of the Bowland gas shale sample used in this study for Nano-CT showing the region (in the top left side) and also the different locations A, B, and C that were used for FIB-SEM serial sectioning.

Multi-scale image acquisition was undertaken using three different imaging techniques (μ -CT, nano-CT and FIB-SEM), providing the 2D and 3D microstructure of the shale sample to be visualised over 6 orders of magnitude in length scale. At the largest scales, imaged using the μ -CT technique, the voxel resolution is approximately $1 \mu\text{m}$ ($930 \times 930 \times 930 \text{ nm}^3$). Consequently, only pores greater than $1 \mu\text{m}$ (and extending to $1000 \mu\text{m}$) can be visualised. At this scale the pores are apparently unconnected (Figure 5.2a). By phase contrast, the nanometer scale FIB-SEM data (Chapter 4) showed both pore volume and connectivity. By using the Nano-CT method, added in this chapter, which operates at a resolution of approximately 100 nm , it was hoped that the scale threshold of connectivity of both pores and kerogen might be judged.

The purpose of chosen Nano-CT region (Figure 5.2) is to bridge the gap between the two different scale measurements (FIB-SEM and μ -CT) that have been presented in earlier work (Chapter 4) in order to complete the understanding of the internal structure of shales at a range of scale within the same sample and also to judge whatever these dataset are either representative of the whole sample, or if there is a need to investigate specific aspects of features occurring in the whole specimen. Consequently - this allows to understand the relationships between the microscale and macroscale properties and interpreted these in the light of the imaged petrophysical properties at different scales within the shale.

At a smaller scale, around 100 nm, the nano-CT technique still has difficulty resolving connectivity between the pores (Figure 5.2b) because its voxel size ($64 \times 64 \times 64 \text{ nm}^3$) is insufficient. However, the nano-CT is able to resolve connectivity for the kerogen, as can be seen in Figure 5.3e.

The FIB-SEM technique has the smallest resolution (voxel size of $19 \times 24 \times 20 \text{ nm}^3$) is able to reveal more details of the microstructure such as pores, kerogen and matrix. The small fractures that provide connections between the larger pores can be recognized at this higher resolution (Figure 5.2c), but some of the larger pores which are thus connected are too large to be imaged. Indeed, the cost of this technique having such a good resolution is that it can only image a small volume of rock which makes the technique unable to visualise the phenomena larger than these dimensions. The pervasive connections at the ultra-small scale measured by FIB-SEM provide the pathways for flow that give gas shales their small, but non-zero, permeability of several to several thousand nanodarcies.

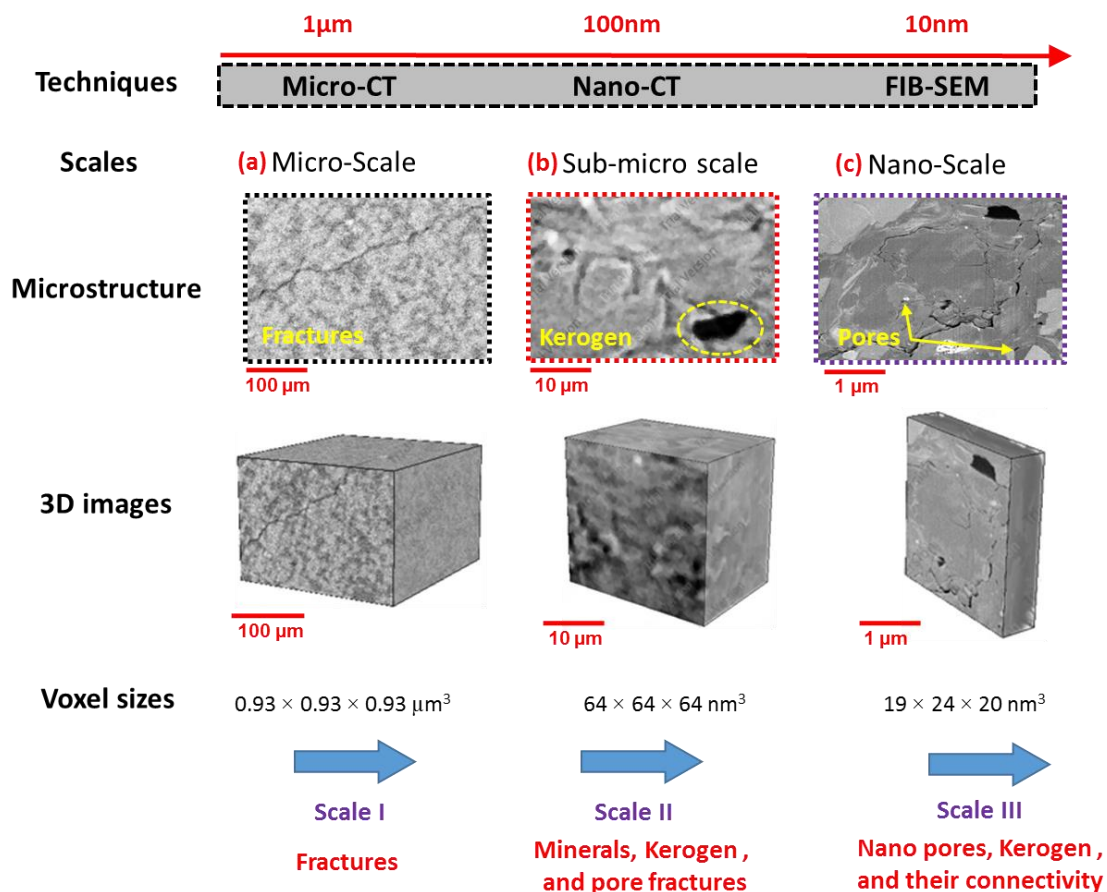


Figure 5.2. Multiscale imaging techniques (FIB-SEM, Nano-CT and μ -CT) on the same rock sample volume used in this chapter.

5.3 Results

5.3.1 Mineral composition analysis and kerogen fraction

The XRD analysis was used to identify the mineralogical composition of the shale sample (Table 5.1). The sample contains predominantly quartz, mica and dolomite together with a smaller amount of pyrite, with proportions of 92.5 vol%, 4.6 vol%, 1.4 vol% and 0.7 vol%, respectively.

Despite kerogen representing an important fraction of shales, both volumetrically and with regard to its significance as a resource, it is not possible to calculate from XRD measurements. Nevertheless, the results of XRD analysis can provide valuable adjunct information for understanding the mineralogy composition and phases in shale samples (Bhargava et al., 2005). In this current chapter, it has been used 3D image analysis of the nano-CT data to obtain the volumetric fraction of the kerogen phase fraction as 32.4 ± 1.45 vol%.

Table 5.1. Mineralogical results from XRD measurements undertaken in this study.

Sample	Quartz	Albite	Microcline	Calcite	Dolomite	Illite	Mica	Siderite	Pyrite
MD-2.7 Km (%)	92.5 \pm 1	0.6 \pm 1	0.2 \pm 1	0.0 \pm 1	1.4 \pm 1	0.0 \pm 1	4.6 \pm 1	0.1 \pm 1	0.7 \pm 1

5.3.2 3D Microstructure of gas shale volumes

The 3D micro-structure of the shale sample has been investigated using Nano-CT images of slices/sections through the sample (Figure 5.3).

Figure 5.3 shows the three-dimensional images of the sample acquired using Nano-CT with significant parameters related to gas transport such as pore, kerogen, and matrix phase fractions. Figure 5.3a shows the raw 3D grey-scale image of the sample on its support needle and from another aspect. This data volume has been thresholded to separate pores, kerogen and the rock matrix. The remainder of the figure assigns the red colour to kerogen, blue to pores and green to rock matrix. Figures 5.3b shows all three different phases. The remaining parts of the figure show single phases and combinations of two phases, the last of which shows the pores colour-coded according to whether they are connected to each other. It can be seen that kerogen composes 32.4 vol% of the sample and is distributed anisotropically, with the kerogen predominantly represented by long thin bodies that are arranged sub-parallel. Qualitatively it appears that there is high connectivity between these kerogen bodies across large proportions of the whole $64 \times 64 \times 64$ nm³ sample volume (Figure 5.3e). By

contrast, pores make up only 0.67 ± 0.009 vol % of the sample (Figure 5.3f). Qualitatively, the pores are smaller, more numerous, more equant and apparently less connected. Figure 5.3g shows a 3D image of the pore space network where the colours indicate those pores which are connected. Apart from a couple of local patches, pores exist predominantly as apparently isolated entities, at least at the scale measured by the nano-CT technique. The FIB-SEM measurements presented earlier in the thesis (Chapter 4) show that the apparent lack of connection of these pores is misleading. The volume fraction of the sample that was classed as matrix amounted to 66.93 vol%.

Table 5.2 displays a brief summary of the most important data including pores and kerogen obtained by different techniques.

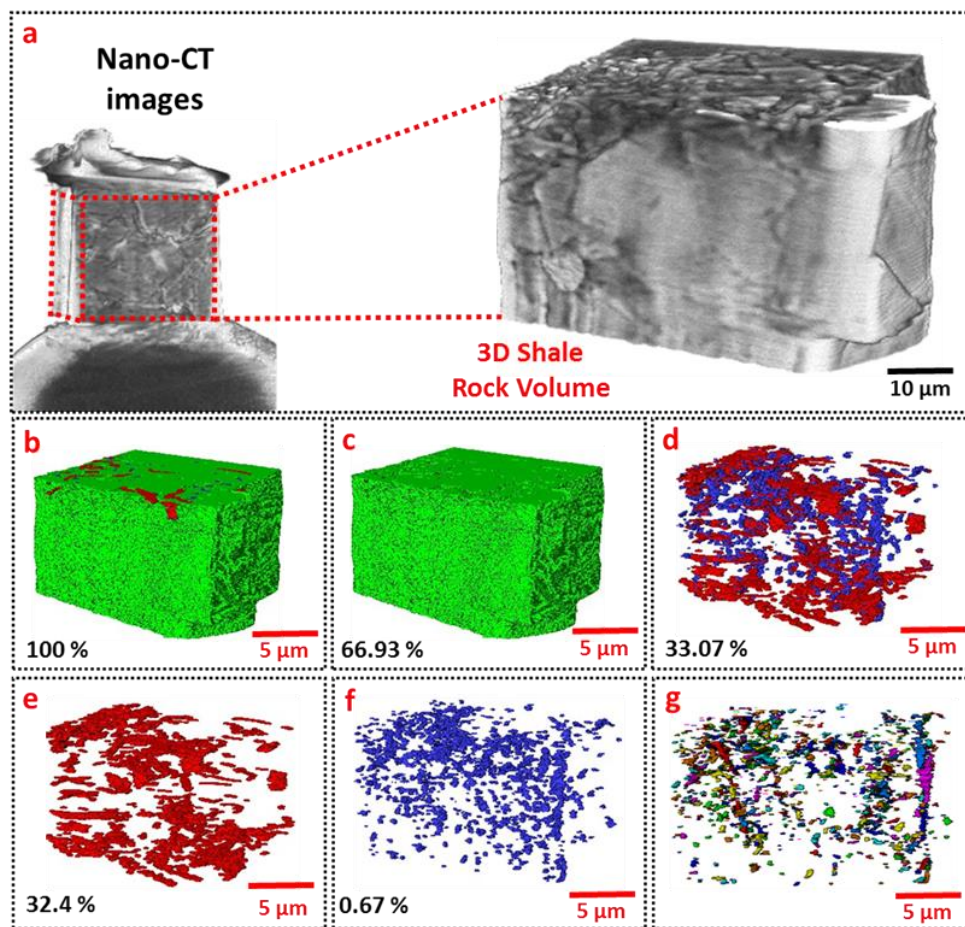


Figure 5.3. Overview of the X-ray nano-tomography (Nano-CT) for a shale rock sample: (a) 3D image of shale sample with a thickness of around $25 \mu\text{m}$, (b) representative 3D image indicating all phases in the sample. By setting thresholds on the greyscale of this 3D solid, the following features can be seen: (c) solid minerals (green), (d) mixed kerogen (red) and pores (blue), (e) the kerogen network alone (red), and (f) pores alone (blue), (g) the 3D image of pores where the colours indicate clusters of connected pores.

Table 5.2. Summary of the rock sample data obtained by different techniques (Chapter 7 contains a full discussion on calculated permeability).

Method (Location)	Imaged size (μm^3)	Voxel size (nm^3)	Measured Porosity (%)	Measured Kerogen (%)	Calculated Permeability (nD)	Reference
FIB-SEM (A)	23×17×30	19×24×20	0.10 ± 0.01	34.8 ±1.74	13.85 ± 3.45	Chapter 4
FIB-SEM (B)	34×25×40	27×34×50	0.52 ± 0.05	38.2 ±1.91	4.16 ± 1.04	
FIB-SEM (C)	28×22×40	21×26×50	0.94 ± 0.09	41.4 ±2.07	150 ± 37.5	
μ -CT	500×500×500	930×930×930	0.06 ±0.008	44.5 ±2.22	2.98 ± 0.745	
Nano-CT	25×25×25	64×64×64	0.67 ± 0.03	32.4 ±1.45	2.61 ± 0.42	This Chapter

5.3.3 Pore volume distribution

Pore volumes were obtained using 3D image analysis of the nano-CT dataset at nanometric scale (i.e., with no smoothing). Figure 5.4 presents the distribution of the relative frequency of the number of pores as a function of their individual pore volume. The range of this distribution ($0.02 \mu\text{m}^3$ and $0.35 \mu\text{m}^3$) reflects the range of scales over which the nano-CT provides data on pore volumes (the lower value represents the linear resolution of the technique, i.e., about 64 nm).

Figure 5.4 shows that there are a large number of pores with the smallest pore volumes, increasing to an unresolved peak at the lower limit of the technique. This suggests strongly that there is a large population of pores with smaller dimensions than the nano-CT technique can resolve. This is in agreement with earlier FIB-SEM measurements have been presented in earlier chapter (Chapter 4) on the same rock sample. The FIB-SEM measurements have shown that there is a population of smaller pores, with volumes ranging between $10^{-5} \mu\text{m}^3$ to about $0.0036 \mu\text{m}^3$. It is these ultra-small pores which are likely to provide the connectivity required to allow gas to flow through shales, and whose small dimensions account for the low permeabilities of shale. These results are in agreement with the observation that pores lower than 10 nm are locally connected and can support diffusive or transitional gas transport (Javadpour et al., 2007). Consequently, results from both nano-CT and FIB-SEM recognise the presence of a population of nanometric scale pores, but the nano-CT technique can only resolve the larger of these pores

It should be noted that the small pores recognised by Javadpour et al. (Javadpour et al., 2007) and also have presented in earlier chapter by using FIB-SEM and now by nano-CT in this work represent a small proportion of the overall porosity of the rock despite their large number and irrespective of the possibility that they most likely control the transport properties of the rock.

Figure 5.4 also shows the same data but on a dual-logarithmic axes showing a negative power-law behaviour, which can be described by the equation $y=0.00347x^{-1.615}$ ($R^2=0.876$). This observation suggests strongly that a large number of pores smaller than the resolution of the nano-CT technique is likely to be present in the sample.

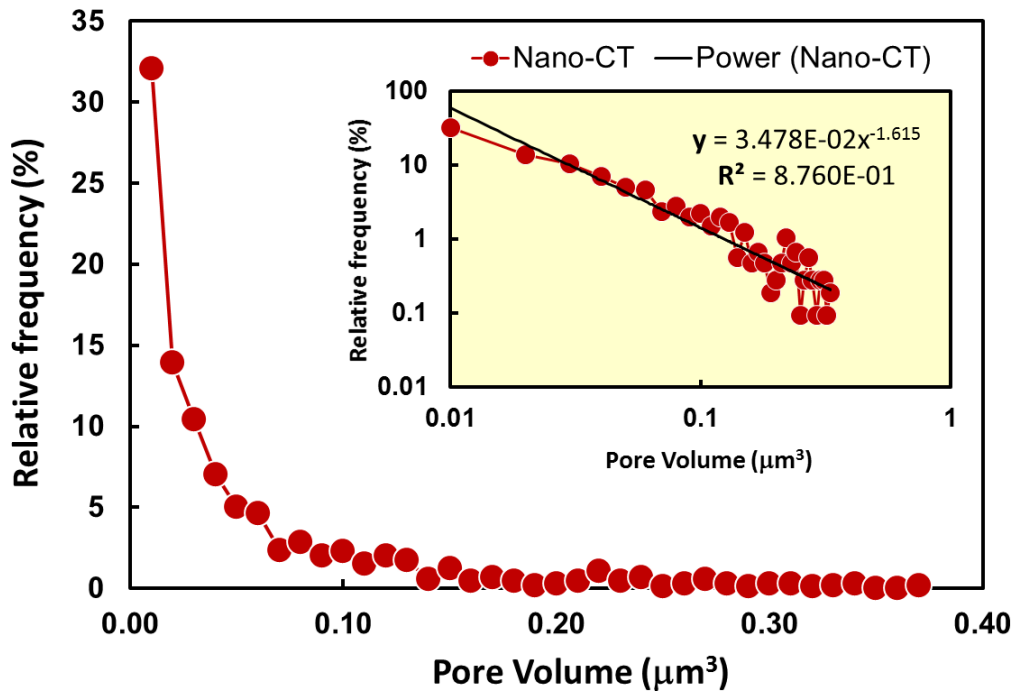


Figure 5.4. The distribution of pore volume calculated from the Nano-CT 3D imaging datasets of the gas shale sample. The inset shows the low pore volume data on an expanded scale.

5.3.4 Pore size distribution

The 3D imaging dataset from the nano-CT technique was also used to calculate the distribution of the relative frequency of the number of pores as a function of their individual pore size (the calculations were undertaken following the approach outlined in Chapter 4). These data have been compared to independent measurements of the relative frequency of the number of pores as a function of their individual pore size obtained using nitrogen adsorption and MIP for the same shale sample, as shown later in this chapter.

Figure 5.5 shows a comparison of the relative volume of pores as a function of their individual pore diameter as measured by nano-CT and MIP techniques. The MIP data provides a smaller range of pore sizes, from 3 to 2000 nm with a peak at about 9.2 nm, whereas the nano-CT measurement provides higher range of pore sizes, ranging between 100 nm to 5000 nm, with a peak at about 800 nm. Since the measurements were made on the same sample, the difference must be systematically linked to the techniques that were used to make the measurements. We could attribute the observed difference to an effect of having different scales for which each of the techniques is sensitive, because the two techniques do not completely overlap. The other possibility is that the MIP technique is measuring a population of pores which is compressed by the high mercury pressures needed to intrude mercury into the small pore spaces. Such an effect would be more likely to occur in relatively plastic shales with small pores, which is the case for the samples. The question remains, however, whether

this effect could account for the two order of magnitude change that would be needed to produce the data observed in [Figure 5.5](#).

Consequently, it would be reasonable to infer that the two different methods are measuring two different populations of pores present at different scales. This is because each technique has its own limitations in terms of sample size and resolution which has an impact on detecting pores within the sample, for example the lower pore size 3 nm can be detected by MIP and larger pores then 300 nm are shown by nano-CT.

Pore size and volume distributions less than 3 nm can be obtained by applying of Barrett-Joyner-Halenda (BJH) method to nitrogen absorption data ([Figure 5.6](#)). This technique measures the amount of gas molecules absorbed to (and subsequently desorbed from) the internal surfaces of pores as a function of applied gas pressure ([Sing., 2001](#)).

In this work the volume of the gas absorbed (and subsequently desorbed) has a range of 0.85-8.30 cm³/g, with corresponding relative pressure (P/P^0) ranging between 0.07-0.9, respectively ([Figure 5.6a](#)), with a transform point of surface area equal to 0.2 ([Figure 5.6b](#)). The pore size distribution as a function of pore diameter, calculated using the BJH method is shown as [Figure 5.6c](#), indicating progressively larger pore volumes occurring in the form of smaller pores. This is similar behaviour to what was observed for the nano-CT data in the inset of [Figure 5.4](#). However, the data are not directly comparable since [Figure 5.4](#) counts fractional pore numbers, while [Figure 5.6c](#) counts pore volume. [Figure 5.6d](#) provides the pore internal area distribution as a function of pore diameter.

Both [Figure 5.6c](#) and [Figure 5.6d](#) indicate the presence of significant pore volume and internal pore area for pores of the diameter of about 200 nm. This is consistent with the nano-CT data shown and discussed previously (red data in [Figure 5.5](#)). The nano-CT data show pores existing in the range 200-1200 nm ([Figure 5.5](#)). These cannot be observed in the nitrogen adsorption data due to limitations in the range of the nitrogen adsorption measurement. The gradual increase in both pore volume ([Figure 5.6c](#)) and pore area ([Figure 5.6d](#)) which occurs as the pore diameter progressively decreases below 800 nm is consistent with the MIP data (green data in [Figure 5.5](#)), where the relatively constant fraction of porosity observed by MIP between 100 nm and 10 nm corresponds to the straight line increase in the nitrogen adsorption data, and the more erratic changes in both the pore volume and pore area data between 10 nm and 2 nm may be associated with the peak in MIP fractional pore volume appearing in [Figure 5.5](#).

According to the De Boer's classification ([De Boer et al., 1964](#)), the pore shapes in this current shale sample are inferred to be penny-shaped (oblate), or to have a very small aspect ratio (i.e., small thickness relative to length). These observations are in broad agreement with analysis of the FIB-SEM data in previous chapter (Chapter 4) as well as the analysis of the nano-CT data in this work, as discussed below.

Table 5 3 Summary of petrophysical properties of gas shale rock sample in this study from N₂ sorption (BET) and mercury injection porosimetry (MIP) techniques.

Sample	BET Surface area (m ² /g)	Single point of surface area (m ² /g)	Single point of pore volume (cm ³ /g)	BET Porosity (%)	MIP Porosity (%)	Calculated Permeability from BET (×10 ⁻⁴ nD)	Calculated Permeability from MIP (nD)
MD-2.7km	2.37	2.239	0.008488	0.0235±0.003	0.6±0.07	4.63±0.02	2.65±0.45

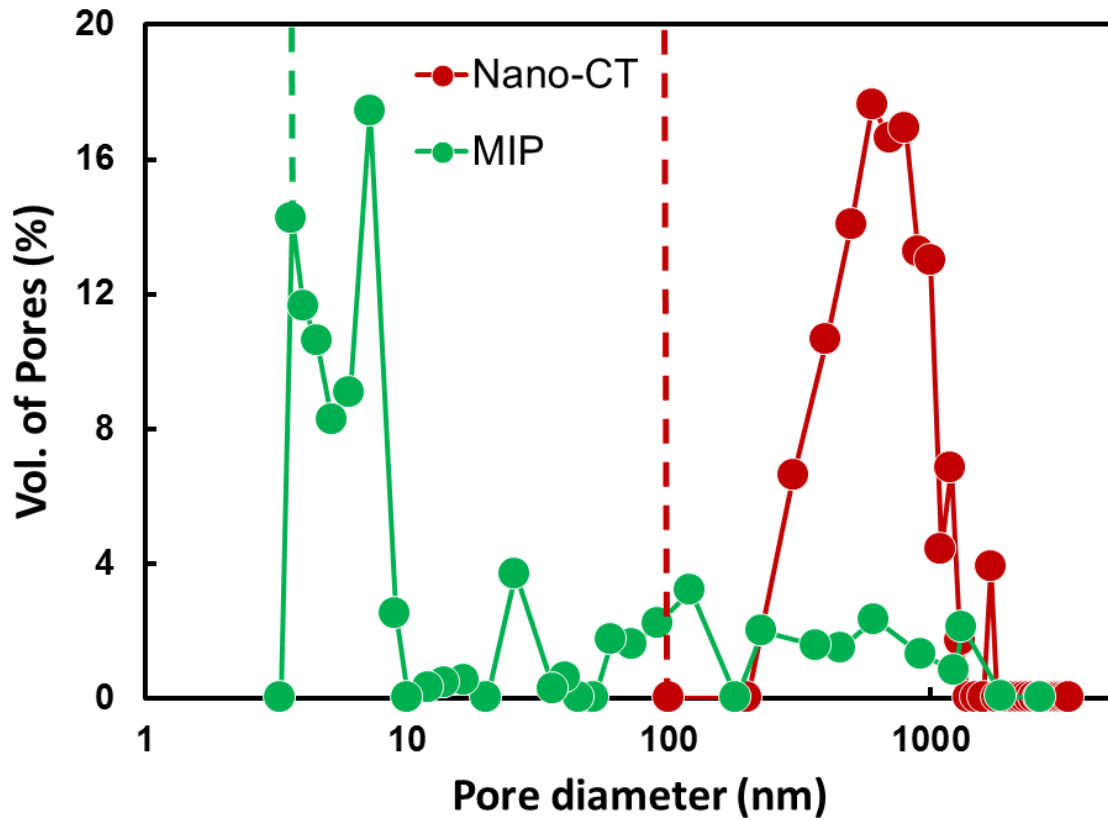


Figure 5 5. The pore size distribution calculated from the Nano-CT (red) and the MIP measurements (green) were made on a sample from the same core plug. Dashed lines show native resolution limits for each technique.

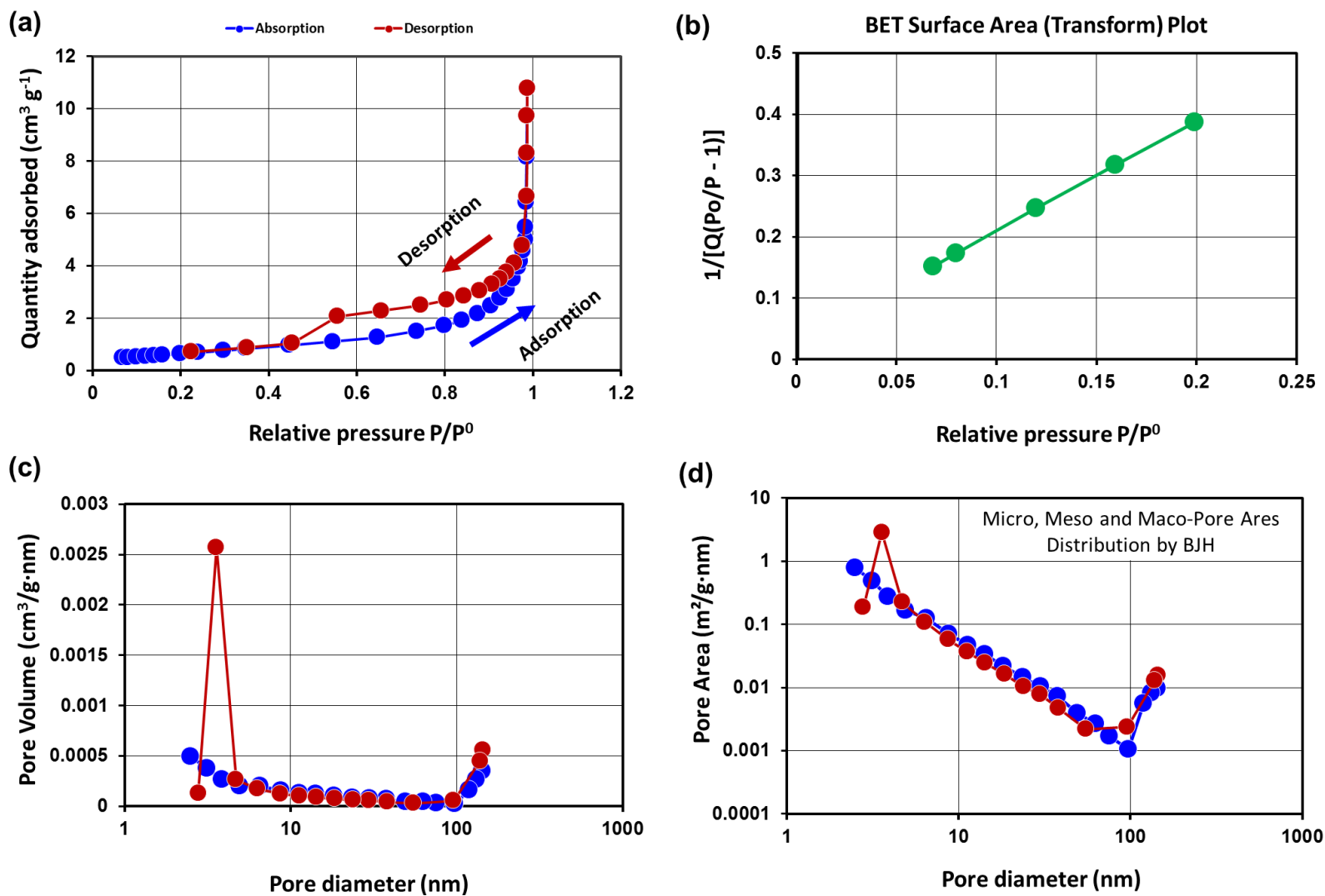


Figure 5.6. (a) The linear isotherms and pore sizes distributions from N₂ sorption experiment, (b) the BET surface area transform at the relative pressure P/P⁰, (c) BJH pore size distribution, according to pore volume, and (d) according to pore areas.

5.3.5 Pore aspect ratio distributions

In this chapter the pore aspect ratios calculated as similar approach of previous work presented in chapter 4 by using the two functions of pore aspect ratios $\gamma_1 = c/b$ and $\gamma_2 = a/c$, where b is the maximum dimension of the pore and c is its width, being defined as the minimum dimension of the pore. Further details on the definitions and calculation of the pore aspect ratios are provided in section 3.7.2 Chapter 3.

Figure 5.7 shows the percentage pore number and percentage pore volume distributions as a function of each aspect ratio, γ_1 (Figure 5.7a) and γ_2 (Figure 5.7b). Both parts of the need to be analysed together in order to fully understand the shape of the imaged pores.

First taking the distributions counted by pore number (blue data), Figure 5.7a shows that γ_1 varies from 0.065 to 0.8, representing pores which vary from those which are over 15 times longer than their smallest dimension to those which are near spherical (the longest dimension is only 1.25 times the smallest dimension and the intermediate dimension must be between the two extremes). Within this wide range of pore shapes there is a pronounced peak where over $36.47 \pm 0.05\%$ of the pores have $\gamma_1 = 0.1667 \pm 0.033$, representing pores which are 6 times as longer than their smallest dimension. Contemporaneously, Figure 5.7b shows that γ_2 varies from 1.1 to 1.9, indicating that some pores are prolate ($\gamma_2 \rightarrow 1$) while others have a semi-axes up to almost twice the minimum dimension, indicating oblate or penny-shaped pores (i.e., $\gamma_2 > 1$). Once again, there is a peak in the distribution which represents about $34.57 \pm 0.05\%$ of the number of pores at $\gamma_2 = 1.457 \pm 0.0285$. This data, when analysed in γ_1 - γ_2 pairs shows that there is a significant well-defined sub-population of pores representing about 35% of the total pore number which have a long axis about 6 times the short semi-axis, and an intermediate semi-axis about 1.457 times the short semi-axis

It is interesting to note that the two distributions of the pore aspect (number and volume of pores) in both γ_1 and γ_2 are significantly different such that it can be seen the same value of the γ_1 aspect ratio (say, 0.1667) in Figure 5.7a. $\gamma_1 = 0.1667$ represents about 17.11% of pore volume but 36.47% of the pores, which suggests that on average pores the value of γ_1 are very small, contributing little in overall pore volume despite their numerousness.

Turning to the distributions counted by pore volume (red data), Figure 5.7a shows that γ_1 varies from 0.065 to 0.8. This is the same range as in the pore number distribution, and implies the same variation in pores from those which are over 15 times longer than their smallest dimension to those which are near spherical. However, there are no sharp peaks in the distribution. Instead, there is a broad peak at $\gamma_1 = 0.30 \pm 0.167$, amounting to just over 10% of the total pore volume and indicating that the longest dimension is only 3.33 times the smallest dimension. Figure 5.7b also shows that the distribution of γ_2 according to pore volume also varies within the same range as when counted by pore

number (1.1 to 1.9). There is a relict of the peak in the distribution at about $\gamma_2=1.457\pm 0.0285$, but this is swamped by larger values of $\gamma_2 < 1.27$. In other words, when counted by pore volume, pores for which $\gamma_2 \rightarrow 1$ (i.e., more prolate) are more dominant.

The distinction between oblate and prolate pores is important because each of these geometrical styles of pore will interact in a different fashion and lead to more or less connectivity for fluid transport.

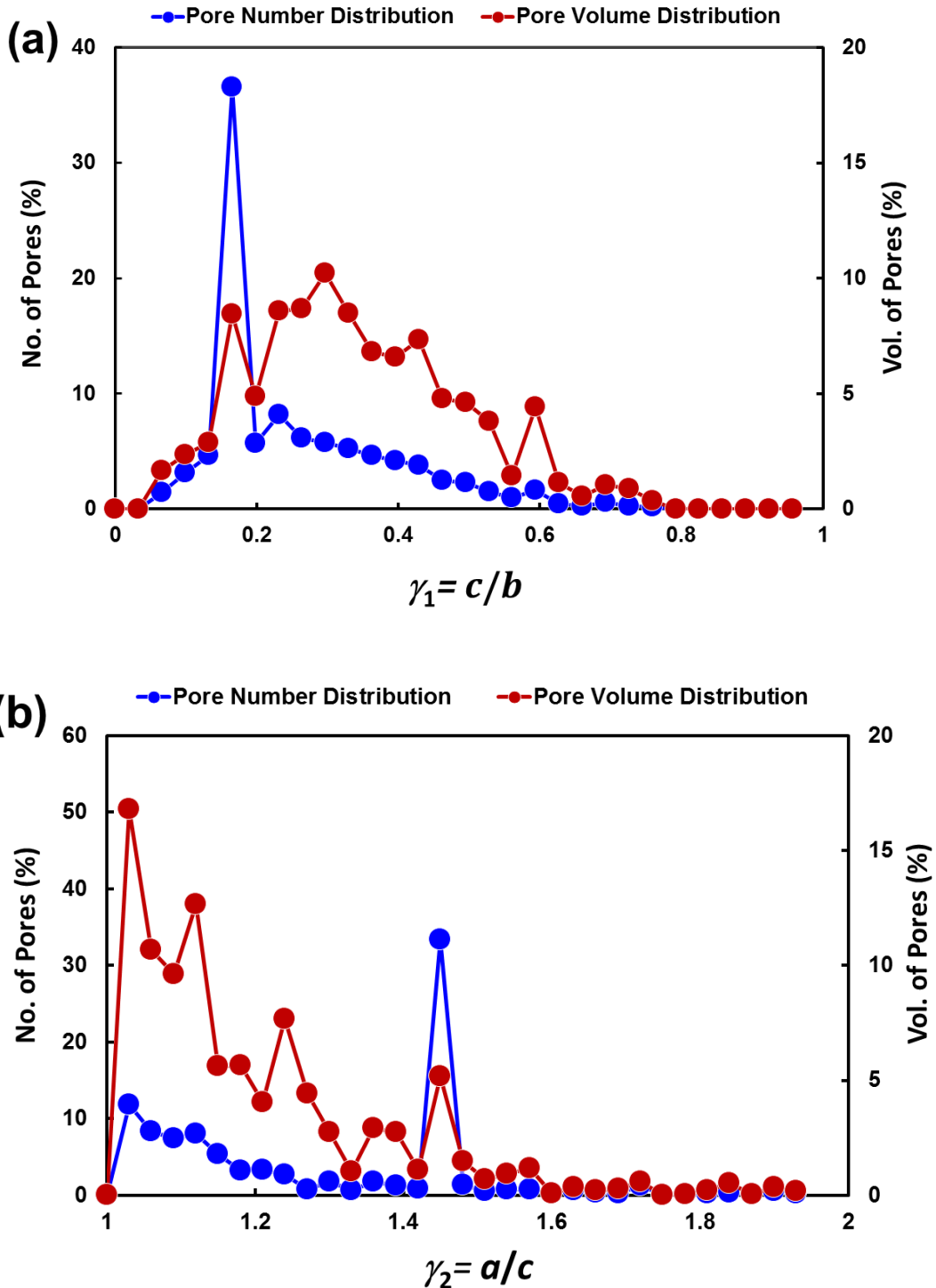


Figure 5.7. The pore-aspect ratio distribution, (a) pore-aspect ratio distributed as a function of the number and volume of pores obtained from γ_1 (oblate) values, and (b) pore-aspect ratio distributed

estimated from γ_2 (prolate) values, estimated by Nano-CT approach using the MD-2.7 km gas shale sample.

5.3.6 Pore surface area to volume ratio

The pore surface area to volume ratio ξ is another indicator of pore shape. The way in which pore surface area to volume ratio and scale-invariant surface area to volume ratio have been calculated were described earlier in section 3.7.3 Chapter 3.

Figure 5.8 shows the distributions of number of pores (blue data) and volume of pores (red data), both expressed as a percentage, as a function of the scale-invariant surface area to volume ratio, σ for the nano-CT data presented in this chapter. The mathematical definition of the scale-invariant surface area to volume ratio is such that only positive values greater than 3 are possible, representing a spherical pore. In our data the minimum value of σ was just greater than 3, while the maximum was about 13.

Figure 5.8 shows a uniform pore number distribution with a pronounced peak at about $\sigma=3.5\pm 0.5$, which indicates that there is a large number of pores which are equant (approximately spherical). However, the equivalent peak is much reduced in the pore volume distribution. It can be seen that the large number of equant pores are all very small. Indeed their apparent equant shape may be due to the fact that these are the single voxel pores that exist at the limits of the nano-CT resolution, and can consequently be considered to be artefacts of measurement. Figure 5.8 shows that pores with a broad range of σ values exist in the sample, some of which have very high values, representing pores which are extremely effective at degassing.

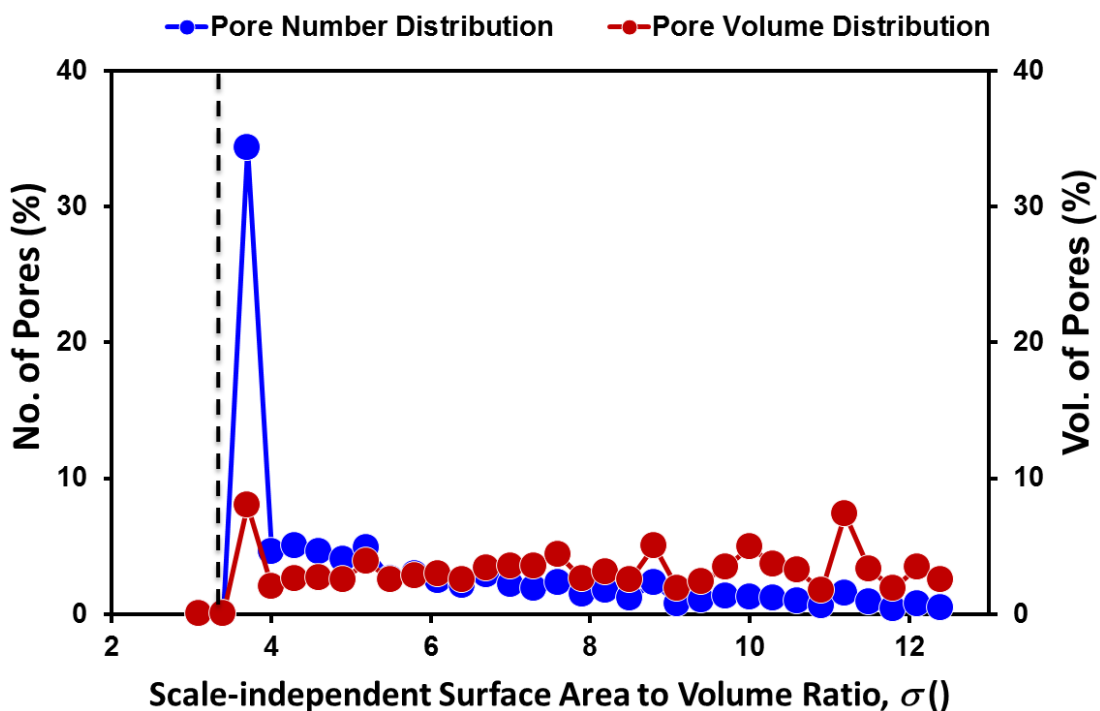


Figure 5 8. The scale-invariant pore surface area to volume distribution, σ , calculated from Nano-CT measurement as percentage of the total numbers and volume of pores of the gas shale sample MD-2.7 km.

5.4 Discussion and interpretation

This chapter extends previous work discussed in Chapter 4 by characterizing the microstructural heterogeneity of gas shale using a variety of techniques such as X-ray Nano-computed tomography (Nano-CT) at higher resolution as well as laboratory measurements (N_2) nitrogen adsorption and (MIP) mercury intrusion porosimetry to infer and characterize the full pore range in the Bowland shale reservoir.

The nano-CT imaging data indicates that the majority of pores have a volume ranging from $0.01 \mu\text{m}^3$ to $0.35 \mu\text{m}^3$ (Figure 5.4). By comparison from the earlier work in Chapter 4, the pore volumes from FIB-SEM and μ -CT analysis were measured in the range $10^{-5} \mu\text{m}^3$ to $0.0036 \mu\text{m}^3$ for FIB-SEM and $0.9 \mu\text{m}^3$ to $31.5 \mu\text{m}^3$ for μ -CT. Taken together, these three datasets imply that shale contains pores with volumes which cover the entire measured range, from as small as $10^{-5} \mu\text{m}^3$ to $31.5 \mu\text{m}^3$. There is no substantial evidence that the three populations observed by each of the three imaging techniques is separate from the point of view of its geometry or the process that have formed them. Rather, they are samples from a wider single continuous population of pores that has been sampled by the measured volume and native resolution of each technique.

The shape and alignment of pores both provide significant control over gas transport in gas shales because they control the connectedness of pores and the tortuosity of flow paths (Glover, 2009; Clennell, 1997). Hence the geometrical and connectivity properties of pores has the potential to exert important control on rock transport properties, including the electrical and hydraulic properties of rocks (Glover, 2009). The shape of pores, parametrised particularly by the scale-invariant surface area to volume ratio, controls the efficacy of gas diffusion from kerogen into pores as well as along kerogen surfaces.

In the Bowland Shale the pores ($0.67 \pm 0.1\%$ of the total rock volume, Figure 5.3f) are mostly associated with the kerogen ($32.4 \pm 1.45\%$ of the total rock volume, Figure 5.3e), occupying space between the kerogen and the matrix of the rock or entirely within the kerogen. For this sample the pores with an equivalent diameter of 100 nm or larger have not shown connectivity, which has also been noted in the work of (Ma et al., 2016). This observation encourages the interpretation (or classification) that kerogen should be considered to be more of a pore-filling phase rather than a rock matrix phase. The association of pores with kerogen has a number of implications. First, the kerogen ensures that the pores have a low connectivity. Second that the pores are well-positioned to be charged with gas diffusing out of the kerogen. Third, the connectivity of kerogen becomes particularly significant due

to the potential presence of other transport forms such as surface diffusion and gas transport through kerogen. This observation raises the possibility that gas transport in shale might be modelled assuming that the connectivity of the kerogen controls gas transport. This latter approach has already been followed (Glover et al., 2006), producing values (0.003-1.66 nD) from nano-CT and FIB-SEM studies of Swedish gas shales that are not only consistent with other methodologies (2.55 nD and 9.92 nD) but also similar to permeability measurements made in the laboratory on the same material (1.74 ± 0.65 nD).

5.5 Conclusions

In this chapter the microstructure of gas shale reservoir has been characterized using a variety of technologies including N₂ adsorption, MIP and also high resolution tomographic method (Nano-CT). These three techniques were all implemented on the same Bowland gas shale sample. Furthermore, these methods have been carried out on the same sample that had already been imaged and quantified using μ -CT and FIB-SEM methodologies, as shown in chapter 4. The result is an unusually rich dataset that covers scale from about 20 nm to 0.5 mm with adjunct nitrogen adsorption and MIP data.

The results show a complex pore micro-structure that varies significantly at different scales in the sample. Overall the sample shows a porosity of $0.67 \pm 0.009\%$ from the nano-CT data, $0.0235 \pm 0.003\%$ from nitrogen adsorption, and $0.60 \pm 0.07\%$ from MIP, which compare with $0.10 \pm 0.01\%$, $0.52 \pm 0.05\%$, $0.94 \pm 0.09\%$ from 3 FIB-SEM measurements and $0.06 \pm 0.008\%$ from μ -CT measurements. The data vary due to the different scales at which each technique interrogates the rock and whether the pores are openly accessible (especially in the case of the nitrogen adsorption value).

Likewise, the measured kerogen content of the rock varies. In this work the measured kerogen fraction is $32.4 \pm 1.45\%$, compared with $34.8 \pm 1.74\%$, $38.2 \pm 1.91\%$, $41.4 \pm 2.07\%$, and $44.5 \pm 2.22\%$ for 3 FIB-SEM measurements and a μ -CT measurement done on the same sample and as reported in earlier work (Chapter 4).

The Bowland shale sample shows pores at all scales. The pore size imaged by nano-CT ranged between 100 nm to 5000 nm, while the corresponding ranges were between 3 and 2000 nm for MIP analysis and between 2 nm to 90 nm for N₂ adsorption. The associated measured pore volumes ranged from $0.01 \mu\text{m}^3$ to $0.35 \mu\text{m}^3$ from the nano-CT data presented in this work. However, pore volumes as low as $10^{-5} \mu\text{m}^3$ have been measured for the same sample by FIB-SEM and as high as $31.5 \mu\text{m}^3$ for the same sample by μ -CT.

The aspect ratios indicate that most of the pores which contribute significantly to pore volume are oblate, i.e. flatter. In addition, the range scale-invariant pore surface area to volume ratio (σ) has been found to vary from 3 to 13 which also suggests that the pores imaged by the nano-CT method tend to be oblate. Oblate pores have greater potential for interacting with other pores compared to equant and needle-shaped prolate pores, as well optimising surface

area for gas to desorb from the kerogen into the pores. Therefore, the distribution of pore aspect ratio and scale-invariant pore surface area to volume ratio (σ) as well as the calculated permeability shows sample MD-2.7 in this work has a high shale gas potential.

Integrating 2D and 3D gas shale rock samples analysis provided in this chapter and in Chapter 4 along with Ultrahigh resolution 3D imaging and predicting gas transport based on imaging detailed in Chapter 6, provides a promising pathway towards understanding the internal microstructure as well as the level of the connectivity of pore and kerogen involved in transport in shale rock samples, and also towards more accurate modelling of hydrocarbon transport in a gas shale reservoir.

The results of this type of multi-scale imaging can be useful not only for shale gas but also for other many applications such as the study of reservoirs and cap-rocks for carbon sequestration, geothermal reservoirs and potential sites for the long-term disposal of radioactive material.

Chapter 6

**Ultrahigh resolution 3D imaging for quantifying
the pore nanostructure of shale and predicting
gas transport**

6.1 Introduction

Gas transport through shale is a very complex process, operating at multiple scales and often poorly understood. This is mainly because the sizes of pores and fractures in shales vary over many orders of magnitude; from only a few nano-meters to several tens of microns (Ambrose et al., 2010; Bai et al., 2013; Curtis et al., 2010). Thus, microstructure and pore systems cannot be imaged effectively using a single technique with a given resolution and field of view. Therefore, multi-scale imaging techniques are required to characterize the shale microstructure.

Previous work in Chapter 5 provided valuable insight into the petrophysical properties of Bowland gas shale formation by using high-resolution X-ray Nano-computed tomography (Nano-CT) with support measurements of low pressure (N₂) nitrogen adsorption and high pressure (MIP) mercury intrusion porosimetry on the same core plugs that were used for the two advanced imaging methods μ -CT and FIB-SEM methods for representing the whole shale rock sample. However-in this current chapter, the two high resolution 3D imaging techniques that have been Nano-CT and FIB-SEM are used to investigate the internal microstructure properties of a gas shale formation from Sweden including porosity, permeability, pore volume, surface area and size distribution on the same exactly a volume “region” of shale rock.

The results in this chapter provide a valuable information of understanding the microstructure properties of shale such as pore and kerogen distributions, and estimate their connectivity by using the two different high-resolution imaging techniques at smaller scale on the same micro volume of shale.

This chapter begins by presenting the preparation of rock sample in section 6.2. The results are then presented in section 6.3. To help understand the causes of the differences between methods, the two imaging techniques have been compared in term of the resolutions and fields of view in section 6.3.1. The numerical modelling along imaging result are also provided in section 6.4. Finally, the findings of these results are summarised in the conclusions section 6.6.

6.2 Material and methods

6.2.1 Rock samples and preparation

The gas shale samples used in this study were collected from a depth of 110 m in a gas shale formation in Sweden, the sample used has been coded as Gripen-7, for future information including location and well names, are provided in Table 3.1 (Chapter 3).

The two techniques have used are Nano-CT and FIB-SEM in this study, and the imaging has been possible with both techniques on the same sample with a characteristic size of 15-25

μm . High resolution imaging such as that have carried out in this study requires very small samples, in order to scan and mill the same region for both techniques, whose preparation is time-consuming and requires significant care. The higher the resolution required, the smaller the samples must be.

The samples are required to be suitably thin in order to produce high-quality images using Nano-CT and FIB-SEM. The mechanical crushing or laser milling of the samples does not produce samples of the correct size. Furthermore, it can cause damage to the pore network within samples. By contrast, ion milling technique can prepare very small samples with minimal damage to the pore-space, and is consequently ideal for the preparation of shale samples for high resolution 3D imaging (Akbarabadi et al., 2017).

In this study, small cubic core samples (25 μm side length) were prepared from reservoir rocks using a Focused-Ion Beam (FIB) milling technique. The preparation of such a sample were discussed in chapter 3 (section 3.2.2)

The pores inside the sample were first characterized using ultrahigh resolution image obtained at an initial state by non-destructive X-ray nano-tomography (Nano-CT), and afterward used the same location within the original sample volume for FIB-SEM higher resolution at the nanometric scale. The FIB-SEM imaging destroys the sample and therefore, this approach has a number of advantages. The first advantage is that FIB sample preparation allows the same sample to be imaged by two different high resolution techniques with minimal damage during preparation. This enable to understand which aspects of the measurements are native to the specimen and which are caused by preparation for all measurements, irrespective of scale, resolution and field of view. The second advantage is that the Nano-CT and FIB-SEM measurements can be made at exactly the same predetermined location in the sample, chosen to investigate a particular feature or to represent a typical location within the sample. The third advantage is that the characteristics of imaging a particular structure with each of the imaging techniques can be compared directly. Consequently, it is possible to distinguish between observations which are related to the imaging technique and those which arise from the sample itself. In the latter case, differences in the results of the two imaging techniques may be used to investigate the variability of heterogeneity and anisotropy of pore and kerogen distributions as a function of scale, and hence estimate their connectivity.

Figure 6.1 shows a comparison of the resolutions and dimensions of shale sample imaging used in this study by $\mu\text{-CT}$, Nano-CT and FIB-SEM techniques. These techniques have been shown to be powerful tools for resolving petrophysical issues, including the visualisation of fine microstructure (Ma et al., 2019), the quantification of the size, size distribution and morphology of the shale phases (mineral matrix, pores and organic matter), and the 3D connectivity of the shale components that ultimately controls the ability of the pore network to transport gas (Curtis et al., 2011; Long et al., 2009; Sakellariou et al., 2003), while Figure

6.2 shows shale rock sample of area of interest ($25 \times 25 \mu\text{m}^2$) for Nano-CT and FIB-SEM imaging.

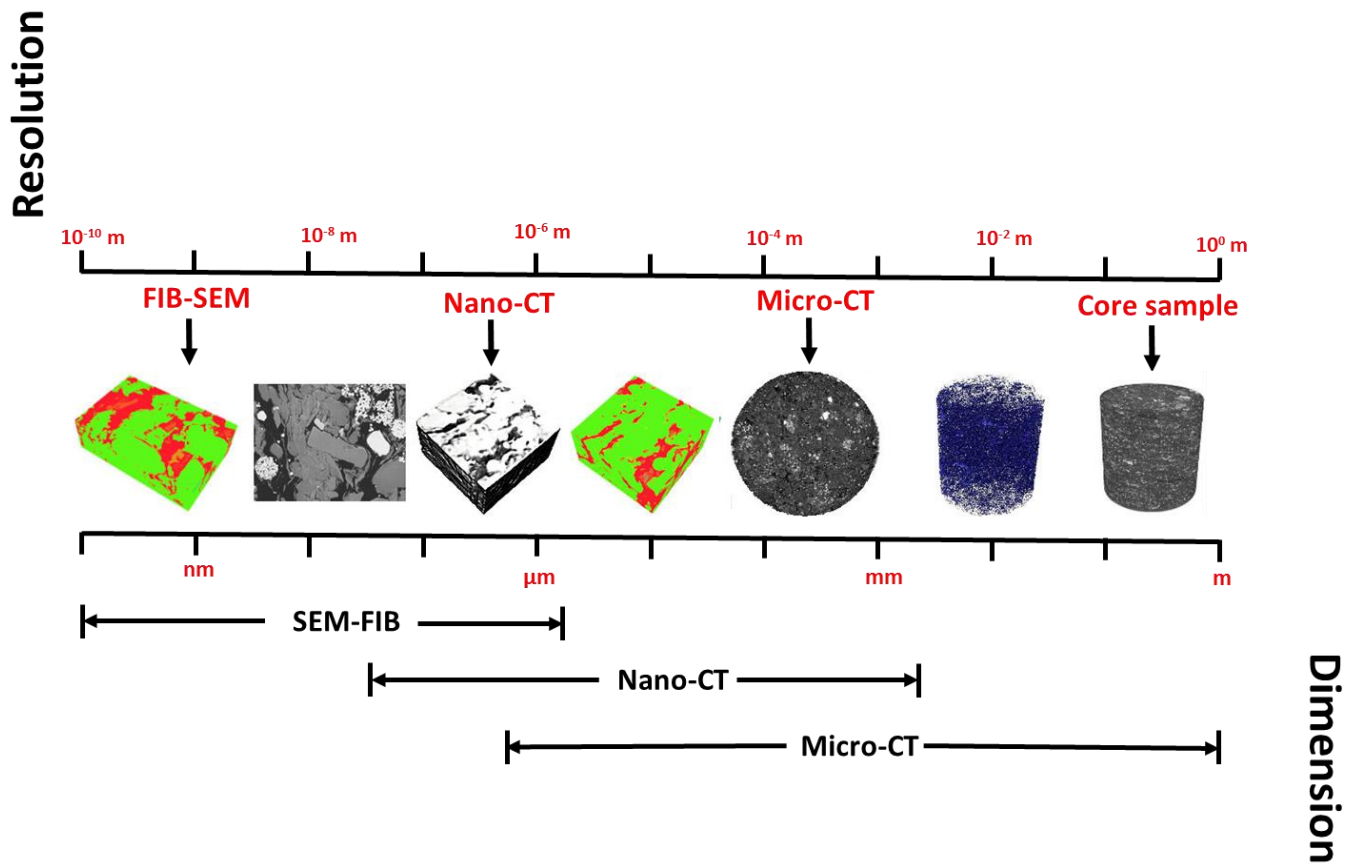


Figure 6 1. Multiscale imaging techniques (FIB-SEM, Nano-CT and μ -CT) used in this study

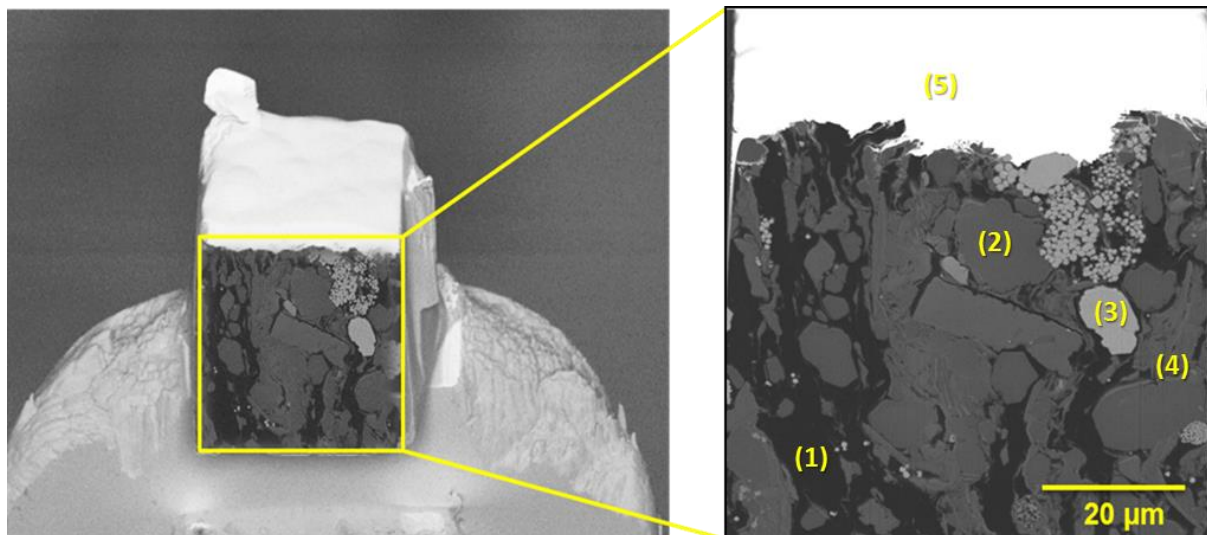


Figure 6 2. Shale rock sample of area of interest in this study for Nano-CT and FIB-SEM imaging. (1) Dark grey, kerogen; (2) medium grey, silicate matrix; (3) light grey, iron pyrites, often in framboidal form, (4) Pores (black) are too small to be seen at this resolution. The covering of the sample which appears white is the layer of Pt (5) that was initially deposited at the start of the sample preparation process

6.2.2 Experimental procedure

The Nano-CT instrument used in this study was the ZEISS Xradia 810 Ultra, at the University of Manchester. The instrument provides imaging pixel resolutions of 64 nm with 1601 projections, and the time exposure of each scan is about 90 sec. The further details on the settings and operations of X-ray nano-tomography are provided in Section 3.3.4.1.

The dual ion beam (FIB-SEM) system (FEI Helios G4 CX DualBeam) was also performance in this study to allow a sample to be cross-sectioned and imaged *in-situ* using 30 keV electrons. The resulting voxel size for this study is approximately $36 \times 45 \times 20 \text{ nm}^3$, with a typical imaged volume of $25 \times 25 \times 15 \text{ }\mu\text{m}^3$. Once agine for more details on the settings and principle of FIB-SEM as well as summary of the main characteristics for each technique, including the experimental parameters, imaging time, and resolution are presented in section 3.3.4.2 and 3.5, respectively in Chapter 3.

Figure 6.3 shows images of the shale sample visualised by each of the two methods on the same region.

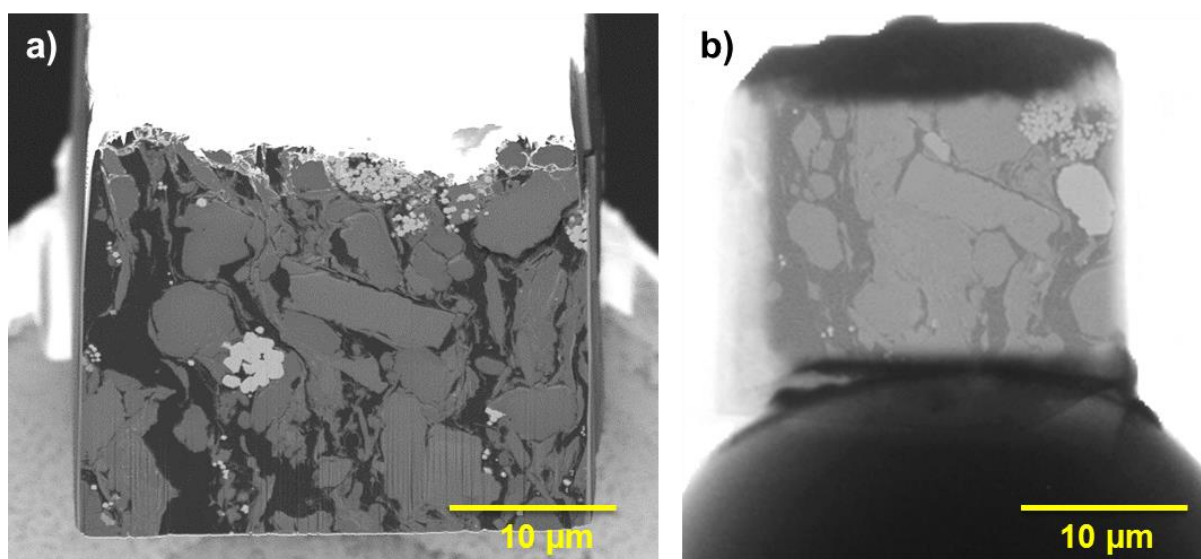


Figure 6.3. (a) Image of the sample using the FIB-SEM technique (face dimensions $25 \times 25 \text{ }\mu\text{m}^2$), (b) 3D image of the sample using Nano-CT scanning for the same shale sample.

The Energy dispersive spectroscopy (EDX) was also implemented in this study to investigate the elemental composition and mineralogy inside the shale sample.

Figure 6.4 shows an EDX mapping of the region of sample as shown being prepared in Figure 6.2 with individual distributions of the main elemental compositions; where (Si) is silicon, the

area shown in yellow is sulfur (S), the green is oxygen (O), carbon (C) is shown in red, and the pink is potassium (K). Close observation of the SEM/EDX images shows very small vertical stripes (Figure 6.3a and 4). This is an artefact known as curtaining which is caused by the ion beam during milling. Curtaining is a major problem when using a broad ion beam milling and is less apparent when milling with a focussed ion beam. Nevertheless, curtaining can affect elemental mapping, as seen particularly in the panel representing oxygen in Figure 6.4, as well as affecting the segmentation process and having some impact upon subsequent image analysis results.

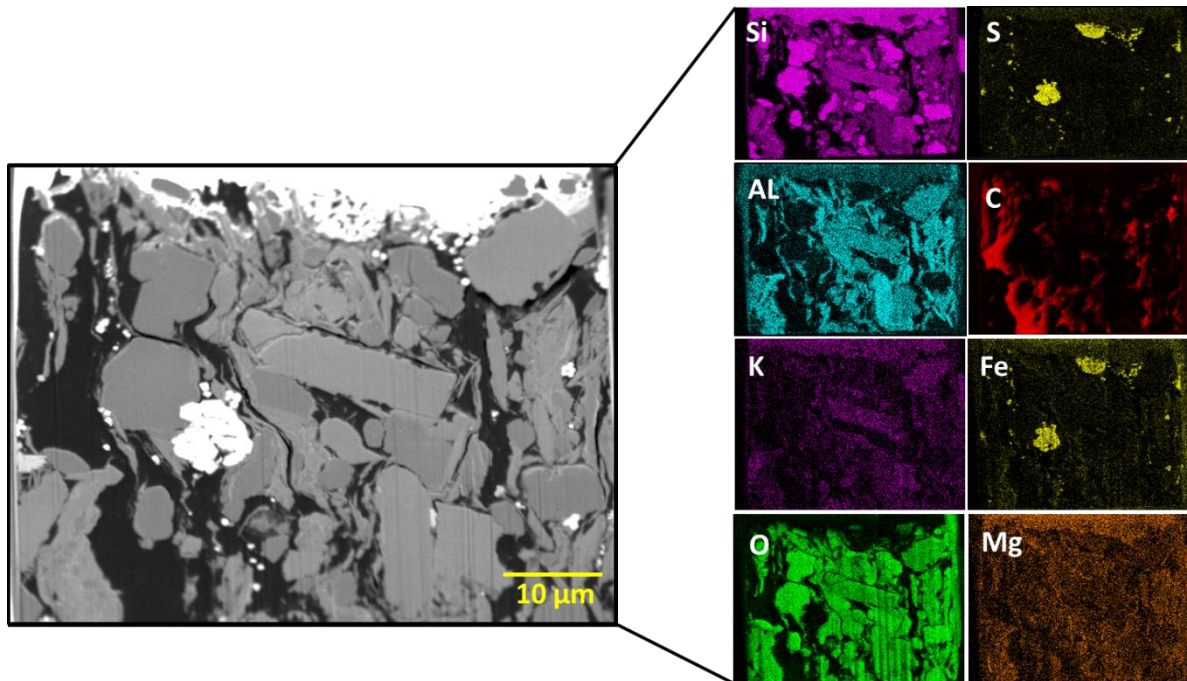


Figure 6.4. An EDX map of a cross-section of the shale sample have used in this study for elemental mapping, where the clastic matrix (high Si, Al, K, O) can be distinguished from the kerogen (high C), and the framboidal iron pyrites are clearly shown by their associated high sulphur (S) values

6.2.3 Supporting measurements

A number of different supporting measurements have been used on the same piece of rock that have used in the imaging technique.

Mercury intrusion porosimetry (MIP) was carried out on associated rock samples to provide independent values of pore throat size, pore size, grain size, pore volume and porosity, as well as capillary pressure (Busch et al., 2017). The porosity has been found to be 1.8 % \pm 0.09. This result was used as a comparison with porosities values obtained from imaging techniques that are presented in (Table 6.2). Further details such as samples preparation are provided in section 3.3.2.1 (Chapter 3).

The Gas Research Institute (GRI) method is another technique have used in this study for measuring porosity and permeability which also relies on gas pressure decay (gas expansion system), but in this case the sample is crushed (Cui et al., 2009; Zamirian et al., 2014). The experimental procedure on how the porosity and permeability were obtained from this measurement are presented separately in section 7.2.2 (Chapter 7).

6.3 Results

In this chapter the 3D reconstructions data were acquired by using Nano-CT and FIB-SEM techniques within an imaged volume of $25 \times 25 \times 25 \mu\text{m}^3$, which makes them very suitable for testing the limitations of Nano-CT and FIB-SEM with regard to shale properties. A wide range of microstructural parameters were calculated for both datasets and compared against each other, including porosity and permeability, together with pore and pore throat size distributions, two aspect ratios and scale-independent surface area to volume ratios. Table 6.1 shows a brief summary of the most important of these results.

Table 6 1 Comparison between the two imaging techniques of the main parameters measured in this paper.

Sample	Technique	Voxel size (nm ³)	Sample Size (μm)	Measured Porosity (%)	Measured Kerogen (%)	MIP Porosity (%)
Gripen-7	Nano-CT	64×64×64	25×25×25	0.43±0.04	19.6±0.8	1.8±0.09
	FIB-SEM	36×45×20	25×25×15	0.70±0.07	26.0±1.3	

6.3.1 Comparison of 3D microstructure of gas shale volumes

A comparison of three-dimensional microstructure sub-volumes of the shale rock sample has been performed based on the Nano-CT and FIB-SEM images of sections through the sample (Figures 6.5 and 6). In both cases, the analysis was carried out with voxels representing the corresponding resolution. The FIB-SEM dataset is smaller than a Nano-CT volume in terms of pixels because only that 15 μm of the 25 μm available in the z-direction was accessed by the 750 slices (see Table 3.2 in Chapter 3)

Figures 6.5 and 6 show 3D images obtained from Nano-CT and FIB-SEM with important parameters relevant to gas transport such as pore, kerogen, and matrix phase fractions. By using the 3D grayscale of the raw data of these two techniques, threshold values can then be set to define microstructural features of interest, particularly the pores, kerogen and other minerals (the lighter equant patches are framboidal pyrites). Surfaces can then be generated around these regions within the thresholds. Figures 6.5b and 6.6b show images of the 3D reconstructions of the solid material for Nano-CT and FIB-SEM. After this has been accomplished, it can be able to separate the material based on grayscale values.

Figures 6.5c-e and 6.6c-e show the 3D images of the pores, kerogen and other minerals, respectively. Based on this thresholding process, a qualitative inspection of the connectivity of the networks can be performed. It has been observed that the FIB-SEM presents a higher value for pores and kerogen than the Nano-CT, and also there is a higher degree of pore and kerogen connectivity across the volume (*cf.* Figure 6.5c-d and Figure 6.6c-d).

In addition to the qualitative analysis of the 3D microstructure, quantitative estimates of the percentage volume of these features have been performed. The estimates obtained, by percentage volume of pores, kerogen and minerals in the reconstructions are 0.43%, 19.60% and 79.97% for Nano-CT, and 0.70%, 26.00% and 73.30% for FIB-SEM respectively.

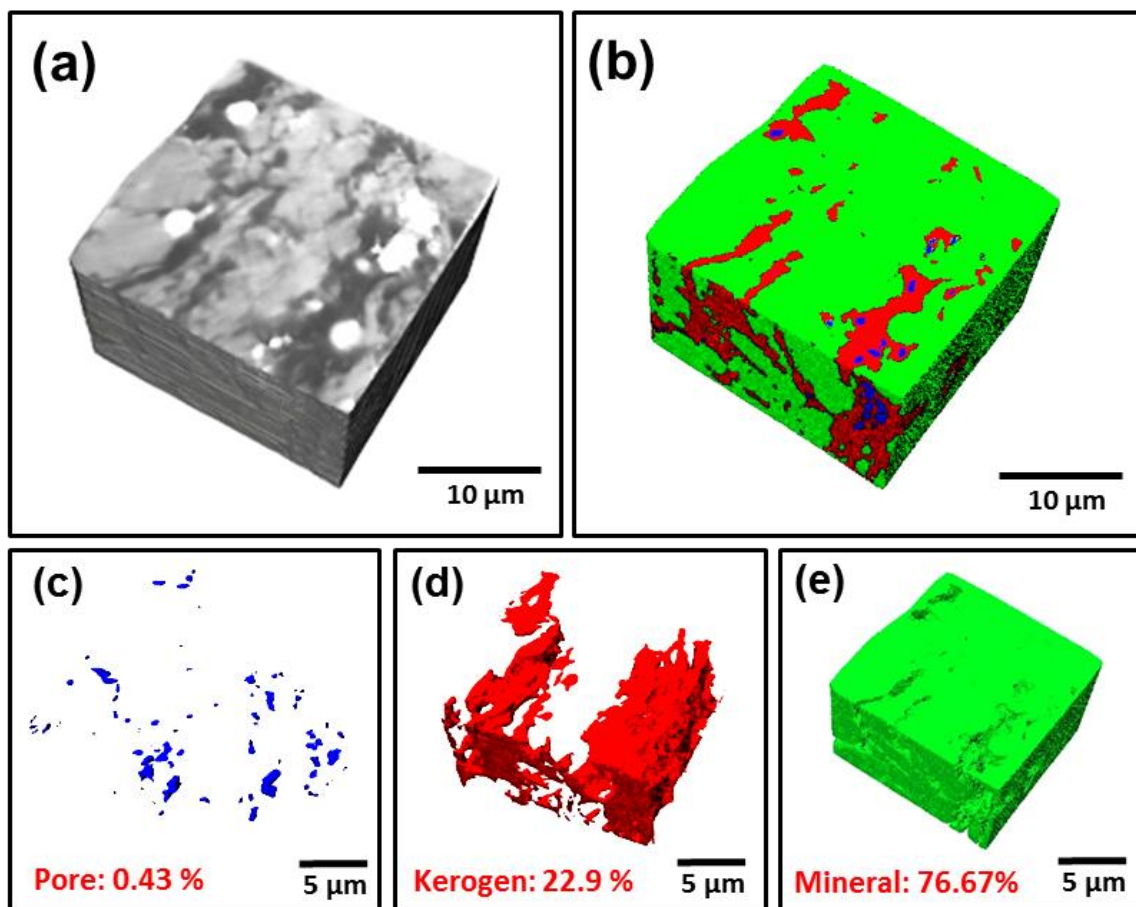


Figure 6 5. Nano-X-Ray Tomography (Nano-CT) for a shale rock sample with an acquired resolution of 64 nm. (a) Raw 3D grayscale image, (b) representative 3D image of all phases in the sample, (c) imaged pores, (d) imaged kerogen, and (e) solid minerals.

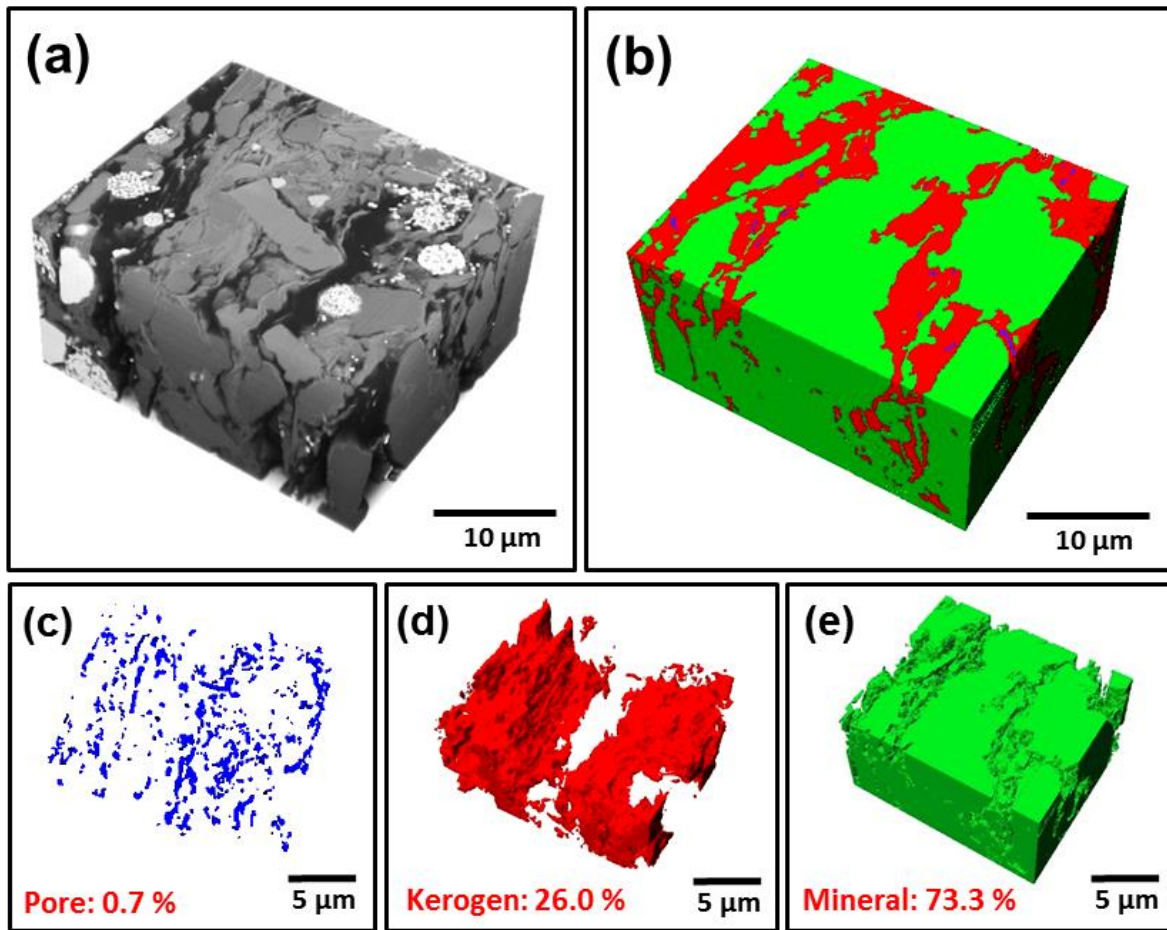


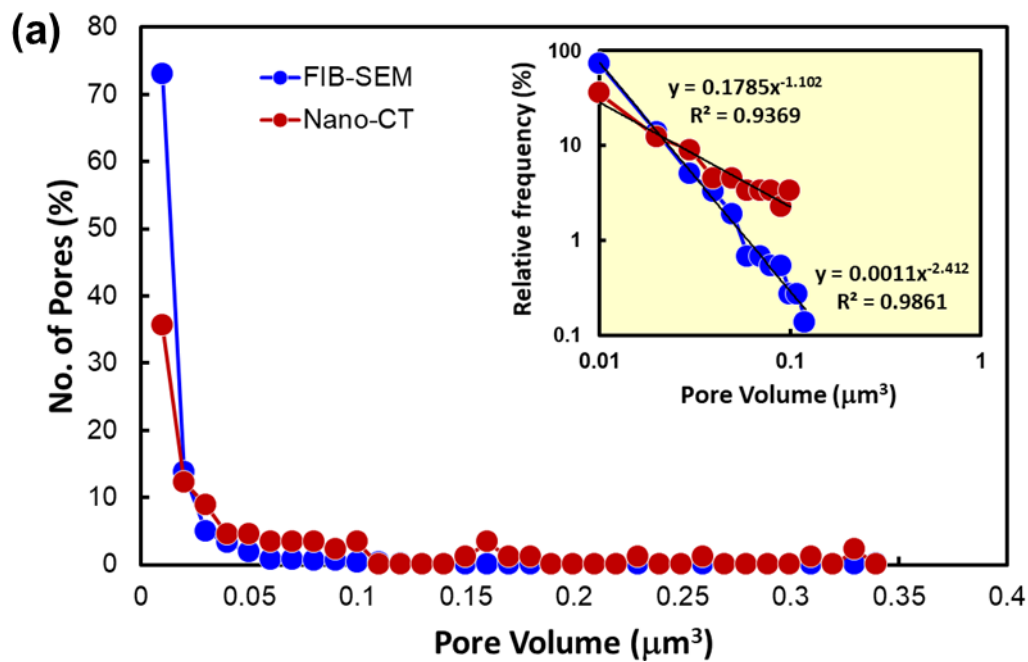
Figure 6.6. FIB-SEM for a shale rock sample shown with an acquired resolution of 20 nm. (a) Raw 3D grayscale image, (b) representative 3D image of all phases in the sample, (c) imaged pores, (d) imaged kerogen, and (e) solid minerals.

The use of the two high resolution 3D imaging methods on the same 25 μm -sided cubic volume of rock in this work have allowed to compare the capability of the two methods in a manner which is not possible for previous studies where the measurements are made on different volumes. [Figure 6.5a](#) and [Figure 6.6a](#) provide 3D images of the same sample volume from the two techniques. The FIB-SEM measurements benefit clearly from their slightly better resolution, giving a sharper and better contrast of the resulting images. The higher resolution of the FIB-SEM technique has resulted in significantly higher measurements of porosity and slightly higher values of kerogen fraction. The larger effect on the estimation of porosity arises because the majority of the porosity is composed of a myriad of pores occurring at the limits of resolution of the two techniques. In this case, a slightly better resolution of the FIB-SEM method allows the imaging of many small pores which were just too small to be imaged by the Nano-CT resolution. This is most clearly observed by comparing the size and number of imaged pores for each technique in [Figure 6.5c](#) and [Figure 6.6c](#).

6.3.2 Pore volume and size distribution

The segmented 3D data image analysis were used to obtain porosity, the relative frequency distribution of the pore volume, size, pore aspect ratios and the scale-independent pore surface area to volume ratio. These parameters were compared for both methods and for the same volume of sample.

Figure 6.7 shows the pore-volume distribution as measured by each of the techniques. The two techniques show remarkably similar results, with the majority of the pores having pore volumes less than $0.05 \mu\text{m}^3$. However the Nano-CT technique images have fewer of the smallest pores as a result of its lower resolution than FIB-SEM. These results suggest that the Nano-CT and FIB-SEM results are not very different in terms of the pore volume, and they both recognise the prevalence of nanoscale pores in this shale sample. However, the higher resolution of the FIB-SEM allows more of the very small pores which are too small for the Nano-CT technique to be taken into account.



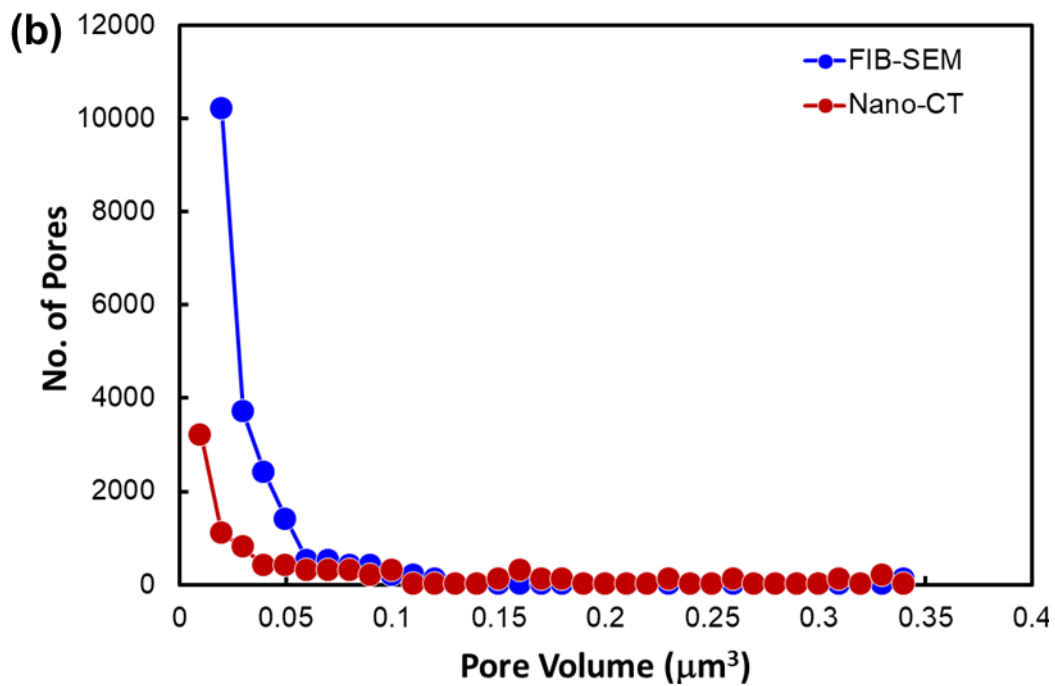


Figure 6.7. (a) presenting of number pore volume distribution, and (b) the number of pore volume distribution that calculated from the Nano-CT (red) and FIB-SEM (blue) 3D imaging datasets for the same measured volume of gas shale sample using 3D image analysis implemented in Avizo® Fire 9.40 software. The inset in (a) shows the low pore volume data on an expanded scale.

The log scale data also shown in [Figure 6.7](#) show well developed negative linear trends, which fits the power law distributions $y=0.0011x^{-2.41}$ and $y=0.1785x^{-1.102}$ and R^2 values of 0.9861 and 0.9369, for FIB-SEM and Nano-CT, respectively. In both techniques the fit was based on those data in the set which ranged from the lowest pore volume not affected by resolution thresholding to that just above the first 0% relative frequency in order that the power law fit could be carried out. Consequently, in this way, it can be able to infer that there may exist a large number of pores smaller than the resolution of the technique.

[Figure 6.8](#) shows a comparison of the pore size distribution obtained using the MIP, FIB-SEM and Nano-CT methods. In terms of the distribution by pore count ([Figure 6.8a](#)), the FIB-SEM provides slightly lower values of equivalent pore diameter (approximately 100-500 nm), while the distribution for the Nano-CT method shown a lower value at 100 nm with peaks at 300 nm, and it is expected that the decrease for smaller values is related to the resolution of the Nano-CT measurement. If the distribution is plotted on the basis of the pore volume represented by each equivalent pore size bin, a different distribution might be obtained than when using other methods. For the Nano-CT data, it is clear that the very few pores with equivalent pore volumes greater than 1000 nm (1 μm) according to [Figure 6.8a](#) have a disproportionate significance in terms of pore volume (*cf.* [Figure 6.8b](#)).

Mercury injection porosimetry was also carried out on a sample of rock taken from close to where the imaging samples were taken in the same core plug. The MIP data does not provide data by individual pore count, but by intruded volume, and consequently, is given only in [Figure 6.8b](#). The range of values for pore size from MIP is 3 nm to 700 nm. The MIP measurements indicate that it is possible, and indeed likely, that there exist pores of dimensions lower than those measured due to the limitations of the resolution. However, other techniques with higher resolution exist and able to resolve pores at 2 nm, such as (N₂/CO₂ adsorption) ([Washburn et al., 2015](#); [Wang et al., 2017](#); [Seaton et al., 1989](#)). Such measurements have been already discussed in Chapter 5.

The mercury intrusion (MIP) approach measures pore volume at a given pressure corresponding to the pore throats permeable to mercury at this pressure and which are connected to the mercury percolation cluster. Consequently, unlike the imaging data, the *x*-axis MIP data must be interpreted as the diameter at which mercury passes through small pore throats to fill larger pores, while the *y*-axis value represents the volume of those larger pores filled through the small pore throats. Hence the apparent large volume of very small pores shown by the MIP technique in [Figure 6.8b](#) is not likely to be the case in reality, with the volumes shown being present in larger pores that can only be accessed by the mercury through smaller pore throats. The interpretation of the MIP should also be carried out with due regard to the compaction and fracturing problems associated with using the MIP technique on shale rocks that were mentioned earlier.

Furthermore, the pore diameter from MIP refers only to the connected pores, this is because mercury is introduced to the pore spaces through connected paths under increasing pressures up to 60,000 psi corresponding to a pore throat of 3 nm ([Figure 6.8](#)). Consequently, the pore size distribution and porosity measured by MIP on the bulk rock sample is restricted to accessible or connected pore spaces. By contrast, both imaging methods include both connected and isolated pores.

For the purposes of [Figure 6.8](#), the pore size for the imaging methods (Nano-CT and FIB-SEM) is the equivalent pore diameter d_{Eq} , which was taken to be the diameter of a sphere with the same pore volume, hence ([Jennings et al., 1988](#)):

$$d_{Eq} = \left(\frac{6V}{\pi}\right)^{1/3} \quad (6.1)$$

Results given later in this study and in other studies indicate that the assumption of spherical pores for the great majority of pores in shales is incorrect, but it has given here as a reference point. Since most pores in shales are oblate, it is misleading to use a single pore diameter.

Different scales techniques available for pore diameter and the characteristics of the shale rock resulting distributions have been used previously in the literature (e.g., [Ma et al., 2016](#), [Peng et al., 2012](#), [Yang and Bao, 2017](#)). Each of these have their own advantages as well as limitations.

Porosities of 0.43% and 0.7% were obtained from the Nano-CT and the FIB-SEM approaches, respectively (Table 6.2). The two measurements are made on exactly the same volume of sample. The MIP measurement was made on a sample that was cut from the same shale core and gave a porosity of 1.8%. The difference in the results may be caused by a number of effects. The small disparity between the two imaging approaches probably arises from the FIB-SEM's higher resolution taking account of a large number of small pores which are below the resolution of the nano-CT approach. The larger difference between the imaging and MIP porosities may be caused by (i) the different resolution within measurements naturally having a different porosity, such as the MIP resolution can only resolved smaller pore at approximately (3.6 nm), thus will give a larger porosity (Busch et al., 2017).(ii) the sample preparation and measurement of the MIP technique inducing porosity in the samples in the form of micro-fractures, and (iii) the larger sample size of the MIP sample (approximately 5 mm in each dimension, compared to 25 μm for the imaging techniques) allowing a small number of large pore to skew the porosity measurement, either erroneously or by including representative pores which the small 3D fields of view of the imaging techniques take no account of. It should also be remembered that the MIP approach only measures connected porosity, while the imaging techniques measure all porosity (within resolution limits). It should note, sometimes the pore connectivity is overestimated by the 3D imaging methods because at the limits of their resolution they may consider a number of disconnected smaller pores as one larger pore (Ewing and Horton., 2002).

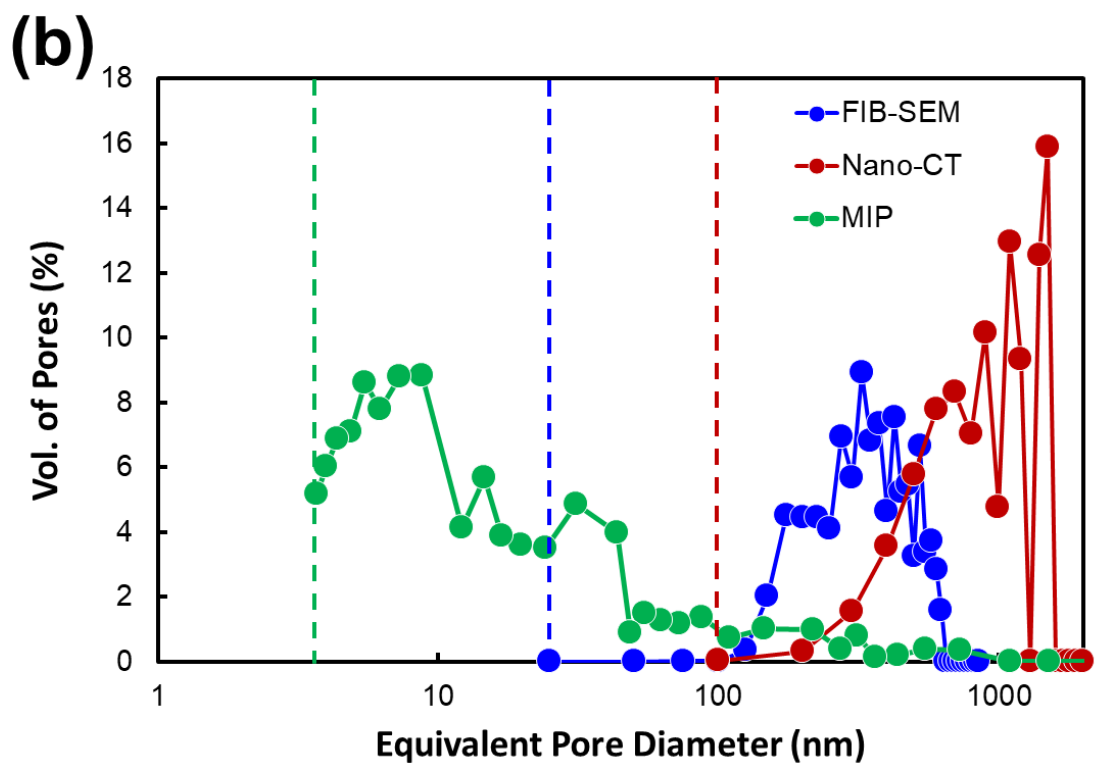
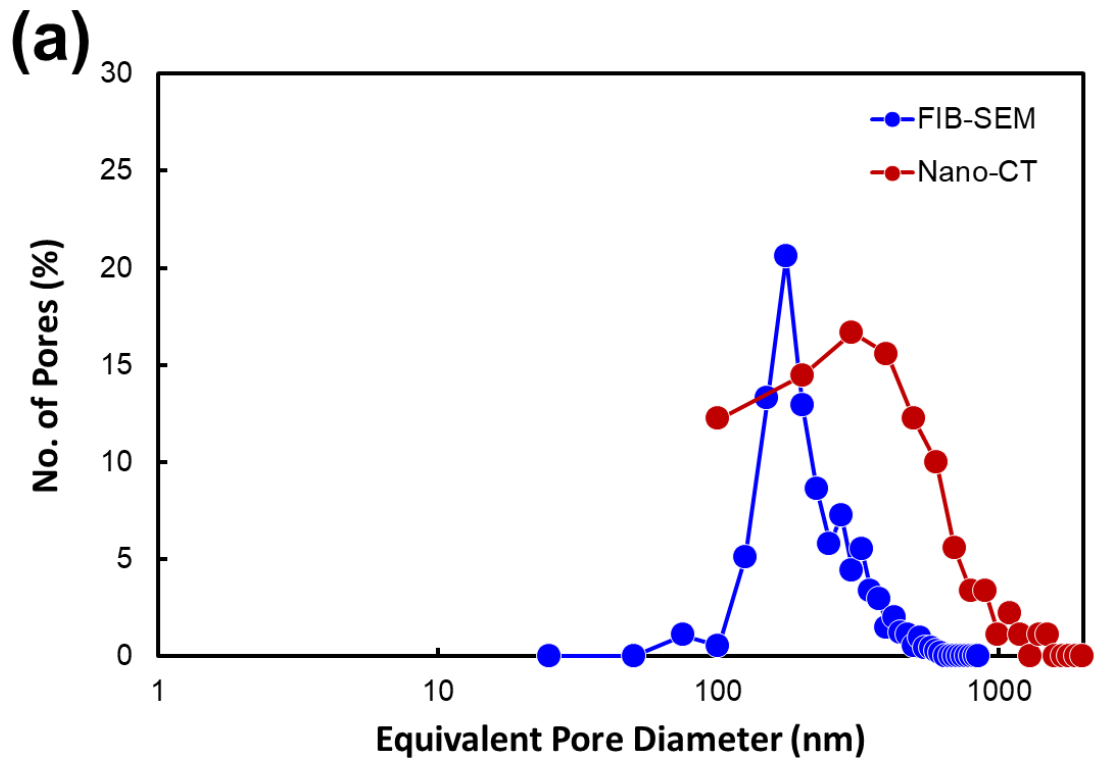


Figure 6 8(a) Pore number, and (b) pore volume distributions of the equivalent pore size estimated from the Nano-CT (red) and the FIB-SEM (blue) 3D imaging datasets for the same measured volume of gas shale sample. The MIP measurements (green) were made on a sample from the same core plug. Dashed lines show native resolution limits for each technique.

6.3.3 Pore aspect ratio distributions

Aspect ratios are measures of the shape of a pore by comparing two characteristic dimensions, often the largest to the smallest, such as the length of a crack to its aperture as mentioned in earlier study.

In this study, the two pore aspect ratios have chosen to use as following as: The first is given by $S = c/b$ (Figure 6.9a-b), where b is the maximum dimension of the pore, and c is the minimum dimension of the pore. The second aspect ratio is given by $L = a/c$ (Figure 6.9c-d), where a is the half-length of the pore mutually perpendicular to both b and c .

The pore aspect ratios are measures of the shape of the pore. If the pore is equant (approaching spherical) then $S \approx L \approx 1$. If the pore is penny-shaped (flattening or elongation), then $S \ll 1$ and $L > 1$. If the pore is pin-shaped (prolate), then $S \ll 1$ and $L \approx 1$. The value of both pore aspect ratios is important because pores which are long and thin ($S \ll 1$) or have a significant sideways extent ($L \neq 1$) have a greater potential for connecting up with other pores, contributing to raising the chances that the pore structure forms an interconnected network which will support gas flow.

Figure 6.9 shows the distribution of the number and volume of pores as a function of the pore aspect ratios, for all data estimated from both the FIB-SEM and Nano-CT methods. It is clear that both aspect ratios differ from unity, indicating that all pores measured by both imaging methods are significantly non-spherical, but better resemble oblate (penny shaped) pores.

Parts (a) and (b) of Figure 6.9 show the S aspect ratio distribution in terms of number and volume, respectively. In both of these a value approaching unity indicates a more equant pore shape. The range of S obtained from nano-scale pores measured by the FIB-SEM method are between 0.025 to 0.65 (Figure 6.9a). By contrast, the range of values of S obtained from the Nano-CT technique are between 0.025 to 0.7. There is remarkable similarity in the range of S aspect ratios given that the data from which they are derived were measured by very different techniques. However, the fine structure in the two distributions is different, with major peaks in the Nano-CT occurring at 0.26 ± 0.08 and 0.4 ± 0.05 , while the minor peak in the FIB-SEM results occurs at 0.3 ± 0.04 . Importantly, however, all of these values are significantly less than unity, with the lowest values (0.025) indicating that the pores are up to 40 times longer than they are wide (Figure 6.9a).

While Figure 6.9a indicates the pore number distribution of the S aspect ratio concerned, transport through pores may be more sensitive to the volume of each of the pores rather than their number. In other words, a large number of pores of a given aspect ratio may be inconsequential compared to a smaller number of pores with a larger volume. Figure 6.9b shows the pore volume distribution of the S aspect ratio. The pore volume is distributed in pores which have S pore aspect ratios for each technique, with peaks at 0.25 ± 0.08 and 0.1 ± 0.05 for Nano-CT and FIB-SEM, respectively. This indicates that the most significant proportion of the pore volume occurs in the shape of pores which are about 4 or 10 times

longer than their aperture according to the measurement method. The FIB-SEM data has a tendency towards the smaller values because it has the extra resolution that allows it to resolve pores which are very thin and which will be more likely to have very small S aspect ratio, compared to the nano-CT method, which would miss these pores.

Comparing parts (a) and (b) of [Figure 6.9](#), it can be seen that the same value of the aspect ratio (say, 0.25) can have very different percentage number of pore and percentage pore volume. For example, according to the Nano-CT measurements, for $S = 0.25$, 10% of the pores by number represents about 24% of pore volume, indicating that, on average, pores with this value of S are larger, while for $S = 0.4$, 13.5% of the pores by number represents about 5% of pore volume, indicating that pores with this value of S are smaller.

[Figure 6.9c](#) shows the pore number distribution of L aspect ratio values acquired from the FIB-SEM and Nano-CT methods. The range value of L obtained from FIB-SEM data lies between 1 to 2, while, the range of values of L obtained from the Nano-CT technique is similar, lying mainly in the range 1 to 1.9. Importantly, however, the both data sets clearly show that the value of the L aspect ratio is only slightly greater than unity, indicating that the pores are mostly needle-shaped. The pore volume distribution of L aspect ratio values ([Figure 6.9d](#)) shows a similar distribution for that of pore number, indicating that both the number and volume of the majority of pores has its two shorter axes about equal, with their form approximating to a needle-shape.

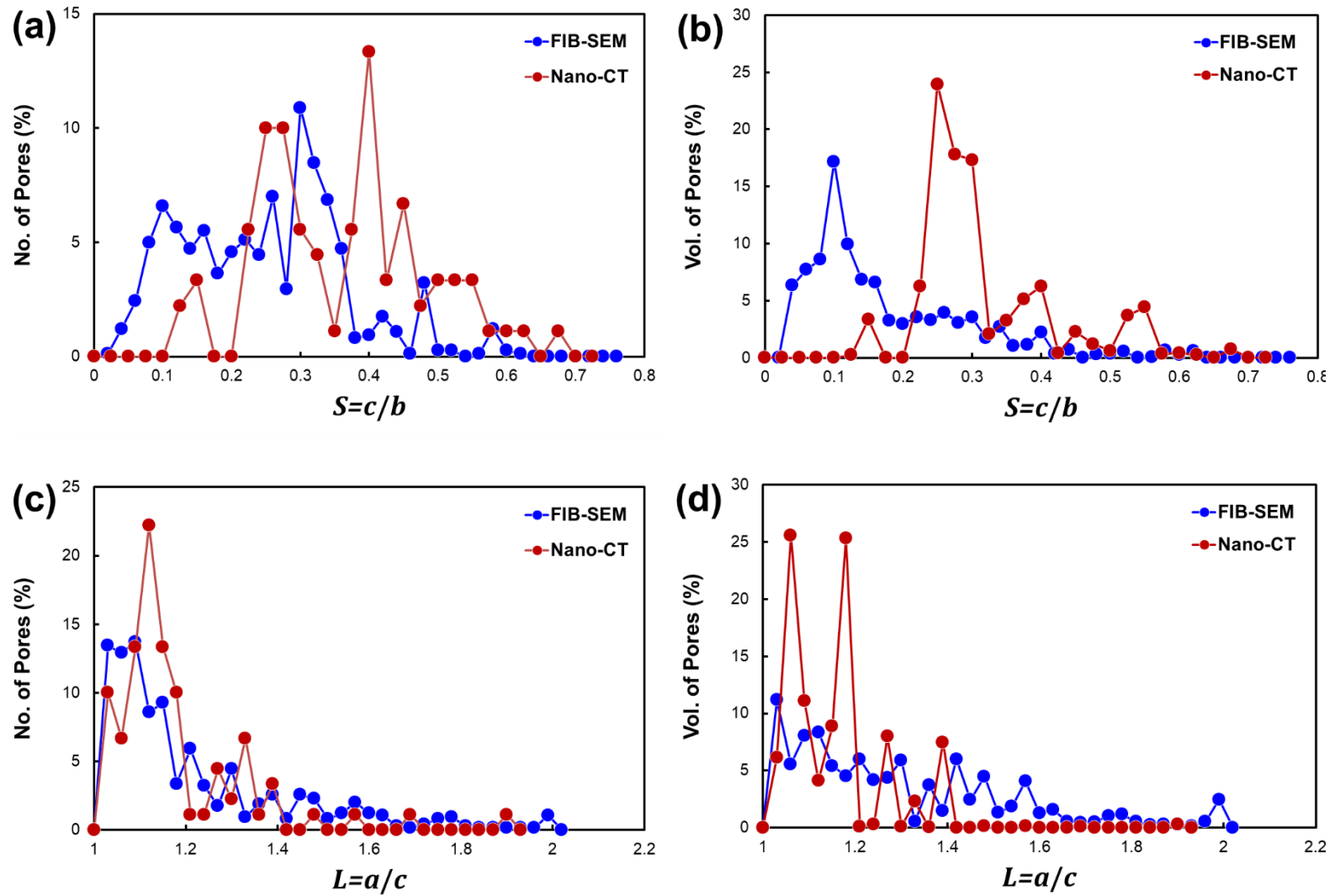


Figure 6 9 the pore-aspect ratio distribution, plotting the overall number of pores expressed as a percentage of the total number of pores in the sample for (a) the S aspect ratio, and (c) the L aspect ratio. The pore aspect ratio as a function of total volume of pores for (b) the S aspect ratio, and (d) the L aspect ratio. In each case data is derived from 3D imaging of the same volume of gas shale sample using both FIB-SEM and Nano-CT techniques.

6.3.4 Pore surface area to volume ratio

The pore surface area to volume ratio ξ is another important parameter for defining the shape of the pore. The way in which pore surface area to volume ratio and scale-invariant surface area to volume ratio have been described earlier in section 3.7.3 Chapter 3.

Figure 6.10 shows the distributions of the percentage number and volume of pores as a function of σ , measured by both Nano-CT and FIB-SEM techniques. Considering the pore number distribution (Figure 6.10a), it should be noted that the values obtained from both Nano-CT and FIB-SEM measurements are always greater than 3, as demanded by the mathematical model. However, there are peaks in both distributions close to 3, indicating that many pores approach sphericity. Thus, the data for both techniques there are a significant number of pores which show σ values up to about 10, gradually decreasing for the FIB-SEM data and clustered at about $\sigma=6.0\pm 1.5$ for the Nano-CT data. These values indicate that there is a tendency away from sphericity for many of the pores in a manner that is consistent with parts (a) and (c) of Figure 6.9.

Considering the pore volume distribution (Figure 6.10b), the signal for values as σ approaches 3 is much increased for the FIB-SEM data and almost to zero for the Nano-CT data, consistent with previous hypothesis. For this figure, the peak in the pore volume occurs at 4.0 ± 1.6 and 7.5 ± 2.0 for the FIB-SEM and Nano-CT data, respectively. This indicates that the pores which contribute more to the pore volume tend to be those that diverge more from sphericity (and using the aspect ratio data are known to be needle-shaped).

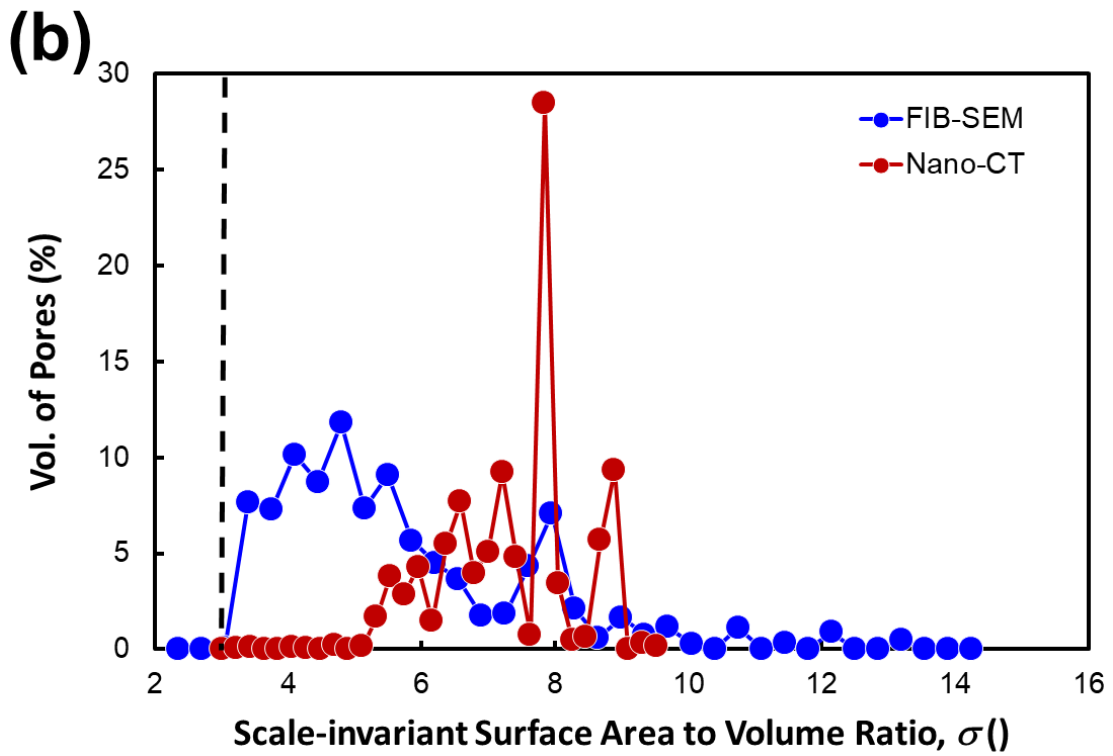
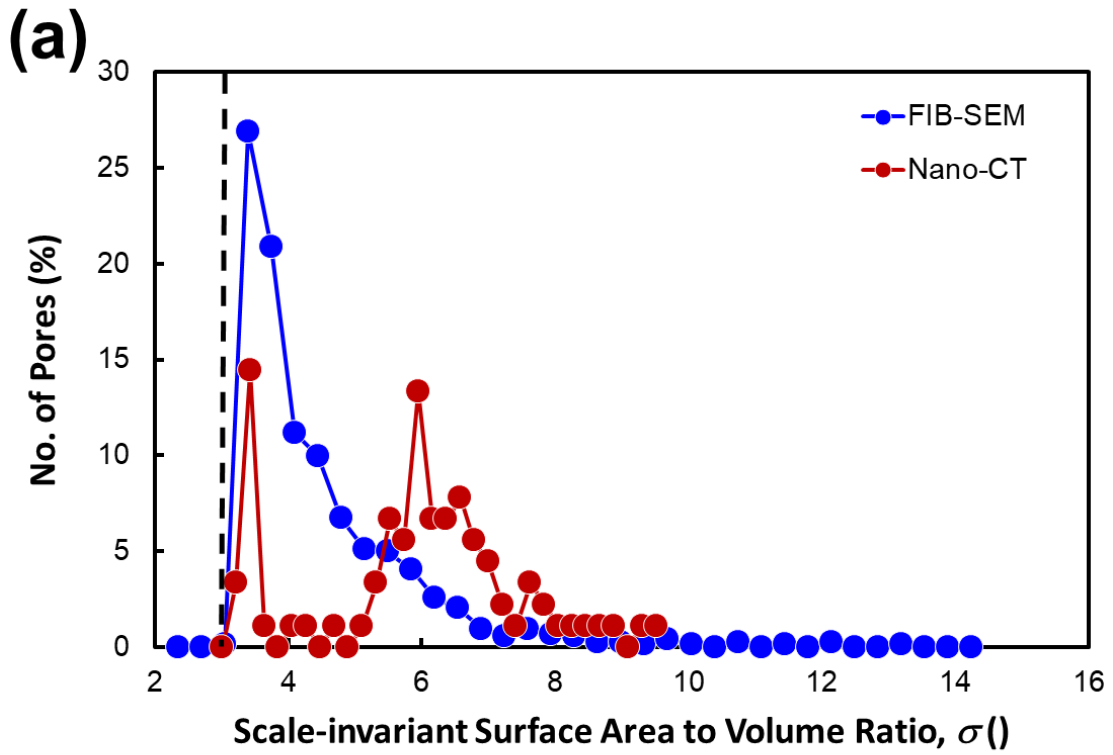


Figure 6 10. The scale-invariant pore surface area to volume σ distributions with respect to (a) percentage number of pores and (b) percentage pore volume, each calculated from 3D imaging of the same volume of gas shale sample using both FIB-SEM and Nano-CT techniques.

6.4 Gas Transport Simulation in Kerogen

Gas transport through shale reservoirs is very complex due to (i) the very small size of pores, (ii) the limited connectivity of pores, and (iii) the presence of multiple physical and chemical processes which both aid and hinder gas transport and which occur at different scales (Washburn et al., 2015). In order to describe the gas transport simulation in the shale, a simulation must be provided with at least one connected path across the whole area of interest.

In this study, the pores were unconnected and therefore the flow through the kerogen have been simulated using approach of (Gilbert Scott, 2020) as well as the pore system.

As connectivity was found within the kerogen network in the image sets, the volumes of interest with a local connected system were selected (Figure 6.9d and 6.10d) for simulation and comparison. Experimental data for associated samples of this rock indicates that the shale does have a measurable permeability at a larger scale and therefore selecting a sub-sample to calculate the permeability is a reasonable approach although it does reduce the representativeness of the results. The results for the permeability along the x -, y - and z -axis respectively are presented in Table 6.2.

Figure 6.11a shows the FIB-SEM images which have been used in this study for simulation within the kerogen as can be seen, while Figure 6.11b shows a diagram of gas molecules (yellow spots) flow through the kerogen.

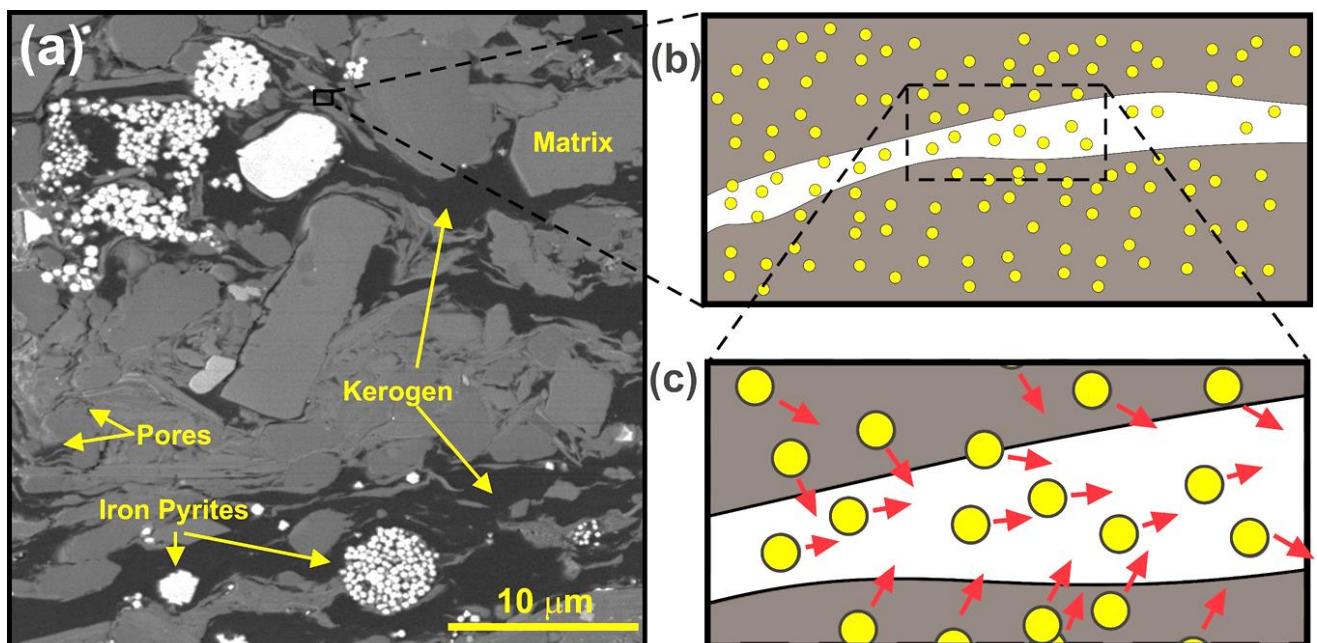


Figure 6.11. (a) FIB-SEM image revealing kerogen (darkest areas) with some of pyrite (lightest areas) in a matrix of medium greys with a few small pores (black), (b) Gas flow in the kerogen (textured brown), the yellow dots represent gas molecules which can flow and accumulate within the kerogen, and the white areas represent pores.

The segmented volumes from the Nano-CT and FIB-SEM images were used to calculate the permeability of the shale using a pore-scale finite volume solver that combines Darcy flow and Stokes flow into a single elliptic flow equation (Chung et al., 2019). This method is an extension of flow-based permeability upscaling (Begg et al., 1985, and 1989) to include pore space explicitly.

The imaging data in this work have been tested by Dr Gilbert Scott using his reported approach (Gilbert Scott, 2020). The imaging data combined with the modelling results from Scott has enabled to describe the gas transport within the shale sample.

For simplicity the single phase incompressible laminar flow (Peng et al., 2015) and the flow to be purely advective have been assumed in this work (Zhang et al., 2012). It can be recognised that this is a gross oversimplification of the physical processes, but the limitations caused by the software that have used and the availability of the data have makes it necessary.

The impacts of gas slippage (Klinkenberg effect) has been ignored in this work which mean that the free path of molecules are comparable with the channel dimension and thus, it can be estimating the high pressure or liquid permeability (Akkutlu et al., 2012). The effects of gas slippage typically increase the permeability at low pressures. However, the effect of absorbed gas molecules on the surfaces of pore has also been ignored which is known to decrease shale permeability at high pressure (Akkutlu et al., 2012)

Each voxel is assigned an effective conductivity, g , which relates the volumetric flow rate, \vec{q} , to the pressure gradient:

$$\vec{q} = -g\nabla P. \quad (6.3)$$

Mineral voxels are assumed to be non-conducting. Kerogen voxels use equation 6.4 to estimate the connectivity within Kerogen and pore voxels utilise Stokes flow using a Finite-Difference Geometrical Pore Approximation (FDGPA) method (Shabro et al., 2012). In the FDGPA method, the connectivity of each pore voxel is a function of two variables: the Euclidean distance of the voxel to the pore wall, d , and the local maximum of the Euclidean distance, d_{max} . The connectivity of kerogen and pore voxels are calculated as follows (Ajiz and Jennings, 1984):

$$g = \begin{cases} \frac{kA}{\mu}, & \text{in kerogen voxels} \\ \frac{A}{8\mu}(2dd_{max} - d^2), & \text{in pore voxels} \end{cases}, \quad (6.4)$$

Where μ is the fluid viscosity and A is the cross-sectional area of the voxel perpendicular to the direction of flow and k is the kerogen permeability.

For the kerogen, a constant effective permeability k of 2.55 nD and 9.92 nD was obtained from the Nano-CT and FIB-SEM data, respectively. These values were estimated from the equation: (Johnson et al., 1986; Glover and Walker., 2009).

$$k = \Lambda^2/8F, \quad (6.5)$$

Where Λ is a value measure of the aperture for fluid flow which controls the permeability in the sample, and F is the formation factor of the rock (Glover and Walker, 2009)

The value of Λ was obtained from the surface area to volume ratio of the kerogen following the approach of Johnson et al (Johnson et al., 1986), where,

$$\Lambda = S_p/V_p, \quad (6.6)$$

The formation factor of the rock was not measured directly in this study. However, the way in which calculated have described in earlier Chapter (3, section 3.6.5 .1).

The estimated shale permeability in x , y and z directions from simulation (Figure 6.12) for Nano-CT and FIB-SEM images is given in Table 6.2.

The FDGPA method essentially uses an analytical solution of the Stokes equation which is exact for cylindrical pore throats but is less accurate for pores with highly elongated cross-sections (Shabro et al., 2012). In this study, the fraction of pore voxels is small and therefore the overall error due to the approximation in the FDGPA method should be small.

The conservation of mass can be expressed as

$$\nabla \cdot \vec{q} = 0, \quad (6.7)$$

Which leads to a generalised Laplace equation,

$$\nabla \cdot (g\nabla P) = 0. \quad (6.8)$$

Two opposite faces of the model are designated; the inlet and outlet, with arbitrary constant pressures differing by ΔP . The other four faces of the model are no-flow boundaries. The generalised Laplace equation is discretised in the voxel model using a two-point flux approximation leading to a system of simultaneous linear equations where the unknowns are pressures in each voxel. Mineral voxels are removed from the calculation (since they are assumed to be non-conducting) and the system of equations obtained is solved using a conjugate gradient algorithm with an incomplete Cholesky factorisation pre-conditioner (Akkutlu et al., 2012). The total inlet (or outlet) flux, Q_T , is calculated and the permeability follows from Darcy's law,

$$k = \frac{Q_T \mu L_T}{A_T \Delta P} \quad (6.9)$$

Where L_T is the length of the model in the direction of flow and A_T is the cross-sectional area of the model perpendicular to the direction of flow.

The permeability was measured in the laboratory on an associated sample using the GRI method, and the experimental procedure on how the permeability obtained from this measurement are presented separately in section 7.2.2 (Chapter 7).

Table 6 2 The calculated permeabilities in the x , y and z directions obtained from simulation for Nano-CT and FIB-SEM and measured in the laboratory.

Flow directions	Permeability from flow simulations		Permeability calculated with Eq. (6.5)		Permeability measured in the laboratory
	Nano-CT	FIB-SEM	Nano-CT	FIB-SEM	
	k (nD)	k (nD)	k (nD)	k (nD)	k (nD)
x -axis	0.003	0.006	2.55	9.92	1.74±0.65
y -axis	0.180	1.43			
z -axis	0.321	1.66			

It is striking that the permeability results close to each other, in the low nano-darcy range, despite arising from different experimental and simulation techniques and based-upon different imaging datasets made using different imaging approaches. This is remarkable given the experimental and simulation difficulties encountered in measuring and calculating such small permeabilities. However, the differences in scales of measurement should be noted. The calculated permeability from flow simulation relates to a scale of around 25 μm whereas the laboratory measured permeability relates to a considerably larger scale of circa 1 mm. The differences in gas pressure may also be significant. The measured permeability relates to pressure recorded with time and can be obtained depends on the pressure and experimental volumes (crushed particles size of shale). Irrespective of the apparent good correlation between the modelled and measured permeabilities, it is useful noting that (i) the comparison is only for one sample, which cannot be considered to be statistically reliable, (ii) there are significant simplifying assumptions in the modelling, including the assumption of incompressibility, and (iii) there might be errors in the experimental measurements.

The simulated permeability components are dominated by the amount and spatial distribution of the kerogen. The simulated permeability is also strongly dependent on the assumed permeability of kerogen, as discussed above. Since the imaged datasets contained no connected kerogen in the x -direction, the permeability in this direction is calculated to be very low for both Nano-CT and FIB-SEM approaches. The FIB-SEM image has 26% kerogen compared with 20% in the Nano-CT image, giving rise to the lower calculated permeabilities for the Nano-CT dataset in both y - and z -directions.

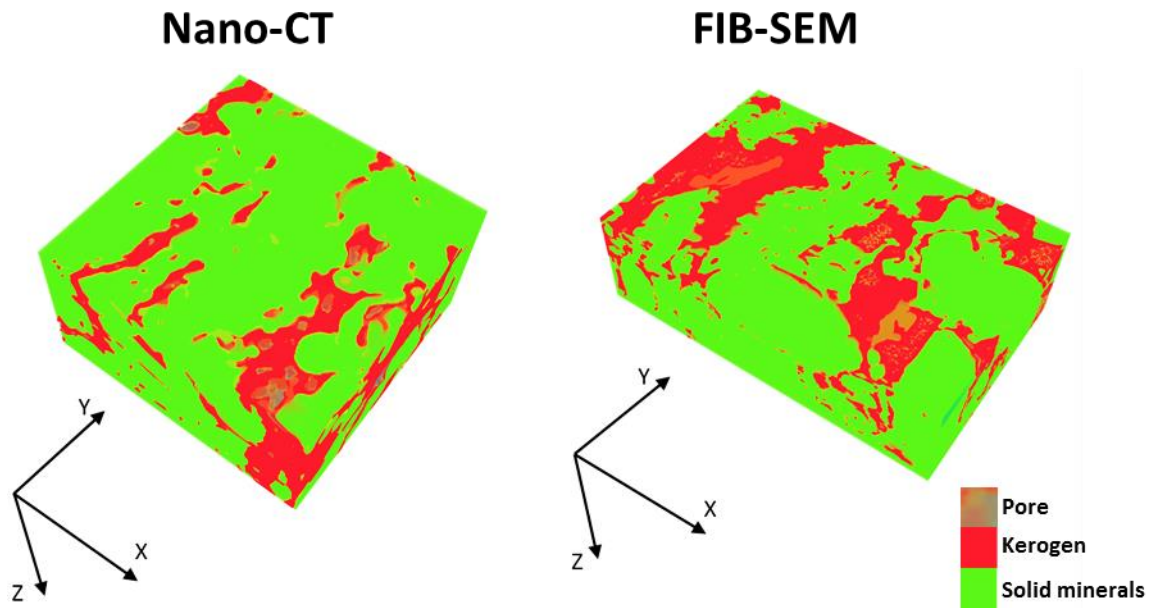


Figure 6.12. Shows the gas flow through kerogen (red colour) in the three directions (x, y and z) for Nano-CT and FIB-SEM.

6.5 Kerogen and pore connectivity

Kerogen is very important in gas shales because it is the source of the hydrocarbon gas. The type, fraction and connectivity of kerogen control the chemical and physical properties of the shale, significantly affecting both the storage and flow of the hydrocarbons (Milliken et al., 2013; Akkutlu et al., 2012). Previous authors have identified kerogen associated with pore systems in shales, and have proposed that gas transport through kerogen might be possible (Javadpour et al., 2007; Ambrose et al., 2012; Wang et al., 2017).

In this study, kerogen and pores have been identified using both Nano-CT and FIB-SEM imaging. The kerogen presents a much higher percentage volume fraction than pores (Table 6.1). Moreover, qualitatively kerogen has a much higher connectivity than the pores, at least at scales higher than the resolution of the imaging techniques (>20 nm). This can be illustrated by comparing parts c and d of Figure 6.5 and Figure 6.6. It is possible, even likely, that pores smaller than the imaging resolution are present and are very well connected. It is interesting that the permeability calculations using Equation (6.5) and the simulations described previously used the kerogen phase as a gas transport medium, and provided permeabilities comparable to those measured experimentally.

The levels of pore and kerogen connectivity that have obtained in this study are very similar to the results of Ma et al. (Ma et al., 2016), and hence it can be considered that the measurements have been used in this study, albeit on a single sample, are not significantly atypical. Consequently, it may be hypothesised that (i) there is a significant pore volume consisting of pores too small to have been currently measured, which are sufficiently well-

connected to provide the permeabilities or (ii) gas transport through the kerogen is more prevalent than previously expected, or (iii) a mixture of both.

It has been also noted that, in the FIB-SEM images, pores were observed to be locally connected in the sample, and some of them are connected to other pores in the matrix (Figure 6.7c). The majority of pores in this sample are isolated at this scale. These locally connected pores were also observed in the previously study as well as studies of (Ma et al., 2018; Saif et al., 2017).

6.6 Conclusions

In this Chapter, the two high resolution 3D imaging techniques (Nano-CT and FIB-SEM) have been used to investigate the pore structure and kerogen structure of the same 25 μm -sized volume of a sample of gas shale. It is increasingly common to carry out either Nano-CT or FIB-SEM imaging on rock samples, but rare to carry out both techniques, and when this is done, authors typically use different samples or different imaged volumes in the same sample. To the knowledge of the author, this is the first time that the two techniques have been applied to the same 25 μm -sided cube of rock, thus allowing a direct comparison of the two different measurement techniques.

The two resulting 3D datasets have each been used in this study to compute a range of micro-physical parameters describing the volume, distribution of the pores and kerogen in the sample. These parameters include pore and kerogen volume and size distributions, pore aspect ratios and scale-invariant surface area to volume ratios.

Both imaging techniques provide 3D images that are clearly of the same sample volume. The FIB-SEM measurements benefit obviously from their slightly better resolution in the sharpness and contrast of the resulting images. The higher resolution of the FIB-SEM technique has resulted in significantly higher measurements of porosity and slightly higher values of kerogen fraction because the extra resolution.

The different amounts of pores, kerogen, silicate matrix and iron pyrites were found in this study by both methods. The porosities and kerogen fractions were found to be 0.7%, 26.0% for FIB-SEM, and 0.43%, 19.6% for Nano-CT, respectively. Overall, the pore volume observed by Nano-CT ranged between 0.017 to 0.35 μm^3 , while the corresponding range for FIB-SEM analysis was between 0.009 and 0.33 μm^3 .

A critical finding was that for both imaging approaches the pores showed very little connectivity and no evidence for the gas transport pathways that the experimental pulse-decay permeability measurements imply.

This study also opens a new path in the better understanding of the level of the connectivity of pore and kerogen involved in transport not only in shale rock samples but also in other nanoporous materials. The novel technique that has been applied in this study can be easily extended to other nanoporous materials used in medical applications, food industry, and catalytic reactions, as well as nano-membranes and fuel cells.

The measurements have been used to calculate the permeability in each Cartesian direction using a Finite-Difference Geometrical Pore Approximation (FDGPA) method, and also using an analytical equation. These calculations both made the assumption that gas flow occurs through the kerogen. There was good agreement between the permeabilities obtained with both of these methods and the permeability measured experimentally using GRI method.

Chapter 7

Measurement and calculation of gas shale permeability

7.1 Introduction

Measurement of shale permeability is of a critical importance in the view of increased accuracy in characterizing reservoir quality and development of unconventional gas reservoirs. However, most standard techniques of measurement shale permeability are suffer from either practical or theoretical shortcomings. The determination of permeability in shale is extremely complex; the complexity arises from very small size of the pores in shales and also from a complex connectivity which is yet not well understood, and remains a major challenging topic. As such, the measurement shale permeability using a steady-state method is take a long time to obtain outcome (Zamirian et al., 2014), and can easily take a few days to stabilise in shale rocks, just like in tight rocks and coal (Moghaddam et al., 2019; Shen et al., 2020). Since the steady-state methods are very slow in estimating permeability in shales, another methods have been used to determine the permeability of shale rocks. Some of the relatively recent methods are based on transient pressure pulse data (Brace et al., 1968; Hsieh et al., 1981; Dicker and Smits, 1988; Jones, 1997) using crushed or full core plugs (Cui et al., 2009) complex pore pressure transients, and pore pressure oscillations (Boitnott, 1997).

Each of the methods have mentioned-above it has an advantage and disadvantage. The crushed sample method, also called the Gas Research Institute (GRI) method, is most commonly applied for shale permeability measurement. This is the simplest method, where two chambers of known volumes are needed, and gas is allowed to expand isothermally into the crushed shale sample chamber from a reference chamber (Cui et al., 2009; Zamirian et al., 2014). The porosity and permeability is then estimated from the pressure versus time data as gas flows into the shale (Luffel et al., 1993). However, when using this method, the porosity and permeability cannot be obtained analytically from the experiments, and to obtain these values a numerical simulation is used, based on the pressure history from the experiments.

Another method which is used for measurements of the porosity and permeability in shale is the Modified Pressure Decay (MPD) approach. This method consists of an upstream and downstream reservoir and a core holder between them into which a cylindrical sample (core plug) is placed. Pressure is then applied to the core sample and the pressure is measured at both ends of the sample. The gas will flow through the sample from the upstream to the downstream reference volume. The upstream and downstream pressure are recorded in time. The pressure decay curve obtained from test is used to determine the porosity and permeability (Lorinczi et al., 2014).

However, these experimental methods all have limited accuracy and require considerable time to implement. Consequently, it may be said that shale permeability can only be determined approximately with conventional experimental methods.

Several studies have compared permeability results from different measurements and have found that permeabilities obtained using the crushed shale method can vary by several orders of magnitude for the same sample (Clarkson et al., 2000; Rushing et al., 2004; Sinha et al., 2013; Ghanizadeh et al., 2014; Moghadam and Chalaturnyk, 2015), and also that permeability

values determined by such techniques depend on the particle size (Tinni et al., 2012; Cui et al., 2009; Profice et al., 2011). Furthermore, the parameter derivation process is complex and simulation models often require knowledge of many properties (e.g., tortuosity) that cannot be measured directly in the laboratory (Lorinczi et al., 2014; Moghadam and Chalaturnyk, 2015).

The aim of the current chapter is to measure and calculate gas permeability using several approaches recently applied in shales in the literature, to explore and provide a better understanding of petrophysical properties in shales and to see how the results obtained by the different approaches compare.

Different approaches often yield different porosity and permeability values in shale, which is due to the different accessibilities of fluids or different sample sizes and shapes. The approach used in this chapter allows to assess variability of the shale samples, with comparing permeability values derived by different methods on shale materials in order to draw conclusions on the applicability of each method. To meet this aim, standard numerical and experimental methods were employed such as the GRI method for permeability measurement, MIP, N₂ adsorption, μ -CT, Nano-CT and FIB-SEM for calculation of permeability.

This chapter outlines first the material used and the experiments conducted, including the shale samples and number of the measurements undertaken (Section 7.2). The results are then presented in Section 7.3. The discussion of the results and a comparison between different measurements are provided in section 7.4. Finally, the key findings are summarised in the conclusions section.

7.2 Material and methods

7.2.1 Rock samples and preparation

The samples analysed in this current study were selected from different gas shale reservoirs which are: (i) the 2.7 km sample from Bowland shale formation (the same sample as used in Chapter 4 and Chapter 5); (ii) the samples from Östergötland gas shale reservoir in Sweden coded as Gripen-7, E9, and F3 from the depth of 110, 110.8 and 120.3 m, respectively. Details of number of the wells and locations are provided in Chapter 3.

A number of different approaches were used in this study to measure porosity and gas permeability. These approaches are characterized by different pore accessibilities, also each of the methods requires special sample size in order to produce good quality results.

The size of the samples is very significant in the methods carried out in this study; as such each method has required a particular volume of sample. A wide range of samples size have been used, from 0.5-3 mm; Figure 7.1 shows different samples size with different methods facilities have applied in this study.

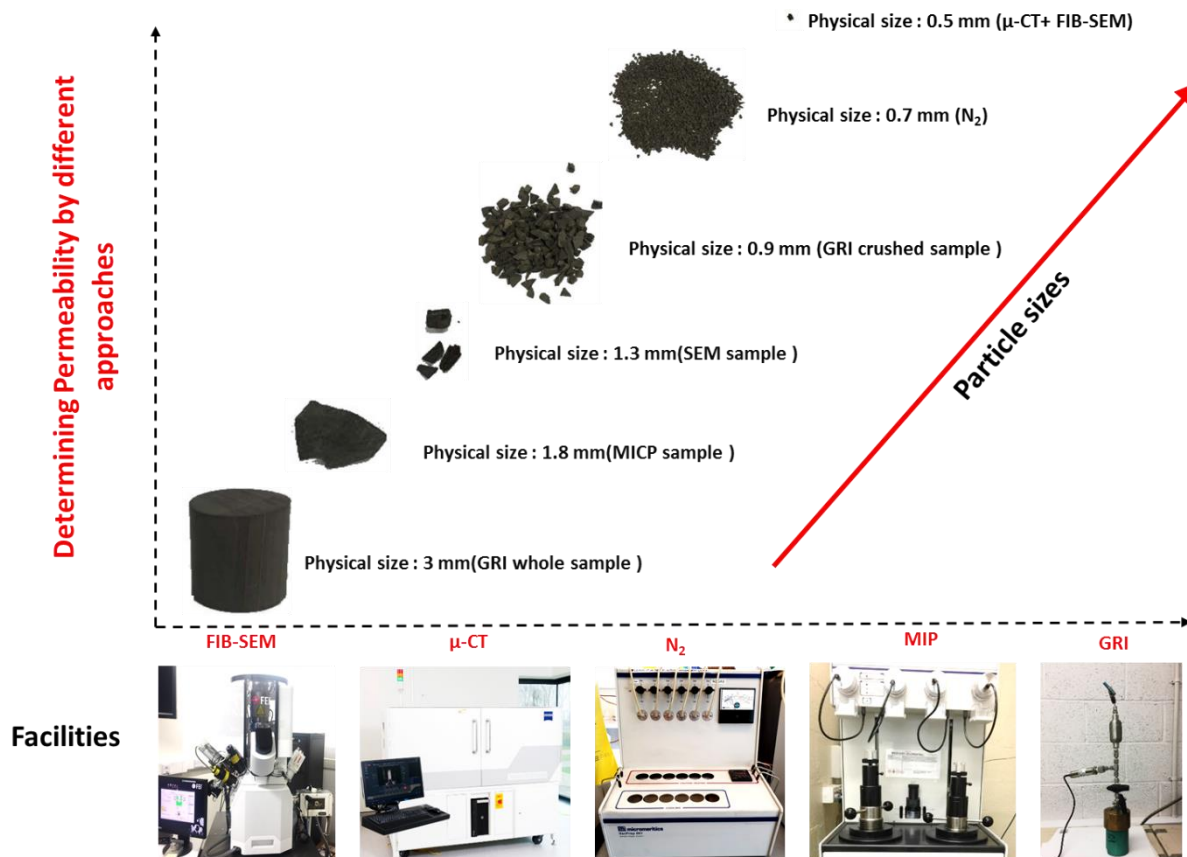


Figure 7.1. Different approaches and corresponding facilities used in this study, with special requirements for sample size varying between 0.5-3 mm, as indicated.

7.2.2 Overview of methods used

The Gas Research Institute (GRI) method (Figure 7.2) has been used in this study for measuring porosity and permeability which also relies on gas pressure decay (gas expansion system), but in this case the sample is crushed (Cui et al., 2009; Zamirian et al., 2014).

The shale core samples from different formations were crushed with mortar and pestle, and were then filtered. After filtering, the particle sizes obtained had an average size between 0.9 -1 mm. The crushed shale particles are then placed into the sample cell as can be seen in Figure 7.2. The experimental apparatus contains a series of valves and volumes, as can be seen in Figure 7.2. Firstly, valve 1 is shut while valve 2 and valve 3 are open. This is followed by opening valve 1 and closing valve 2 to allow the gas to fill up the reference volume at a pressure between 50-300 psi. Then valve 1 is closed. After the reference volume has reached thermal equilibrium, valve 3 is closed and valve 2 is opened. Gas expands from the reference volume into the sample cell filled with rock particles.

The porosity was obtained directly from the experimental as a known parameter from the bulk volumes and pressure differences (Equation 7.1) (Rybalcenko , 2017)

$$\phi = \frac{P_1 V_1 - P_2 (V_1 + V_2 - V_b)}{P_2} \quad (7.1)$$

Where V_1 the reference cell volume (cm^3) is, V_2 is the sample cell volume (cm^3), P_1 is the initial reference cell pressure (psig) and P_2 is the final stabilized pressure (psig) (Figure 7.2).

The permeability values were obtained based on history matching the pressure decay curves between the experiment and simulation, as can be seen in Figure 7.3.

History matching-type of modelling using industry-standard simulators (Eclipse™ software) was undertaken to invert pressure decay data from experiments to estimate permeability. This type of derivation method was chosen due to its simplicity, ability to estimate the permeability on shale samples. The principle behind this procedure is to correctly represent the sample and experimental volumes.

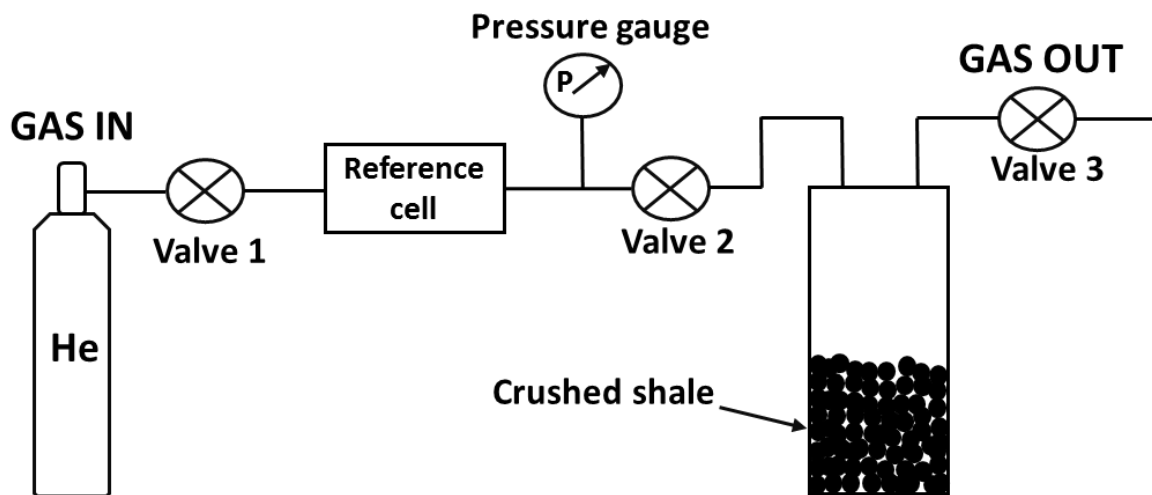


Figure 7.2. Diagram of the apparatus for GRI porosity and permeability measurements.

Figure 7.3 shows an agreement between the measured permeability and simulation using Eclipse™) of the crushed shale sample. The Permeability measurement with the GRI technique, also known as crushed rock are extremely dependent on particle size. Therefore permeability change as function particle size reflects the change in structure from particle size to particle size (Comisky et al., 2011). There are few possible sources of error in the present experiments such as (i) the influence of particle sizes have used to perform the experiment, (ii) the pressure that have recorded during the experiment, it might not be reach to the equilibration when the experiment is run on crushed shale, in which case the experiment is run for 2-3 hours, and not enough time to record pressure decay curve. Also it has also been observed that in the current experiment, there is large (gap) different between the pressures

from the experiment and simulation at time 20-30 h (Figure 7.3), which is not matching up, this because a different particle sizes or the pressure has not been recorded correctly for this sample. The similar behaviour has also been observed in work of (Moghadam et al., 2015; Tinni et al., 2012; Peng and Loucks et al., 2016; Fisher et al., 2017). Therefore- this implies that the crushed particle measurement cannot be used to measure matrix permeability in shale (not representative for shale). It can be used only as a relative measurement.

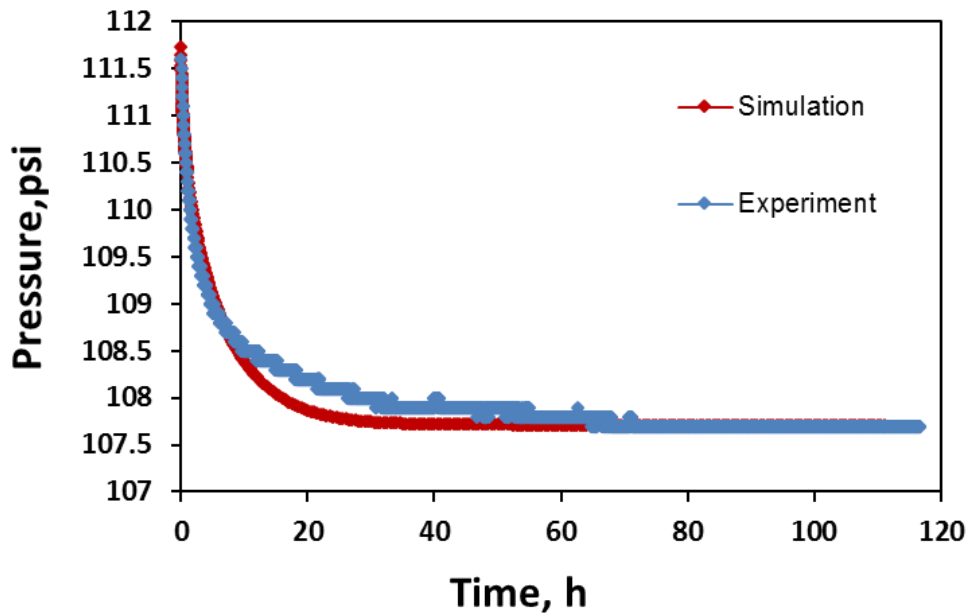


Figure 7.3. A typical plot of history match for pressure (experiment and simulation using Eclipse™) of the crushed shale sample test.

In reference to [Figure 7.4a](#), it has been noticed that after the initial pressure, the pressure stabilises quickly when Valve 1 is open with Valve 2 closed as the reference volume is charged with gas. However, the pressure dropped quickly in [Figure. 7.4b](#) when the Valve 1 and Valve 3 are closed and Valve 2 is opened. During this process the gas in the reference volume is shared with all of the volume around and inside the shale sample.

[Figure 7.5](#) shows the process of gas behaviour during gas expansion during the experiment. The outcome of this experiment are presented later in this chapter.

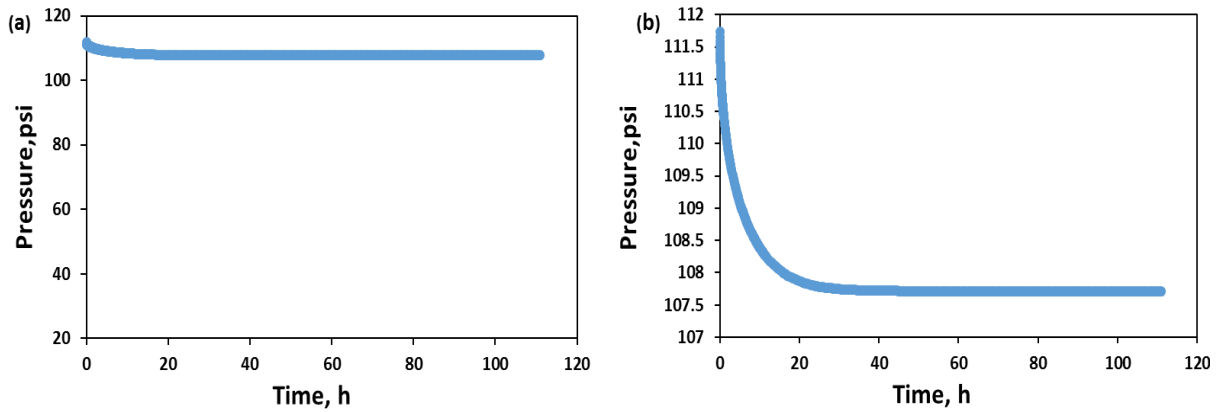


Figure 7.4. The pressure data recorded during the experiments. (a) charging the reference volume with a fixed mass of gas at a fixed pressure, (b) sharing the gas with the sample chamber ((Valve 1 and Valve 3 are closed with Valve 2 open).

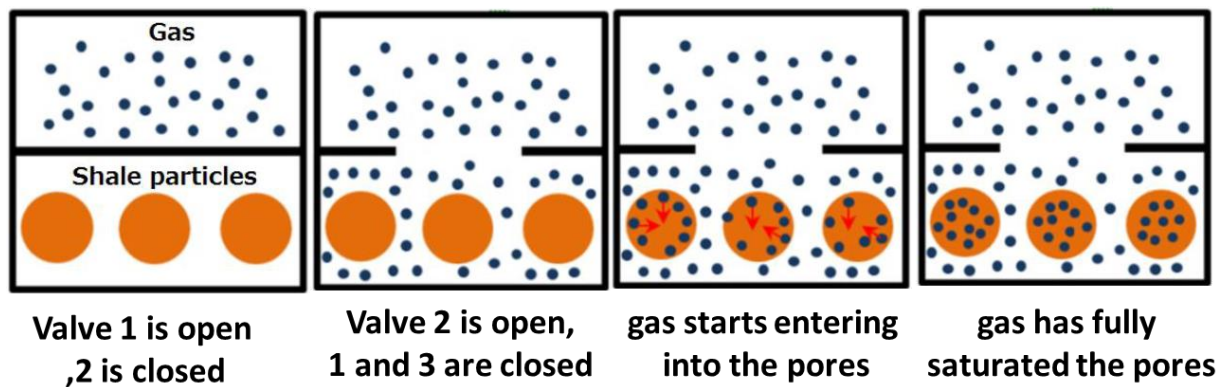


Figure 7.5. Diagram illustrating the processes of gas behaviour during pressure expansion. Once the valve is opened the gas surrounds the pores (at time $t=0$), then at time $t = t_1$ the gas starts entering the pores and at $t = t_{eq}$ the gas has fully saturated the pores.

Mercury injection (MIP) at higher pressure, nitrogen adsorption (N_2) at low pressure were carried out and also tomography measurements (μ -CT, and Nano-CT) as well as dual-ion beam (FIB-SEM) system were also used to obtain information about the imaging the microstructure surface, porosity and pore size distribution of shale rocks sample. This information has also been used to estimate permeability, which is discussed later in this chapter. More details on the μ -CT, Nano-CT and FIB-SEM scanning conditions, pixel size and volume as well as MIP, N_2 adsorption are provided in Chapter 3.

7.2.3 Crushed GRI simulation

The crushed GRI modelling in this work is based on the reported approach by Rybalcenko (2017)

In the modelling, each particle of crushed shale material was assumed to be a shard of $10 \mu\text{m} \times 10 \mu\text{m} \times 100 \mu\text{m}$. The permeability is also assumed to be (100 mD) surrounded the particle.

Extra $1 \times 1 \times 10^3 \mu\text{m}^3$ cells at the top of the model were included to represent the expansion volume.

Once the model is created, the history matching is performed using Eclipse™ software. Eclipse™ runs many simulations of the model using a predefined range of parameters as describe above which are then used to derive a response surface. The software then compares the outcome of the simulation to the experimental data of the model. Based on the quality of the fit between the simulated and the experimental data, the software generates a new series of parameters and identifies the ones that produce the best fit (Rybalcenko, 2017).

7.3 Results

7.3.1 Mineral composition analysis

The mineralogical compositions and TOC contents for all the rock samples tested are presented in Table 7.1. It is shown that the values of the TOC have arrange from (11.9 to 20.18 %). Among all the samples, sample MD-2.7 has the lowest TOC value (11.9%), while highest value shown in sample F3 (20.18%). Moreover, the average values of TOC average for shale sample groups are calculated as 15.5%. As it is known, TOC value refers to the amount of carbon found in an organic matter contained in a sample, thus it is a key element for gas storage and controlling gas generation in shale reservoirs.

Table 7.1 also indicates that the mineral components contained in all shale samples mainly include quartz, calcite, dolomite and albite and most shale samples also contain some pyrite. Furthermore, for the three samples collected from the Sweden shale formation (Grpn7, F3 and E9), the mineral compositions are similar. Particularly, in their average contents of quartz are 27%. For the other samples collected from the Bowland shale formation (in Lancashire, UK), it was found that sample MD-2.7 contents the highest amount of quartz and mica (92.5% and 4.6% respectively) with the lowest pyrite content (i.e., 0.7 %).

It was also found that the samples colours are different due to their organic contents as well as mineral compositions. For example, the samples which contain siderite such as Grpn7 show a darker brown, while the samples with high content of quartz such as MD-2.7 are much darker in colour than the other two samples (F3 and E9).

Table 7 1. Shows the analysis results of the X-ray diffraction (XRD, mineral composition by wt %) and total organic carbon (TOC) as weight percentages for shale samples.

Samples	Quartz	Albite	Microcline	Calcite	Dolomite	Illite	Mica	Kaolin	Pyrite	Siderite	TOC
Grpn7	29.1	3.7	9.4	1.1	1.3	22.6	10.9	2.7	16	0.9	15.87
F3	25.9	3.5	13.6	0	0	21.4	12.8	3.6	16.9	0	20.18
E9	24.8	4.2	10.7	0	0	15.6	21.9	3.5	16.4	0	14.30
MD2.7	92.5	0.6	0.2	0	1.4	0	4.6	0	0.7	0	11.9

7.3.2 Permeability estimation theory

Permeability is a crucial parameter for assessing shale gas formation because it controls the accessibility of the hydrocarbon within the shale reservoir. However, it is extremely difficult to obtain directly especially in shale materials due to their highly heterogeneous microstructure as well as extremely small size of the pores.

It has also been observed in this current study crack-like pores may be visible in FIB but not in micro-CT. This is because of the different voxel resolution and magnification of the two methods. Namely, in the μ -CT experiment the resolution is $\sim 1 \mu\text{m}$, but limitations of the scan area, which is often focused on an area of approximately $1 \times 1 \mu\text{m}$ diameter, means that the measurement may not detect all connected pores or cracks at this scale, and therefore can impact estimate permeability. In contrast, FIB has a resolution of around 20 nm and is able to reveal more details of the microstructure such as pores, kerogen and matrix at this scale. Therefore the higher resolution enables small cracks or fracture boundaries to be seen clearly, and small branching fractures can be identified at this higher resolution.

There are various ways to predict permeability, many of which are empirical such as methods are presented in this study based on different other known parameters which do not need calibration to an empirical data set. The specific measurement and analytical methods are presented in the following subsection.

7.3.2.1 μ -CT and FIB permeability

The permeability for μ -CT and FIB approaches have been estimated in this study using the standard pore surface area and the volume of the pores; the equation used by this approach is expressed as (Johnson et al., 1986):

$$k = \Lambda^2 / 8F, \quad (7.2)$$

Where Λ is a measure of the aperture for fluid flow which controls the permeability in the sample, and F is the formation factor of the rock (Glover et al., 2009).

The value of Λ was obtained from the surface area and volume of the pores following the approach of [Johnson et al. \(1986\)](#) where,

$$\Lambda = S_p/V_p. \quad (7.3)$$

The formation factor of the rock was not measured directly in this study. Instead, it was estimated using

$$F = \phi^{-m}, \quad (7.4)$$

Where ϕ is the measured porosity and m is the phase exponent for pores from the generalised Archie's law ([Glover et al., 2010, 2015](#)). For this study, it was assumed that $m=3$. This value was chosen since the cementation exponent for shales is known to vary between about 2.34 and 4.17 ([Revil and Cathles, 1999](#)). The results for the shale permeability are given in [Table 7.3](#).

7.3.2.2 Nano-CT / Kozeny-Carman permeability

The permeability is predicted for this technique by using the Kozeny–Carman equation ([Bear 1988; Mostaghimi et al., 2013](#)). This estimation is based on the porosity and specific surface area. This equation is expressed as ([Kozeny, 1927](#)):

$$k = \Psi^2 \frac{\phi^3 D_p^2}{180 (1-\phi)^2}, \quad (7.5)$$

Where ϕ is porosity, D_p is the characteristic diameter of pores and Ψ is the sphericity of the pore. The sphericity is a measure of the geometrical shape of the pore in three-dimensions (i.e., how oblate or prolate). It was not determined in this study directly, but estimated based on the volume and surface area of the pore using ([Busch et al., 2017](#)):

$$\Psi = \frac{\pi^{1/3} (6V_p)^{2/3}}{S_p}, \quad (7.6)$$

Where V_p is the pore volume and S_p is the pore surface area of pores. The results for the calculated shale permeability are presented in [Table 7.3](#).

7.3.2.3 MIP/RGPZ permeability

The permeability can be estimated from MIP data by using the RGPZ model ([Glover et al., 2006](#)). This model is derived analytically and does not need calibration. The RGPZ takes the heterogeneity of rock into consideration by using the electrical cementation exponent to represent the degree to which pores through the rock are connected (the void capacity through which a fluid can flow). The RGPZ model is given by

$$k_{RGPZ} = \frac{d_{grain}^2 \phi^{3m}}{4am^2}, \quad (7.7)$$

Where d_{grain} is the grain diameter which controls the flow properties of the porous medium, and was estimated using the following approach (Glover et al., 2009)

$$d_{grain} = 1.6585 \sqrt{\frac{am^2}{8\phi^{2m}}} d_{pore\ throat} , \quad (7.8)$$

Where $d_{pore\ throat}$ is the size of a pore and was measured directly from MIP, and m is the cementation exponent (dimensionless) from the generalized Archie's law (Glover et al., 2010; 2015). For this study, it has assumed that $m = 3$. This value was chosen since the cementation exponent for shales is known to vary between about 2.34 and 4.17 (Revil et al., 1999), ϕ is the porosity (as a fraction), and a is constant that is thought to be close to 8/3 for porous granular media (Rashid et al., 2015). The estimated permeabilities for the all samples are presented in Table 7.3.

7.3.2.4 Nitrogen adsorption (BET)/Kozeny-Carman permeability

The Kozeny-Carman equation was also used to estimate permeability using nitrogen adsorption data. This approach is based on the measured porosity and BET specific surface area of the sample (Eseme et al., 2012). This equation is given as

$$k = \frac{C_{kc}\phi^3}{S^2(1-\phi)^2} , \quad (7.9)$$

Where S is specific surface area (m^2/g) from the BET analysis, ϕ is the fractional porosity, and C_{kc} is the constant of Kozeny-Carman ($2.064 \times 10^{-13} m^6 kg^{-2}$) (Eseme et al., 2012) which includes tortuosity and a generalised factor to account for different pore shapes (Eseme et al., 2012). The results of the permeability estimated from BET sorption are also presented in Table 7.3.

7.3.3 Hydraulic connectivity estimation theory

Hydraulic conductivity is a physical property which measures the ability of the material to transfer fluid through pore spaces and fractures in the presence of an applied hydraulic gradient. Estimation of hydraulic conductivity is a measure of how easily gas can pass through a shale rock. The high values of conductivity indicate that permeable material (rock) through which gas can pass easily, while low values indicate that the material (rock) is less permeable.

Hydraulic conductivity is not measured directly in this study but was estimated based on the RGPZ equation (Equation 7.3, Glover et al., 2006), and the electrical connectedness model (Glover, 2010). The electrical connectedness G is given as:

$$G = \chi_e \phi = \phi^m , \quad (7.10)$$

Where χ_e is the electrical connectivity and has form of

$$\chi_e = \phi^{m-1} . \quad (7.11)$$

Using (7.10), and (7.11), the porosity term in the RGPZ equation can be expressed as:

$$\phi^{3m} = G^3 = \chi_e^3 \phi^3 . \quad (7.12)$$

Using also Equations (7.7) and (7.12),

$$k = \frac{d^2 \chi_e^3 \phi^3}{4am^2} . \quad (7.13)$$

Rearranging Equation (7.13),

$$\chi_e = \left(\frac{4am^2 k}{d^2 \phi^3} \right)^{1/3} . \quad (7.14)$$

The hydraulic connectivity for gas flow is the square root of the electrical connectivity (Glover, 2015).

$$\chi_h = \left(\frac{4am^2 k}{d^2 \phi^3} \right)^{1/6} . \quad (7.15)$$

Thus, the equation of hydraulic connectivity which has been used in this study is expressed as:

$$\chi_h = \phi^{(m-1)/2} , \quad (7.16)$$

Where ϕ is the fractional porosity, and m is cementation exponent. For this study, it was assumed that $m = 3$.

Two types of errors might be expected when using this approach: (i) errors in measurement of the raw data during the imaging process such as segmentation, (ii) errors in calculation of hydraulic conductivity, especially if a method of analysis is used which is not appropriate to the sample such as shale rock.

7.3.4 Porosity and Permeability results

The summary for all results of the measurements and calculation of porosity, permeability, including those obtained by the crushed shale method, as well as hydraulic connectivity for shale samples investigated by different techniques are presented in Table 7.2, 7.3 and 7.4. A discussion of these results is provided later in this chapter.

Table 7 2 The porosities results of the investigated rock samples obtained by different measurements.

Sample code	GRI Porosity (%)	MIP Porosity (%)	μ -CT porosity (%)	Nano-CT porosity (%)	FIB-SEM porosity (%)	BET Porosity (%)	Arithmetic Mean of All Methods (%)
Grpn7	6.26±1.09	1.8±0.09	3.57±0.65	0.43±0.04	0.70±0.07	-	0.0255±0.0244

F3	3.66±0.60	2.8±0.48	-	-	-	-	0.0323±0.0290
E9	4±0.9	3.0±0.50	3.85±0.70	0.51±0.048	0.66±0.06	0.71±0.08	0.0213±0.0167
MD2.7	-	0.6±0.07	0.06±0.008	0.67±0.03	0.52±0.05	0.0235±0.003	0.00375±0.00323

Table 7 3 The permeabilities results of the rock samples investigated in this study, obtained by different methods.

Sample code	GRI Permeability (nD)	MIP Permeability (nD)	μ-CT Permeability (nD)	Nano-CT Permeability (nD)	FIB-SEM Permeability (nD)	BET Permeability (nD)	Arithmetic Mean of All Methods (%)
Grpn7	1.74±0.06	24.7±4.45	11.6±2.45	3.75±0.45	0.17±0.02	-	8.392±9.798
F3	15±3.02	80.3±20.03	-	-	-	-	47.65±47.358
E9	4.5±1.35	62.8±10.80	10.92±2.40	-	0.126±0.01	9.36±2.44	17.541±24.249
MD 2.7	-	2.65±0.45	2.98±0.745	2.61±0.42	56.2±8.22	4.63±1.47	13.814±22.087

Table 7 4 The hydraulic connectivity results for the shale rock samples investigated in this study, obtained by different approaches.

Sample code	GRI Hydraulic Connectivity	MIP Hydraulic Connectivity	μ-CT Hydraulic Connectivity	Nano-CT Hydraulic Connectivity	FIB-SEM Hydraulic Connectivity	BET Hydraulic Connectivity	Arithmetic Mean of All Methods (%)
Grpn7	0.2501±0.09	0.134±0.06	0.1889±0.075	0.065±0.005	0.083±0.004	-	0.1445±0.09388
F3	0.1913±0.08	0.167±0.070	-	-	-	-	0.1793±0.16057
E9	0.2±0.085	0.173±0.085	0.1962±0.065	0.071±0.002	0.081±0.003	0.084±0.004	0.1343±0.06154
MD 2.7	-	0.077±0.003	0.0245±0.001	0.081±0.009	0.072±0.001	0.0153±0.0003	0.0542±0.03731

Figure 7.6 shows the relationship between the connectivity and porosity. It is clear that electrical and hydraulic connectivity are increasing with increases in the porosity values, which suggests that the porosity of shale determines how easily gas can pass through the shale rock.

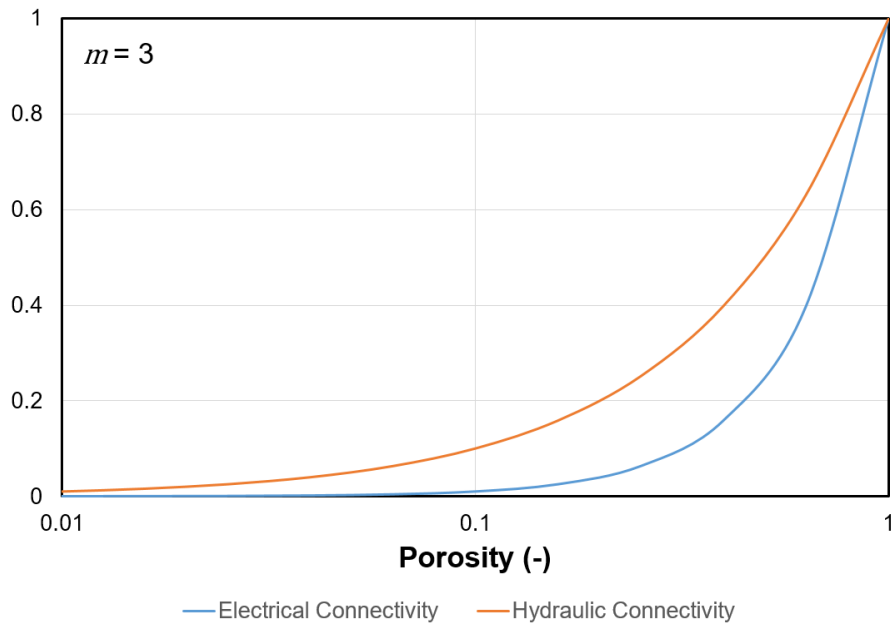


Figure 7.6. Shows the theoretical variation of electrical connectivity (Eq. 7.11) and hydraulic connectivity (Eq. 7.16) as a function of porosity for the shale rock samples for $m=3$.

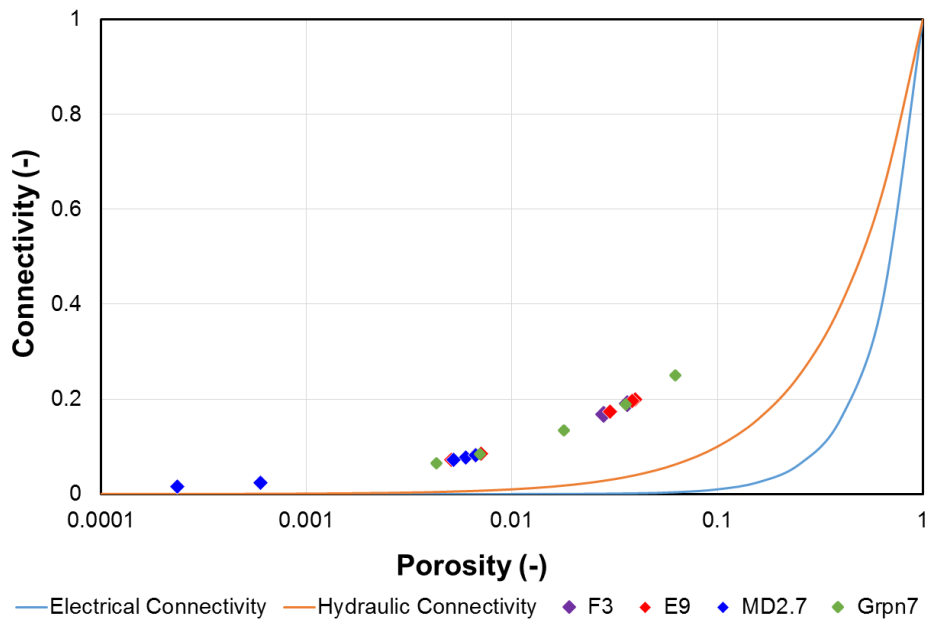


Figure 7.7. Shows the connectivity for each rock sample (F3, E9, MD2.7 and Grpn7) as a function of porosity as well as compare with electrical and hydraulic connectivity for the shale rock samples.

7.4 Discussion and interpretation

In this study, a variety of techniques have been used on gas shale samples obtained from different reservoir depths to measure and calculate porosity and permeability, in order to explore and better understand sample contents as well as petrophysical properties, and to compare the values obtained by the different approaches.

The crushed shale method is used to estimate porosity and permeability, as it can be seen from [Table 7.2](#) and [7.3](#), the GRI porosity of the crushed samples is in the range of 3.66-6.26% while permeability is in the range of 1.74-15 nD, under confining pressure. It is noted that the F3 sample has larger permeability (15 nD) than Grpn7 and E9 samples. These results suggest that sample F3 have a few large particle size of crushed shale ([Figure 7.8](#)), in other words the permeability measured with this technique depends on the particle size as also indicated in [Tinni et al. \(2012\)](#); [Cui et al. \(2009\)](#); [Profice et al. \(2011\)](#).

[Peng and Loucks \(2016\)](#) have indicated that the permeability of shale depends on the amount of the crushed shale or scale (amount) of samples which means that the large particle size of crushed shale (larger shale fragments) would give higher permeabilities values. [Cui et al. \(2009\)](#) reported that high permeability values obtained from crushed shale method (CSM) which due to large size of the particle that used in CSM. However, SEM and μ -CT analysis shows that shale particles always contain a large density of microfractures ([Fisher et al., 2017](#)) which also could impact and could increase permeability values within shales. It was also observed that in this study the μ -CT data suggest the presence of micro-fractures in the images ([Figure 7.8](#)). These micro-fractures would allow easy access the helium into shale during the experiments therefore would present higher permeability values ([Fisher et al., 2017](#)).

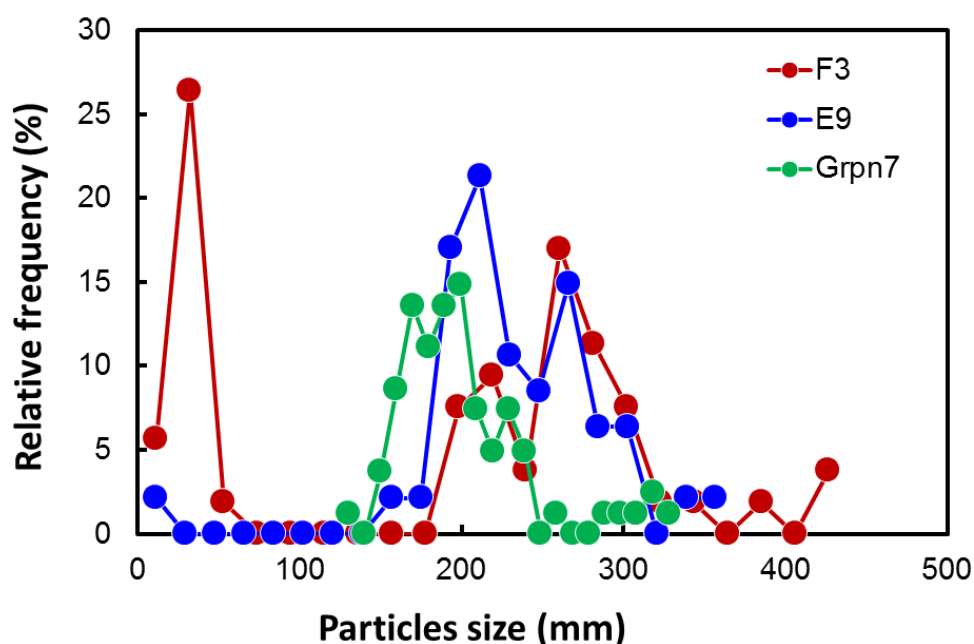


Figure 7 8. Particles size distribution of crushed shale samples for F3, E9 and Grpn7 samples

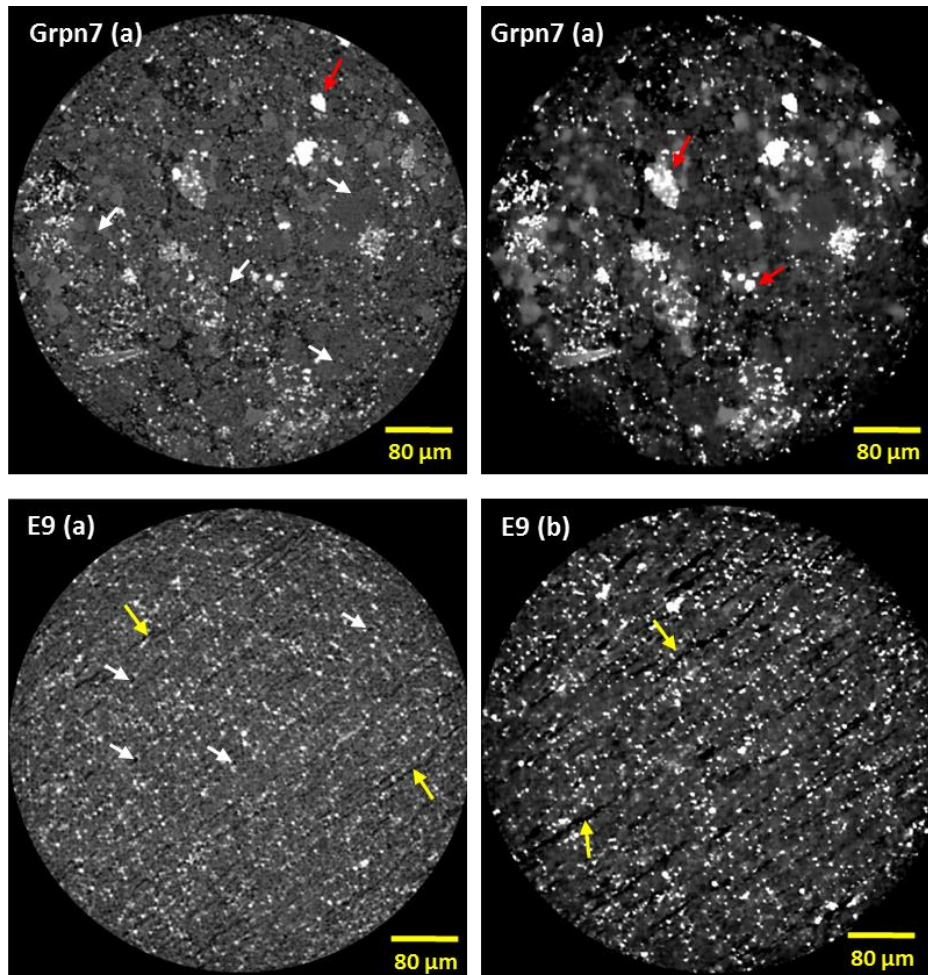


Figure 7 6. (a) Example of 2D of the μ -CT images on Grpn7 and E9 shale samples, respectively, with diameter of 0.5 mm at resolution of 0.94 μ m, (b) non-local means filtered have been applied on the same slice of samples. Darker grey sections represent pores as marked by **white arrows**, while the white spots are pyrite (**red arrows**) and microfractures (**yellow arrows**) as can be observed from the image (b) for Grpn7 and E9 samples, respectively.

Referring to the analysis of the MIP permeability results (Table 7.3), the way in which permeability is calculated is described above (Section 7.3.2). These ranges of results observed are similar to the ones indicated in Peng and Loucks (2016). Moreover, a one-to-one comparison of GRI permeability measurements for samples Grpn7, F3 and E9 suggests that MIP permeability generally agrees well with GRI permeability, e.g., value of GRI permeability for Grpn7 sample is 1.74 nD with corresponding value of 24.7 nD for MIP. These results also suggest that there is no gap or much difference between the GRI permeability from crushed shale method with MIP estimated permeability based on RGPZ equation. Moreover, it is also

found that the values of Nano-CT and FIB-SEM estimation permeability (Table 7.3) have a lower range than other measurements. A major reason for this might be possible limitations of different measurements which could provide different values (such as resolution in both of the measurements) as can impact the pore structure. However, the MIP and GRI methods consider only open pores, therefore, the porosity and permeability measured with shale rock is accessible only for connected pores, whereas imaging methods e.g. μ -CT, Nano-CT, and FIB-SEM methods measure both open and closed pores and the results are significantly affected by imaging. In addition, another reason might be the imaging process such as threshold selection (segmentation) which could also impact on the outcome of porosity and permeability. Bai et al. (2013) presented that the porosity of Fayetteville shale has changed from 14% to 49% when the threshold increased from 42 to 54 (Bai et al., 2013). Wang et al. (2017) have also reported that the changing value of the porosity within shale depends on the threshold segmentation (Wang et al., 2017). According to these studies, the selection of segmentation thresholds has an important impact on porosity and permeability particularly within the structure of shale.

Considering the connectivity results (Figure 7.6), it has been noted that the connectivity has a positive correlation with porosity, which indicates that the connectivity values increase depending on the porosity (Figure 7.6).

Tables 7.2 and 7.3 show porosity and permeability of shale measured using several approaches that recently applied in shales. It was found that the mercury injection (MIP) technique is inappropriate for use with gas shales (Yuan et al., 2019). This is because shale materials have very low permeability, and mercury is a non-wetting phase. Therefore, extremely high pressures are required to force mercury into even the largest of the pores, and these pressures are large enough to compress the rock sample and perhaps damage the pores. Consequently, all pore size and porosity data provided by this technique is likely to be invalid for shale. Similarly, the GRI method relies on gas pressure decay (gas expansion system). This method is also unsuitable for shale because it only determines permeability of shale based on pressure is recorded as a function of time, and thus producing misleading outcomes on the measurement, particularly in crushed shale samples because crushing the sample would change the properties of the rock.

It has been also observed that sample MD-2.7 from Bowland shale reservoir has very low porosity (Table 7.2) and permeability (Table 7.3) than the other samples. This result suggests that the gas transport through the pores in this sample is unlikely to be important, but cannot be ignored, as it is very important and a basis for understanding permeability in the rock. This level of heterogeneity and extremely low porosity and permeability has also been noted in the work of Ma et al. (2016) on the same shale reservoir (Bowland).

7.5 Conclusion

In this study, the porosity and permeability have been measured and calculated using multiple experimental approaches including GRI, MIP, N₂ adsorption, μ -CT, Nano-CT and FIB-SEM in order to explore and provide a better understanding of petrophysical properties and to make a comparison among the different approaches. The major results are summarized as follows:

- 1) The porosity and permeability of shale have been measured using crushed shale method. The present study has conducted experimental measurements on crushed shale, and it was found that the sample fragments/size have an important impact on the measured permeability values, i.e., samples measurement with larger particle size (larger diameter) resulted in higher permeability (Figure 7.7). The reason behind this is most likely that the large particle size samples might possibly have artificial fractures that were generated during the preparation of the samples in the laboratory.
- 2) The MIP porosities and permeabilities generally agree well with GRI porosities and permeabilities which suggests that there is not much difference between each other in that both measurements consider only open pores, therefore, the porosity and estimate permeability measured within shale rock is accessible only for connected pores.
- 3) By analysing the electrical and hydraulic connectivity it was found that these properties have positive relationship with porosity, which suggests that connectivity is increasing with increasing the porosity values, so it is dependent on the porosity of shale.
- 4) The results for permeability estimation from imaging analysis (Nano-CT, and FIB-SEM) showed that permeability from these two techniques have lower range then the one obtained by others measurements. This might possibly be due to limitations of measurements (such as resolution in the both of techniques) as this can impact on the pore structure, and also to the fact that both techniques measure both open and closed pores and therefore, the results are significantly affected by image quality. Moreover, the imaging process such as thresholds selection (segmentation) might be another possible reason for the differences in the porosity and permeability values.

Chapter 8

Conclusions and Future Work

8.1 Conclusions

In this study, it has been presented that multi-scale imaging with quantification methods are powerful tools for characterisation the microstructural properties of gas shales, particularly of pore volume, sizes, network, porosity, permeability, pore aspect ratio and surface area to volume distributions. The X-ray micro-computed tomography (μ -CT), ultrahigh resolution nano-computed tomography (Nano-CT) and focused ion beam scanning electron microscopy (FIB-SEM) are used in this study to provide valuable microstructure information in 2D/3D at multiple length scales, with voxel/pixel sizes of 1 μ m, 64 nm, 50 nm and \sim 20 nm, respectively. In addition physical measurements such as the Gas Research Institute (GRI) porosity and permeability method, mercury injection porosimetry (MIP), and nitrogen (N_2) adsorption are also used in combination with the aforementioned tomographic imaging methods in order to visualise and quantify shale structures at different scales which cannot be recognised from imaging results alone.

The main key contributions of this study are given below:

- (1) A multi-scale imaging (nm- μ m-mm) has been successfully applied in 2D/3D dimensions on a small shale rock to describe the important microstructures properties of gas shale.
- (2) Microstructural properties including porosity, pore size, pore volume distribution, and pore aspect ratio, internal surface area to volume of pore, pore connectivity and permeability in 3D within gas shale samples have been visualised and quantified.
- (3) Pore size distributions of shale rocks at all ranges of scales from 2 nm up to 1000 μ m has been captured by using a variety of technologies including N_2 adsorption, MIP and tomographic method (μ -CT, Nano-CT) and also high resolution FIB-SEM respectively.
- (4) The shapes and connectivity of pores have been characterised, which are very important aspects in shale gas reservoirs because pore shape controls the connectivity of the rock thus should be significant in defining the permeability of the shale.
- (5) A small of piece of the shale rock sample have used for macroscale measurement (μ -CT), while the same sample is subjected to microscale measurements (FIB-SEM) at multiple locations to describe the network of pores, kerogen and other mineral phases over various scales (nm- μ m). The gain in resolution is to detect the microscale and nanoscale features, however this comes at the expense of the volume analysed. It is suggested that multiple locations on same shale sampling volume are used to obtain results to statistical significance.
- (6) For the first time, a small cubic core sample of (15-25 μ m side length), prepared from an original core sample of around 3 mm in length and diameter, was subjected to

Nano-CT and milling on FIB-SEM in order to link between the two different measurements. The results have provided valuable range of aspects including resolutions and 3D fields of view (3D visualisation of the pore and kerogen network). The results were also compared directly the structure of shale on each of the imaging techniques, which indicated that the pore structure is strongly dependant on the resolution within the shales.

This study of multi-scale imaging was applied to samples from different gas shale reservoirs including Bowland gas shale (in the UK), and Östergötland gas shale (in Sweden). The microstructure properties were imaged and analysed including pores, kerogen and minerals. A high resolution SEM under backscattered secondary electron (BSE) mode with Energy Dispersive X-ray (EDX) analysis was used to reveal a complex and compositional elemental information of fine-grained microstructure inside shale samples. Pore size and volume distributions from both mercury injection and nitrogen sorption experiments are correlated well with 3D tomographic imaging. The pore volumes distribution are in range of $\sim 1 \times 10^{-5} \mu\text{m}^3$ to $31.5 \mu\text{m}^3$ in most of shale reservoirs, while the pore sizes distribution shows ranges of ~ 2 nm to 5000 nm for N_2 and MIP, respectively. The frequency distributions show major peaks at around 2.5 nm while the minor peaks at around ~ 250 nm which is mainly made up of elongated pores (penny-shaped).

The shape of the pores can be significant in shale gas reservoirs because pore shape controls the rate of gas desorption and connectivity of the rock. The distribution of pore aspect ratio and scale-invariant pore surface area to volume ratio (σ) for pores which contribute significantly to the overall pore volume has been found to range from 3 to 30. The pore shape also controls the mechanical properties of the rock and the likelihood that pores will interlink to form a pervasive pore network for fluid flow.

The results shows also that pore microstructure is highly dependent upon the scale. Such a microstructure is important for the assessment of the potential of gas shales based on the connectivity and pores at each scale and the ability of the rock to be hydraulically fractured. The reconstructed matrix, kerogen, and pore space volumes from each approach showed significant scale-dependent differences in the microstructure.

The shale samples displayed a low connectivity of the pore system and a high connectivity of kerogen as typical features in many shale reservoirs, which suggests that gas flow through shale samples cannot be mainly through the pores. In other words the gas transport through the pores is unlikely to be important, but cannot be ignored, as is very important and basis for understanding permeability in the rock. However, the high connectivity of kerogen provides the potential pathways for gas flow throughout the whole sample.

It was also observed that pores within shale samples are oblate at all scales, and the smaller pores are visible by FIB-SEM, which indicating that they are more likely to connect with each other. However, the large pores are shown in μ -CT and Nano-CT. A number of permeability have also been calculated for all the measurements including μ -CT, Nano-CT, FIB-SEM images,

providing 2.98 nD from μ -CT, 2.61 nD for the nano-CT, and 13.8 nD from FIB-DEM data. These permeability estimation are in broadly agreeing with experimental approaches (GRI, MIP, N₂ adsorption), and shown samples used have a high shale gas potential.

Finally, the geometrical characterisations in this study leads to an improved understanding of mineral, kerogen and pore networks in shales covering a wide range of scales. The results of this type of multiscale imaging can be useful not only for shale gas but also for other many applications such as the study of reservoirs and cap rocks for carbon sequestration, geothermal reservoirs, and potential sites for the long-term disposal of radioactive material . Additionally, the novel technique that has been applied in this study can be also easily extended to other nanoporous materials used in medical applications, engineering applications (mechanical, chemical, civil, and also in biomechanical engineering), food industry, and catalytic reactions, as well as nano-membranes and fuel cells.

8.2 Future work suggestions

Based on the detailed study in multi-scale imaging of the microstructures properties of shales undertaken in this thesis, some opportunities of further studies can be identified, such as, correlative techniques along with 3D imaging, and numerical modelling based on the imaging results. Consequently, some future research areas of imaging might have two key aspects: correlative imaging, and modelling based image details.

8.2.1 Correlative imaging

Although the 3D imaging technique has been shown to be powerful tool to visualise and quantify fine microstructure distribution in gas shales, this cannot be used alone for the complete understanding of microstructure properties of shales. Therefore the 2D/3D imaging techniques such as SEM, EDX, μ -CT, Nano-CT and FIB-SEM, as well as some physical measurements including XRD, GRI, N₂ and MIP measurements could be applied to produce valuable information for the same sample or even the same region of interest in a sample. A typical of the preparation of small size of samples volume $25 \times 25 \times 25 \mu\text{m}$ and the 3D images can be acquired by means of non-destructive technique (μ -CT, Nano-CT) followed by a destructive technique (FIB-SEM) to produce high-resolution microstructural information, meaning that the same volume of sample can be analysed using two methods on the same region of shale which is a part of a correlative imaging work.

In addition, some of physical measurements can be applied after scans and milling within the same rock samples, for example, using GRI, XRD and N₂ measurements. Not only can these correlative techniques verify the volume percentages of shale sample but can also provide more details of understanding and quantification of pores which cannot be recognized from imaging results.

In summary, the sample preparation and image process could be extremely challenging, particularly dealing with different measurements on the same sample, these correlative methods together with multi-scale imaging will have a significant influence on future studies of microstructures of gas shale.

8.2.2 Modelling based imaging

The Modelling approaches can be used to estimate the permeability (flow) through pores within shales, which are still poorly understood. The basic pore system model includes the network and pore size distribution, as well as the associated kerogen or minerals, and the permeability prediction depend on the quantified pore system.

The flow properties in gas shale can be estimated based on modelling procedures such as absolute and relative permeabilities. There are different numerical methods that are applied or used to estimate the flow through pore. These can be allocated into two types: (i) network modelling, and (ii) direct simulation on image voxels.

In network modelling, the network (pore space) is extracted from the 3D image that obtained from tomographic methods such as μ -CT, Nano-CT and FIB-SEM imaging through which the relevant to the flow transport (Blunt et al., 2013; Øren and Bakke, 2003; Piri and Blunt, 2005; Raeini et al., 2017). In general, the pore-connectivity in shale is very complex due to the very small size of pores. In order to describe the gas transport through a sample, a simulation must be provided with at least one connected path across the whole area of interest. In this study, the pores within samples were unconnected and therefore the flow through the kerogen have been simulated as well as the pore system.

When pore sizes are above 100 nm or so, permeability simulation based on Darcy' law can be used for gas transport, and the assumption of the fluid conditions including single phase incompressible and laminar flow (Peng et al., 2015; Zhang et al., 2012), while for the pores sizes under 100 nm, the permeability can be simulated using the lattice Boltzmann method (LBM) based on Knudsen diffusion (Chen et al., 2015; Javadpour, 2009). Additionally, for pores below 20 nm, the pore size can be measured by nitrogen adsorption and mercury injection experiments. These pores are estimated to cover a locally connected flow paths for gas molecules and that can be used to build up the whole pore network model combined with visible pores in imaging data.

On the other hand, in direct simulation, the main equations of the transport and flow are dependent on known parameters including resolution (voxel size) and image size, porosity, pore-size, pore volume, grain diameter and surface area. The permeability can be determined based on these parameters and this approach does not need calibration to an empirical data set. Furthermore, for both of analytical permeability methods and calculations are presented in Chapters 6 and 7.

9. References

- Abramowitz, M., Stegun, I.A. and Romer, R.H., 1988. Handbook of mathematical functions with formulas, graphs, and mathematical tables.
- Ajiz, M.A. and Jennings, A., 1984. A robust incomplete Choleski-conjugate gradient algorithm. *International Journal for numerical methods in engineering*, 20(5), pp.949-966.
- Akbarabadi, M., Saraji, S., Piri, M., Georgi, D. & Delshad, M. 2017. Nano-scale experimental investigation of in-situ wettability and spontaneous imbibition in ultra-tight reservoir rocks. *Advances in Water Resources*, 107, 160-179.
- Akkutlu, I. Y. & Fathi, E. 2012. Multiscale gas transport in shales with local kerogen heterogeneities. Paper SPE-146422-PA, Society of Petroleum Engineers. *SPE Journal*, 17 (4), 1002-1011.
- Aligizaki, K.K., 2005. Pore structure of cement-based materials: testing, interpretation and requirements. Crc Press.
- Ambrose, R.J., Hartman, R.C., Diaz-Campos, M., Akkutlu, I.Y. and Sondergeld, C.H. 2010. New pore-scale considerations for shale gas-in-place calculations. SPE-131772, paper presented at the Unconventional Gas Conference, SPE, Pittsburgh, PA, February 23-25.
- Ambrose, R.J., Hartman, R.C., Diaz-Campos, M., Akkutlu, I.Y., Sondergeld, C.H. 2012. Shale gas-in-place calculations Part I: new pore-scale considerations. Paper SPE-131772-PA, Society of Petroleum Engineers. *SPE Journal*, 17 (1).
- Ambrose, R.J., Hartman, R.C., Diaz-Campos, M., Akkutlu, Y., Sondergeld, C.H. 2010. New pore-scale considerations for shale gas in place calculations. Paper SPE-131772-MS, Society of Petroleum Engineers. Paper presented at the Petroleum Engineers Unconventional Gas Conference, 23-25 February, Pittsburgh, Pennsylvania, USA.
- Andrew, M., Bijeljic, B. and Blunt, M.J., 2013. Pore-scale imaging of geological carbon dioxide storage under in situ conditions. *Geophysical Research Letters*, 40(15), pp.3915-3918.
- Andrews, I.J., 2013. The Carboniferous Bowland Shale gas study: geology and resource estimation. British Geological Survey/Department of Energy and Climate Change, London.
- Bahr, K. 1997. Electrical anisotropy and conductivity distribution functions of fractal random networks and of the crust: the scale effect of connectivity. *Geophysical Journal International*, 130(3), 649-660.
- Bai, B., Elgmati, M., Zhang, H. and Wei, M., 2013. Rock characterization of Fayetteville shale gas plays. *Fuel*, 105, pp.645-652.
- Bai, B., Zhu, R., Wu, S., Yang, W., Gelb, J., Gu, A., Zhang, X. & Su, L. 2013a. Multi-scale method of Nano(Micro)-CT study on microscopic pore structure of tight sandstone of Yanchang Formation, Ordos Basin. *Petroleum Exploration and Development*, 40, 354-358.
- Barrett, E.P., Joyner, L.G. and Halenda, P.P., 1951. The determination of pore volume and area distributions in porous substances. I. Computations from nitrogen isotherms. *Journal of the American Chemical society*, 73(1), pp. 373-380.
- Bear, J., 1988. Dynamics of fluids in porous media. Elsevier, New York
- Begg, S.H. and King, P.R. 1985. Modelling the Effects of Shales on Reservoir Performance: Calculation of Effective Vertical Permeability. Paper SPE 13529, Society of Petroleum Engineers. doi:10.2118/13529-MS.

- Begg, S.H., Carter, R.R. and Dranfield, P. 1989. Assigning Effective Values to Simulator Gridblock Parameters for Heterogeneous Reservoirs, Paper SPE 16754, Society of Petroleum Engineers. doi:10.2118/16754-PA.
- Berg, S., Ott, H., Klapp, S.A., Schwing, A., Neiteler, R., Brussee, N., Makurat, A., Leu, L., Enzmann, F., Schwarz, J.O. and Kersten, M., 2013. Real-time 3D imaging of Haines jumps in porous media flow. *Proceedings of the National Academy of Sciences*, 110(10), pp.3755-3759.
- Bertier, P., Schweinar, K., Stanjek, H., Ghanizadeh, A.M.I.N., Clarkson, C.R., Busch, A.N.D.R.E.A.S., Kampman, N.I.K.O., Prinz, D.I.R.K., Amann-Hildenbrand, A.L.E.X.A.N.D.R.A., Krooss, B.M. and Pipich, V.I.T.A.L.I.Y., 2016. On the use and abuse of N₂ physisorption for the characterization of the pore structure of shales. In *The Clay Minerals Society Workshop Lectures Series (Vol. 21, pp. 151-161)*.
- Best, M., Katsube, T., 1995. Shale permeability and its significance in hydrocarbon exploration. *The Leading Edge* 14, 165-170.
- Bhargava, S., Awaja, F. and Subasinghe, N.D., 2005. Characterisation of some Australian oil shale using thermal, X-ray and IR techniques. *Fuel*, 84(6), pp. 707-715.
- Bin, B., Rukai, Z., Songtao, W., Wenjing, Y.A.N.G., Gelb, J., Gu, A., ZHANG, X. and Ling, S.U., 2013. Multi-scale method of Nano (Micro)-CT study on microscopic pore structure of tight sandstone of Yanchang Formation, Ordos Basin. *Petroleum Exploration and Development*, 40(3), pp.354-358.
- Blunt, M.J., Bijeljic, B., Dong, H., Gharbi, O., Iglauer, S., Mostaghimi, P., Paluszny, A. and Pentland, C., 2013. Pore-scale imaging and modelling. *Advances in Water resources*, 51, pp.197-216.
- Boitnott, G.N., 1997, January. Use of complex pore pressure transients to measure permeability of rocks. In *SPE Annual Technical Conference and Exhibition*. Society of Petroleum Engineers.
- Boruah, A. and Ganapathi, S., 2015. Microstructure and pore system analysis of Barren Measures shale of Raniganj field, India. *Journal of Natural Gas Science and Engineering*, 26, pp. 427-437.
- Brace, W., Walsh, J.B. and Frangos, W.T., 1968. Permeability of granite under high pressure. *Journal of Geophysical research*, 73(6), pp.2225-2236.
- Brighenti, G., 1989, January. Effect of confining pressure on gas permeability of tight sandstones. In *ISRM International Symposium*. International Society for Rock Mechanics and Rock Engineering.
- Britt, L., 2012. Fracture stimulation fundamentals. *Journal of Natural Gas Science and Engineering*, 8, pp.34-51.
- Brunauer, S., Emmett, P.H. and Teller, E., 1938. Adsorption of gases in multimolecular layers. *Journal of the American chemical society*, 60(2), pp. 309-319
- Buades, A., Coll, B. and Morel, J.M., 2005. A non-local algorithm for image denoising. In *2005 IEEE Computer Society Conference on Computer Vision and Pattern Recognition (CVPR'05) (Vol. 2, pp. 60-65)*.
- Bultreys, T., De Boever, W., Cnudde, V., 2016. Imaging and image-based fluid transport modeling at the pore scale in geological materials: A practical introduction to the current state-of-the-art. *Earth-Science Rev.* 155, 93–128.

- Busch, A., Schweinar, K., Kampman, N., Coorn, A., Pipich, V., Feoktystov, A., Leu, L., Amann-Hildenbrand, A. and Bertier, P., 2017. Determining the porosity of mudrocks using methodological pluralism. Geological Society, London, Special Publications, 454(1), pp. 15-38.
- Bustin, R.M., Bustin, A.M., Cui, A., Ross, D. and Pathi, V.M., 2008. Impact of shale properties on pore structure and storage characteristics. In SPE shale gas production conference. Society of Petroleum Engineers.
- Casse, F., J. (1974). The effect of temperature and confining pressure on fluid flow properties of consolidated rocks. Doctor of Philosophy, Stanford University. PB-262732; SGP-TR-3, 196
- Chalmers, G.R., Bustin, R.M. and Power, I.M., 2012. Characterization of gas shale pore systems by porosimetry, pycnometry, surface area, and field emission scanning electron microscopy/transmission electron microscopy image analyses: Examples from the Barnett, Woodford, Haynesville, Marcellus, and Doig units Characterization of Gas Shale Pore Systems. AAPG Bulletin, 96(6), pp. 1099-1119.
- Chareonsuppanimit P., Mohammad S.A., Robinson R.L., Gasem K.A.M., 2012, High pressure adsorption of gases on shales: Measurements and modelling, International Journal of Coal Geology, 95, 34-46.
- Chen, C., Hu, D., Westacott, D. and Loveless, D., 2013. Nanometer-scale characterization of microscopic pores in shale kerogen by image analysis and pore-scale modeling. Geochemistry, Geophysics, Geosystems, 14(10), pp.4066-4075.
- Chen, F., Lu, S. and Ding, X., 2014. Organoporosity evaluation of shale: a case study of the Lower Silurian Longmaxi Shale in southeast Chongqing, China. The Scientific World Journal, 2014.
- Chen, L., Zhang, L., Kang, Q., Viswanathan, H.S., Yao, J. and Tao, W., 2015. Nanoscale simulation of shale transport properties using the lattice Boltzmann method: permeability and diffusivity. Scientific reports, 5(1), pp.1-8.
- Chenevert, M.E. and Sharma, A.K., 1993. Permeability and effective pore pressure of shales. SPE Drilling & completion, 8(01), pp.28-34.
- Choquette, P.W., Pray, L.C., 1970. Geologic nomenclature and classification of porosity in sedimentary carbonates. AAPG Bulletin 54, 207-250
- Chung, T., Wang, Y.D., Armstrong, R.T. and Mostaghimi, P. 2019. Approximating Permeability of Microcomputed-Tomography Images Using Elliptic Flow Equations. Paper SPE 191379, Society of Petroleum Engineers. doi:10.2118/191379-PA.
- Clarkson, C.R. and Bustin, R.M., 2000. Binary gas adsorption/desorption isotherms: effect of moisture and coal composition upon carbon dioxide selectivity over methane. International Journal of Coal Geology, 42(4), pp.241-271.
- Clarkson, C.R., Jensen, J.L. and Chipperfield, S., 2012. Unconventional gas reservoir evaluation: what do we have to consider?. Journal of Natural Gas Science and Engineering, 8, pp.9-33.
- Clarkson, C.R., Jensen, J.L., Pedersen, P.K., Freeman, M., 2012a. Innovative methods for flow-unit and pore-structure analyses in a tight siltstone and shale gas reservoir. AAPG Bulletin 96, 355-374.
- Clarkson, C.R., Solano, N., Bustin, R.M., Bustin, A.M.M., Chalmers, G.R.L., He, L., Melnichenko, Y.B., Radliński, A.P. and Blach, T.P., 2013. Pore structure characterization of North American shale gas reservoirs using USANS/SANS, gas adsorption, and mercury intrusion. Fuel, 103, pp.606-616.

- Clarkson, C.R., Wood, J., Burgis, S.E., Aquino, S.D., Freeman, M. and Birss, V.I., 2012b. Nanopore structure analysis and permeability predictions for a tight gas/shale reservoir using low-pressure adsorption and mercury intrusion techniques. In SPE Americas Unconventional Resources Conference. Society of Petroleum Engineers.
- Clennell, M. B. 1997. Tortuosity: a guide through the maze. Geological Society, London, Special Publications, 122, 299-344.
- Cnudde, V. and Boone, M.N., 2013. High-resolution X-ray computed tomography in geosciences: A review of the current technology and applications. *Earth-Science Reviews*, 123, pp.1-17.
- Cohen, M., 2012. South Africa energy minister favors tapping shale-gas fields. Bloomberg.
- Comisky, J.T., Santiago, M., McCollom, B., Buddhala, A. and Newsham, K.E., 2011. Sample size effects on the application of mercury injection capillary pressure for determining the storage capacity of tight gas and oil shales. In Canadian unconventional resources conference. Society of Petroleum Engineers.
- Conner, W.C., Cevallos-Candau, J.F., Weist, E.L., Pajares, J., Mendioroz, S., Cortes, A., 1986. Characterization of pore structure: porosimetry and sorption. *Langmuir* 2, 151–154.
- Cramer, D.D., 2008. Stimulating unconventional reservoirs: lessons learned, successful practices, areas for improvement. In SPE Unconventional Reservoirs Conference. Society of Petroleum Engineers.
- Cui X, Bustin AMM, Bustin RM (2009) Measurements of gas permeability and diffusivity of tight reservoir rocks: different approaches and their applications. *Geofluids* 9:208–223
- Curtis, J.B. 2002. Fractured shale-gas systems, *AAPG Bulletin*, 86(11), 1921-1938.
- Curtis, M. E., Sondergeld, C. H., Ambrose, R. J. & Rai, C. S. 2012. Microstructural investigation of gas shales in two and three dimensions using nanometer-scale resolution imaging. *AAPG Bulletin*, 96, 665-677.
- Curtis, M., Ambrose, R., Sondergeld, C., 2010. Structural characterization of gas shales on the micro- and nano-scales. Paper SPE-137693-MS, Society of Petroleum Engineers. Paper presented at the Canadian Unconventional Resources and International Petroleum Conference, 19-21 October, Calgary, Alberta, Canada.
- Curtis, M.E., Ambrose, R.J., Sondergeld, C.H. and Rai, C.S. 2011. Investigation of the relationship between organic porosity and thermal maturity in the Marcellus Shale. Paper SPE-144370-MS, Society of Petroleum Engineers. Paper presented at the North American Unconventional Gas Conference and Exhibition, 14-16 June, The Woodlands, Texas, USA.
- Dann, R., Turner, M., Close, M. and Knackstedt, M., 2011. Multi-scale characterisation of coastal sand aquifer media for contaminant transport using X-ray computed tomography. *Environmental Earth Sciences*, 63(5), pp.1125-1137.
- De Boer, J.H. and Lippens, B., 1964. Studies on pore systems in catalysts II. The shapes of pores in aluminium oxide systems. *Journal of Catalysis*, 3(1), pp. 38-43.
- Desbois, G., Urai, J.L., Kukla, P.A., Konstanty, J. and Baerle, C., 2011. High-resolution 3D fabric and porosity model in a tight gas sandstone reservoir: A new approach to investigate microstructures from mm-to nm-scale combining argon beam cross-sectioning and SEM imaging. *Journal of Petroleum Science and Engineering*, 78(2), pp.243-257.

- Dewhurst, D.N., Aplin, A.C., Sarda, J.P., Yang, Y., 1998. Compaction-driven evolution of porosity and permeability in natural mudstones: An experimental study. *Journal of Geophysical Research: Solid Earth* 103, 651-661.
- Dicker, A.I. and Smits, R.M., 1988, January. A practical approach for determining permeability from laboratory pressure-pulse decay measurements. In *International meeting on petroleum engineering*. Society of Petroleum Engineers.
- Driskill, B., Walls, J., DeVito, J. and Sinclair, S.W., 2013. 11 Applications of SEM Imaging to Reservoir Characterization in the Eagle Ford Shale, South Texas, USA.
- Dudley, D., 2019. BP Statistical Review of World Energy, June 2019. London BP.
- Ecker, C., Dvorkin, J., Nur, A.M., 2000. Estimating the amount of gas hydrate and free gas from marine seismic data. *Geophysics* 65, 565-573.
- EIA. 2019. U.S. Crude Oil and Natural Gas. U.S. Energy Information Administration. Retrieved December 2019, from <https://www.eia.gov/naturalgas/crudeoilreserves/pdf/usreserves.pdf>
- EIA. 2020. Annual Energy Outlook 2020 with projections to 2050. Retrieved from January 2020, <https://www.eia.gov/outlooks/aeo/pdf/aeo2020.pdf>
- Epting, W.K., Gelb, J. and Litster, S., 2012. Resolving the Three-Dimensional Microstructure of Polymer Electrolyte Fuel Cell Electrodes using Nanometer-Scale X-ray Computed Tomography. *Advanced Functional Materials*, 22(3), pp.555-560.
- Esemé, E., Krooss, B.M. and Littke, R., 2012. Evolution of petrophysical properties of oil shales during high-temperature compaction tests: Implications for petroleum expulsion. *Marine and Petroleum Geology*, 31(1), pp. 110-124.
- Etminan, S.R., Javadpour, F., Maini, B.B., Chen, Z., 2014. Measurement of gas storage processes in shale and of the molecular diffusion coefficient in kerogen. *International Journal of Coal Geology* 123, 10-19.
- Ewing, R.P., Horton, R., 2002. Diffusion in sparsely connected porespace: temporal and spatial scaling. *Water Resources Research*, 38 (12), 1285.
- Fangwen, C., Xue, D., Shuangfang, L. and Yiwen, J., 2017. The pore characterization of the lower silurian Longmaxi shale in the southeast Chongqing, China using FE-SEM, LTNA and MIP methods. *Journal of Nanoscience and Nanotechnology*, 17(9), pp.6482-6488.
- Fisher, Q., Lorinczi, P., Grattoni, C., Rybalcenko, K., Crook, A. J., Allshorn, S., Burns, A. D. & Shafagh, I. 2017. Laboratory characterization of the porosity and permeability of gas shales using the crushed shale method: Insights from experiments and numerical modelling. *Marine and Petroleum Geology*, 86, 95-110
- Geng, L., Li, G., Zitha, P., Tian, S. and Sheng, M. 2016. A fractal permeability model for shale gas flow through heterogeneous matrix systems. *Journal of Natural Gas Science and Engineering*, 35, 593-604.
- Ghanizadeh, A., Gasparik, M., Amann-Hildenbrand, A., Gensterblum, Y. and Krooss, B.M., 2014. Experimental study of fluid transport processes in the matrix system of the European organic-rich shales: I. Scandinavian Alum Shale. *Marine and Petroleum Geology*, 51, pp.79 - 99.
- Glorioso, J.C. and Rattia, A., 2012, March. Unconventional reservoirs: basic petrophysical concepts for shale gas. In *SPE/EAGE European unconventional resources conference & exhibition-from potential to production* (pp. cp-285). European Association of Geoscientists & Engineers.

- Glover P.W.J. (2010). A generalised Archie's law for n phases: *Geophysics*, 75(6), E247-E265, doi: 10.1190/1.3509781.
- Glover P.W.J. (2015). Geophysical Properties of the Near Surface Earth: Electrical Properties, In: Gerald Schubert (editor-in-chief) *Treatise on Geophysics*, 2nd edition, Vol 11. Oxford: Elsevier, 89-137.
- Glover P.W.J. 2009. What is the cementation exponent? A new interpretation: *The Leading Edge*, 556, 82-85.
- Glover, P. W. J. 2018. Modelling pH-Dependent and Microstructure-Dependent Streaming Potential Coefficient and Zeta Potential of Porous Sandstones. *Transport in Porous Media*, 124, 31-56.
- Glover, P. W. J. Geophysical Properties of the Near Surface Earth: Electrical Properties. In Gerald Schubert (Editor-in-Chief) *Treatise on Geophysics*, 2nd ed.; Elsevier: Oxford, 2015; Vol. 11, pp 89– 137.
- Glover, P.W. and Walker, E., 2009. Grain-size to effective pore-size transformation derived from electrokinetic theory. *Geophysics*, 74(1), pp. E17-E29
- Glover, P.W., 2010. A generalized Archie's law for n phases. *Geophysics*, 75(6), pp.E247-E265.
- Gregg, S.J., Sing, K.S.W., 1982. Adsorption, surface area and porosity academic. New York 242–245.
- Gundermann, T. and Odenbach, S., 2014. Investigation of the motion of particles in magnetorheological elastomers by X- μ CT. *Smart materials and structures*, 23(10), p.105013.
- Guo C., Xu J., Wei M., & Jiang R. (2014). Pressure transient and rate decline analysis for hydraulic fractured vertical wells with finite conductivity in shale gas reservoirs. *Journal of Petroleum Exploration and Production Technology*, 1–9.
- Guo, C., Wei, M. and Liu, H., 2015. Modeling of gas production from shale reservoirs considering multiple transport mechanisms. *PloS one*, 10(12), p.e0143649.
- Hajizadeh, A., Safekordi, A., Farhadpour, F.A., 2011. A multiple-point statistics algorithm for 3D pore space reconstruction from 2D images. *Adv. Water Resour.* 34, 1256–1267.
- Haskett, S.E., Narahara, G.M. and Holditch, S.A., 1988. A method for simultaneous determination of permeability and porosity in low-permeability cores. *SPE formation evaluation*, 3(03), pp.651-658.
- Haswell, R., Zeile, U., Mensch, K., 2008. Van Gogh's painting grounds: an examination of barium sulphate extender using analytical electron microscopy—SEM/FIB/TEM/EDX. *Microchim. Acta* 161, 363–369.
- Heath, J.E., Dewers, T.A., McPherson, B.J.O.L., Petrusak, R., Chidsey, T.C., Rinehart, A.J., Mozley, P.S., 2011. Pore networks in continental and marine mudstones: Characteristics and controls on sealing behavior. *Geosphere* 7, 429-454.
- Heller, R., Vermynen, J., Zoback, M., 2014. Experimental investigation of matrix permeability of gas shales. *AAPG Bulletin* 98, 975-995.
- Hill D. G., Nelson C.R., 2000, Gas productive fractured shales - an overview and update, *GasTIPS*, 6(2), 4-13.
- Hill, R.J., Zhang, E., Katz, B.J., Tang, Y. 2007. Modeling of gas generation from the Barnett Shale, Fort Worth Basin, Texas. *AAPG Bulletin*, 91(4), 501-521.
- Hsieh, P.A., Tracy, J.V., Neuzil, C.E., Bredehoeft, J.D. and Silliman, S.E., 1981, June. A transient laboratory method for determining the hydraulic properties of 'tight' rocks—I. Theory. In

International Journal of Rock Mechanics and Mining Sciences & Geomechanics Abstracts (Vol. 18, No. 3, pp. 245-252

- Hughes, J.D., 2015. Shale Gas Reality Check- Revisiting the U.S. Department of Energy Play-by-play Forecasts through 2040 from Annual Energy Outlook 2015. Post Carbon Institute, California, USA.
- Hurlimann, M.D., Helmer, K.G., Latour, L.L. and Sotak, C.H., 1994. Restricted diffusion in sedimentary rocks. Determination of surface-area-to-volume ratio and surface relaxivity. *Journal of Magnetic Resonance, Series A*, 111(2), pp. 169-178.
- Iassonov, P., Gebrenegus, T. and Tuller, M., 2009. Segmentation of X-ray computed tomography images of porous materials: A crucial step for characterization and quantitative analysis of pore structures. *Water Resources Research*, 45(9).
- Ishitani, T., Umemura, K., Ohnishi, T., Yaguchi, T. and Kamino, T., 2004. Improvements in performance of focused ion beam cross-sectioning: aspects of ion-sample interaction. *Microscopy*, 53(5), pp. 443-449.
- IUPAC, 1994. Physical Chemistry Division Commission on Colloid and Surface Chemistry, Subcommittee on Characterization of Porous Solids: Recommendations for the characterization of porous solids (Technical Report). *Pure and Applied Chemistry* 66 1739-1758.
- Iwai, H., Shikazono, N., Matsui, T., Teshima, H., Kishimoto, M., Kishida, R., Hayashi, D., Matsuzaki, K., Kanno, D., Saito, M. and Muroyama, H., 2010. Quantification of SOFC anode microstructure based on dual beam FIB-SEM technique. *Journal of Power Sources*, 195(4), pp.955-961.
- Jackson, J.A., Mehl, J.P., Neuendorf, K.K., 2005. *Glossary of geology*. Springer. Berlin. ISBN 3-540-27951-2.
- Jarvie D.M., Hill R.J., Ruble T.E., Pollastro R.M., 2007, Unconventional shale-gas systems: the Mississippian Barnett Shale of north-central Texas as one model for thermogenic shale-gas assessment, *AAPG Bulletin*, 91(4), 475-499.
- Jarvie, D.M., 2010. Worldwide shale resource plays and potential. *AAPG European Region ICE*, Kiev, Ukraine, pp.17-19.
- Jarvie, D.M., Hill, R.J. and Pollastro, R.M., 2005. Assessment of the gas potential and yields from shales: The Barnett Shale model. *Oklahoma Geological Survey Circular*, 110(2005), pp.37-50.
- Javadpour, F., 2009. Nanopores and apparent permeability of gas flow in mudrocks (shales and siltstone). *Journal of Canadian Petroleum Technology*, 48(08), pp.16-21.
- Javadpour, F., Fisher, D. & Unsworth, M. 2007. Nanoscale gas flow in shale gas sediments.
- Jennings, B.R. and Parslow, K., 1988. Particle size measurement: the equivalent spherical diameter. *Proceedings of the Royal Society of London. A. Mathematical and Physical Sciences*, 419(1856), pp. 137-149.
- Jennings, H.M., Thomas, J.J., Gevrenov, J.S., Constantinides, G. and Ulm, F.J., 2007. A multi-technique investigation of the nanoporosity of cement paste. *Cement and Concrete Research*, 37(3), pp.329-336.
- Jiao, K., Yao, S., Liu, C., Gao, Y., Wu, H., Li, M. and Tang, Z., 2014. The characterization and quantitative analysis of nanopores in unconventional gas reservoirs utilizing FESEM-FIB and

image processing: An example from the lower Silurian Longmaxi Shale, upper Yangtze region, China. *International Journal of Coal Geology*, 128, pp.1-11.

- Johnson, D.L., Koplik, J. and Schwartz, L.M., 1986. New pore-size parameter characterizing transport in porous media. *Physical review letters*, 57(20), p. 2564.
- Jones, S.C., 1997. A technique for faster pulse-decay permeability measurements in tight rocks. *SPE formation evaluation*, 12(01), pp.19-26.
- Josh, M., Esteban, L., Delle Piane, C., Sarout, J., Dewhurst, D.N. and Clennell, M.B., 2012. Laboratory characterisation of shale properties. *Journal of Petroleum Science and Engineering*, 88, pp.107-124.
- Kargbo DM, Wilhelm RG, Campbell DJ. Natural Gas Plays in the Marcellus Shale: Challenges and Potential Opportunities. *Environ Sci Technol* 2010; 44: 5679–5684.
- Kargbo, D.M., Wilhelm, R.G. and Campbell, D.J., 2010. Natural gas plays in the Marcellus Shale: Challenges and potential opportunities.
- Ketcham, R.A. and Carlson, W.D., 2001. Acquisition, optimization and interpretation of X-ray computed tomographic imagery: applications to the geosciences. *Computers & Geosciences*, 27(4), pp. 381-400.
- Klaver, J., Desbois, G., Littke, R., Urai, J.L., 2015. BIB-SEM characterization of pore space morphology and distribution in postmature to overmature samples from the Haynesville and Bossier Shales. *Marine and Petroleum Geology* 59, 451-466.
- Klaver, J., Desbois, G., Urai, J.L. and Littke, R., 2012. BIB-SEM study of the pore space morphology in early mature Posidonia Shale from the Hils area, Germany. *International Journal of Coal Geology*, 103, pp.12-25.
- Klinkenberg L J. (1941). The Permeability of Porous Media to Liquids and Gases. *Drilling and production practice*.
- Knudsen, M., 1934. *The Kinetic Theory of Gases*, Methuen & Co. Ltd., London.59-130.
- Korfiatis, P., Skiadopoulos, S., Sakellaropoulos, P., Kalogeropoulou, C. and Costaridou, L., 2007. Combining 2D wavelet edge highlighting and 3D thresholding for lung segmentation in thin-slice CT. *The British journal of radiology*, 80(960), pp.996-1004.
- Kozeny, J., 1927. *Über kapillare leitung des wassers in boden: Sitzungsberichte der Wissenschaften*, 136, 271–306.
- Kranz, R.L., 1983. Microcracks in rocks: A review. *Tectonophysics* 100, 449-480.
- Krueger, R., 1999. Dual-column (FIB–SEM) wafer applications. *Micron* 30, 221–226.
- Landis, E.N. and Keane, D.T., 2010. X-ray microtomography. *Materials characterization*, 61(12), pp. 1305-1316.
- Lasagni, F., Lasagni, A., Engstler, M., Degischer, H.P. and Muecklich, F., 2008. Nano-characterization of cast structures by FIB-tomography. *Advanced Engineering Materials*, 10(1-2), pp.62-66.
- Law, B.E., Curtis, J.B. 2002. Introduction to petroleum systems, *AAPG Bulletin*, 86, pp1851-1852
- Lazar, O.R., Bohacs, K.M., Macquaker, J.H., Schieber, J. and Demko, T.M., 2015. Capturing Key Attributes of Fine-Grained Sedimentary Rocks In Outcrops, Cores, and Thin Sections: Nomenclature and Description Guidelines. *Journal of Sedimentary Research*, 85(3), pp. 230-246.

- Lee, S., Speight, J.G., Loyalka, S.K., 2007. Handbook of Alternative Fuel Technologies, Green Chemistry and Chemical Engineering. CRC Press.
- Leeftink, T.N., 2015. Comparative analysis of shale permeability measurements.
- Lehr, J. 2019. Understand how shale gas companies drill horizontally. Accessed on 10/03/201, from <https://www.cfact.org/2019/04/03/do-you-really-understand-how-shale-gas-companies-drill-horizontally/>
- Lemmens, H., Butcher, A., Botha, P., 2011. FIB/SEM and SEM/EDX: a New Dawn for the SEM in the Core Lab? J. Petrophysics SPWLA 52, 1–12.
- Li, B., Liu, R. and Jiang, Y. 2016. A multiple fractal model for estimating permeability of dual porosity media. Journal of Hydrology, 540, 659-669.
- Littke R., Krooss B., Uffmann A.K., Schulz H.-M., Horsfield B., 2011, Unconventional Gas Resources in the Paleozoic of Central Europe, Oil and Gas Science and Technology, 66(6), 953-978.
- Long, H., Swennen, R., Foubert, A., Dierick, M. and Jacobs, P., 2009. 3D quantification of mineral components and porosity distribution in Westphalian C sandstone by microfocus X-ray computed tomography. Sedimentary Geology, 220(1-2), pp. 116-125.
- Loucks, R.G., Reed, R.M., Ruppel, S.C. and Hammes, U., 2012. Spectrum of pore types and networks in mudrocks and a descriptive classification for matrix-related mudrock pores. AAPG bulletin, 96(6), pp.1071-1098.
- Loucks, R.G., Reed, R.M., Ruppel, S.C. and Jarvie, D.M., 2009. Morphology, genesis, and distribution of nanometer-scale pores in siliceous mudstones of the Mississippian Barnett Shale. Journal of sedimentary research, 79(12), pp.848-861.
- Lowell, S., Shields, J.E., Thomas, M.A. and Thommes, M., 2012. Characterization of porous solids and powders: surface area, pore size and density (Vol. 16). Springer Science & Business Media.
- Lu, J., Ruppel, S.C., Rowe, H.D., 2014. Organic matter pores and oil generation in the Tuscaloosa marine shale. AAPG Bulletin. 20,140,915.
- Lu, S., Chen, F. and Ju, Y., 2017. Type and Quantitative Evaluation of Micropores in Longmaxi Shale of Southeast Chongqing, China. Journal of Nanoscience and Nanotechnology, 17(9), pp.7035-7043.
- Luffel, D. L., Hopkins, C. W., Holditch, S. A. and Shettler, P. D. (1993). "Matrix Permeability G2014. Direct and Inverse Methods for Determining Gas Flow Properties of Shale. 2014, 1-26.
- Luffel, D., Curtis, J., Guidry, K., 1996. Development of Laboratory and Petrophysical Techniques for Evaluating Shale Reservoirs. Gas Research Institute Chicago, p. 304.
- Ma, L., Dowey, P. J., Rutter, E., Taylor, K. G. & Lee, P. D. 2019. A novel upscaling procedure for characterising heterogeneous shale porosity from nanometer-to millimetre-scale in 3D. Energy, 181, 1285-1297.
- Ma, L., Fauchille, A.L., Dowey, P.J., Pilz, F.F., Courtois, L., Taylor, K.G. and Lee, P.D., 2017. Correlative multi-scale imaging of shales: a review and future perspectives. Geological Society, London, Special Publications, 454(1), pp.175-199.
- Ma, L., Slater, T., Dowey, P. J., Yue, S., Rutter, E. H., Taylor, K. G. & Lee, P. D. 2018. Hierarchical integration of porosity in shales. Scientific Reports, 8, 11683.

- Ma, L., Taylor, K. G., Lee, P. D., Dobson, K. J., Dowey, P. J and Courtois, L. 2016. Novel 3D centimetre-to nano-scale quantification of an organic-rich mudstone: The Carboniferous Bowland Shale, Northern England. *Marine and Petroleum Geology*, 72, 193-205.
- Ma, Y., Pan, Z., Zhong, N., Connell, L. D., Down, D. I., Lin, W. and Zhang, Y. 2016. Experimental study of anisotropic gas permeability and its relationship with fracture structure of Longmaxi Shales, Sichuan Basin, China. *Fuel*, 180, 106–115, doi:10.1016/j.fuel.2016.04.029.
- Ma, Y., Zhong, N., Li, D., Pan, Z., Cheng, L. and Liu, K., 2015. Organic matter/clay mineral intergranular pores in the Lower Cambrian Lujiaping Shale in the north-eastern part of the upper Yangtze area, China: A possible microscopic mechanism for gas preservation. *International Journal of Coal Geology*, 137, pp.38-54.
- MacBeth, C., HajNasser, Y., Stephen, K. and Gardiner, A., 2011. Exploring the effect of meso-scale shale beds on a reservoir's overall stress sensitivity to seismic waves. *Geophysical Prospecting*, 59(1), pp.90-110.
- Magoon, L.B. and Dow, W.G., 1991. The petroleum system-from source to trap. *AAPG Bulletin (American Association of Petroleum Geologists);(United States)*, 75(CONF-910403-).
- Mair, R., Bickle, M., Goodman, D., Koppelman, B., Roberts, J., Selley, R., Shipton, Z., Thomas, H., Walker, A., Woods, E. and Younger, P., 2012. Shale gas extraction in the UK: a review of hydraulic fracturing.
- Marsh, H., 1987. Adsorption methods to study microporosity in coals and carbons—a critique. *Carbon*, 25(1), pp.49-58.
- Mastalerz, M., Schimmelmann, A., Drobniak, A., Chen, Y., 2013. Porosity of Devonian and Mississippian New Albany Shale across a maturation gradient: Insights from organic petrology, gas adsorption, and mercury intrusion. *AAPG Bulletin* 97, 1621-1643.
- Mckernan, R., Rutter, E., Mecklenburgh, J., Taylor, K., Covey-Crump, S., 2014. Influence of Effective Pressure on Mudstone Matrix Permeability: Implications for Shale Gas Production, SPE/EAGE European Unconventional Resources Conference and Exhibition. Society of Petroleum Engineers. SPE-167762-MS.
- Meko, T. and Karklis, L. 2017. The United States of oil and gas, *Washington Post*.
- Michael, G., 2001. X-ray computed tomography. *Physics Education* 36, 442.
- Milliken, K.L., Rudnicki, M., Awwiller, D.N. and Zhang, T., 2013. Organic matter–hosted pore system, Marcellus formation (Devonian), Pennsylvania. *AAPG bulletin*, 97(2), pp.177-200.
- Milner, M., McLin, R., Petriello, J., 2010. Imaging texture and porosity in mudstones and shales: Comparison of secondary and ion-milled backscatter SEM methods, in: *Canadian Unconventional Resources and International Petroleum Conference*. Society of Petroleum Engineers.
- Mishra, P.K., Akbar, B., 2011. Effectiveness of Digital Rock Physical Laboratories In Characterisation Of Heterogenous And Complex Carbonates- A Synthesis, *International Petroleum Technology Conference*. International Petroleum Technology Conference, Bangkok, Thailand.
- Moghadam, A.A. and Chalaturnyk, R., 2015, October. Laboratory investigation of shale permeability. In *SPE/CSUR Unconventional Resources Conference*. Society of Petroleum Engineers.

- Moghaddam, R.N. and Jamiolahmady, M., 2019. Steady-state relative permeability measurements of tight and shale rocks considering capillary end effect. *Transport in Porous Media*, 128(1), pp.75-96.
- Montgomery, S.L., Jarvie, D.M., Bowker, K.A., Pollastro, R.M., 2005. Mississippian Barnett Shale, Fort Worth basin, north-central Texas: Gas-shale play with multi-trillion cubic foot potential. *AAPG Bulletin* 89, 155-175.
- Moridis, G.J., Blasingame, T.A. and Freeman, C.M., 2010, January. Analysis of mechanisms of flow in fractured tight-gas and shale-gas reservoirs. In *SPE Latin American and Caribbean Petroleum Engineering Conference*. Society of Petroleum Engineers.
- Mostaghimi, P., Blunt, M.J. and Bijeljic, B., 2013. Computations of absolute permeability on micro-CT images. *Mathematical Geosciences*, 45(1), pp. 103-125.
- Nelson, P.H., 2009. Pore-throat sizes in sandstones, tight sandstones, and shales. *AAPG bulletin*, 93(3), pp.329-340.
- Nielsen, A.T. and Schovsbo, N.H., 2006. Cambrian to basal Ordovician lithostratigraphy in southern Scandinavia. *Bulletin of the Geological Society of Denmark*, 53, pp.47-92.
- Nolte, D.D., Pyrak-Nolte, L.J. and Cook, N.G.W. 1989. The fractal geometry of flow paths in natural fractures in rock and the approach to percolation. *Pure and Applied Geophysics PAGEOPH*, 131(1-2), 111-138.
- Ogilvie, S.R., Isakov, E. and Glover, P.W.J. 2006. Fluid flow through rough fractures in rocks: A new matching model for rough rock fractures. *Earth and Planetary Science Letters*, 604 241(3-4), 454-465.
- Okabe, H. and Blunt, M.J., 2004. Prediction of permeability for porous media reconstructed using multiple-point statistics. *Physical Review E*, 70(6), p.066135.
- Okabe, H. and Blunt, M.J., 2005. Pore space reconstruction using multiple-point statistics. *Journal of Petroleum Science and Engineering*, 46(1-2), pp.121-137.
- Okabe, H. and Blunt, M.J., 2007. Pore space reconstruction of vuggy carbonates using microtomography and multiple-point statistics. *Water Resources Research*, 43(12).
- Olson, R.K., Grigg, M.W., 2008. Mercury injection capillary pressure (MICP) a useful tool for improved understanding of porosity and matrix permeability distributions in shale reservoirs. *Am. Assoc. Pet. Geol. Search Discov. Artic.* 40322.
- Øren, P.E. and Bakke, S., 2003. Reconstruction of Berea sandstone and pore-scale modelling of wettability effects. *Journal of petroleum science and engineering*, 39(3-4), pp.177-199.
- Ougier-Simonin, A., Renard, F., Boehm, C. and Vidal-Gilbert, S., 2016. Microfracturing and microporosity in shales. *Earth-Science Reviews*, 162, pp. 198-226
- Ozkan, E., Raghavan, R.S. and Apaydin, O.G., 2010, January. Modeling of fluid transfer from shale matrix to fracture network. In *SPE Annual Technical Conference and Exhibition*. Society of Petroleum Engineers.
- Pan, Z., Ma, Y., Connell, L.D., Down, D.I. and Camilleri, M., 2015. Measuring anisotropic permeability using a cubic shale sample in a triaxial cell. *Journal of Natural Gas Science and Engineering*, 26, pp.336-344.
- Passey, Q.R., Bohacs, K.M., Esch, W.L., Klimentidis, R., Sinha, S., 2010. From Oil-Prone Source Rock to Gas-Producing Shale Reservoir - Geologic and Petrophysical Characterization of Unconventional Shale Gas Reservoirs, *Petroleum Engineers Unconventional Gas Conference*, Pittsburgh, Pennsylvania. SPE-131350-MS

- Peng, S. & Loucks, B. 2016. Permeability measurements in mudrocks using gas-expansion methods on plug and crushed-rock samples. *Marine and Petroleum Geology*, 73, 299-310.
- Peng, S., Hu, Q., Dultz, S. & Zhang, M. 2012. Using X-ray computed tomography in pore structure characterization for a Berea sandstone: Resolution effect. *Journal of Hydrology*, 472-473, 254-261.
- Peng, S., Yang, J., Xiao, X., Loucks, B., Ruppel, S.C. and Zhang, T., 2015. An integrated method for upscaling pore-network characterization and permeability estimation: example from the Mississippian Barnett Shale. *Transport in Porous Media*, 109(2), pp.359-376.
- Penumadu, D. and Dean, J., 2000. Compressibility effect in evaluating the pore-size distribution of kaolin clay using mercury intrusion porosimetry. *Canadian Geotechnical Journal*, 37(2), pp. 393-405.
- Piri, M. and Blunt, M.J., 2005. Three-dimensional mixed-wet random pore-scale network modeling of two-and three-phase flow in porous media. I. Model description. *Physical Review E*, 71(2), p.026301.
- Pollastro, R.M., Hill, R.J., Jarvie, D.M., Henry, M.E., 2003. Assessing Undiscovered Resources of the Barnett-Paleozoic Total Petroleum System, Bend Arch-Fort Worth Basin Province, Texas.
- Pommer, M., Milliken, K., 2015. Pore types and pore-size distributions across thermal maturity, Eagle Ford Formation, southern Texas. *Am. Assoc. Pet. Geol. Bull.* 99, 1713–1744.
- Profice, S., Lasseux, D., Jannot, Y., Jebara, N. and Hamon, G., 2012. Permeability, porosity and klinkenberg coefficient determination on crushed porous media. *Petrophysics*, 53(06), pp.430-438.
- Qing, W., Guojun, J., Hongpeng, L., JINGRU, B., Shaohua, L., 2010. Variation of the pore structure during microwave pyrolysis of oil shale. *Oil Shale* 27, 135–146.
- Raeini, A.Q., Bijeljic, B. and Blunt, M.J., 2017. Generalized network modeling: Network extraction as a coarse-scale discretization of the void space of porous media. *Physical Review E*, 96(1), p.013312.
- Rashid, F., Glover, P.W.J., Lorinczi, P., Collier, R. and Lawrence, J., 2015. Porosity and permeability of tight carbonate reservoir rocks in the north of Iraq. *Journal of Petroleum Science and Engineering*, 133, pp. 147-161.
- Rather, J.B., 1918. An accurate loss-on-ignition method for the determination of organic matter in soils. *Industrial & Engineering Chemistry*, 10(6), pp. 439-442.
- Revil, A. and Cathles Iii, L.M., 1999. Permeability of shaly sands. *Water Resources Research*, 35(3), pp. 651-662.
- Rezaee, R. and Rothwell, M., 2015. Gas shale: global significance, distribution, and challenges. *Fundamentals of Gas Shale Reservoirs*, pp.1-19.
- Ricard, L.P., MacBeth, C., HajNasser, Y., Schutjens, P., 2012. An evaluation of pore pressure diffusion into a shale overburden and sideburden induced by production-related changes in reservoir fluid pressure. *Journal of Geophysics and Engineering* 9, 345–358.
- Rine, J.M., Smart, E., Dorsey, W., Hooghan, K. and Dixon, M., 2014. Comparison of Porosity Distribution within Selected North American Shale Units by SEM Examination of Argon-Ion Milled Samples.

- Rivard, C., Lavoie, D., Lefebvre, R., Séjourné, S., Lamontagne, C. and Duchesne, M., 2014. An overview of Canadian shale gas production and environmental concerns. *International Journal of Coal Geology*, 126, pp.64-76.
- Rosenbrand, E., Fabricius, I.L., Fisher, Q. and Grattoni, C., 2015. Permeability in Rotliegend gas sandstones to gas and brine as predicted from NMR, mercury injection and image analysis. *Marine and Petroleum Geology*, 64, pp.189-202.
- Ross D.J.K., Bustin R. M., 2007, Impact of mass balance calculations on adsorption capacities in microporous shale gas reservoirs, *Fuel*, 86, 2696-2706.
- Ross D.J.K., Bustin R. M., 2009, the importance of shale composition and pore structure upon gas storage potential of shale gas reservoirs, *Marine and Petroleum Geology*, 26, 916-927.
- Roy, S., Raju, R., Chuang, H.F., Cruden, B.A., Meyyappan, M., 2003. Modeling gas flow through microchannels and nanopores. *Journal of Applied Physics* 93, 4870-4879.
- Rushig, J. A., Newsham, K. E., Lasswell, P. M., Cox, J. C. and Blasingame, T. A. (2004). Klinkenberg-Corrected Permeability Measurements in Tight Gas Sands: Steady-State Versus Unsteady-State Techniques. Annual Technical Conference and Exhibition. Houston, USA, SPE, 18. 10.2118/89867-MS.
- Rybalcenko, K., 2017. Gas flow measurements in shales: laboratory, field and numerical investigations (Doctoral dissertation, University of Leeds).
- Saif, T., Lin, Q., Butcher, A. R., Bijeljic, B. & Blunt, M. J. 2017. Multi-scale multi-dimensional microstructure imaging of oil shale pyrolysis using X-ray micro-tomography, automated ultra-high resolution SEM, MAPS Mineralogy and FIB-SEM. *Applied Energy*, 202, 628-647.
- Sakellariou, A., Sawkins, T.J., Senden, T.J., Arns, C.H., Limaye, A., Sheppard, A.P., Sok, R.M., Knackstedt, M.A., Pinczewski, W.V., Berge, L.I. and Øren, P.E., 2003. Micro-CT facility for imaging reservoir rocks at pore scales. In SEG Technical Program Expanded Abstracts 2003 (pp. 1664-1667). Society of Exploration Geophysicists.
- Sakellariou, A., Sawkins, T.J., Senden, T.J., Arns, C.H., Limaye, A., Sheppard, A.P., Sok, R.M., Knackstedt, M.A., Pinczewski, W.V., Berge, L.I. and Øren, P.E. 2003. Micro-CT facility for imaging reservoir rocks at pore scales. SEG Annual Meeting, Dallas, Texas, October 26-31.
- Sakhaee-Pour, A. and Bryant, S., 2012. Gas Permeability of Shale. SPE Reservoir Evaluation and Engineering, Paper SPE 146944, pp. 401-409.
- Saleh, A.A. and Castagna, J.P., 2004. Revisiting the Wyllie time average equation in the case of near-spherical pores. *Geophysics*, 69(1), pp. 45-55.
- Saraji, S. and Piri, M., 2015. The representative sample size in shale oil rocks and nano-scale characterization of transport properties. *International Journal of Coal Geology*, 146, pp.42-54.
- Schaffer, M., Wagner, J., Schaffer, B., Schmied, M. and Mulders, H., 2007. Automated three-dimensional X-ray analysis using a dual-beam FIB. *Ultramicroscopy*, 107(8), pp. 587-597.
- Schnook, J.L., 2012. Shale gas and hydrofracturing.
- Scholten, J.J.F., 1967. Mercury porosimetry and allied techniques, in: *Porous Carbon Solids*. Academic Press New York, pp. 225–250.
- Schrod, J.T., Ocampo, A., 1984. Variations in the pore structure of oil shales during retorting and combustion. *Fuel* 63, 1523–1527.
- Schulz, H.M., Horsfield, B. and Sachsenhofer, R.F., 2010, January. Shale gas in Europe: a regional overview and current research activities. In Geological Society, London, Petroleum Geology Conference series (Vol. 7, No. 1, pp. 1079-1085). Geological Society of London.

- Seaton, N.A. and Walton, J.P.R.B., 1989. A new analysis method for the determination of the pore size distribution of porous carbons from nitrogen adsorption measurements. *Carbon*, 27(6), pp. 853-861.
- Shabro, V., Torres-Verdín, C., Javadpour, F. and Sepehrnoori, K., 2012. Finite-difference approximation for fluid-flow simulation and calculation of permeability in porous media. *Transport in porous media*, 94(3), pp. 775-793.
- Sharma R. India plans shale gas block auctions. *The Wall Street Journal*; 2012.
- Shearing, P.R., Gelb, J., Yi, J., Lee, W.K., Drakopolous, M. and Brandon, N.P., 2010. Analysis of triple phase contact in Ni-YSZ microstructures using non-destructive X-ray tomography with synchrotron radiation. *Electrochemistry Communications*, 12(8), pp.1021-1024.
- Shen, S., Fang, Z. and Li, X., 2020. Laboratory measurements of the relative permeability of coal: A review. *Energies*, 13(21), p.5568.
- Sheppard, A.P., Sok, R.M. and Averdunk, H., 2004. Techniques for image enhancement and segmentation of tomographic images of porous materials. *Physica A: Statistical mechanics and its applications*, 339(1-2), pp. 145-151.
- Shi, M., Yu, B., Xue, Z., Wu, J. and Yuan, Y., 2015. Pore characteristics of organic-rich shales with high thermal maturity: A case study of the Longmaxi gas shale reservoirs from well Yuye-1 in southeastern Chongqing, China. *Journal of Natural Gas Science and Engineering*, 26, pp.948-959.
- Shu, Y., Xu, Y., Jiang, S., Zhang, L., Zhao, X., Pan, Z., Blach, T.P., Sun, L., Bai, L., Hu, Q. and Sun, M., 2020. Effect of Particle Size on Pore Characteristics of Organic-Rich Shales: Investigations from Small-Angle Neutron Scattering (SANS) and Fluid Intrusion Techniques. *Energies*, 13(22), p.6049.
- Sigal, R.F., 2009. A methodology for blank and conformance corrections for high pressure mercury porosimetry. *Measurement Science and Technology*, 20(4), p. 045108.
- Sing, K., 2001. The use of nitrogen adsorption for the characterisation of porous materials. *Colloids and Surfaces A: Physicochemical and Engineering Aspects* 187, 3-9.
- Sinha, S., Braun, E. M., Determan, M. D., Passey, S. A., Leonardi, J. A., Wood III, A. C., Zirkle, T. and Kudva, R. A. (2013). Steady-State Permeability Measurements on Intact Shale Samples at Reservoir Conditions - Effect of Stress, Temperature, Pressure, and Type of Gas. *Middle East Oil and Gas Show and Conference Manama, Bahrain, SPE*, 15. 10.2118/164263-MS.
- Sisk, C., Diaz, E., Walls, J., Grader, A. & Suhrer, M. 2010. 3D Visualization and Classification of Pore Structure and Pore Filling in Gas Shales. *SPE Annual Technical Conference and Exhibition. Florence, Italy: Society of Petroleum Engineers*.
- Sivel, V.G.M., Van den Brand, J., Wang, W.R., Mohdadi, H., Tichelaar, F.D., Alkemade, P.F.A. and Zandbergen, H.W., 2004. Application of the dual-beam FIB/SEM to metals research. *Journal of Microscopy*, 214(3), pp.237-245.
- Slatt, R.M. and O'Brien, N.R., 2011. Pore types in the Barnett and Woodford gas shales: Contribution to understanding gas storage and migration pathways in fine-grained rocks. *AAPG bulletin*, 95(12), pp.2017-2030.
- Soeder, D.J., 1988. Porosity and permeability of eastern Devonian gas shale. *SPE Formation Evaluation* 3, 116-124. SPE-15213-PA.
- Sok, R.M., Knackstedt, M.A., Varslot, T., Ghous, A., Latham, S. and Sheppard, A.P., 2010. Pore scale characterization of carbonates at multiple scales: Integration of Micro-CT, BSEM, and

FIBSEM. *Petrophysics-The SPWLA Journal of Formation Evaluation and Reservoir Description*, 51(06).

- Sondergeld, C.H., Ambrose, R.J., Rai, C.S., Moncrieff, J., 2010. Micro-structural studies of gas shales, SPE Unconventional Gas Conference. Society of Petroleum Engineers. Pittsburgh, Pennsylvania, SPE-131771-MS.
- Sondergeld, C.H., Rai, C.S., Curtis, M.E., 2013. Relationship between Organic Shale Microstructure and Hydrocarbon Generation, SPE Unconventional Resources Conference-USA. Society of Petroleum Engineers. Texas, USA, SPE-164540-MS.
- Speight, J.G., 2012b. Origin and Properties of Oil Shale, Shale Oil Production Processes.
- Spencer, T., Sartor, O. and Mathieu, M., 2014. Unconventional wisdom: an economic analysis of US shale gas and implications for the EU. *Studies*, 2, p.14.
- Stauber, M. and Müller, R., 2008. Micro-computed tomography: a method for the non-destructive evaluation of the three-dimensional structure of biological specimens. In *Osteoporosis* (pp. 273-292).
- Sun, H.Q. and Luo, Y.J., 2009. Adaptive watershed segmentation of binary particle image. *Journal of microscopy*, 233(2), pp. 326-330.
- Tang, X., Jiang, Z., Jiang, S. and Li, Z., 2016. Heterogeneous nanoporosity of the Silurian Longmaxi Formation shale gas reservoir in the Sichuan Basin using the QEMSCAN, FIB-SEM, and nano-CT methods. *Marine and Petroleum Geology*, 78, pp.99-109.
- Thommes, M. and Cychoz, K.A., 2014. Physical adsorption characterization of nanoporous materials: progress and challenges. *Adsorption*, 20(2-3), pp.233-250.
- Tinni, A., Fathi, E., Agarwal, R., Sondergeld, C.H., Akkutlu, I.Y. and Rai, C.S., 2012, January. Shale permeability measurements on plugs and crushed samples. In *SPE Canadian Unconventional Resources Conference*. Society of Petroleum Engineers.
- Torsæter, M., Vullum, P.E., Nes, O.M., Rinna, J., 2012. Nanostructure vs macroscopic properties of Mancos shale, pp. 1086-1098.
- Tuo, J.C.; Wu, C.J.; Zhang, M.F. Organic matter properties and shale gas potential of Paleozoic shales in Sichuan Basin, China. *J. Nat. Gas Sci. Eng.* 2016, 28, 434–446.
- U.S. Energy Information Administration (USEIA). 2011. World Shale Gas Resources: an initial assessment of 14 regions outside the United States. Report prepared by Advanced Resources International Inc. www.eia.gov/analysis/studies/worldshalegas/
- Van Brakel, J., Modrý, S., Svata, M., 1981. Mercury porosimetry: state of the art. *Powder Technol.* 29, 1–12.
- Vanorsdale C. R., 1987, Evaluation of Devonian Shale Gas Reservoirs, SPE Reservoir Engineering, SPE 14446.
- Vengosh, A., Warner, N., Jackson, R. & Darrah, T. 2013. The Effects of Shale Gas Exploration and Hydraulic Fracturing on the Quality of Water Resources in the United States. *Procedia Earth and Planetary Science*, 7, 863-866.
- Virnovsky, G. A., Skjaeveland, S. M., Surdal, J. and Ingsoy, P. (1995). Steady-State Relative Permeability Measurements Corrected for Capillary Effects. Annual Technical Conference & Exhibition Dallas, USA, SPE, 11. 10.2118/30541-MS.
- Vlassenbroeck, J., Dierick, M., Masschaele, B., Cnudde, V., Van Hoorebeke, L. and Jacobs, P., 2007. Software tools for quantification of X-ray microtomography at the UGCT. *Nuclear*

Instruments and Methods in Physics Research Section A: Accelerators, Spectrometers, Detectors and Associated Equipment, 580(1), pp. 442-445.

- Walsh, J.B., 1965. The effect of cracks on the compressibility of rock. *J. Geophys. Res.* 70, 381-389
- Wang, F.P. and Reed, R.M., 2009. Pore networks and fluid flow in gas shales. In SPE annual technical conference and exhibition. Society of Petroleum Engineers.
- Wang, Q., Chen, X., Jha, A.N. and Rogers, H., 2014. Natural gas from shale formation—the evolution, evidences and challenges of shale gas revolution in United States. *Renewable and Sustainable Energy Reviews*, 30, pp.1-28.
- Wang, S., Pomerantz, A. E., Xu, W., Lukyanov, A., Kleinberg, R. L. & Wu, Y.-S. 2017. The impact of kerogen properties on shale gas production: A reservoir simulation sensitivity analysis. *Journal of Natural Gas Science and Engineering*, 48, 13-23.
- Wang, Y., Pu, J., Wang, L., Wang, J., Jiang, Z., Song, Y.F., Wang, C.C., Wang, Y. and Jin, C., 2016. Characterization of typical 3D pore networks of Jiulaodong formation shale using nano-transmission X-ray microscopy. *Fuel*, 170, pp.84-91.
- Wang, Y., Wang, L.H., Wang, J.Q., Jiang, Z., Jin, C. and Wang, Y.F., 2017. Investigating microstructure of Longmaxi shale in Shizhu area, Sichuan Basin, by optical microscopy, scanning electron microscopy and micro-computed tomography. *Nuclear Science and Techniques*, 28(11), pp.1-10.
- Warner, D., 2011. Shale gas in Australia: a great opportunity comes with significant challenges. *Preview*, pp.18-21.
- Washburn, E.W., 1921. Note on a method of determining the distribution of pore sizes in a porous material. *Proceedings of the National academy of Sciences of the United States of America*, 7(4), p.115.
- Washburn, K.E., Birdwell, J.E., Foster, M. and Gutierrez, F., 2015. Detailed description of oil shale organic and mineralogical heterogeneity via Fourier transform infrared microscopy. *Energy & Fuels*, 29(7), pp.4264-4271.
- Webb, P.A. 2001. An introduction to the physical characterization of materials by mercury intrusion porosimetry with emphasis on reduction and presentation of experimental data. *Volume and Density for Particle Technologists*. Micromeritics Instrument.
- Westermarck S., 2000, Use of mercury porosimetry and nitrogen adsorption in characterisation of the pore structure of mannitol and microcrystalline cellulose powders, granules and tablets, PhD Thesis, Department of Pharmacy, University of Helsinki (Finland).
- Wu Y-S, Fakcharoenphol P. (2011). A Unified Mathematical Model for Unconventional Reservoir Simulation. Presented at EUROPEC/EAGE Annual Conference and Exhibition in Vienna, Austria, 23–26May. SPE-142884-MS.
- Wu, T., Li, X., Zhao, J. and Zhang, D., 2017. Multiscale pore structure and its effect on gas transport in organic-rich shale. *Water Resources Research*, 53(7), pp.5438-5450.
- Y Leon, C.A.L., 1998. New perspectives in mercury porosimetry. *Advances in colloid and interface science*, 76, pp.341-372.
- Yan, F. & Han, D.-H. 2013. Measurement of elastic properties of kerogen. *SEG Technical Program Expanded Abstracts 2013*. Society of Exploration Geophysicists.

- Yang, T., Li, X. and Zhang, D. 2015. Quantitative dynamic analysis of gas desorption contribution to production in shale gas reservoirs. *Journal of Unconventional Oil and Gas Resources*, 9, 18–30, doi:10.1016/j.juogr.2014.11.003
- Yang, Y. & Bao, F. 2017. Characteristics of shale nanopore system and its internal gas flow: A case study of the lower Silurian Longmaxi Formation shale from Sichuan Basin, China. *Journal of Natural Gas Geoscience*, 2, 303-311.
- Yang, Y. and Aplin, A.C., 2007. Permeability and petrophysical properties of 30 natural mudstones. *Journal of Geophysical Research: Solid Earth*, 112(B3).
- Zamirian, M., Aminian, K.K., Ameri, S. and Fathi, E., 2014, September. New steady-state technique for measuring shale core plug permeability. In *SPE/CSUR unconventional resources conference—canada*. Society of Petroleum Engineers.
- Zhang, H., Zhu, Y., Wang, Y., Kang, W. and Chen, S., 2016. Comparison of organic matter occurrence and organic nanopore structure within marine and terrestrial shale. *Journal of Natural Gas Science and Engineering*, 32, pp.356-363.
- Zhang, J. and Scherer, G.W., 2011. Comparison of methods for arresting hydration of cement. *Cement and Concrete Research*, 41(10), pp.1024-1036.
- Zhang, J. and Scherer, G.W., 2012. Permeability of shale by the beam-bending method. *International Journal of Rock Mechanics and Mining Sciences*, 53, pp.179-191.
- Zhang, J., Li, X., Wei, Q., Gao, W., Liang, W., Wang, Z. and Wang, F., 2017. Quantitative characterization of pore-fracture system of organic-rich marine-continental shale reservoirs: A case study of the Upper Permian Longtan Formation, Southern Sichuan Basin, China. *Fuel*, 200, pp.272-281.
- Zhang, N., Zhao, F., Guo, P., Li, J., Gong, W., Guo, Z. and Sun, X., 2018. Nanoscale pore structure characterization and permeability of mudrocks and fine-grained sandstones in coal reservoirs by scanning electron microscopy, mercury intrusion porosimetry, and low-field nuclear magnetic resonance.
- Zhang, S., Klimentidis, R.E. and Barthelemy, P., 2012, August. Micron to millimeter upscaling of shale rock properties based on 3D imaging and modeling. In *International Symposium of the Society of Core Analysts (Vol. 27, p. 30)*.
- Zhang, S., Klimentidis, R.E. and Barthelemy, P., 2012a. Micron to millimeter upscaling of shale rock properties based on 3D imaging and modeling. In *International Symposium of the Society of Core Analysts (Vol. 27, p. 30)*.
- Zhang, Z. and Scherer, G.W., 2017. Supercritical drying of cementitious materials. *Cement and Concrete Research*, 99, pp.137-154.
- Zhang, Z. and Scherer, G.W., 2019. Evaluation of drying methods by nitrogen adsorption. *Cement and Concrete Research*, 120, pp.13-26.
- Zhengwen, Z., Grigg, R. and Ganda, S. (2003). Experimental Study of Overburden and Stress Influence on Non-Darcy Gas Flow in Dakota Sandstone. *SPE Annual Technical Conference and Exhibition*. Denver, Colorado, USA, SPE, 10. 10.2118/84069-MS.
- Zils, S., Timpel, M., Arlt, T., Wolz, A., Manke, I. and Roth, C., 2010. 3D visualisation of PEMFC electrode structures using FIB nanotomography. *Fuel Cells*, 10(6), pp.966-972.
- Fisher, Q.J., Haneef, J., Grattoni, C.A., Allshorn, S. and Lorinczi, P., 2018. Permeability of fault rocks in siliciclastic reservoirs: Recent advances. *Marine and Petroleum Geology*, 91, pp.29-42.

- Fauchille, A.L., Hedan, S., Prêt, D., Valle, V., Cabrera, J. and Cosenza, P., 2014. Relationships between desiccation cracking behavior and microstructure of the Tournemire clay rock by coupling DIC and SEM methods. *Proceedings of IS on Geomechanics from Micro to Macro*, Cambridge, UK. CRC Press/Balkema, Leiden, The Netherlands, 1421, p.1424.
- Zhang, T., Ellis, G.S., Ruppel, S.C., Milliken, K. and Yang, R., 2012. Effect of organic-matter type and thermal maturity on methane adsorption in shale-gas systems. *Organic geochemistry*, 47, pp.120-131.
- Fathi, E. and Akkutlu, I.Y., 2013. Lattice Boltzmann method for simulation of shale gas transport in kerogen. *Spe Journal*, 18(01), pp.27-37.
- Kou, R., Alafnan, S.F. and Akkutlu, I.Y., 2017. Multi-scale analysis of gas transport mechanisms in kerogen. *Transport in Porous Media*, 116(2), pp.493-519.
- Kang, S.M., Fathi, E., Ambrose, R.J., Akkutlu, I.Y. and Sigal, R.F., 2011. Carbon dioxide storage capacity of organic-rich shales. *Spe Journal*, 16(04), pp.842-855.
- Sondergeld, C.H., Ambrose, R.J., Rai, C.S. and Moncrieff, J., 2010, February. Micro-structural studies of gas shales. In *SPE unconventional gas conference*. OnePetro.
- Scott, G. G, 2020. *Multiscale Image Based Pore Space Characterisation and Modelling of North Sea Sandstone Reservoirs* (Doctoral dissertation, University of Aberdeen).